ON THE NATURE OF NEUTRON STARS IN ACCRETING SYSTEMS

Adelle Jane Goodwin

SUPERVISED BY:
A. Prof. Duncan K. Galloway
Prof. Alexander Heger

A thesis submitted for the degree of
Doctor of Philosophy
at the School of Physics and Astronomy,
Monash University, Australia

January, 2021

COPYRIGHT NOTICE

"We are not at the end but at the beginning of a new physics. But whatever we find, there will always be new horizons continually awaiting us."
– Michio Kaku, Astrophysicist

Did you know that you can tell a lot about what is happening on land from what is happening in the sky above? Ever wondered how to navigate home when lost in the bush? Or how to use the sky and stars to predict environmental changes? What if I were to tell you that a brief glance at a single constellation in the sky can tell you about current local animal behaviour, seasonal change, the availability of food sources, and impending weather patterns? – Krystal de Napoli, Gomeroi woman and Astrophysicist

This thesis acknowledges the oldest astronomers: Aboriginal and Torres Strait Islanders from Australia, who looked to the skies some 65,000 years ago and began studying, understanding, and using the stars throughout their rich history. This thesis acknowledges the Traditional Owners of country throughout Australia, particularly the Wurundjeri tribe, on who's land this research was primarily carried out. I pay my respects to their Elders past and present, and recognise the significant contributions of their ~65,000 years of Astronomy research.

For my grandmothers Janet and Ruth, two strong, resilient women; who taught me a woman never can't..

ABSTRACT

When a neutron star is formed in a binary system, it can accrete material from the companion star. This accretion onto the surface of the neutron star releases extraordinary amounts of energy and is visible across the electromagnetic spectrum. Under certain conditions, the material accumulating on the surface of a neutron star can ignite and burn in an unstable way, resulting in a spectacular explosion known as a Type I thermonuclear X-ray burst. These processes give us insight into the extremes of physics including the most dense matter known, nuclear reactions in energetic environments, and how material moves in strong magnetic and gravitational fields.

Observations and models of accreting neutron stars have discovered much since their discovery in the 1970s, including constraints on the dense equation of state, and the nuclear reaction pathways that can occur under extreme conditions. The dense equation of state is still not well constrained, however, and there are many nuclear reaction rates that are yet to be constrained, and many observational phenomenon that are yet to have robust explanations, such as oscillations that occur during some X-ray bursts. In this thesis we present new observations and modelling techniques that explore the physics of accreting neutron star systems, including the mechanism behind accretion outbursts, the energetics of X-ray bursts, and possible evolutionary pathways.

We present the first 2D model of the accreted layers on the surface of a neutron star that explores the heat conduction and transport to infer the ignition location of X-ray bursts. Through detailed modelling of the energetics of X-ray bursts, we analyse the energy extracted during a burst, the amount of energy released as neutrinos, and we develop a simple relation for the total energy released in a burst based on the hydrogen content. We present the detection of X-ray bursts for the first time from the accreting neutron star XMMU J181227.8–181234, and classify the system as a candidate ultracompact binary. We develop a new method of obtaining accreting neutron star system parameters using a Bayesian approach to match observations of X-ray burst trains with a model, and demonstrate the software through a case study of the accretion-powered millisecond pulsar SAX J1808.4–3658. Using the system constraints we obtain through X-ray burst modelling, we perform evolutionary track calculations for SAX J1808.4–3658, accounting for irradiation and evaporation of the donor star due to the accretion luminosity and the pulsar radiation pressure. Finally, we present the most detailed observations of an accreting neutron star coming into outburst to date, providing important observational constraints for our theoretical understanding of accretion disks, including direct evidence that supports the theory that accretion outbursts are caused by hydrogen ionisation in the accretion disk.

This work contributes broadly to our understanding of accreting neutron stars, their evolution, accretion disk structure and instabilities, nuclear reactions in extreme environments, and the energetics of X-ray bursts.

DECLARATION

I hereby declare that this thesis contains no material which has been accepted for the award of any other degree or diploma at any university or equivalent institution and that, to the best of my knowledge and belief, this thesis contains no material previously published or written by another person, except where due reference is made in the text of the thesis[1].

This thesis includes six original papers published in peer reviewed journals. The core theme of the thesis is observations, modelling, and theoretical understanding of accreting neutron stars. The ideas, development and writing up of all the papers in the thesis were the principal responsibility of myself, the student, working within the School of Physics and Astronomy under the supervision of Assoc. Prof. Duncan Galloway and Prof. Alexander Heger.

The inclusion of co-authors reflects the fact that the work came from active collaboration between researchers and acknowledges input into team-based research. Co-authors are not Monash students unless indicated. In the case of Chapters 3, 4, 5, and 6 my contribution to the work involved the following:

- **Chapter 3**

  Publication title: *'Neutrino losses in Type I thermonuclear X-ray bursts: An improved nuclear energy generation approximation'*

  Status: Published

  Contribution: Model grid calculations, contributed to project idea, data analysis, manuscript authorship (70%)

  Co-authors:

  - Alexander Heger: Kepler model, analysis tool for finding free nuclear energy, contributed to project idea, manuscript input (20%)
  - Duncan Galloway: Manuscript input, contributed to project idea (10%)

  Publication title: *'X-ray burst ignition location on the surface of accreting pulsars: Can bursts ignite at the hotspot?'*

  Status: Submitted

  Contribution: Model design, implementation, data analysis, manuscript authorship (65%)

  Co-authors:

  - Alexander Heger: model design and implementation, manuscript input (25%)
  - Frank Chambers: model design (5%)
  - Anna Watts: original project idea, manuscript input (3%)

1 Please find the licenses issued to me to allow me to reproduce certain figures and copyright permissions from the relevant journals here: https://figshare.com/s/06cbbb772f935f0d1984

– Yuri Cavecchi: model design, manuscript input (2%)

- **Chapter 4**

  Publication title: *'XMMU J181227.8–181234: a new ultracompact X-ray binary candidate'*

  Status: Published

  Contribution: Data analysis, manuscript authorship (65%)

  Co-authors:

  – Duncan Galloway: Spectral modelling using `xspec`, contributed to project idea, manuscript input (10%)
  – Jean in 't Zand: Initial bursts discovery, contributed to project idea, manuscript input (12%)
  – Erik Kuulkers: Manuscript input (2%)
  – Anna Bilous: Search for burst oscillations, manuscript input (8%)
  – Laurens Keek: Manuscript input (3%)

  Publication title: *'Enhanced optical activity 12 days before X-ray activity, and a 4 day X-ray delay during outburst rise, in a low-mass X-ray binary'*

  Status: Published

  Contribution: Swift X-ray and UV data proposal and analysis, manuscript authorship, coordination of the team, final data analysis, data interpretation (55%)

  Co-authors:

  – David Russell: Optical observation processing, disk model, data interpretation, manuscript input (15%)
  – Duncan Galloway: Outburst prediction, manuscript input (3%)
  – Maria Cristina Baglio: LCO observations, optical observation method description, manuscript input (5%)
  – Aastha Parikh: UV data analysis (3%)
  – David Buckley: SALT spectra data (3%)
  – Jeroen Homan: NICER data processing and method (5%)
  – Daniel Bramich: LCO observations data processing (2%)
  – Jean in 't Zand: Manuscript comments (1%)
  – Craig Heinke: Manuscript comments, Swift X-ray data upper limits (2%)
  – Enrico Kotze: SALT spectrum processing (2%)
  – Domitilla de Martino: Manuscript comments, SALT observations (1%)
  – Alessandro Papitto: Manuscript comments, SALT observations (1%)
  – Fraser Lewis: LCO observations (1%)
  – Rudy Wijnands: UV data analysis (1%)

- **Chapter 5**

  Publication title: *'A Bayesian approach to matching thermonuclear X-ray burst observations with models'*

  Status: Published

  Contribution: Code development, data analysis, manuscript authorship, contributed to project idea (75%)

  Co-authors:

  - Duncan Galloway: Initial project idea, manuscript input (10%)
  - Alexander Heger: Manuscript input (5%)
  - Andrew Cumming: Original Settle model, manuscript input (5%)
  - Zac Johnston: Manuscript input (5%, Monash student)

- **Chapter 6**

  Publication title: *'The binary evolution of SAX J1808.4–3658: Implications of an evolved donor star'*

  Status: Published

  Contribution: Model runs, data analysis, manuscript authorship (85%)

  Co-authors:

  - Tyrone Woods: Initial project idea, manuscript input (15%)

The papers are presented exactly as published, and permission to include these papers as presented in this thesis is included in the Author Rights Policy of the relevant journal copyright statements.

Adelle Jane Goodwin
19 January 2021

I hereby certify that the above declaration correctly reflects the nature and the extent of the student's and co-authors' contributions to this work. In instances where I am not the responsible author I have consulted with the responsible author to agree on the respective contributions of the authors.

A. Prof. Duncan K. Galloway
19 January 2021

PUBLICATION LIST

Publications appearing in this thesis:

1. A. J. Goodwin, A. Heger and D. K. Galloway (Jan. 2019). 'Neutrino Losses in Type I Thermonuclear X-Ray Bursts: An Improved Nuclear Energy Generation Approximation'. *ApJ* 870.2, 64, p. 64. DOI: 10.3847/1538-4357/aaeed2. arXiv: 1808.02225 [astro-ph.HE]

2. A. J. Goodwin et al. (July 2019b). 'XMMU J181227.8-181234: a new ultracompact X-ray binary candidate'. *MNRAS* 486.3, pp. 4149–4157. DOI: 10.1093/mnras/stz1094. arXiv: 1904.10970 [astro-ph.HE]

3. A. J. Goodwin et al. (Dec. 2019a). 'A Bayesian approach to matching thermonuclear X-ray burst observations with models'. *MNRAS* 490.2, pp. 2228–2240. DOI: 10.1093/mnras/stz2638. arXiv: 1907.00996 [astro-ph.HE]

4. A. J. Goodwin and T. E. Woods (May 2020). 'The binary evolution of SAX J1808.4-3658: implications of an evolved donor star'. *MNRAS* 495.1, pp. 796–805. DOI: 10.1093/mnras/staa1234. arXiv: 2003.02970 [astro-ph.HE]

5. A. J. Goodwin et al. (June 2020a). 'A 12 day delay between optical and X-ray activity during outburst rise in a low-mass X-ray binary'. *arXiv e-prints*, arXiv:2006.02872, arXiv:2006.02872. arXiv: 2006.02872 [astro-ph.HE]

6. A. J. Goodwin et al. (Oct. 2020b). 'X-ray burst ignition location on the surface of accreting X-ray pulsars: Can bursts preferentially ignite at the hotspot?' *MNRAS* submitted

Co-authored publications:

1. D. K. Galloway, A. J. Goodwin and L. Keek (Apr. 2017). 'Thermonuclear Burst Observations for Model Comparisons: A Reference Sample'. *PASA* 34, e019, e019. DOI: 10.1017/pasa.2017.12. arXiv: 1703.07485 [astro-ph.HE]

2. D. K. Galloway et al. (Aug. 2019). 'High-Energy Transients: Thermonuclear (Type-I) X-Ray Bursts'. In *Southern Horizons in Time-Domain Astronomy*. Ed. by R. E. Griffin. Vol. 339. IAU Symposium, pp. 121–126. DOI: 10.1017/S1743921318002363. arXiv: 1803.00223 [astro-ph.HE]

3. Y. Cavecchi et al. (July 2020). 'The efficiency of nuclear burning during thermonuclear (Type I) bursts as a function of accretion rate'. *arXiv e-prints*, arXiv:2007.08081, arXiv:2007.08081. arXiv: 2007.08081 [astro-ph.HE]

4. M. C. Baglio et al. (Oct. 2020). 'Probing jet launching in neutron star X-ray binaries: the variable and polarized jet of SAX J1808.4–3658'. *ApJ* submitted

ACKNOWLEDGMENTS

First and foremost, I would like to thank my supervisors, Duncan and Alex. None of this research would have been possible without your endless time, effort, advice, encouragement, feedback, and patience. Thank you for always having time for me and never making me feel like my silly questions were actually silly. From when I first began my research journey back in 2015 you both have helped me grow, learn, and challenged me to become the best researcher possible. 6 papers in 3.5 years may seem like the impossible, but we did it!
I would also like to thank my collaborators who provided me support, feedback, advice, encouragement, and valuable discussions: Jean, Andrew, Tyrone, Anna, Frank, Yuri, Craig, Dave, Zac, Adam, and Hendrick.
Next I would like to acknowledge the endless love and support I received over the last 3.5 years from my family. Mum, Dad, Emma, Danny, Laila, Mia, Ben, Paula, Ally, Christoph, Ebony, Kiara: thank you for being my biggest fans and support network. To my twin, Jacinda, who understands me at a level no one else on this world quite gets - thank you for everything Binny.
Next my friends and colleagues from Monash - Lucy, Daniel, James, Vaishali, Dave, Conrad, Andy, Tom, Andrew: you guys made everything possible by supporting me, listening to me rant, and knowing when it was time to just stop and have some wine. A special acknowledgement to Shaun: you are so missed.
To my Nanna Gran who was always nearby with a cup of tea and some sensible advice; and to my Pop, who was always there to get excited when I called him to tell him about my latest paper: thank you for everything and I miss you both.
And finally, Rory. Thank you for everything you are and that you do for me. Whether it was answering my texts every time I needed to write "affect" or "effect"[2], to travelling the world with me while I was off attending conferences, to making sure I'd eaten when I was tired and stressed: this was all possible because of you, so thank you.

I acknowledge support by an Australian Government Research Training Program scholarship. This work benefited from support, in part, by the National Science Foundation under Grant No. PHY-1430152 (JINA Center for the Evolution of the Elements) and from the Astronomical Society of Australia.

2 If there are any affects that should be effects or vice versa in this thesis I place all responsibility on Rory

CONTENTS

ABBREVIATIONS

AMSP: Accretion-powered Millisecond Pulsar
AMXP: Accretion-powered Millisecond X-ray Pulsar
LMXB: Low Mass X-ray Binary
HMXB: High Mass X-ray Binary
CV: Cataclysmic variable star
QPOs: Quasi-periodic Oscillations

TELESCOPES

NICER: Neutron Star Interior Composition Explorer
INTEGRAL: INTErnational Gamma-Ray Astrophysics Laboratory
Swift: Neil Gehrels Swift Observatory
RXTE: Rossi X-ray Timing Explorer
XMM-Newton: X-ray Multi-Mirror Mission
Chandra: Chandra X-ray Observatory
SALT: South African Large Observatory
LCO: Las Cumbres Observatory
BeppoSAX
ANS Observatory: Astronomical Netherlands Satellite

PHYSICAL CONSTANTS

Solar mass, $M_\odot = 1.989 \times 10^{33}\,g$
Gravitational constant, $G = 6.6743 \times 10^{-8}\,cm^3\,g^{-1}\,s^{-2}$
Speed of light, $c = 2.998 \times 10^{10}\,cm\,s^{-1}$
Stefan-Boltzmann constant, $\sigma = 5.6704 \times 10^{-5}\,erg\,cm^{-2}\,s^{-1}\,K^{-4}$
Boltzmann constant, $k = 1.380649 \times 10^{-16}\,erg\,K^{-1}$
Planck constant, $h = 6.6261 \times 10^{-27}\,cm^2\,g\,s{-}1$
Proton mass, $m_p = 1.6726 \times 10^{-24}\,g$

1 INTRODUCTION AND BACKGROUND

One of the most fundamental forces in the Universe is gravity. Gravity is familiar to us: it keeps our feet planted firmly on the Earth, it gives weight to everyday objects, and is the reason our planet formed from a series of small rocks, dust, and gas, enabling life to develop. On a larger scale gravity keeps the Earth firmly bound to our source of heat and light, the Sun, and it formed the Universe as we know it today into structures through the formation of stars, planets, galaxies, and galaxy clusters.

Gravitational attraction exists between all things but the strength of this attraction is determined by one thing: mass. It is for this reason that gravity often has the largest influence on macroscopic scales between stars, galaxies, black holes, and neutron stars, and less of an influence at the subatomic level between protons, neutrons, electrons, and other particles. The more compact a large mass is, the stronger its gravitational field. Thus, the strongest gravitational fields exist around the most massive and compact objects we know of: neutron stars and black holes. Inside of these strong gravitational fields gravity powers some of the most energetic events we observe in the Universe.

Compact objects are the dense remnants left over after a star ends the nuclear burning phase of its life. They include white dwarfs, neutron stars, and black holes. Neutron stars are among the most dense objects in the universe, and as such are unique laboratories of fundamental physics. Isolated neutron stars and black holes are hard to detect, as they do not emit radiation through nuclear burning like a classical star. But, neutron stars and black holes with binary companions, or those that get close enough to a nearby star or gas cloud, may emit X-rays and gamma rays due to the supply of gas to the compact object. These accretion events, powered by the gravitational potential energy released as gas spirals in to the compact objects, produce extraordinary amounts of energy. This high-energy radiation enables us to detect compact objects with telescopes and view directly how material moves in their strong gravitational fields. Such "accreting" neutron stars and black holes thus give us direct information about the extremes of physics: from the densest matter known, through nuclear reactions in energetic environments, to how material moves in strong magnetic and gravitational fields.

1.1 ACCRETING NEUTRON STARS

1.1.1 *Discovery and history*

Neutron stars were first proposed as objects that were formed during the collapse of a star at the end of the nuclear burning phase of its life. Supernova explosions had been observed (e.g. Baade and Zwicky, 1934), and the extraordinary amount of energy produced by these explosions required an extraordinary explanation. In

the early 1930s, Baade and Zwicky (1934) recognised that the apparent observed frequency of supernovae explosions of one per galaxy per one thousand years, the approximate lifetime of a star of 10^{12} years, and the approximate number of stars in a "nebula" of 10^9 stars could indicate that a star undergoes one supernova in its lifetime. They suggested that during the explosions neutrons produced at the surface of an ordinary star would fall in towards the center and produce a neutron star, reaching densities similar to those found inside an atomic nucleus. It's interesting to note that Baade and Zwicky proposed the concept of a neutron star just 2 years after the discovery of the neutron by Chadwick (1932).

This prediction that normal stars could transform into neutron stars during a supernova explosion was further supported by the observation of large redshift[1] in the spectra of a supernova explosion from IC 4182 in 1937 (Minkowski, 1939). Zwicky (1938) suggested that this large redshift could be explained by gravitational redshift, caused by the strong gravitational field of the dense neutron star that was forming. Thus the concept of a highly collapsed star, consisting primarily of neutrons, gained traction and neutron stars became a credible astronomical object. However, since neutron stars were not expected to be undergoing nuclear fusion, there was little hope at the time of directly observing an isolated neutron star, and over the next 30 years not many developments were made.

With the discovery of extrasolar X-ray sources by Giacconi et al. (1962) came new developments for neutron stars. They sent 3 geiger counters on a rocket in order to observe the reflected X-ray radiation of the moon, and instead discovered a large amount of radiation scattered throughout the area of the sky they observed. This radiation was presumed to be soft X-rays[2], which Giacconi et al. (1962) concluded had to be from sources outside of the solar system.

In 1967, PhD student Jocelyn Bell Burnell discovered unusual pulsating radio signals in observations with the Mullard Radio Observatory. The emission seemed to come from an object within the galaxy, and strangely, the pulses observed repeated with a precise period, so exact that it could be measured to one part in 10^7 seconds (Hewish et al., 1968). The absence of parallax in the observations allowed Hewish et al. (1968) to conclude that this pulsed emission originated somewhere far outside of the solar system, and based on the pulse properties they deduced that the object had to be less than 10^3 km in size, and the energy emitted during a single pulse was approximately 10^{17} erg. Conveniently, 2 years before this discovery, Finzi (1965) had proposed a mechanism for emission of electromagnetic radiation by neutron stars: through the vibrational energy of the star. This prompted Hewish et al. (1968) to conclude that the pulsed radio emission they had observed was likely a pulsating neutron star, consequently discovering the first pulsar and one of the only direct observational signatures of neutron stars.

1 Redshift is the shift of light to longer (redder) wavelengths, usually because the object emitting the light is moving away from the observer. In strong gravitational fields, to an observer outside of the influence of the gravitational field, light can also appear to be redshifted, which is known as gravitational redshift. Gravitational redshift is a direct consequence of Einstein's theory of general relativity.

2 Soft X-rays are usually defined as lower energy X-rays with energies in the range 0.1–5 keV, whereas hard X-rays are usually defined as higher energy X-rays, with energies of approximately 5–100 keV.

At the same time, when one of the X-ray sources discovered by Giacconi et al. (1962) was identified as the known supernova remnant the Crab Nebula (Hayakawa and Matsuoka, 1964; Bowyer et al., 1964), it became apparent that many of the X-ray sources could be supernova remnants, and the X-ray emission in the Crab Nebula was likely produced by a neutron star. It wasn't until the optical detection of the X-ray source Sco X–1 (Sandage et al., 1966), which wasn't a known supernova remnant, that it was suggested that some of these Galactic X-ray sources could be other classes of objects. Sandage et al. (1966) noticed that the optical and UV emission of Sco X–1 was similar to the emission observed by novae or U Gemorium stars, which were known accreting white dwarfs. It soon was realised by Shklovsky (1967) that the cooler, optical emission in this source combined with some very hot X-ray emission in a compact region could in fact be the observational signature of an accreting neutron star. They concluded that if the coincidence of the optical emission similar to an old nova with the X-ray emission was correct, then the emission could be explained by an efficient stream of gas flowing from a companion star in a close binary system toward a central object, which is a neutron star. Thus the second observational signature of neutron stars was discovered, enabling rapid advancements in the understanding of these exotic objects, and the behaviour of matter at extreme densities.

Now, more than 85 years since the neutron star was first proposed, we have observed more than 2,000 within our Galaxy (e.g. Manchester et al., 2005). Whilst there should be approximately 1 billion neutron stars in the Milky Way Galaxy (e.g. Camenzind, 2007), the fact that we have only observed a relatively small number of them is indicative of just how hard they are to find. Young neutron stars are more likely to be pulsars, releasing visible electromagnetic radiation, and over time neutron stars cool since they do not generate their own heat. Thus most of the known radio pulsars are young radio pulsars. However, if a neutron star interacts with surrounding material, for example by accreting from a companion star, the neutron star can retain, or even gain, heat, and emit electromagnetic radiation for most of its life. These are the accreting neutron stars, which are important objects for our understanding of dense matter, strong gravitational fields, and nuclear reactions in extreme environments. Whilst we have discovered much about these exotic systems since their discovery approximately 50 years ago, there are many questions still left unanswered.

1.2 OBSERVATIONS OF ACCRETING NEUTRON STARS

There are two different classes of X-ray binaries: low mass X-ray binaries (LMXBs), where the companion star is a low mass star ($\lesssim 1\,M_\odot$); and high mass X-ray binaries (HMXBs), where the companion star is a high mass star ($\gtrsim 1\,M_\odot$). In this work we primarily focus on LMXBs, and note that the observational signatures and evolutionary pathways of HMXBs can be quite different to LMXBs.

Accreting neutron star systems can appear observationally as both persistent and transient X-ray sources. Transient sources can be inactive for years, and then suddenly flare into outburst releasing extraordinary amounts of energy when material transfers directly onto the neutron star from a surrounding disk. Persistent

sources may accrete persistently from the companion and remain continuously active. A diagram of an accreting neutron star in an LMXB is shown in Figure 1.1.

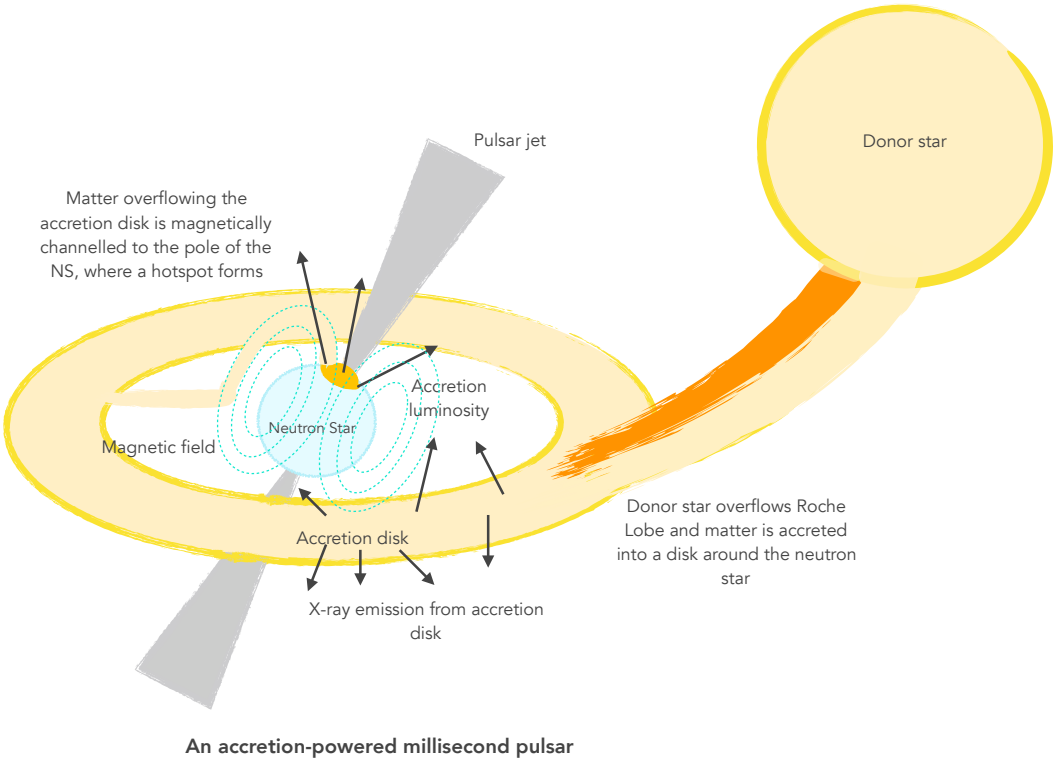

FIGURE 1.1: A diagram of an accreting neutron star which happens to also be a pulsar.

Woosley and Taam (1976) and Taam (1984) were among the first to describe the accumulation of matter onto a neutron star by postulating that matter which is transferred to the neutron star is not accreted directly by the star, but forms an accretion disk (see Section 1.3 for more detail on accretion disks). Tidal forces then enable matter to move inward in the disk by removing angular momentum from the material and returning the angular momentum back to the orbit, causing the matter to spiral to the neutron star surface. This is the source of the first type of X-ray emission that is observed from these systems: persistent emission from the accretion flow.

Taam (1984) also described the violent thermonuclear processes that ignite this accreted hydrogen or helium rich layer on the surface of the neutron star. These so-called "X-ray bursts" are the source of bright flashes ($L \sim 10^{38}$ erg) sometimes observed coming from these systems. X-ray bursts represent the second type of emission that is observed from accreting neutron star systems, which is much more energetic but shorter lasting (10s of seconds) than the persistent emission. Transient systems sometimes exhibit thermonuclear X-ray bursts when they are in outburst.

1.2.1 *Neutron star properties*

Neutron star properties are crucial in understanding how matter behaves at extreme densities, among other things. Accreting neutron star systems are unique as they often provide the ability to obtain constraints on system parameters that are difficult to obtain for isolated neutron stars.

1.2.1.1 *Mass, radius, and equation of state*

Mass and radius measurements of neutron stars are particularly sought after due to their ability to help constrain the poorly understood equation of state of dense matter. The equation of state describes the physical state of dense matter under the conditions found inside a neutron star. Usually an equation of state describes the relationship between density, pressure, volume, and temperature.

Obtaining mass constraints of observed neutron stars is only possible in specific circumstances; for example if the neutron star is a pulsar in a binary orbit. For neutron stars in binary orbits, the binary mass function, f, is given by (e.g. Shapiro and Teukolsky, 1983)

$$f = \frac{(m_2 \sin i)^3}{(m_1 + m_2)^2} = \frac{4\pi^2 (a_1 \sin i)^3}{G P_{orb}{}^2} \tag{1.1}$$

where m_1 is the neutron star mass, m_2 is the companion mass, a_1 is the semi-major axis of the orbit, i is the binary inclination (defined as the angle between the line of sight and the orbital angular momentum vector), and P_{orb} is the orbital period.

The Keplerian parameters P_{orb} and $a_1 \sin i$ can be measured through precise pulsar timing (Manchester and Taylor, 1977) if the neutron star is a pulsar. Thus if accurate constraints on the companion mass and the inclination can be obtained, the pulsar mass can be inferred. In edge on binaries the inclination is well constrained if transits are observed, and the companion mass can be constrained to varying accuracy through optical observations.

The most massive neutron star discovered to date is the millisecond pulsar J0740+6620, with a mass of $2.14^{+0.2}_{-0.18}\,M_\odot$ (Cromartie et al., 2020). The mass was measured using the Shapiro time delay, which is the small delay in pulse arrival times observed when the pulsar passes behind the companion star, and is caused by the curvature of spacetime by the companion star. The discovery of such a massive neutron star has enabled some possible equation of states to be ruled out, and has shed some light on the theoretical mass limit for a neutron star.

1.2.1.2 *Gravitational field*

Neutron stars have very strong gravitational fields. The surface gravity, g is related to the mass and radius via (e.g. Shapiro and Teukolsky, 1983)

$$g = \frac{GM}{R^2}(1+z) \tag{1.2}$$

where z is the gravitational redshift ($1 + z = \sqrt{1 - 2GM/Rc^2}$), M is the neutron star gravitational mass and R is the neutron star radius in the observer frame.

Gravitational redshift is a direct consequence of Einstein's theory of general relativity and is the phenomenon that light being emitted from a strong gravitational field can appear redshifted to an observed far away due to the influence of the gravitational field (e.g. Manchester, 2017b).

Thus if the mass and radius are known, for example through pulsar mass measurements, one can infer the gravitational field strength and redshift of the neutron star.

1.2.2 *Inclination*

The geometry of the accretion disk in accreting neutron star systems and the angle at which it is observed can affect the angular distribution of the X-ray emission, as the accretion disk can reflect, block, or add to radiation emitted. The accretion disk can affect the persistent emission and cause it not to be isotropic, depending on the angle at which the system is viewed (Lapidus and Sunyaev, 1985), as can be seen in Figure 1.1. X-ray burst emission is also affected by the angle at which the system is viewed, but is affected differently to the persistent emission, as it is thought to be emitted from the entire surface of the neutron star (whereas persistent emission comes from just the location of accretion). Thus there are two different anisotropy factors defined when considering the effect of the system inclination, ξ_p for the persistent emission and ξ_b for the burst emission.

There are different models that have been developed to account for the anisotropies in the X-ray emission from accreting neutron star systems (Fujimoto, 1988; Lapidus and Sunyaev, 1985; He and Keek, 2016, e.g.). The relationship between the anisotropy factors and the inclination of the accretion disk depend on assumptions made about the shape and extent of the accretion disk. Thus there are some differences in the relationships derived under different assumptions by different authors. Among the first, Fujimoto (1988) compared observed burst fluences and persistent fluxes of two sources (EXO 0748–676 and 4U/MXB 1636–53) to place constraints on the angular distribution of the burst and persistent emission. They assumed a geometrically thick disk and evaluated the anisotropy factors based on this assumption however they did not take into account the deflection of light rays in the gravitational field. Lapidus and Sunyaev (1985) studied the angular distribution of emission by assuming a geometrically thin accretion disk that stretches down to the stellar surface. However, using this assumption it was difficult to interpret the burst energetics. More recently, He and Keek (2016) derived the relationship between the anisotropies and the disk inclination for different concave accretion disks. They explored four different geometries: flat, trapezoidal, triangular, and curved. The flat disk geometry yields very similar anisotropy derivations to those derived by Fujimoto (1988), and is perhaps the simplest case. We describe the anisotropy relations for this flat disk structure below, which we use in Chapter 5.

The anisotropy factors for both the burst and persistent emission, ξ_b and ξ_p respectively, are related to the intrinsic luminosity ($L_{b,p}$) and observed fluxes ($F_{b,p}$) of the system via

$$L_{b,p} = 4\pi d^2 \xi_{b,p} F_{b,p} \tag{1.3}$$

where d is the distance to the source.

Under the assumption that the accretion disk and star are axisymmetric, ξ_b and ξ_p only depend on the inclination angle, θ, which is the angle between the rotation axis and the direction from which the system is viewed by an observer (Fujimoto, 1988). Under the assumption that all persistent energy radiates isotropically from the disk plane (i.e. the flat disk shape described by He and Keek (2016)), the persistent emission anisotropy is related to the inclination angle via

$$\xi_p^{-1} = 2|\cos\theta| \tag{1.4}$$

Thus for systems with small inclination angles (observed from near the rotation axis), the persistent flux is stronger by a factor of two than if the emission was isotropically distributed. For large inclination angles (systems observed near the disk plane), the persistent flux is not affected at all.

For the burst emission anisotropy, under the assumption that photons are emitted spherically symmetrically from the stellar surface during a burst, and assuming that the burst flux is composed of the direct flux from the stellar surface plus the reflected flux from the disk, the burst anisotropy factor is given by

$$\xi_b^{-1} = \frac{1}{2} + |\cos\theta| \tag{1.5}$$

Thus the anisotropy is larger for the persistent flux than for the burst flux in all cases.

When considering direct observations of the persistent and burst fluxes from accreting neutron star systems, it is necessary to correct the luminosities observed by these anisotropy factors. However, often the inclination angle of the system is not well constrained (unless a transit is observed), so this can be difficult and often the inclination is not accounted for in reported observations.

1.3 ACCRETION DISKS

In order to understand accreting neutron stars, we first need to understand the process of accretion, and the formation of accretion disks. Accretion is one of the most powerful means of producing energy in the Universe. An accretion disk is a circular structure of diffuse material in orbit around a central gravitating body (e.g. Pringle, 1981). They are a common phenomenon in astrophysics, and can be found in a wide range of systems from protoplanetary disks, to active galactic nuclei, quasars, and around compact objects in binary systems. An accretion disk is formed when matter falling into the potential well of a gravitating body forms a disk spinning around the central object (e.g. Pringle and Rees, 1972). If infalling matter experiences free radial infall to the central object, an accretion disk will not be formed. However, if the accreting material possesses significant angular momentum from, for example, Roche Lobe overflow or a common envelope in a binary system, free fall is prevented. When this material is sufficiently close to the primary gravitating body, centrifugal forces are comparable to gravitational

forces, and the accreted matter will begin to rotate in a circular orbit (Shakura and Sunyaev, 1973), forming an accretion disk.

The gravitational potential energy released as a mass m is accreted onto the surface of a body with mass M and radius R is

$$\Delta E_{acc} = \frac{GMm}{R} \approx 10^{20} \frac{M}{M_\odot} \frac{R}{10\,\mathrm{km}}^{-1} \frac{m}{1\,\mathrm{g}} \quad \mathrm{erg} \tag{1.6}$$

where G is the gravitational constant.

The energy released by an accreting neutron star with $M \approx M_\odot$ and $R \approx 10\,\mathrm{km}$, ΔE_{acc} is approximately 10^{20} erg per accreted gram (Frank, King and Raine, 2002). Comparing this energy to that released through nuclear fusion of hydrogen, 6×10^{18} erg per gram, the energy released via accretion onto a neutron star is about 20 times greater, demonstrating that accretion onto a compact object is a very efficient energy release mechanism. The most luminous objects in the Universe, such as quasars (where the compact object is a massive black hole), are powered by the extraction of gravitational potential energy from material as it is accreted onto a gravitating body. The efficiency of energy release during accretion increases as M/R increases, and thus accretion onto neutron stars and black holes provides some of the most energetic and luminous events in the known Universe.

In order to extract the accretion energy, the mass, m, in orbit around the accreting body must move inwards from it's orbit. An object in a circular orbit around a central gravitating body will spiral inwards if angular momentum is extracted from the object. An accretion disk consists of diffuse gas that can release energy as it spirals inwards towards the central body (Pringle, 1981), providing the necessary object that enables accretion energy to be released.

Accretion disks are found around many different kinds of objects in the Universe. As matter in an accretion disk spirals inwards towards the central gravitating body, the infalling material can emit radiation due to gravitational and frictional forces (Pringle and Rees, 1972). The spectrum of this electromagnetic radiation is dependent on the mass of the central object, with accretion disks of young stars and protostars radiating in infrared, whereas those around neutron stars and blacks holes can emit much higher energy radiation, in X-rays. Frank, King and Raine (2002) described how the emitted spectrum of accreted material can be characterised by a radiation temperature, $T_{rad} = h\bar{\nu}/k$, where h is the Planck constant, $\bar{\nu}$ is the typical photon frequency, and k is the Boltzmann constant. The radiation temperature is limited by the blackbody temperature, T_b, which is the temperature a source would have if it radiated entirely as a blackbody spectrum, and the thermal temperature, T_{th}, which is the temperature of accreted material if it's gravitational potential energy were converted entirely into kinetic energy (Frank, King and Raine, 2002). The radiation temperature should lie between the blackbody and thermal temperatures, with T_b providing a lower limit of the temperature and T_{th} providing an upper limit. The blackbody temperature is given by

$$T_b = \left(\frac{L_{acc}}{4\pi R^2 \sigma} \right)^{1/4} \tag{1.7}$$

where σ is the Stefan-Boltzmann constant, and L_{acc} is the accretion luminosity, given by (e.g. Frank, King and Raine, 2002)

$$L_{acc} = \frac{GM\dot{M}}{R} = 1.3 \times 10^{36} \left(\frac{\dot{M}}{10^{16} g\,s^{-1}}\right) \left(\frac{M}{M_\odot}\right) \left(\frac{10\,km}{R}\right) \quad erg\,s^{-1} \tag{1.8}$$

where $\dot{M}$ is the accretion rate.

The thermal temperature is given by

$$T_{th} = \frac{GMm_p}{3kR} \tag{1.9}$$

where m_p is the proton mass.

Thus the energy ($h\bar{\nu}$) of photons emitted from accretion onto a $1.4\,M_\odot$ and 10 km radius neutron star is between 1 keV and 55 MeV. These energies correspond to medium to hard X-ray wavelengths, and possibly γ-ray wavelengths for larger mass black holes. An accreting white dwarf, on the other hand, with solar mass and 5,000 km radius, may be expected to emit photons of lower energy, in the range 6 eV to 100 keV, or optical and UV wavelengths. A protostellar accretion disk has a temperature around 0.8 eV (Armitage, 2015), and thus may be expected to emit photons in the infrared wavelengths. Therefore, through direct observation of the spectra of accretion disks, information about the central body may be determined, and we may infer the presence of neutron stars in some accreting systems.

1.3.1 *Thin disks and the α-disk theory*

It is difficult to extract angular momentum from a solid body in orbit, however, a blob of gas in a circular orbit will be able to redistribute the angular momentum among the gas particles. Some of these gas particles will be able to spiral inwards in the potential well of the gravitating body if there exists an effective mechanism for transporting angular momentum outward (Shakura and Sunyaev, 1973), and the accretion energy can be released. In order for matter in an accretion disk to spiral in towards the gravitating body and release accretion energy, there needs to exist an efficient mechanism for transport of angular momentum outwards. This problem was first recognised by Shakura and Sunyaev (1973), who characterised the efficiency of this mechanism of angular momentum transport in a parameter, α, the effective accretion disk viscosity. They described a scenario in which turbulent motions in the disk enable angular momentum to be transferred outward, and quantified the efficiency of this angular momentum transport

$$\alpha = \frac{\nu_t}{\nu_s} + \frac{H^2}{4\pi\rho\nu_s^2} \tag{1.10}$$

where ν_s is the sound velocity, ν_t is the turbulent velocity, H is the scale height of the disk, and ρ is the density.

In general in a thin accretion disk around a compact object, $\alpha < 1$ (e.g. Shakura and Sunyaev, 1973), and Tetarenko et al. (2018b) found that $0.2 < \alpha < 1$ in models of LMXBs.

Thus viscosity transports angular momentum in accretion disks, and enables the accreted material to spread into a disk, rather than a ring that does not extend

towards the central object. An important parameter that sets the structure of the disk is how efficiently it can cool (King, 2006). The cooling rate of the disk in the simplest case is set by Blackbody radiation, i.e. $Q_{cool} = \sigma T_{eff}^4$ (Lasota, 2001). If the disk can cool efficiently enough, the disk becomes thin, and the density scale height will obey

$$H \approx \frac{c_s}{v_K} R \ll R \tag{1.11}$$

where c_s is the local sound speed and v_K is the Kelperian velocity, given by

$$v_K = \left(\frac{GM}{R}\right)^{1/2} \tag{1.12}$$

In a thin disk, the surface density, Σ, changes on the viscous timescale, which is given by

$$t_{visc} = \frac{R\Delta R}{\nu} \tag{1.13}$$

where ΔR is the typical scale of the density gradient, $\Delta R \approx \sqrt{HR}$, and ν is the kinematic viscosity

$$\nu = \alpha c_s H \tag{1.14}$$

The viscous timescale describes the timescale on which we could expect the surface density and luminosity of an accretion disk to change. This timescale is thus important to consider when describing outbursts in accreting neutron star systems, which are thought to be caused by disk instabilities (see Section 1.7.1).

For a relatively small disk with a radius of 5×10^8–2×10^{10} cm, $H/R \approx 0.01$, $c_s \approx 20$ km/s, such as a disk found in an LMXB, the viscous timescale could range from approximately 2–10 d for α of 0.003–0.9.

1.4 FORMATION AND EVOLUTION OF ACCRETING NEUTRON STARS

Only specific evolutionary channels allow for a compact binary system containing a neutron star that can accrete from its companion. To understand the formation and evolution of accreting neutron stars, first we must understand the evolution of isolated neutron stars.

A neutron star is born with a relatively strong magnetic field (e.g. $\sim 10^{12}$ G), and spinning relatively quickly. Over time, a neutron star will spin down due to rotational loss of kinetic energy, and the magnetic field strength will decay (e.g. Bhattacharya and van den Heuvel, 1991). The emission mechanism of a pulsar is thought to be related to the magnetic field channeling charged particles along the magnetic field lines, with open magnetic field lines located near the magnetic poles, as seen in Figure 1.2.

Charged particles located along closed field lines will corotate with the pulsar, and remain in the system. Conversely, charged particles located along open magnetic field lines will not corotate with the neutron star, and will leave the magnetosphere of the system, producing high energy emission (Goldreich and Julian, 1969). In order for the escaping charged particles to produce high energy emission, a voltage must exist above the polar cap. As detailed by Ruderman and Sutherland

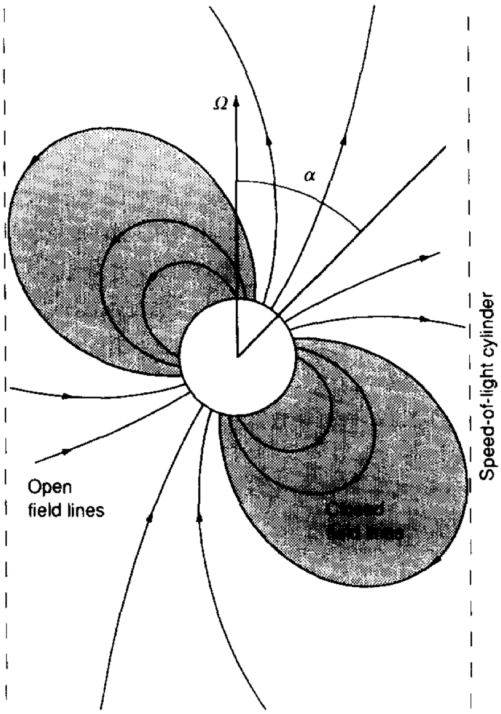

FIGURE 1.2: The geometry of a pulsar and its magnetosphere. Figure reproduced with permission from Bhattacharya and van den Heuvel (1991) Figure 1.

(1975), there is a critical pulsar period and magnetic field strength at which pair creation can continue, and pulsar emission occur. This critical period is

$$P_{crit} = 1.7 B_{12}^{8/13} R_6^{21/13} \rho_6^{-4/13} (15\chi)^{-2/3} \quad s \tag{1.15}$$

where B_{12} is the magnetic field strength in units of 10^{12} G and χ is given by

$$\chi = \frac{\bar{h}\omega}{2mc^2} \frac{B_\perp e\bar{h}}{m^2c^3} \tag{1.16}$$

where $B_\perp \approx (r_{p+}/\rho)B$ is the perpendicular magnetic field, r_{p+} is the radius of the polar cap region out of which a net flow of positive charges maintains the magnetosphere, and ρ is the radius of curvature of the field line along which a sample electron moves.

The critical period and magnetic field combination for which pulsar emission is possible is often referred to as the pulsar "death line", and it is for this reason that radio pulsars are usually young neutron stars, as the weaker magnetic fields and slower spin periods of old neutron stars usually do not allow for pulsar emission.

A radio pulsar is fundamentally different to an X-ray pulsar in terms of their emission mechanisms. Radio pulsars are usually young neutron stars with strong magnetic fields that have not reached the "death line" and thus still emit observable pulsed emission from the polar cap region of the neutron star (e.g. Manchester, 2017b). An X-ray pulsar is formed in a binary system with a normal star, and is not expected to be observable as a radio pulsar, as a wind or corona in the binary system would disperse the pulsed signal and render it non-observable (e.g.

Bhattacharya and van den Heuvel, 1991). Instead, when the binary system has evolved sufficiently to a point that mass transfer can occur from the companion to the neutron star, this accretion causes the system to become observable as an X-ray binary (e.g. Tauris and van den Heuvel, 2006). In some cases, when the magnetic field of the neutron star is of sufficient strength, the accreted material may be channelled to the magnetic poles of the neutron star, causing a hotspot to develop at each pole, and the X-ray emission of the neutron star to appear pulsed (e.g. Nagase, 1989). Thus, not all X-ray binaries that contain an accreting neutron star are accreting pulsars, rather a small subset are. In many of the known accreting pulsars, the spin period has been observed to be decreasing, indicating that the neutron star is in the process of being spun-up through the process of accretion (Patruno and Watts, 2012).

However, an X-ray pulsar may become a radio pulsar and there are many known binary radio pulsars. These pulsars are thought to have once been an X-ray pulsar system, and the binary system has evolved to the point that mass transfer no longer occurs. The combination of weak magnetic field and relatively fast spin period in these systems can be explained by the neutron star spin period having been decreased through the many years of accretion. These so-called "transitional pulsars" are discussed in Section 1.5. Thus even though the neutron star may have a relatively weak magnetic field, its fast spin period ensures it can still emit as a radio pulsar (Smarr and Blandford, 1976).

To understand the evolution of LMXBs, we also need to understand the binary evolution of these systems, and the factors that influence changes in the binary orbits.

1.4.1 *Binary Orbital Evolution*

The gravitational potential of a binary system is given by (e.g. Tauris and van den Heuvel, 2006)

$$\phi = -\frac{GM_1}{r_1} - \frac{GM_2}{r_2} - \frac{GMr_3^2}{2a^3} \tag{1.17}$$

where M_1 and M_2 are the masses of the two stars, r_1 and r_2 are the distance to the center of mass for each star, a is the orbital separation, r_3 is the distance to the rotational axis of the binary, and M is the total mass of the binary, assuming a circular orbit.

Assuming that in a close binary system tidal forces have circularised the orbit, that the two stars exhibit synchronised co-rotation, and that the gravitational fields of the two stars can be described by point masses, there exist fixed equipotential surfaces in a co-moving frame (Kuiper, 1941). The Roche-lobe is defined as the equipotential surface that passes through the first Lagrangian point (L_1, e.g. van den Heuvel, 1994), shown in Figure 1.3.

Mass transfer via Roche-lobe overflow is the primary mechanism via which accreting neutron stars in LMXBs accrete from their companion. Roche-lobe overflow occurs when the companion evolves to fill its Roche-lobe and due to the unbal-

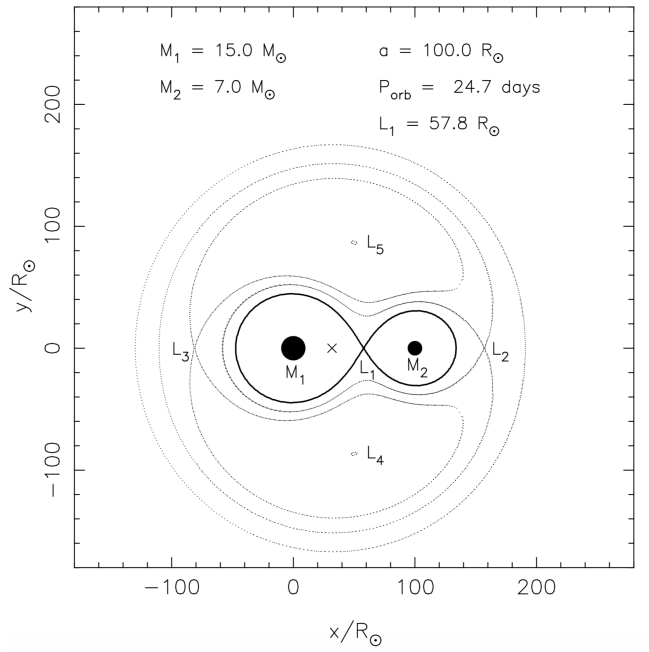

FIGURE 1.3: The equatorial plane showing the equipotential surfaces in a binary. The solid line shows the Roche-lobe, and passes through the inner Lagrangian point, L_1. Figure reproduced with permission from Tauris and van den Heuvel (2006).

anced pressure at L_1, mass transfers from the companion to the accretor. Eggleton (1983) approximated the radius of the Roche-lobe as

$$\frac{R_L}{a} = \frac{0.49q^{2/3}}{0.6q^{2/3} + \ln(1 + q^{1/3})} \tag{1.18}$$

where $q = M_{donor}/M_{accretor}$ is the mass ratio of the binary system.

Mass transfer via Roche-lobe overflow will continue until the companion star no longer fills its Roche-lobe, usually when it has lost $\gtrsim 70\%$ of its mass (Tauris and van den Heuvel, 2006).

However, the question remains: how do LMXBs evolve to the point that a neutron star exists with a Roche-lobe overflowing companion? To understand this question, we must delve into the orbital angular momentum evolution of binary systems. There are three main phases of compact binary evolution that we will discuss in the formation of an accreting neutron star. The first is the formation of the neutron star in a binary system, second is the evolution of that neutron star binary system into a compact binary in which mass transfer can occur via Roche-lobe overflow, and finally is the evolution of the binary during and after mass transfer.

The orbital angular momentum, J is described by

$$J^2 = \frac{G(M_1 M_2)^2}{M_1 + M_2} a\sqrt{1 - e^2} \tag{1.19}$$

where e is the eccentricity of the orbit.

Differentiating this equation we obtain the rate of change of the orbital separation, $\dot{a}$

$$\frac{\dot{a}}{a} = \frac{\dot{J}}{J} - 2\frac{\dot{M}_1}{M_1} - 2\frac{\dot{M}_2}{M_2} + \frac{\dot{M}_1 + \dot{M}_2}{M} \tag{1.20}$$

During mass transfer, if the accretor is more massive than the companion star, the orbit will expand, or if the opposite is true, the orbit will contract.

The total change in orbital angular momentum is given by

$$\dot{J} = \dot{J}_{GR} + \dot{J}_{ML} + \dot{J}_{MB} + \dot{J}_{LS} \tag{1.21}$$

where $\dot{J}_{GR}$, $\dot{J}_{ML}$, $\dot{J}_{MB}$, and $\dot{J}_{LS}$ are the orbital angular momentum changes caused by gravitational radiation, mass loss, magnetic braking, and spin-orbit coupling. More detailed descriptions and the equations that describe these individual orbital angular momentum changes are given in Chapter 6.

During the early phases of evolution of the binary system prior to one of the stars becoming a neutron star, the predominant cause of changes in the orbit are mass loss and common envelope evolution. Later on, when there exists a neutron star and a normal star, magnetic braking and gravitational radiation have a much more predominant affect on the orbit, but mass loss can still contribute to orbital changes depending on how efficiently mass is transferred to the neutron star.

The current prevalent theory that describes the progenitors of neutron star LMXBs is that they are born in uneven mass binary systems (e.g. a $15\,M_\odot$ and $1.5\,M_\odot$ star) with relatively large orbital periods (e.g. 1500 d, Tauris and van den Heuvel, 2006). The low mass star evolves much more slowly than the high mass star, resulting in the high mass star expanding into a red giant and filling its Roche-lobe well before the low mass star has evolved through hydrogen burning. The resulting contraction of the orbit caused by mass being transferred from the more massive star to the smaller star causes a common envelope phase in the binary system. During this phase, the orbit will spiral in, decreasing the orbital period significantly to something $\leqslant 1$ d. At this point the high mass star has lost a significant amount of mass, either to the low mass star or ejected from the system, such that it is a $\approx 5\,M_\odot$ helium star. This star will promptly undergo a supernova explosion, forming a neutron star. This kind of scenario is succinctly outlined in Tauris and van den Heuvel (2006), and presented in Figure 1.4. The exact binary orbital parameters that enable the neutron star and normal star orbit to remain bound during the supernova and formation of the neutron star are not well known. It is thought that the explosion could force the orbit to expand a little, and introduce some eccentricity (e.g. Manchester, 2017a).

Once the neutron star is formed, the binary continues to contract over time until Roche-lobe overflow from the low mass companion begins onto the neutron star. At this point the low mass companion may have evolved into a white dwarf, or may remain an evolved low mass star. This process can result in very compact binary orbits, with periods $\leqslant 1$ d (e.g. Podsiadlowski, Rappaport and Pfahl, 2002).

During the second mass transfer phase of evolution, the system may be observed as an LMXB, with periods of quiescence and outburst as the accretion disk fills due to mass transfer from the companion, and deposits material onto the neutron star during outburst episodes. The accretion torque exerted on the neutron star can result in the spin period of the neutron star increasing, and in rare cases the

neutron star may become a millisecond X-ray pulsar (Manchester, 2017a). During this mass transfer the orbit will expand since the companion star is less massive than the neutron star, ultimately leading to the cessation of mass transfer. The companion star may have evolved into a white dwarf at this point, or may be considered a low mass brown dwarf star, depending on its mass. It is thought that these systems may evolve into detached systems in some cases, meaning that millisecond X-ray pulsars could be the progenitors for the population of isolated radio millisecond pulsars we observe today (e.g. di Salvo et al., 2008).

1.5 ACCRETION-POWERED MILLISECOND PULSARS

Accretion-powered millisecond pulsars (AMSPs) are neutron stars that are spun up through the process of accretion to millisecond spin periods. They are a special class of accreting neutron star, in which pulsations are observed in their X-ray lightcurves. It is for this reason that AMSPs are often called accretion-powered X-ray pulsars (AMXPs), as opposed to radio pulsars that emit pulsed emission in the radio. AMSPs are particularly useful to study as their pulsations provide precise measurements of their spin periods, as well as orbital ephemeris. In 1982, a radio pulsar was discovered, 1919+21, with a spin period of just 1.558 ms (Backer et al., 1982). This millisecond pulsar raised many new and exciting questions for scientists at the time. As discussed in Section 1.4, "normal" pulsars exhibit a decrease in their spin period as they age due to magnetic dipole radiation (Wijnands, 2004). What puzzled scientists with 1919+21 was that this pulsar appeared to be old (with no evidence of a new formation event) (Backer et al., 1982), and so should have had a much slower spin period. This new discovery raised questions about the formation and evolution of pulsars, prompting the suggestion from Alpar et al. (1982) that sufficiently low magnetic field neutron stars accreting matter in a Keplerian disk could be spun up to millisecond periods by the accretion process; a hypothesis soon to be known as the "recycling scenario".

The discovery of a number of radio pulsars with millisecond periods < 10 ms, ages of billions of years and weak surface magnetic fields ($B \sim 10^8 - 10^9$ G) further confirmed that there was indeed a popullsation of old, fast-spinning pulsars that could be explained by the "recycling scenario" theory (Wijnands, 2004). So the search began for direct evidence of the "recycling scenario": coherent X-ray pulsations in a low mass X-ray binary system, to catch a pulsar in the act of spinning up through accretion. In 1998 the discovery of coherent X-ray pulsations in the accretion-powered millisecond pulsar SAX J1808.4–3658 (in 't Zand et al., 1998) confirmed the theory.

The new X-ray transient was detected by in 't Zand et al. (1998) during observations on September 12–17, 1996, using the Wide Field Cameras aboard the *BeppoSAX* satellite. Two Type I X-ray bursts (see Section 1.6) were detected during the observations, which confirmed that the system contained an accreting neutron star, but no persistent pulsations were detected in the persistent flux in the 1996 outburst.

In 1998, a new transient X-ray source, XTE J1808–369, was observed by the All-Sky Monitor aboard the *Rossi X-ray Timing Explorer* (*RXTE*) telescope, which was

within a few arcminutes of SAX J1808.4–3658 and thus likely to be the same source. Wijnands and Klis (1998) analysed the data and discovered clear X-ray pulsations in the lightcurve with a frequency near 401 Hz, the spin period of the pulsar. Thus the "recycling scenario" theory was confirmed and the first accretion-powered millisecond X-ray pulsar was discovered.

Now, more than 20 years since the first AMSP was discovered, there are 21 known sources that exhibit clear millisecond pulsations in their lightcurves, listed in Table 1.1 (note that we have included the intermittent pulsar Aql X–1). All of these systems exhibit short ($\lesssim$ 10 days) orbital periods, and very low mass ($\lesssim 1 M_\odot$) companions (Podsiadlowski, Rappaport and Pfahl, 2002).

As pointed out in the review by Patruno and Watts (2012), the AMSPs exhibit a very wide range of characteristics, including different outburst recurrence times, spin periods, companion star types, luminosities, and magnetic field strengths. Nevertheless, there are common traits to all AMSP systems, including relatively faint outburst luminosities ($L \sim 10^{36}\,\mathrm{erg\,s^{-1}}$) that could indicate low mass accretion rates; relatively short orbital periods, with $P < 12\,\mathrm{hr}$; and small donor stars with masses mostly less than $0.2\,M_\odot$ (with Swift J1749.4–2807 a notable exception). Furthermore, a large fraction ($\approx 45\%$) of AMSPs exist in either ultracompact binary systems, where the donor star is a white dwarf, or orbit a low mass "brown dwarf". While many AMSP companions have been classified as brown dwarf stars, we find evidence in Chapter 6 that the donor star in SAX J1808.4–3658 actually is not a brown dwarf, but an evolved, stripped main sequence star. It is possible that the evolutionary paths of the other AMSPs orbiting brown dwarfs could be similar.

The fastest spinning AMSP is IGR J00291+5934, with a spin frequency of 599 Hz. There appears to be a sharp cut off in spin frequency around 700 Hz, which is consistent with the spin frequency distribution of radio pulsars and could have implications for the neutron star equation of state. As discussed by Patruno and Watts (2012), the NS spin frequency cut off based on the break-up frequency of all realistic equations of state is well in excess of 1000 Hz, however, from observations it appears that the true cut-off spin frequency is well below this.

All of the known AMSPs are transient systems, and exhibit X-ray pulsations only during outburst (e.g. Patruno and Watts, 2012). Up until around 2007, it was widely believed that all AMSPs exhibited X-ray pulsations during outbursts. However, this was disproved when HETE J1900.1–2455 went into outburst in 2005 (Galloway et al., 2006). For the first part of the outburst it behaved typically, showing pulsations. The pulsations soon became intermittent and eventually disappeared completely. This was puzzling and exciting for scientists at the time, as it could help provide observational evidence for the difference between non-pulsating low mass X-ray binaries and pulsating accretion-powered millisecond pulsars (Patruno and Watts, 2012). There are now 3 sources, HETE J1900.1–2455, Aql X–1, and SAX J1748.9–2021, that have intermittent pulsations during outburst, which has raised some debate about whether these sources can be considered true AMSPs. The most notable intermittent pulsar is Aql X–1, which has only shown coherent pulsations once during a short 150 s data segment of its 1998 outburst (Casella et al., 2008).

SOURCE	ν_{spin} (HZ)	P (HR)	M_c ($M_\odot$)	COMPANION	REF.
SAX J1808.4–3658	401	2.01	0.043	BD	[1, 2, 3, 4, 5]
XTE J1751–305	435	0.71	0.014	He WD	[6, 7]
XTE J0929–314	185	0.73	0.0083	C/O WD	[8, 9, 10]
XTE J1807–294	190	0.67	0.0066	C/O WD	[11, 12, 13, 14, 15]
XTE J1814–338	314	4.27	0.17	MS	[16, 17]
IGR J00291+5934	599	2.46	0.039	BD	[18, 19, 20, 21, 22, 23]
HETE J1900.1–2455	377	1.39	0.016	BD	[24]
Swift J1756.9–2508	182	0.91	0.007	He WD	[25, 26]
Aql X–1	550	18.95	0.6	MS	[27, 28]
SAX J1748.9–2021	442	8.77	0.1	MS/SubG ?	[29, 30]
NGC 6440 X–2	206	0.95	0.0067	He WD	[31]
IGR J17511–3057	245	3.47	0.13	MS	[32, 33]
Swift J1749.4–2807	518	8.82	0.59	MS	[34]
IGR J17498–2921	401	3.84	0.17	MS	[35]
IGR J18245–2452	254	11.03	0.17	MS	[36, 37]
MAXI J0911–655	345	0.74	> 0.024	WD/BD?	[38]
IGR J17379–3747	476	1.9	>0.06	BD	[39]
IGR J17591–2342	526	8.8	0.42	MS	[40, 41, 42, 43]
IGR J17062–6143	164	> 0.3	> 0.004	?	[44, 45, 46]
IGR J16597–3704	105	0.75	$> 6.5 \times 10^{-3}$	?	[47, 48]
IGR J17494–3030	376	1.25	> 0.015	?	[49]

TABLE 1.1: Known accretion-powered millisecond pulsars. ν_{spin} is the spin period, P is the orbital period, M_c is the companion star mass. Table adapted from Patruno and Watts (2012), with new sources added.

[1] Patruno et al. (2012); [2] Galloway and Cumming (2006); [3] Chakrabarty and Morgan (1998); [4] Goodwin et al. (2020a); [5] in 't Zand et al. (1998) ; [6] Markwardt et al. (2002); [7] Papitto et al. (2008) ; [8] Remillard, Swank and Strohmayer (2002); [9] Galloway et al. (2002); [10] Nelemans, Jonker and Steeghs (2006); [11] Markwardt, Smith and Swank (2003); [12] Kirsch et al. (2004); [13] Chou et al. (2008); [14] Tasheva and Stefanov (2019); [15] Riggio et al. (2008); [16] Papitto et al. (2007); [17] Strohmayer et al. (2003); [18] Bult, van Doesburgh and van der Klis (2017); [19] Ferrigno et al. (2017); [20] Sanna et al. (2017); [21] Baglio et al. (2017); [22] De Falco et al. (2017a); [23] Lewis et al. (2010); [24] Kaaret et al. (2006); [25] Krimm et al. (2007); [26] Rai and Paul (2019); [27] Zhang et al. (1998); [28] Casella et al. (2008); [29] Altamirano et al. (2008); [30] in 't Zand et al. (1999); [31] Bult, Patruno and van der Klis (2015); [32] Falanga et al. (2011); [33] Papitto et al. (2010); [34] Ferrigno et al. (2011); [35] Falanga et al. (2012); [36] De Falco et al. (2017b); [37] Ferrigno et al. (2014); [38] Bult (2017); [39] Sanna et al. (2018c); [40] Kuiper et al. (2020); [41] Tse, Chou and Hsieh (2020); [42] Sanna et al. (2020); [43] Sanna et al. (2018b); [44] Degenaar et al. (2013); [45] Strohmayer and Keek (2017); [46] Keek et al. (2017); [47] (Tetarenko et al., 2018a); [48] Sanna et al. (2018a); [49] Ng et al. (2020)

1.5.0.1 *Millisecond Variability*

Interestingly, persistent pulsations are not the only kind of millisecond variability that is observed in the X-ray emission from AMSPs. There are three different kinds of millisecond variability: kilohertz quasi-periodic oscillations, X-ray burst oscillations, and persistent accretion-powered pulsations (Chakrabarty, 2005).

Kilohertz and millihertz quasi-periodic oscillations (QPOs) were first discovered by Klis et al. (1996). They used *RXTE* to observe sub-millisecond quasi-periodic oscillations in the X-ray flux of Scorpius X–1, a luminous low mass X-ray binary containing a neutron star with a weak magnetic field. The cause of QPOs is not well known, but it has been suggested that they could be caused by marginally stable burning in the accreted fuel layers (e.g. Tse, Chou and Hsieh, 2020).

X-ray burst oscillations are nearly coherent millisecond oscillations that occur during some X-ray bursts (Chakrabarty, 2005), and are thought to be caused by asymmetries in the temperature or nuclear burning on the surface of the neutron star (see Watts, 2012, for a review). They were first detected by Strohmayer et al. (1996) with the proportional counter aboard the *RXTE* when they observed millisecond variability in the X-ray emission from the LMXB 4U 1728–34. Burst oscillations were deteced in some bursts in the 2002 outburst of SAX J1808.4-3658 at the known spin frequency of the pulsar (401 Hz), which led (Chakrabarty et al., 2003) to conclude that burst oscillations as nuclear-powered pulsations approximately trace the spin of accreting neutron stars.

Finally, the persistent emissions of accretion-powered low mass X-ray binary systems contain coherent millisecond pulsations that track the neutron star spin period (Chakrabarty, 2005). These pulsations were discovered by Wijnands and Klis (1998) in SAX J1808.4–3658 and are the type of pulsations predicted by the "recycling scenario".

1.6 THERMONUCLEAR X-RAY BURSTS

An important phenomenon that can occur in accreting neutron star systems is thermonuclear X-ray bursts; the most frequently observed thermonuclear-powered explosions in the Universe. In the early 1970s it was discovered that accreted material on the surface of a neutron star can undergo nuclear fusion, and thermonuclear runaways (Woosley and Taam, 1976; Hansen and van Horn, 1975; Rosenbluth et al., 1973; Ayasli and Joss, 1982). Nuclear fusion of accreted hydrogen on the surface of a neutron star can release $\approx 7\,\mathrm{MeV}$ per nucleon, and will occur in accreted layers due to compression caused by the density and pressure of the accreted atmosphere (Hansen and van Horn, 1975). Under certain conditions, with temperatures $> 10^7\,\mathrm{K}$, this nuclear burning can become unstable and a thermonuclear runaway can occur, initiating the rapid proton capture (rp) process (Woosley and Taam, 1976). Type I thermonuclear X-ray bursts are short ($\sim$10 s), bright ($L\sim 10^{38}\,\mathrm{erg\,s^{-1}}$) explosions on the surface of accreting neutron stars caused by thermonuclear runaway of the accreted fuel (e.g. Galloway and Keek, 2017). Type II X-ray bursts, which are not discussed in this thesis, are thought to be caused by accretion instabilities (e.g. Lewin, van Paradijs and Taam, 1993). In this thesis any reference to X-ray bursts refers to Type I bursts, unless otherwise specified.

Depending on the rate at which matter accretes onto the neutron star's surface, its composition, the base temperature of the neutron star, and the surface gravity of the neutron star, X-ray bursts may be observed with specific energies, recurrence times, and durations. Some accreting neutron star systems have not been observed to produce X-ray bursts while in outburst, some have been observed to produce a couple of X-ray bursts during an outburst, and others have been observed to produce frequent bursts every outburst. The large range in observed properties of X-ray bursts may be attributed to the broad range in individual system properties, as well as limited and non-continuous observations of accreting neutron stars in outburst.

It is now widely understood that in low mass X-ray binary systems, fuel (H/He) for the Type I burst is accreted onto the neutron star and accumulates on the surface, forming a layer that can be several meters thick (Galloway and Keek, 2017). The accreted material is compressed and heated hydrostatically, and eventually the temperature and density at the base of the accreted layer becomes high enough that the fuel ignites. This causes unstable and rapidly spreading burning that devours all of the available fuel in seconds, causing a short and energetic flash (e.g. Galloway et al., 2008). There are many comprehensive reviews available that describe the theory and observations of thermonuclear X-ray bursts (e.g. Galloway and Keek, 2017; Cumming, 2004; Strohmayer and Bildsten, 2003; Bildsten, 2000).

1.6.1 *Nuclear Burning in Thermonuclear X-ray Bursts*

The nuclear reactions that occur during X-ray bursts determine the observed shape of lightcurves, duration of bursts, and frequency of bursts. The primary parameter that influences the nuclear reactions that occur is the fuel composition, but the temperature, density, and pressure of the environment are also important. Current theory suggests there are five main nuclear reaction pathways involved in the accreted fuel on the surface of a neutron star before and during a thermonuclear X-ray burst. These include the (hot) CNO cycle, the 3α-process, the α-process, the αp-process, and the rp-process (e.g. Bildsten, 1998).

The nuclear burning can be separated into steady burning that occurs in the accreted fuel prior to the X-ray burst ignition, and the unstable thermonuclear runaway that occurs during an X-ray burst. The different nuclear reactions and their pathways are shown in Figure 1.5.

The (hot) CNO cycle and the 3α-process can occur during steady burning. The (hot) CNO cycle burns hydrogen into helium, involving two β-decays. The 3α-process burns helium into carbon, requiring slightly hotter temperatures than the CNO cycle ($T\sim 10^8$ K), and is thought to be the primary cause of X-ray burst ignition (Joss, 1978). Above temperatures of $\sim 10^9$ K during thermonuclear runaway, the α-process forms heavier elements from the products of the CNO cycle and the 3α-process (e.g. Fujimoto, Hanawa and Miyaji, 1981). Similarly, the αp-process also forms heavier elements from the products of the CNO cycle and 3α-process, but the reactions are catalysed by protons, and thus forms nuclei on the proton rich side of the stability. Finally, the rapid-proton capture process (rp-process) begins with the products of the previous nuclear reaction pathways and is a suc-

cessive chain of proton captures and β-decays, easily producing elements beyond ^{56}Fe (Wallace and Woosley, 1981). The stopping point of the rp-process is not well known, but is thought to be somewhere around Tellurium (Schatz et al., 2003).

If the fuel burning in a burst is proton rich, there can be extended rp-process burning, resulting in longer X-ray bursts, with the lightcurves appearing to have extended tails. Conversely, if the fuel is helium rich, and proton deficient, there is no extended rp-process burning, and the bursts are generally brighter, but shorter.

There are a few important parameters that describe X-ray bursts. These include:

- E_b: the burst fluence. This is the time integrated flux of the burst. Unit: erg.
- F_p: the persistent flux. This represents the flux from accretion onto the neutron star, and can be used to constrain the accretion rate if other system parameters are known.
- Δt: the recurrence time of the bursts. Often the observed recurrence time is not representative of the intrinsic recurrence time since observations are rarely continuous, and recurrence times can range from ≈ 1 hr to many days. Unit: hour.
- α: the ratio between the persistent flux and the burst flux, which represents the ratio between the gravitational energy and nuclear energy in the system. Unit: no units.
- $\dot{m}$: the accretion rate onto the neutron star. This represents the rate at which material is transferred from the accretion disk to the neutron star. Unit: in cgs $g\,s^{-2}$, but often given in units of the Eddington accretion rate[3].
- τ: the decay time. This represents the time taken for the burst to decay from its maximum luminosity to return to the non-burst flux level. Unit: seconds.
- M and R: the neutron star mass and radius.
- g and $1+z$: the surface gravity and gravitational redshift.
- X and Z: the composition of the accreted fuel. X is the hydrogen abundance and Z is metallicity, often assumed to be the abundance of CNO elements.
- Q_b: the base flux or base heating of the neutron star on top of which the accreted layer accumulates. Usually assumed to be 0.1–0.15 MeV/nucleon

1.6.2 *Observations of Thermonuclear X-ray Bursts*

The first X-ray burst was observed in 1975 from the X-ray source 4U 1820–30. Grindlay et al. (1976) observed two bursts in the 1–30 keV X-ray energy range with the *ANS* observatory that were characterised by a sharp increase in flux by a factor of 20–30 over $\approx$1 s, then an $\approx$8 s exponential decay. They classified these events as a new kind of X-ray emission: X-ray bursts. They deduced that the events may imply

3 The Eddington accretion rate is given by $\dot{M}_{Edd} = \frac{0.7}{1+X} \times 10^{-8}\,M_\odot\ yr^{-1}$, where X is the H mass fraction.

the existence of a collapsed core in the globular cluster NGC 6624 they were associated with. However, they implied the source could be a 10^3 $M_\odot$ black hole, but we now know that fuel cannot build up on the surface of a black hole, and thus we do not observe X-ray bursts from black holes. 4U 1820–30 is a helium-accreting X-ray bursting neutron star (e.g. Suleimanov et al., 2017), which explains why the X-ray bursts were relatively short.

Now, 45 years later, we have observed thousands of X-ray bursts from hundreds of bursting neutron star binaries. Galloway et al. (2020) provided the most complete public archive of X-ray burst observations to date. MINBAR lists 7083 bursts from 85 sources, consisting of observations from proportional counters aboard the Rossi X-ray Timing Explorer (*RXTE*), *BeppoSAX*, and *INTEGRAL* space telescopes between 1996 and 2012.

Typical bursts are short-lasting (~10–100 s), and energetic (~10^{39}–10^{40} ergs). The X-ray spectra of Type I bursts exhibit a characteristic short (~1 s) rise time and longer tail (~30 s), as seen in Figure 1.6. In Figure 1.6 it is clear that burst profiles are diverse in shape and duration, which can be attributed to differences in system parameters, such as fuel composition (e.g. Galloway et al., 2008).

Photospheric radius expansion occurs when the luminosity reaches the Eddington limit (i.e. when the gravitational force inwards balances the radiation pressure outwards), which causes the radiation pressure to lift the surface layers of the star. Double-peaks sometimes observed in the ligtcurves of bursts are thought to indicate the occurrence of photospheric radius expansion (Lewin, Vacca and Basinska, 1984). This is an important observational phenomenon, as the Eddington limit is fixed, so it enables Type I X-ray bursts to be used as "standard candles", and the distance to some sources estimated (e.g. Kuulkers et al., 2003; Basinska et al., 1984).

A selection of X-ray burst lightcurves from two sources are plotted in Figure 1.7, demonstrating the variability in lightcurves of bursts, even from the same source.

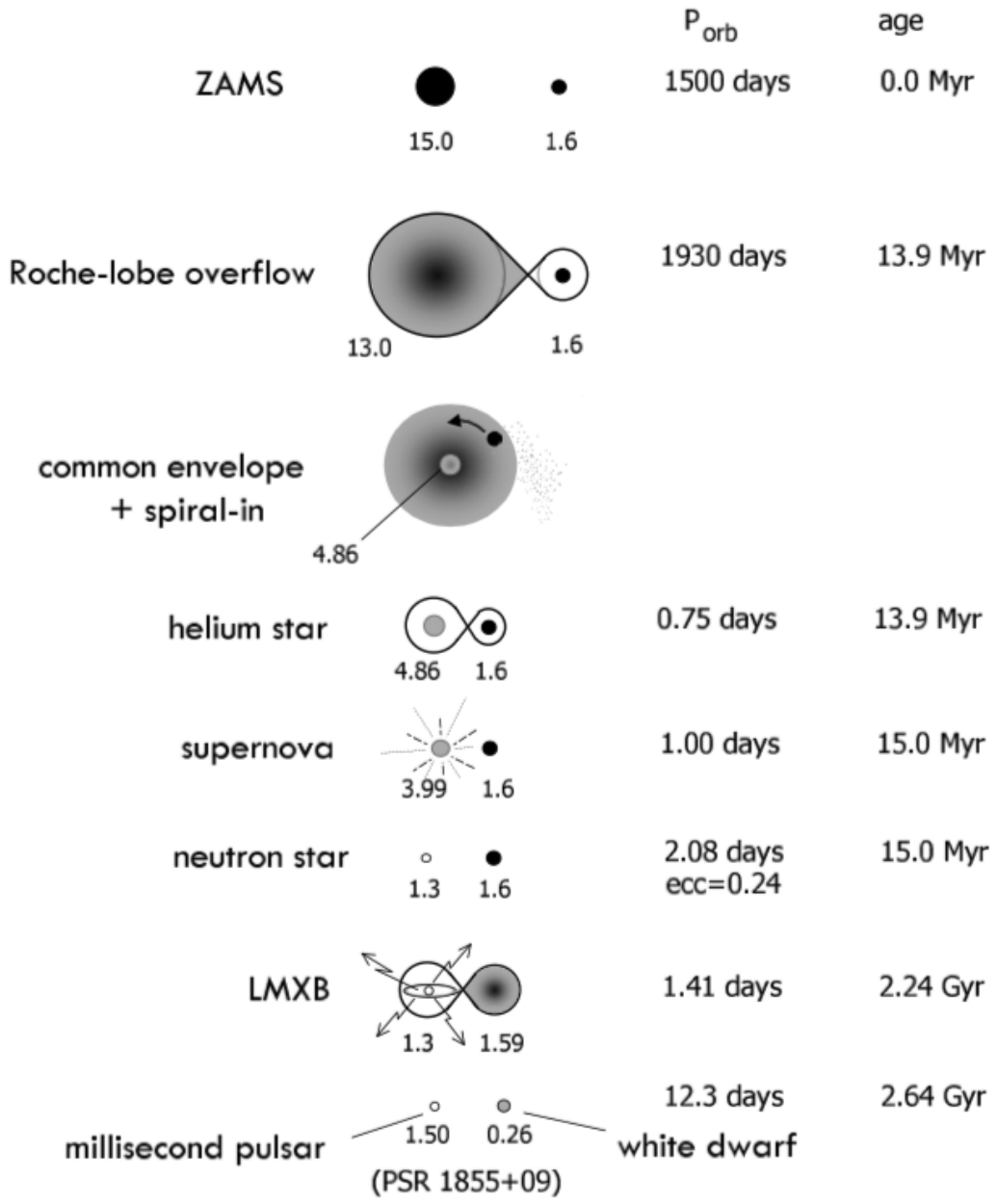

FIGURE 1.4: A diagram of the formation pathway of an accreting pulsar. Figure reproduced with permission from Tauris and van den Heuvel (2006).

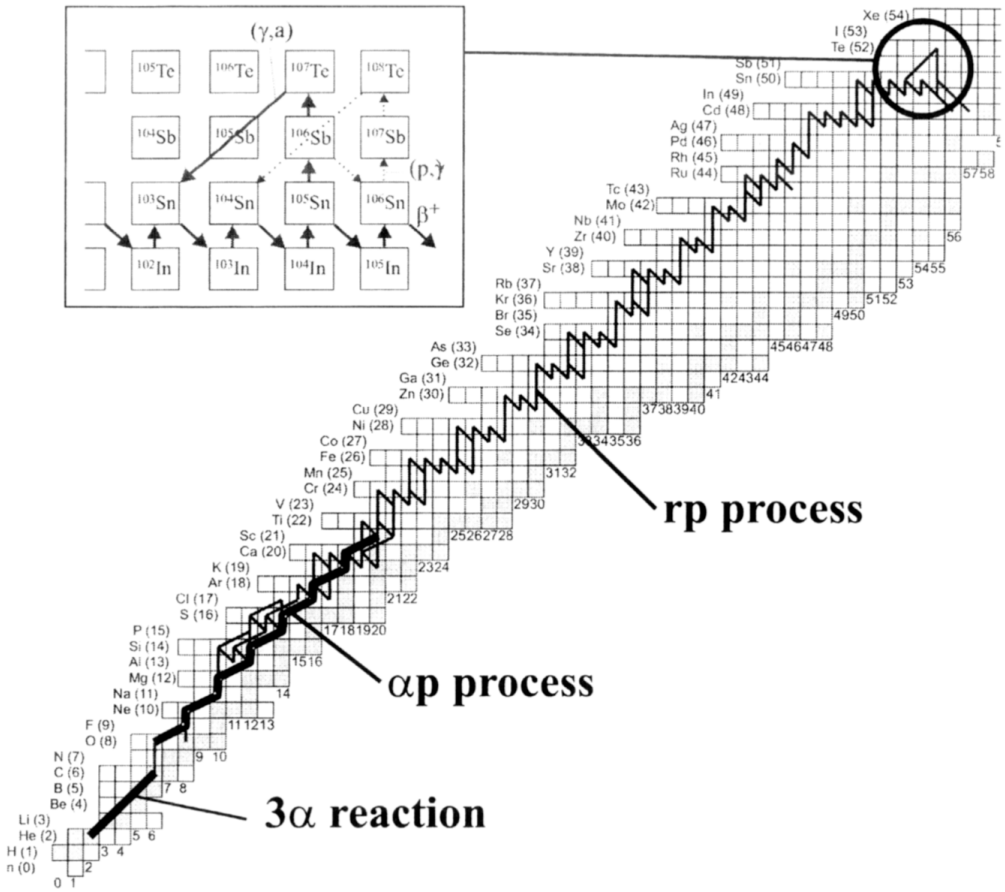

FIGURE 1.5: The different nuclear reactions that occur during an X-ray burst, and the pathways through which heavier elements are created. Figure reproduced with permission from Schatz et al. (2003) Figure 1.

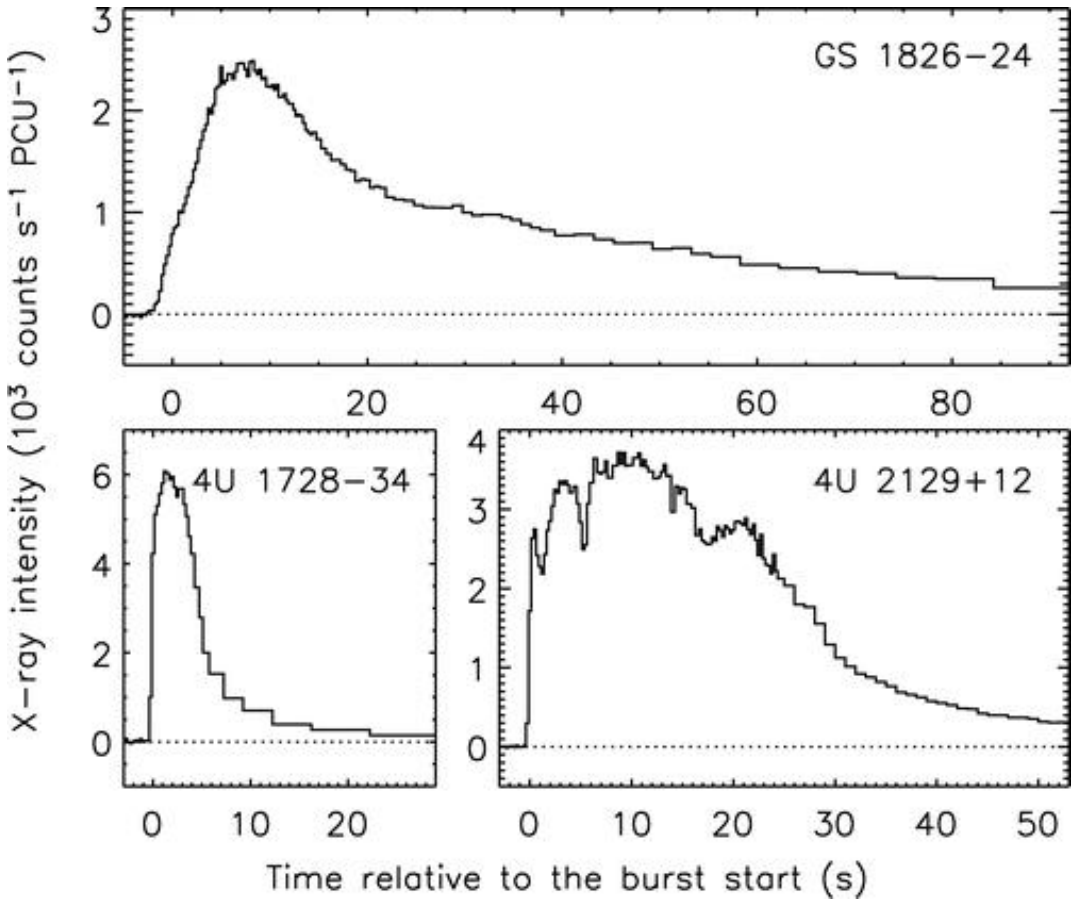

FIGURE 1.6: Example light curves of 3 bursts observed by *RXTE*. The source for each burst is listed in the top right hand corner of the frame and the persistent emission has been subtracted (dotted line). Note the diversity in the shape of the lightcurves, primarily attributed to differences in fuel composition. Figure reproduced with permission from Galloway et al. (2008), Figure 1.

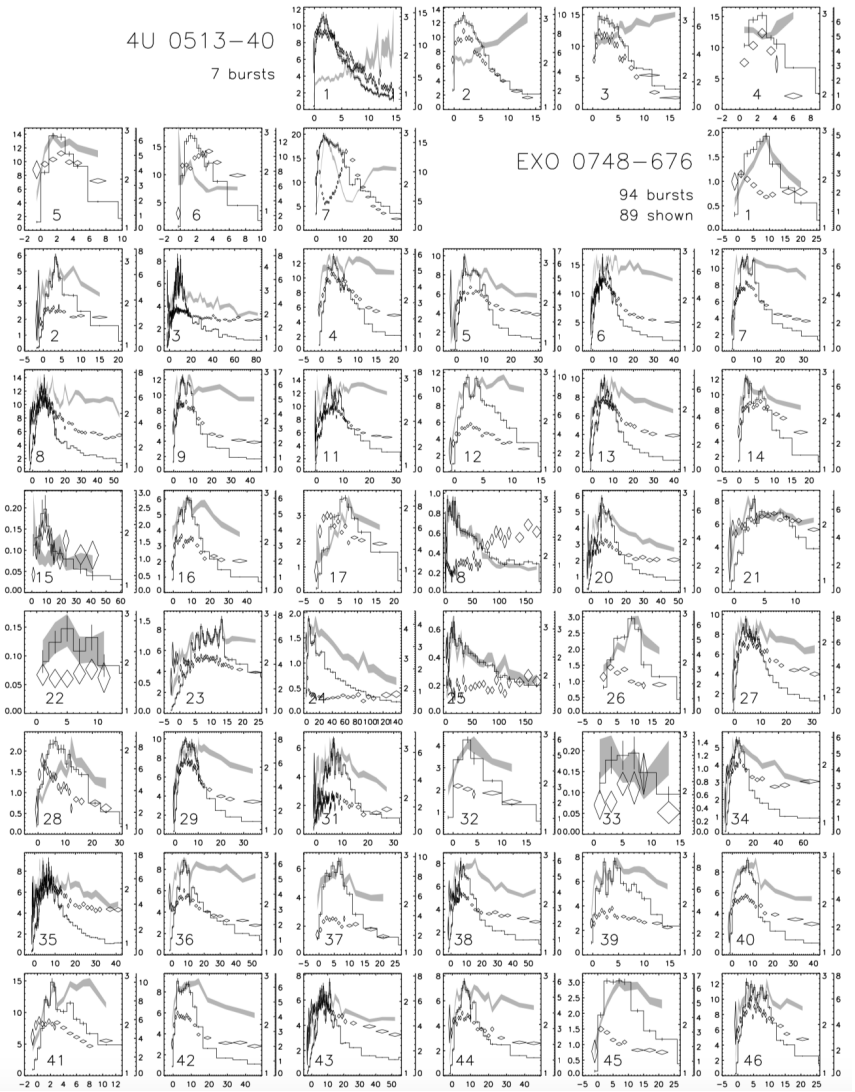

FIGURE 1.7: A collection of thermonuclear X-ray burst observed lightcurves from 4U 0513–40 and EXO 0748–676. Each panel shows the bolometric burst flux in units of 10^{-9} erg cm^{-2} s^{-1}. Figure reproduced with permission from Galloway et al. (2008), Figure 9.

CASE	$\dot{m}_{Edd}$	STABLE BURNING	BURSTS	REF.
3/V	$\lesssim 0.01$	stable He	Deep H flash	[1,2]
2/IV	0.01 – 0.1	stable H	Deep He flash and shallow H flash	[3,4]
-/-	0.04 – 0.08	stable H	He	[4,5,6]
1/III	0.08 – 0.11	stable H/He	none	[7]
-/II	0.11- 1.0	marginally stable H/He	mixed H/He	[8,9]
0/I	$\gtrsim 1.0$	stable H/He	none	[10]

TABLE 1.2: Burning regimes in the accreted layers on the surface of accreting neutron stars. Table adapted from Galloway et al. (2008), Keek and Heger (2016), and Galloway, Goodwin and Keek (2017). Note that the Roman numeral ordering is reversed in Galloway, Goodwin and Keek (2017), and the Arabic numbers refer to the cases described by Fujimoto, Hanawa and Miyaji (1981).
References: 1. Peng, Brown and Truran (2007); 2. Cooper and Narayan (2007); 3. Galloway and Cumming (2006); 4. Woosley et al. (2004); 5. Galloway et al. (2004b); 6. Fisker, Schatz and Thielemann (2008); 7. Keek and Heger (2016); 8. Narayan and Heyl (2003); 9. Heger, Cumming and Woosley (2007); 10. Schatz et al. (2001)

1.6.3 *Burning Regimes*

Depending on the accretion rate and composition of the fuel, different burning regimes can be defined that describe the type of stable burning that can occur in the accreted fuel layers, and the primary composition of the burst, if burst conditions can be reached. Fujimoto, Hanawa and Miyaji (1981) initially described four different cases of burning: high accretion rates, where the accreted fuel burns stably (case I), lower accretion rates, where hydrogen burns unstably and bursts with much longer tails due to the rp-process are observed (case II/III), and finally even lower accretion rates, where hydrogen burns to helium stably in the lower layers of the atmosphere and unstable helium ignition is the primary source of the bursts (case IV). Keek and Heger (2016) proposed an additional burning regime, and described the burning regimes as outlined in Table 1.2.

It is clear that there can be some strange behaviour where stability is reached for specific accretion rates. Since the accretion rate can vary for an individual source across an outburst, it is thought that some systems may only exhibit bursts for short periods, then return to stable burning of the accreted fuel.

1.6.4 *Models of Thermonuclear X-ray Bursts*

Since the discovery of X-ray bursts, modelling of these energetic events has played a significant role in our understanding. Models can predict observed burst rise times, durations, energies and recurrence times, and can be compared to observations. Models are useful because they also allow constraints on non-observable parameters, such as the composition of the accreted fuel, that enable us to gain a greater understanding of the physics underlying these extraordinary explosions, as well as insight into the evolution of LMXBs.

Early models (e.g. Woosley and Taam, 1976; Fujimoto, Hanawa and Miyaji, 1981; Taam, 1980; van Paradijs, Penninx and Lewin, 1988; Cumming and Bildsten, 2000)

exploit the correlation between burst energies and recurrence times using analytic or semi-analytic approaches to integrate a time-independent ignition column under simple assumptions. More recent models (e.g. Woosley et al., 2004; Paxton et al., 2011) focus more heavily on the nuclear physics driving the bursts, implementing a deeper understanding of the nuclear reactions that occur to predict burst energies based on fuel composition and accretion rates. The most advanced of these models, KEPLER (Woosley et al., 2004) and MESA (Paxton et al., 2011), use time-dependent adaptive nuclear reaction networks to model the burning before, and during a burst in more detail, as well as solving the full hydrostatic stellar structure equations, at the cost of longer run times. However, even the most advanced models are still one-dimensional. More details on specific models of X-ray bursts are provided in Chapter 2.

X-ray bursts are a complex phenomenon, and there are many challenges to developing a comprehensive model that encompasses all of the underlying physics. Woosley et al. (2004) described four challenges that simulations of X-ray bursts face.

The first challenge they describe is the geometry of accretion, the distribution of accreted fuel, and the location of the ignition of a burst: *"Is the accretion uniformly distributed over the surface of the neutron star prior to runaway and does the burst commence almost simultaneously over that surface?"*. These questions are, perhaps surprisingly, quite difficult to obtain a definite answer. The observation of burst oscillations during X-ray bursts that usually drift around the spin period of the neutron star have motivated scientists to suggest that they could be caused by the burning front of an X-ray burst as it spreads around the neutron star, or temperature/burning asymmetries on the surface of the neutron star. This suggestion would imply that X-ray bursts do not burn uniformly on the surface of the neutron star, and that rotation plays a key role in the ignition, and spreading of flame fronts (see Strohmayer and Bildsten, 2003, for a review). Since most burst models are one-dimensional, they assume spherical symmetry, and do not model these kinds of effects. Recently, there have been attempts at modelling the flame front and spreading during the ignition of a burst in two and three-dimensions, most notably by Cavecchi and Spitkovsky (2019). The presence of hotspots on the surface of AMSPs has motivated suggestions that these are caused by magnetic channelling of the accreted fuel as it is transferred from the accretion disk to the neutron star. The question remains, however, if a hotspot on the surface of a neutron star could induce X-ray burst ignition preferentially at the hotspot, or if the fuel spreads over the surface of the star before ignition conditions are reached.

The second challenge Woosley et al. (2004) describe is that *"the nuclear physics is complex, with no single or even several reactions governing the energy generation rate"*. There are over a thousand nuclear reactions that may occur during unstable burning and the rp- and αp-processes, and a comprehensive model must individually calculate the energy release of each of these reactions in order to obtain an accurate measure of the energy released during a burst. Both KEPLER and MESA include nuclear reaction networks, however, many nuclear reaction rates are still quite uncertain, and we rely on experimentalists to provide more precise measurements. Nevertheless, it is not always possible to calculate a full nuclear reaction network

as these models are computationally expensive, and so we rely on approximations to the energy generations in simpler X-ray burst models.

The third challenge described by Woosley et al. (2004) is that a comprehensive model must simulate an entire train of bursts, rather than a single burst that most simple models are able to simulate. Consecutive bursts likely ignite in the ashes of previous bursts, which creates thermal and compositional "inertia" (Taam, 1980), and can affect the properties of subsequent bursts. Again, KEPLER and MESA solve the full set of hydrostatic equations of stellar structure, and thus are able to track the accumulation of fuel, and the conditions of the accretion column in subsequent bursts as they ignite in the ashes of previous bursts.

The final challenge that Woosley et al. (2004) describe is the comparison of predicted and observed X-ray burst spectra. Often simulated burst spectra cannot be directly compared to observed burst spectra, but discovering ways in which this is possible will enable a deeper understanding of the physics that drives the burst rise times, lightcurve shape, and exponential decay times. Recently, Johnston, Heger and Galloway (2018) modelled an observed burst train of the AMSP SAX J1808.4–3658 using KEPLER, and provided a comparison of the observed and modelled burst lightcurves, shown in Figure 1.8.

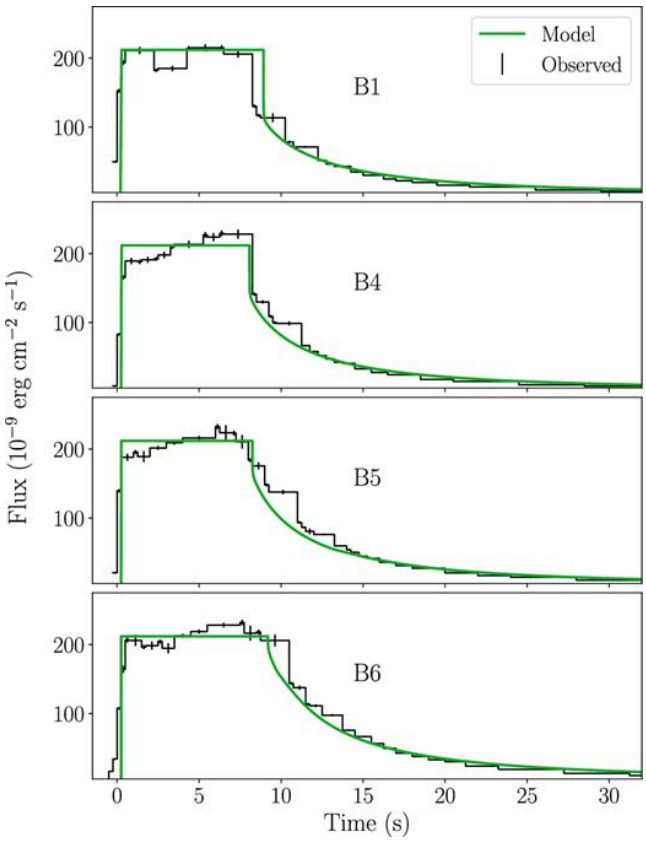

FIGURE 1.8: Observed (black) and modelled (green) X-ray burst lightcurves for the source SAX J1808.4–3658. Figure from Johnston, Heger and Galloway (2018), Figure 4.

1.7 MODELS OF ACCRETING NEUTRON STARS

1.7.1 *The Disk Instability Model*

The thermal-viscous disk instability model (DIM) is the current prevalent theory that describes outbursts of dwarf novae and LMXBs see Hameury, 2020; Dubus, Hameury and Lasota, 2001; Lasota, 2001, for reviews. Outbursts in dwarf novae and transient LMXBs are characterised by an abrupt increase in luminosity of several orders of magnitude over a few days, followed by an exponential decay on a timescale of a month before the system returns to its low luminosity ($L \sim 10^{33}\,\mathrm{erg\,s^{-1}}$) quiescent state.

The first observational record of a dwarf nova (or U Geminorum-type variable star) is U Geminorum in 1855 (Pogson, 1857). U Geminorum is a classic example of a dwarf novae system, in which a white dwarf is in a close orbit with a red dwarf star, and undergoes outburst every few months. A century after U Geminorum was discovered, Hōshi (1979) suggested a mechanism for the periodic outbursts: they described a scenario in which the surface density of the accretion disk increases by continual mass transfer until a certain critical value is reached, at which time a thermal instability occurs inside the disk, raising the temperature by more than a factor of 10. The material in the disk then travels inward to the white dwarf due to angular momentum transport, triggering a luminous accretion episode. The discovery that models of accretion disks were unstable at temperatures corresponding to the ionisation of hydrogen (e.g. Meyer and Meyer-Hofmeister, 1981) further solidified the thermal-viscous disk instability model as the mechanism behind outbursts.

Now, more than 40 years later, the DIM has evolved, and various key components have been added, including the effects of irradiation. Whilst the DIM was initially developed to explain outbursts of dwarf novae-type systems, the similarity in the fast-rise exponential-decay behaviour between these outbursts and those of transient LMXBs has motivated the same underlying mechanism of outburst to be proposed for both types of systems (e.g. van Paradijs, 1996; Cannizzo, Wheeler and Ghosh, 1985). However, significant modifications have to be introduced in order to explain some of the fundamental observational properties of transient LMXBs, including disk truncation and irradiation (van Paradijs, 1996).

According to the DIM, the outburst-quiescence cycle of an LMXB or nova may proceed as follows: first, during quiescence, mass accumulates into a cold disk via Roche-Lobe overflow from the companion. Material does not transfer directly to the compact object, since it has angular momentum from the companion star being in orbit, and thus forms an accretion disk instead. Matter accumulates until the disk reaches a critical radius or surface density, and the disk temperature rises to the critical value required to ionise hydrogen. This causes a heating front to propagate through the disk, bringing it to a hot, bright state, and commencing the outburst (e.g. Hameury, 2020). The outburst lasts on the order of a month, during which time accretion onto the compact object gives rise to X-ray emission. The outburst then follows an exponential decay in luminosity as the disk cools, and the system returns to quiescence to begin building up mass in the disk for the

next outburst. This explanation is a very simplified picture of what is happening during an outburst of an LXMB, and there is variation observed in the behaviour of many systems. One key property is the time delay between when the disk instability first occurs, and the heating front begins to propagate in the disk, and when the outburst commences, and accretion luminosity onto the compact object is observed.

Dubus, Hameury and Lasota (2001) describe two different kinds of outburst, depending on how long it takes for the heating front to propagate in to the inner disk. In the standard DIM, two heating fronts are formed at the point of ignition, and they propagate both inwards and outwards from the ignition radius (Menou, Hameury and Stehle, 1999). In “inside-out" outbursts, the ignition occurs at a small radius, and the inward propagating front reaches the inner disk much faster than the outward propagating front reaches the outer disk. In “outside-in" outbursts, the ignition occurs at a larger disk radius, and can take much longer for the heating front to reach the inner disk. Dubus, Hameury and Lasota (2001) describes the primary difference between “inside-out" and “outside-in" outbursts: that during quiescence the density profile of the disk is approximately linearly proportional to the radius, which implies that “outside-in" heating fronts always progress through regions of decreasing surface density. Whereas, in “inside-out" outbursts, the outward front can encounter regions of higher densities, and if the front does not transport enough matter to raise the density, it stalls and a cooling front can develop. Thus “inside-out" outburst fronts propagate slowly, leading to slower rise times than “outside-in" outbursts. When irradiation is accounted for, it does not change the structure of the heating front, but it does change the maximum radius to which an “inside-out" outburst can propagate.

The location of ignition of the heating front is thought to depend on the mass transfer rate from the secondary and the disk’s size (Smak, 1984; Hameury et al., 1998). For low mass transfer rates, the accreted matter will drift down the cold disk, and the maximum surface density will accumulate in the inner disk, giving rise to inside-out outbursts. If the mass transfer rate is high, the mass accumulation time at the outer radius can become lower than the drift time, and an outside-in outburst will be triggered by the higher surface density in the outer disk. Dubus, Hameury and Lasota (2001) found that the mass transfer rate required for an outside-in outburst to occur in their model of a LMXB was higher than the accretion rate for which the disk was stable, thus indicating that inside-out outbursts are more likely for this kind of system. They conclude that ignition near the outer edge of a large, irradiated disk is difficult to obtain.

There is evidence that the viscosity of the accretion disk in CVs changes when the disk goes from the low state (quiescent, accreting state) to the high state (unstable, outburst state). In order to generate a model that matches the amplitude and cycle frequency of dwarf novae systems, the disk requires a lower viscosity in quiescence than in outburst (Smak, 1984; Lin, Papaloizou and Faulkner, 1985). This is known as a “two-α” model, since there are two viscosities; α_c for during quiescence and α_h for during outburst.

According to Dubus, Hameury and Lasota (2001), the DIM fails to describe 3 fundamental observational properties of soft X-ray transient outbursts. These are:

the long recurrence time of outbursts, in which it can be years between outbursts in certain systems; the fact that the tail of outbursts are not dominated by reflare episodes, which are observed only in a few systems; and the luminosities observed are brighter than expected if the accretion disk reaches down to the compact object. Thus it was evident that some key modifications were required of the classic DIM for soft X-ray transient systems. These include: inner disk truncation (caused by a strong magnetic field of the neutron star), accretion disk and donor star irradiation (caused by luminosity from the central regions of the disk or a corona), evaporation during quiescence, mass transfer variations, and the existence of winds and outflows that can exert a torque on the accretion disk. Menou et al. (2000) included a truncated disk in their models, however, required much lower αs than CVs ($\alpha \approx 0.01$), and could not reproduce the observed short rise times of LMXB outbursts. Dubus, Hameury and Lasota (2001) included a truncated disk, evaporation during quiescence, and irradiation during outburst and found that they could generate an adequate model of an LMXB with similar viscosities to those used in CV models.

Despite the numerous improvements, modifications, and observational tests the DIM has been subject to since it was first proposed in the 1970s, it still does not perfectly encapsulate everything about an LMXB outburst, since there is so much variation in observational properties from system to system.

1.8 THESIS OUTLINE

This research aims to further understand accreting neutron star systems by using computer models and observations. We study how the strong gravitational field of the neutron star affects its environment, the thermonuclear explosions that occur on their surface, and the geometry and structure of the accretion disk and accretion flow around a neutron star. This thesis answers four broad questions:

1. What causes the onset of accretion outbursts and how does observational data constrain the current theory that describes accretion disk structure?
2. How much energy does an X-ray burst release and on what factors does it depend?
3. Can a hotspot on the surface of a neutron star induce off-equator ignition of X-ray bursts?
4. Can observations of accreting neutron stars be combined with models to infer system parameters, such as neutron star mass and radius, that we cannot observe?
5. How do accreting neutron star systems evolve, how did they begin, and how will they end?

In this thesis, we present a combination of observations and models that explore accreting neutron star systems. In Chapter 2 we provide more detail into the methods and modelling techniques used in this work. In Chapter 3 we present two published works on modelling X-ray bursts and the affect of accretion hotspots on

the surface of a neutron star. In Chapter 4 we present two observational papers, the first presenting the discovery of X-ray bursts from XMMU J181227.8–181234 in archival data, and the second presenting an observational campaign we led in 2019 that provides the first comprehensive observations of the rise to outburst of an accreting neutron star system. In Chapter 5 we present software that we developed to match observations of an accreting neutron star in outburst with a model, to predict parameters we can not observe, applied to the AMSP SAX J1808.4–3658. In Chapter 6 we present evolutionary track calculations we performed using `MESA` of the AMSP SAX J1808.4–3658, given the system has been observed to have peculiar orbital period evolution. Finally, in Chapter 7 we present a summary of this work, and future outlook.

2

METHODS

In this chapter we outline the methods used in each of the papers presented in this thesis in an overarching way. We focus on the specific models and software used, observational techniques, and parameterisation of the problems addressed in this work.

2.1 MODELS

Models of accreting neutron stars cover a broad range of phenomenon, including binary evolution, thermonuclear X-ray bursts, the neutron star equation of state, accretion disk structure and stability, and accretion flows. Models of the binary evolution of accreting neutron stars often treat the neutron star as a point mass, and perform calculations of the evolution of the companion star and the orbit. Models of thermonuclear X-ray bursts range from full time-dependent hydrodynamical simulations to analytic studies of the accretion column. Full time-dependent calculations are advantageous as they enable thermal and compositional inertia to be modelled, in which the changes in composition and temperature due to previous bursts are tracked and accounted for. Analytic calculations, whilst often containing considerably less physics, are useful as they are less computationally expensive to run whilst still allowing extended parameter studies. Most current models of X-ray bursts do not consider complex questions that are currently poorly understood, such as how the burning front spreads across the star after ignition occurs, what determines the number of hotspots on the surface of the star, or the cause of asymmetry near the end of the burst as the material is cooling. There are recent studies, however, that use simplified nuclear reaction networks to explore flame spreading on the surface of a neutron star during a burst (e.g. Cavecchi and Spitkovsky, 2019).

2.1.1 *Settle*

`Settle` is a semi-analytic ignition code developed by Cumming and Bildsten (2000) that models the atmosphere of an accreting neutron star to find the ignition conditions for a thermonuclear Type I X-ray burst. Whilst models such as `Kepler` are designed to comprehensively model X-ray bursts, they are very computationally expensive to run, as they often require large nuclear reaction networks. Semi-analytic models such as `Settle`, are simpler and computationally less expensive to run. Studies have applied `Settle` to observations of regular Type I bursters, such as 4U 1820–30 (Cumming, 2003), GS 1826–24 (Galloway et al., 2004a) and SAX J1808.4–3658 (This work, Chapter 5 Galloway and Cumming, 2006).

Modelling the burning layer during a burst involves complex physics and simple models such as `Settle` must make many assumptions during the modelling pro-

cess. `Settle` uses one-dimensional hydrostatic models of the neutron star atmosphere, assuming the hot burning material decouples from the cooler underlying ashes during a burst. The model does not include thermal or compositional inertia, due to the lack of time-dependence in the calculations.

The column depth, y, is defined such that $dy = -\rho\, dz$, where z is the radial coordinate in the star. The pressure in `Settle` obeys $dP/dz = -\rho g$ where ρ is the density and g is the surface gravity.

The temperature profile of the accumulating fuel layer is calculated given the accretion rate, and the accreted layer is allowed to build up until the one-zone condition for a thermal runaway is satisfied at the base of the layer. This ignition condition is simply given by (Fushiki and Lamb, 1987a)

$$\frac{d\epsilon_{3\alpha}}{dT} > \frac{d\epsilon_{cool}}{dT} \tag{2.1}$$

where $\epsilon_{3\alpha}$ is the energy production rate of helium burning via the triple-α reaction and ϵ_{cool} is the effective local cooling rate. $\epsilon_{3\alpha}$ can be approximated by (Fushiki and Lamb, 1987b)

$$\epsilon_{3\alpha} = 5.3 \times 10^{21} f \frac{\rho_5^2 Y^3}{T_8^3} \exp\left(\frac{-44}{T_8}\right) \quad \text{ergs}\, g^{-1}\, s^{-1} \tag{2.2}$$

where f is the screening factor, Y is the helium mass fraction, T_8 is $T/10^8$ (K), and ρ_5 is $\rho/10^5$ ($g\, cm^{-3}$).

The effective local cooling rate can be approximated by (Cumming and Bildsten, 2000)

$$\epsilon_{cool} \approx \frac{acT^4}{3\kappa y^2} \tag{2.3}$$

Effectively, the ignition condition in Equation 2.1 states that a burst (triggered by thermal instability) will occur when the local heating rate is greater than the local cooling rate. Unfortunately, `Settle` does not account for heating due to additional nuclear reactions that can occur in the accreted fuel layer or compressional heating, however, it is well understood that bursts are usually triggered by the heating due to the triple-α reaction (e.g., Bildsten, 1998).

Hydrogen is assumed to burn via the hot CNO cycle during accumulation, which provides an energy generation rate of (Cumming and Bildsten, 2000)

$$\epsilon_H = 5.94 \times 10^{13} \left(\frac{Z_{CNO}}{0.01}\right) \quad \text{ergs}\, g^{-1}\, s^{-1} \tag{2.4}$$

where Z_{CNO} is the mass fraction of CNO nuclei.

Since hydrogen burns at a constant rate in the beta-limited CNO cycle, the time to burn all of the hydrogen (t_H) is dependent only on Z and the initial hydrogen abundance, X_0. Cumming and Bildsten (2000) calculated t_H to be

$$t_H \approx 11 (\frac{0.02}{Z_{CNO}})(\frac{X}{0.71}) \quad \text{hr} \tag{2.5}$$

Other studies, such as Lampe, Heger and Galloway (2016), however, show that t_H is

$$t_H = 9.8(\frac{X}{0.7})(\frac{0.02}{Z_{CNO}}) \quad \text{hr} \tag{2.6}$$

which agrees within the precision of a similar derivation by Fujimoto, Hanawa and Miyaji (1981), in which they derived:

$$t_H = 9.7(\frac{0.02}{Z_{CNO}}) \quad \text{hr} \tag{2.7}$$

for $X = 0.7$.

Lampe, Heger and Galloway (2016) deduced that the discrepancy in Cumming and Bildsten (2000)'s depletion time for hydrogen could be attributed to the derivation by Cumming and Bildsten (2000) failing to incorporate neutrino energy losses in the CNO cycle.

A burst is triggered when helium burning becomes unstable at the base of the accumulated layer, which occurs at a temperature of $\approx 2 \times 10^8$ K and densities of $\sim 10^5 - 10^6\,\mathrm{g\,cm^{-3}}$. The composition of the burst, and thus many of its properties, is dependent on the accumulation time before ignition conditions are met at the base of the accreted column. In general, when the accretion rate is higher ($\dot{m} \gtrsim 0.03\dot{m}_{Edd}$), helium burning becomes unstable before hydrogen has depleted in the ignition column, and the bursts ignite in a hydrogen rich environment. Conversely, if the accretion rate is lower, the burst will ignite in a pure helium environment since there is time for all of the hydrogen to be converted to helium prior to the burst igniting. In the code this is implemented by defining the column depth at which hydrogen runs out (y_d)

$$y_d = 6.8 \times 10^8(\frac{\dot{m}}{0.01\dot{m}_{Edd}})(\frac{0.01}{Z_{CNO}})(\frac{X_0}{0.71}) \quad \mathrm{g\,cm^{-2}} \tag{2.8}$$

and if ignition conditions are met at a column depth $y < y_d$, a mixed H/He burst occurs, otherwise the burst ignites in a pure helium environment.

As outlined in Cumming and Bildsten (2000), the thermal profile of the accreted layer is given by the heat equation

$$\frac{dT}{dy} = \frac{3\kappa F}{4acT^3} \tag{2.9}$$

where κ is the opacity, and F is the outward heat flux.

In `Settle`, the entropy equation is assumed to be

$$\epsilon = -\frac{dF}{dy} \tag{2.10}$$

The temperature profile is found by integrating Equations 2.9 and 2.10 from the top (fixed to $y = 5 \times 10^4\,\mathrm{g\,cm^{-2}}$) to the base of the accreted column using an adaptive step-size Runge-Kutta integration method (see Vetterling et al., 2002, p.721). ϵ is set to ϵ_H for $y < y_d$ and 0 for $y > y_d$. The ignition depth (y_b) is found by integrating iteratively until the ignition condition (Eq. 2.1) is met.

The input parameters for `Settle` include: NS mass (M), radius (R), composition of the accreted fuel (X and Z), accretion rate ($\dot{m}$), and base flux (Q_b). The neutron

star mass and radius set the gravitational redshift and surface gravity. The composition of the accreted fuel sets the composition of the burst based on the time taken for ignition conditions to be met. Once the ignition depth is found, the accretion rate, metallicity, and calculated ignition depth (y_b) set the predicted recurrence time of bursts via

$$\Delta t = \frac{(1+z)y_b}{\dot{m}} \tag{2.11}$$

where $1+z$ is the redshift correction to convert the recurrence time from the neutron star frame to the observer frame.

The fluence (E_b) and α values of the burst are calculated using

$$E_b = \frac{4\pi R^2 y_b Q_{nuc}}{1+z} \tag{2.12}$$

$$\alpha = \frac{Q_{grav}}{Q_{nuc}} \tag{2.13}$$

where $Q_{grav} \approx GM/R \approx 290\,\mathrm{MeV\,nucleon^{-1}}$ is the gravitational energy, M is the neutron star mass, R is the neutron star radius, and Q_{nuc} is the total energy generation of the burst, which originally was given by Cumming and Bildsten (2000) to be

$$Q_{nuc} = 1.4 + 4\bar{X} \quad \mathrm{MeV/nucleon} \tag{2.14}$$

where $\bar{X}$ is the average hydrogen mass fraction of the ignition column, $\bar{X} = X(1.0 - \frac{0.5y_b}{y_d})$.

In Chapter 3, however, we re-calibrate this relation using `Kepler` and find that the total energy generation of a burst is more accurately given by

$$Q_{nuc} = 1.35 + 6.05\bar{X} \quad \mathrm{MeV/nucleon} \tag{2.15}$$

In this work we have updated the CNO energy generation rate (Equation 2.4), the time to burn hydrogen 2.5, and the nuclear energy generation of a burst (Equation 2.15) from the original values used in Cumming and Bildsten (2000). In Chapter 5 we present a comparison of `Kepler` and `Settle` burst predictions, and provide details on a correction applied to `Settle` to account for differences.

2.1.2 *KEPLER*

`Kepler` is a 1-dimensional, multi-zone, implicit hydrodynamics Lagrangian stellar evolution code that has a wide range of applications from modelling stellar evolution, to supernovae, to X-ray bursts on accreting neutron stars (Weaver, Zimmerman and Woosley, 1978). It integrates the time-dependent equations of conservation of momentum, mass, and energy, in spherical symmetry, as outlined by Weaver, Zimmerman and Woosley (1978). The version of `Kepler` used in this work does not model rotation or magnetic fields. It allows for a general mixture of radiation, ions, and degenerate or relativistic electrons and implements the Ledoux criterion for convection. Accretion is treated as in Taam, Woosley and Lamb (1996). Whereas `Kepler` can include post-Newtonian approximation, we do not use this

here as the accretion layer is usually much thinner than its radius and the domain is well approximated as a local Newtonian frame. Corrections must be applied to compare the results obtained with observations in the observer reference frame for different assumptions of neutron star radius and mass. What matters for the bare simulations is the gravitational acceleration in the rest-frame of the simulated layer.

When modelling X-ray bursts, `Kepler` is able to simulate chains of bursts, tracking changes in composition in the accreted layer during accretion, the bursts, and the ashes that consequent bursts may ignite in. It calculates the nuclear energy generation and composition changes at each timestep during accretion, and the code checks if the Ledoux criterion for instability is satisfied at each timestep, enabling episodes of convection and thermohaline mixing between bursts (Woosley et al., 2004). In practice, only the outer $\approx 2 \times 10^{25}$ g ($\lesssim 10$ m, excluding the ≈ 60 m substrate) of the neutron star crust is simulated, which is orders of magnitude larger than the mass accreted during a simulated outburst, and the layer is able to act as a repository for thermal inertia. The "substrate" is usually set to consist of pure iron (or other non-nuclear-reactive substances), and the luminosity at the base of the substrate (or the base flux) can be manually set in the generator file. Before accretion is switched on the substrate is given time to relax to a thermal steady state.

The adaptive nuclear reaction network implemented in `Kepler` for simulating X-ray bursts tracks up to 1300 isotopes ranging from $Z = 1$ to $Z = 84$, as described in Woosley et al. (2004). Reaction rates are taken from either experiment, shell model, or statistical model calculations. Most reaction rates are taken from the Hauser-Feshbach NON-SMOKER code (Rauscher and Thielemann, 2000), excepting nuclei with mass $A = 44 - 63$, where rates are experimentally undetermined, the (p, γ) rates are taken from shell model calculations by Fisker et al. (2001). `Kepler` adopts experimentally determined rates wherever possible[1].

An example train of X-ray bursts simulated by `Kepler` is shown in Figure 2.1 (Woosley et al., 2004), highlighting the detail able to be obtained in `Kepler` models, as well as the importance of modelling trains of bursts to account for compositional and thermal inertia.

1 see http://www-pat.llnl.gov/Research/RRSN/

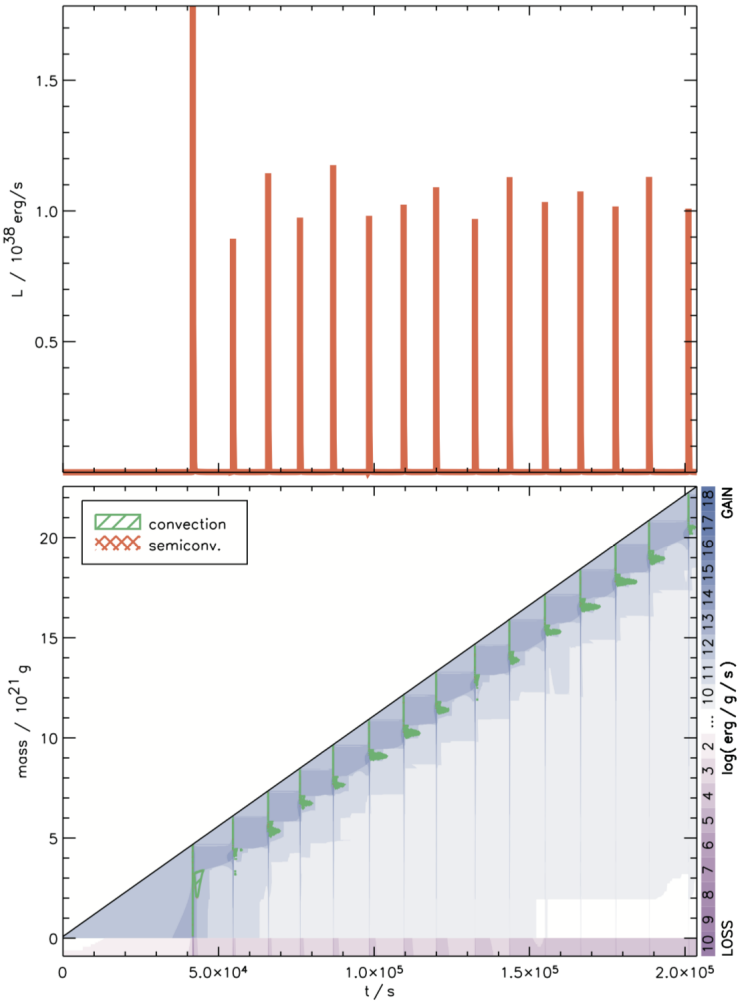

FIGURE 2.1: A `Kepler` simulated X-ray burst train for model with parameters H mass fraction $X = 0.759$, CNO metallicity $Z = 0.05\,Z_\odot$, and accretion rate $\dot{m} = 17.5 \times 10^{-10}\,M_\odot\,yr^{-1}$. Top panel: The lightcurve of the simulated bursts. Note that the first burst is almost always significantly brighter than subsequent bursts. Bottom panel: A Kippenhahn diagram of the bursts. Blue shading indicates net energy generation and pink shading indicates net energy losses. The heat flow and burning in the ashes of previous bursts is clearly visible. Figure reproduced with permission from Woosley et al. (2004).

In this work we use Kepler for two separate purposes. Firstly, in Chapter 3, we use Kepler to simulate the total energy generation (and other properties) of X-ray bursts for a range of initial compositions and accretion rates. We perform calculations of a grid of 84 Kepler models and analyse the properties of the bursts produced. We also use Kepler in Chapter 3 to extract an opacity table that gives the value of opacity for different temperature and density combinations, to extract a density and temperature distribution for use in a our 2D model of the heat transport mechanisms in the accreted layers on the surface of an accreting neutron star, as well as for 1D models of the effect of a hotspot on the surface.

The Kepler generator files used to perform both sets of calculations in Chapter 3 are available in Appendix A.

2.1.3 *MESA*

Modules for Experiments in Astrophysics (MESA, Paxton et al., 2011, 2013, 2015, 2018, 2019)[2] is a publicly available 1-dimensional stellar evolution code that has the capability of modelling a wide range of stellar evolutionary scenarios, from low mass to massive stars, binary evolution, and even accreting neutron stars and X-ray bursts. It was developed by Paxton and co-authors in the early 2000s, with the primary goal of creating a publicly available, open source resource for education, research, and outreach purposes. MESA has been used widely in the Astrophysics literature to model an enormous range of phenomenon; here we focus on the usage and setup of MESA for the applications relevant to this work.

In general terms, MESA solves the stellar structure equations numerically in Fortran, with automatic mesh refinement, analytic Jacobians, and coupled solution of the structure and composition equations. It assumes spherical symmetry, and divides the structure into cells, the number of which depend on the complexity of nuclear burning, composition, gradients of state variables, etc. MESA solves the coupled composition and structure equations for each cell using a Newton-Raphson scheme, and converges on a solution at each timestep by iteratively improving on the trial solution (for which it uses the previous model from the previous timestep). The convergence criteria are numerous and can be manually altered by a user, or automatically adjusted by MESA during a computationally expensive calculation (e.g. during the He core flash phase of stellar evolution). The Henyey, Vardya and Bodenheimer (1965) prescription for convection is adopted using the mixing length theory, and is time dependent.

The nuclear reaction network implemented by MESA involves over 300 rates for elements up to nickel, and includes the weak reaction rates for hydrogen burning. There are multiple network options, including net, which uses nuclear reaction rates from publicly available code[3], including a basic network of eight isotopes: ^{1}H, ^{3}He, ^{4}He, ^{12}C, ^{14}N, ^{16}O, ^{20}Ne, and ^{24}Mg, as well as extended networks. Alternatively, one can use the JINA Reaclib database for thermonuclear reaction rates (Rauscher and Thielemann, 2000; Cyburt et al., 2010), which covers more than 76,000 nuclear reactions with more than 4500 isotopes.

2 http://mesa.sourceforge.net
3 http://cococubed.asu.edu/code_pages/codes.shtml

MESA has 2 main modules, MESAstar and MESAbinary. MESAstar can be used on its own to evolve a single star, and MESAbinary uses MESAstar to evolve two stars in a binary, or a compact object (point source) and a star in a binary.

2.1.3.1 *Application to binary evolution*

MESAbinary has been used extensively to model binary evolution, including accreting neutron star binary systems (e.g. Jia and Li, 2016; Chen, 2017; Fragos et al., 2019). Usually in these simulations the neutron star is assumed to be a point mass, and mass transfer is calculated using the Ritter (1988) scheme and the Eggleton (1983) Roche Lobe overflow scheme. Orbital angular momentum changes are attributed to the Peters (1964) gravitational radiation prescription, the Rappaport, Verbunt and Joss (1983) magnetic braking prescription, and mass ejected from the system. The mass ejected can be manually adjusted to include mass ejected from the donor, accretor, and circumbinary coplanar toroid, with ejection from each location causing different changes to the orbital angular momentum. During accretion episodes in MESAbinary, small amounts of mass are added to the model's outer layer, and the stellar structure is readjusted (Paxton et al., 2011). The amount of mass accreted is calculated using the Eggleton (1983) scheme for Roche-Lobe overflow.

2.1.3.2 *Application to X-ray bursts*

MESAbinary can be used to model X-ray bursting accreting neutron star systems, as in Paxton et al. (2015) and Meisel (2018). Parameters such as accretion rate, $\dot{M}$, base flux, Q_b, metallicity, Z, and H mass fraction, X, can be set, similar to Kepler. Nuclear reaction rates can be set to the JINA Reaclib database, using 304 isotopes of Fisker, Schatz and Thielemann (2008). In the X-ray burst calculations performed by Meisel (2018) they use a neutron star envelope 0.01 km thick, and an inner boundary of mass 1.4 $M_\odot$ and radius 11.2 km. The envelope contains ~1000 zones and the local gravity of each zone is corrected for general relativistic effects using a post-Newtonian correction. Some example burst trains and lightcurves from MESA models of a helium accretor are shown in Figure 2.2. Qualitatively it seems Kepler and MESA simulations of X-ray bursts produce similar results, however there has been no thorough quantitative comparison.

In this work we use MESA to evolve a low mass neutron star X-ray binary. We use MESAbinary and evolve one star, with the other (the neutron star) being a point mass. We allow for mass transfer, and wrote additional modules to include the effects of evaporation and irradiation on the internal structure of the donor star, and the orbit. We also wrote an additional module to allow for mass ejected at the inner Lagrangian point of the binary system, for reasons outlined in Chapter 6. These routines are incorporated into MESA using the extras functionality. The MESA inlists we used to perform the calculations in Chapter 6 are available in Appendix A, as well as the extras routines.

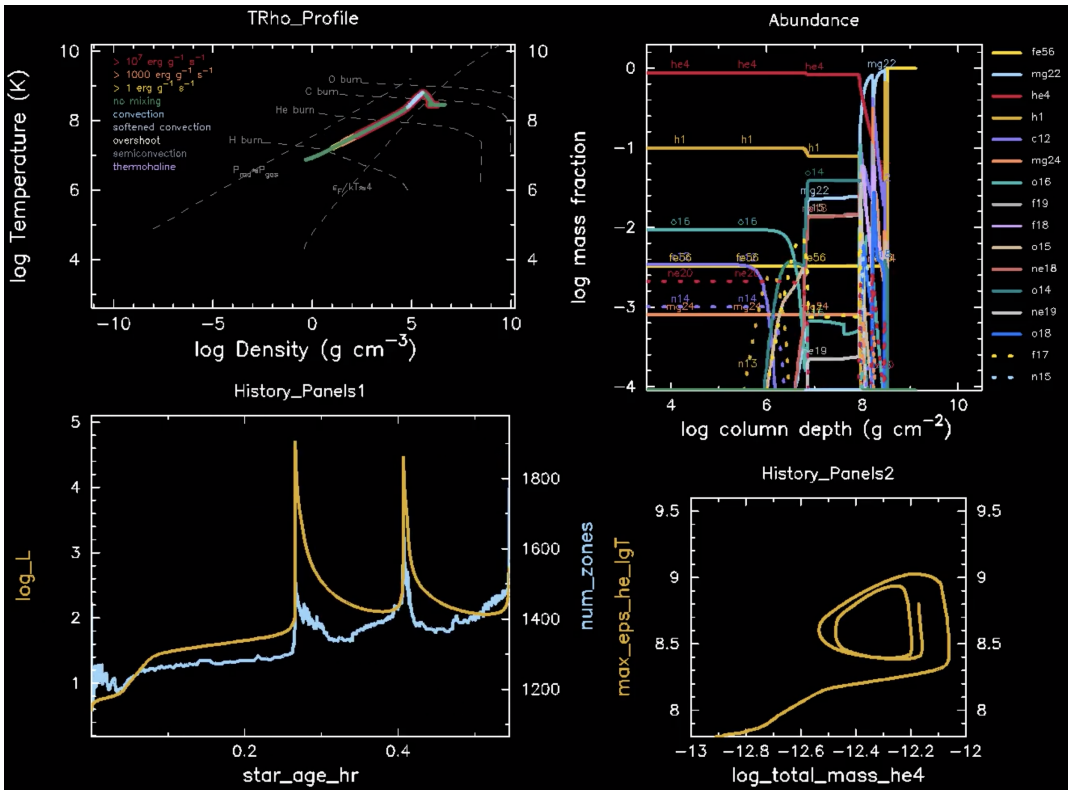

FIGURE 2.2: MESA simulated X-ray burst trains for a helium accreting model with accretion rate $3 \times 10^{-8}\,M_\odot\ yr^{-1}$. The bottom left panel shows the X-ray burst lightcurve, where 3 bursts have been simulated. The top right panel shows the abundance of different elements with column depth.

2.2 OBSERVATIONAL TECHNIQUES

Processing and reduction of X-ray observations is necessary in order to extract useful information, such as fluxes, from the data. In this work we analysed both *RXTE*/PCA and *Swift*/XRT telescope data using the HEASoft `xspec` package.

2.2.1 *HEASoft*

HEASoft[4] is a collection of tools and software packages for use in analysing observational data from many instruments. In this work, we analyse X-ray data from *RXTE* and *Swift*, primarily using the HEASoft package `xspec` to carry out spectral fitting.

When we obtain spectral observations of a source, the telescope measures the photon counts, C, within specific instrument channels, I. As discussed in detail by Ingham and Arnaud (*The Xselect User's Guide*), the observed spectrum is related to the actual spectrum ($f(E)$)of the source via

$$C(I) = \int f(E)R(I,E)dE \tag{2.16}$$

4 https://heasarc.gsfc.nasa.gov/docs/software/heasoft/

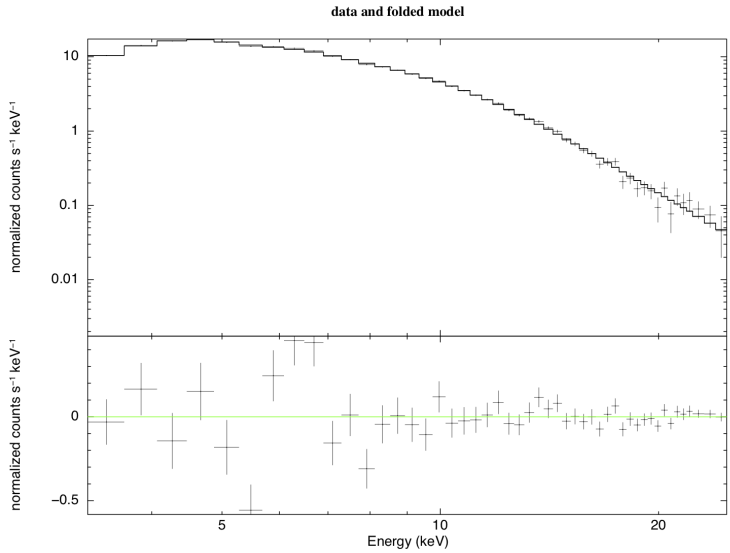

FIGURE 2.3: Example spectrum extracted from `xspec` for *RXTE* data of XTE J1814–338 in outburst, as presented in Chapter 3. Top panel: the scatter points indicate the raw observational data and the line shows the model fit, in this case an absorbed blackbody. Bottom panel: the residuals of the model fit from the raw data.

where $R(I, E)$ is the instrumental response, proportional to the probability of an incoming photon with energy E being detected in channel I.

Usually, a model spectrum, $f(E)$, is chosen that can be described by a few parameters ($f(E, p1, p2, ..)$) and is fit to the observed telescope data. Finding the "best-fit" model spectrum can be done in multiple ways, the most common of which uses a χ^2 minimisation technique.

One can choose the parametrised model spectrum to represent what may be expected based on the type of source observed. When modelling accreting neutron stars, we often choose to fit the spectrum with a blackbody or powerlaw, or multiplicative components.

`xspec` allows for many different types of model spectrum, including absorbed blackbodies, powerlaws, as well as modifying additive components by energy-dependent factors, for example for photoelectric absorption.

2.3 BAYESIAN ANALYSIS AND MARKOV CHAIN MONTE CARLO METHODS

At the core of Bayesian theory is the concept of using prior information to inform probabilities. Bayes's theorem states that for two random quantities, θ and y,

$$p(\theta|y) = \frac{p(y|\theta)p(\theta)}{p(y)} \tag{2.17}$$

where $p()$ is a probability distribution and $p(|)$ is a conditional distribution (e.g., Berger, 1985; Joyce, 2003).

Bayesian analysis involves combining prior information, $p(\theta)$, with some sample information, y, into a posterior distribution of θ given y, $p(\theta|y)$ from which inference can be made. The sample information may be in the form of a likelihood,

$p(y|\theta)$. In the case of Chapter 5 in this work, the sample information ($p(y|\theta)$) corresponds to a likelihood function that assesses how well observations (y) of a burst train match predictions from `Settle` for a certain set of θ parameters. We define y as the observed recurrence time, energy, and α values of the bursts, and $p(y|\theta)$ is a likelihood function that is largest when the observations exactly match the predictions from `Settle`. The θ parameters include the composition of the accreted fuel, the accretion rate, the base flux, the NS mass, radius, and other model parameters. We define priors for each of the θ parameters, that represent expectations of what the probability distribution for each of these parameters should be, without considering the specific observations we are matching. The θ parameters are what we are interested in obtaining constraints on, and through using Bayesian inference we are able to obtain posterior distributions for each of these parameters. The posterior distributions thus provide a posterior probability distribution for θ by combining the prior beliefs about θ with information contained in the sample information (e.g. Berger, 1985).

However, as explained by Berger (1985), determining the prior information is not always straightforward, and it can be heavily affected by our beliefs. A prior is defined as the probability distribution of a certain quantity that contains one's beliefs about the quantity before any data is considered. Priors can be uninformative and uniform, where upper and lower bounds are chosen for parameters in θ and a uniform probability distribution is assumed between those bounds. Or, a more informed prior probability distribution can be implemented, which takes into account some understanding of the expected distribution of the quantity. Usually priors are informed by past information (experiments), or could be deduced from a purely subjective understanding of the quantity. If there is no relevant expectation of the probability distribution a quantity may have, an uninformative prior may be used. For example, in Chapter 5, we use a probability distribution as a prior for metallicity, Z, where we obtain the probability distribution from a model of the galaxy at the location of the source we are interested in. In this case, the prior distribution is non-uniform and we are using previous knowledge about the possible values for the metallicity, before considering the values of metallicity the evidence (or our model) finds likely. Conversely, for the hydrogen mass fraction, X, we have no a priori expectation of the probability distribution except that it cannot be less than 0 or more than the value of X for the Universe at the time of the Big Bang. In this case we thus use a uniform prior with bounds $0 < X < 0.76$.

2.3.1 *Markov Chain Monte Carlo methods*

Markov Chain Monte Carlo (MCMC) is a numerical method for sampling from a probability distribution to obtain posterior distributions. In Bayesian inference, it enables the posterior distribution to be computed through exploration of the parameter space. MCMC methods are particularly useful if the likelihood (or model) is computationally expensive to compute, as they are designed to efficiently sample the posterior probability distribution, without requiring a full calculation of the posterior. An MCMC method generates samples, x, from a given probability distribution, $p(x)$, which is the target density (e.g. Foreman-Mackey et al., 2013). In

so doing, the target probability distribution can be inferred, without needing to evaluate $p(x)$ everywhere. Furthermore, the accuracy of an MCMC estimate depends only on the variance of θ, and not the dimensionality of the parameter space (MacKay, 2003).

There are various implementations of MCMC that use different approaches to sample the posterior probability distribution. In this work we use a particular MCMC method called the Metropolis-Hastings method (Metropolis et al., 1953), as outlined in Foreman-Mackey et al. (2013) and below.

The Metropolis-Hastings method involves "walkers" which take "steps" in random directions to explore parameter space and sample from the posterior probability distribution of θ.

The Metropolis-Hastings algorithm begins with the assumption that at a current state, x, $p(x)$ can be evaluated at any point x, to within a multiplicative constant, such that a function $p^*(x)$ can be evaluated where

$$p(x) = p^*(x)/Z \tag{2.18}$$

where Z is a normalising constant (MacKay, 2003).

The overall goal of the algorithm is to draw samples from the posterior probability density, to determine where $p(x)$ is biggest, without having to evaluate $p(x)$ everywhere.

As outlined in detail in MacKay (2003), the algorithm uses a proposal density, Q, which depends on the current state, x, and can be any fixed density from which samples can be drawn. Under the assumption that $p^*(x)$ can be evaluated for any x, a new state is generated from the proposal density $Q(x'; x)$. The algorithm then must decide whether to accept or reject the new proposed state. To do this, it computes

$$a = \frac{p^*(x')}{p^*(x)} \frac{Q(x; x')}{Q(x'; x)} \tag{2.19}$$

If $a \geqslant 1$, the new state is accepted. If $a < 1$, the new state is accepted with probability a. If the step is accepted, then the next step starts with $x = x'$, or if the step is rejected, then the next step starts with $x = x$ (i.e., there is no movement in parameter space). The algorithm continues taking steps in this manner for as many steps as the user desires, and there can be multiple walkers which each perform their own set of steps in parameter space. The process is ideally run until a "chain" is generated that consists of samples that are effectively independent samples from p.

Determining the number of steps required in order for the algorithm to effectively sample the target posterior distribution $p(x)$, however, is not straightforward. This is where we consider convergence of the MCMC chains. As the number of steps taken approaches infinity, the probability distribution of x will approach $p(x) = p^*(x)/Z$ for any positive Q. It can be difficult to assess whether the generated samples are effectively independent samples of p, since successive samples are dependent in this algorithm. Foreman-Mackey et al. (2013) suggest the autocorrelation time and acceptance fraction can be useful measures of the convergence and performance of the chains.

The acceptance fraction is simply the number of proposed steps that were accepted (e.g. Foreman-Mackey et al., 2013; Rosenthal, 2011). It can be a reliable measure of whether the samples are representative of the target density. If the acceptance fraction is ~ 0, almost all proposed steps were rejected, and the chain will thus have only a few independent samples, and not be representative of the target density. Conversely, if the acceptance fraction is very high (~ 1), almost all proposed steps were accepted, and the algorithm is simply performing a random walk in parameter space without converging on a region of higher probability, where the target density may be. Most studies agree that the acceptance fraction should be between 0.2 to 0.5, however, there is some uncertainty in this, since it can also depend on how big steps are in parameter space; if a walker takes very small steps the acceptance fraction will likely be very high, but is not representative of the target density, or if the walker takes steps that are too large the acceptance fraction will likely be very low and the walker may never move from its initial position (e.g., Rosenthal, 2011).

The autocorrelation time is a measure of the number of evaluations of the posterior probability distribution necessary to produce independent samples of the target density (e.g., MacKay, 2003). If the autocorrelation time is long, then more samples must be generated in order to obtain a representative sampling of the target density.

2.3.2 *emcee*

In Chapter 5, we use a Python implementation of MCMC, called `emcee`[5] (Foreman-Mackey et al., 2013), to combine observations of X-ray bursts with the `Settle` model to determine system parameters we cannot observe directly. We call this software Bayesian Estimation of Accreting Neutron Star parameters (BEANS)[6]. `emcee` implements the affine invariant ensemble sampler (meaning it is insensitive to covariances among parameters as it performs equally well under all linear transformations) proposed by Goodman and Weare (2010), based on a Metropolis-Hastings algorithm.

The likelihood function, prior probability distributions, model, and the observed data can all be easily input into `emcee`, as well as the number of walkers and steps desired for the MCMC algorithm. The posterior distribution of θ is then sampled and values for the parameters within θ can thus be obtained, with uncertainties.

Figure 2.5 shows an example usage of `emcee`, for a simple straight line model, $y = mx + b$, and some randomly generated synthetic data (Figure 2.4) to simulate fitting a straight line to some scatter points. The θ model parameters include m, b and f (where f is some fractional amount the variance in the Gaussian likelihood is underestimated by).

For this simple case, a Gaussian likelihood function was used where

$$\ln p(y|x, \sigma, m, b, f) = -\frac{1}{2}\sum_n \left[\frac{(y_n - mx_n - b)^2}{s_n^2} + \ln(2\pi s_n^2)\right] \tag{2.20}$$

5 https://emcee.readthedocs.io/en/stable/

6 What is an Astronomy project without a terrible acronym?

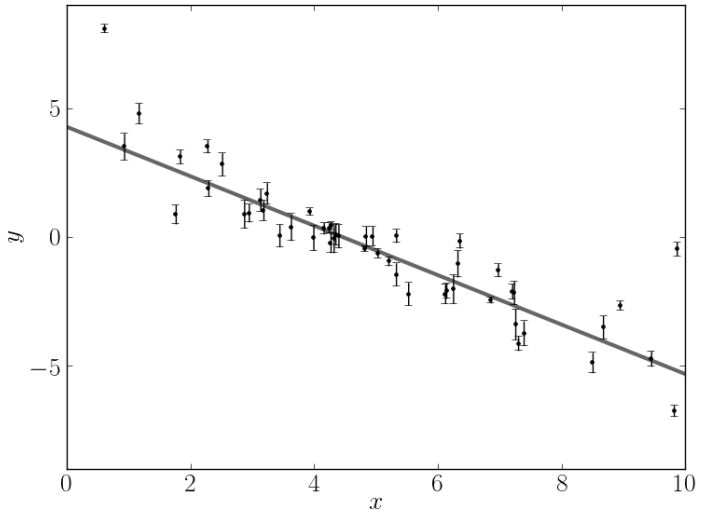

FIGURE 2.4: Synthetic dataset (circles) and model (line) for the simple `emcee` example. Figure generated from an example presented on https://emcee.readthedocs.io/en/stable/.

where $s_n^2 = \sigma_n^2 + f^2(mx_n + b)^2$, σ is the variance of the Gaussian distribution and f is some fractional amount the variance is underestimated by.

Uniform prior distributions were assumed such that

$$-5.0 < m < 0.5 \tag{2.21}$$

$$0.0 < b < 10.0 \tag{2.22}$$

$$-10.0 < \ln f < 1.0 \tag{2.23}$$

The two dimensional projections of the posterior probabilities obtained for each of the three θ parameters are shown in Figure 2.5.

In this case there is a clear correlation between b and m, as is expected since they are dependent in the straight line model, as can be easily seen in the 2D visualisation in Figure 2.5.

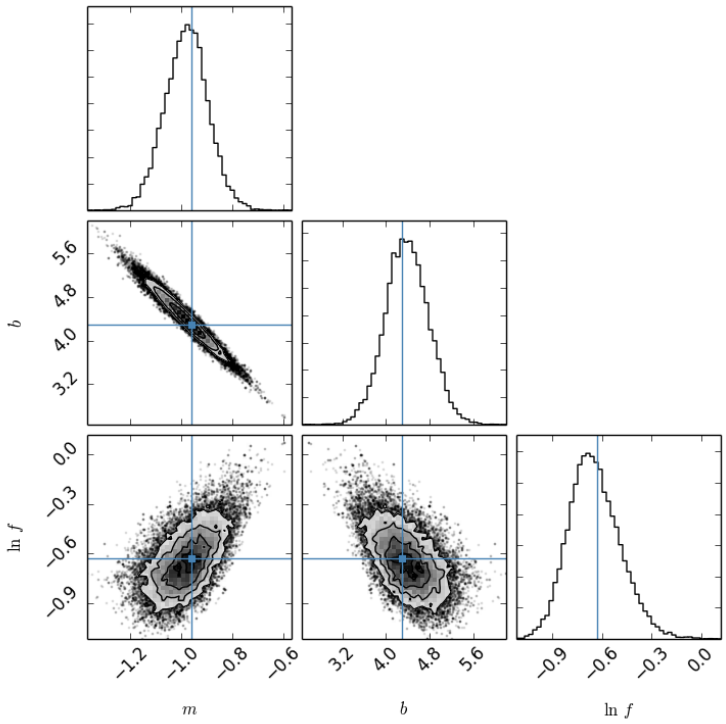

FIGURE 2.5: Example posterior distributions estimated by `emcee` for marginalisation over three parameters to fit a straight line to some synthetic data. Blue lines indicate the true value for each parameter. Figure generated from an example presented on https://emcee.readthedocs.io/en/stable/.

3

MODELS OF ACCRETING NEUTRON STARS

Modelling of accreting neutron star systems is important in deepening our understanding of the physics of these systems, as well as signalling where our understanding of the physics may fail to reproduce observed phenomenon. In this chapter we present two published works of studies that involve modelling of X-ray bursts on the surface of accreting neutron star systems.

3.1 NEUTRINO LOSSES IN TYPE I THERMONUCLEAR X-RAY BURSTS: AN IMPROVED NUCLEAR ENERGY GENERATION APPROXIMATION

Analytic models of X-ray bursts that do not perform full nuclear reaction network calculations must make assumptions about the total energy released during a burst. Analytic models are useful as they are less computationally expensive than the more robust models, and thus can be used in scenarios that require many model runs, for example, a Markov Chain Monte Carlo algorithms (see Chapter 2). In the first study presented in this thesis chapter we address the problem of providing a simplified energy generation rate of an X-ray burst based on the hydrogen content of the ignition column that may be used in these simple analytic calculations, as well as to infer hydrogen fraction from observations of X-ray burst energies. We also provide estimates of the total amount of energy released in the form of neutrinos during a burst, and find it is significantly less than assumed in previous studies.

Published in:
A. J. Goodwin, A. Heger and D. K. Galloway (Jan. 2019). 'Neutrino Losses in Type I Thermonuclear X-Ray Bursts: An Improved Nuclear Energy Generation Approximation'. *ApJ* 870.2, 64, p. 64. DOI: 10.3847/1538-4357/aaeed2. arXiv: 1808.02225 [astro-ph.HE]

Draft version September 28, 2020
Typeset using LaTeX **twocolumn** style in AASTeX62

Neutrino Losses in Type I Thermonuclear X-Ray Bursts: An Improved Nuclear Energy Generation Approximation

A. J. Goodwin,[1,2] A. Heger,[1,2,3] and D. K. Galloway[1,2]

[1] *School of Physics and Astronomy, Monash University, Clayton, Vic 3800, Australia*
[2] *Monash Centre for Astrophysics*
[3] *Tsung-Dao Lee Institute, Shanghai 200240, China*

(Received July 15, 2018; Revised September 20, 2018; Accepted November 4, 2018)

Submitted to ApJ

ABSTRACT

Type I X-ray bursts are thermonuclear explosions on the surface of accreting neutron stars. Hydrogen rich X-ray bursts burn protons far from the line of stability and can release energy in the form of neutrinos from β-decays. We have estimated, for the first time, the neutrino fluxes of Type I bursts for a range of initial conditions based on the predictions of a 1D implicit hydrodynamics code, Kepler, which calculates the complete nuclear reaction network. We find that neutrino losses are between 6.7×10^{-5} and 0.14 of the total energy per nucleon, $Q_{\rm nuc}$, depending upon the hydrogen fraction in the fuel. These values are significantly below the 35 % value for neutrino losses often adopted in recent literature for the *rp*-process. The discrepancy arises because it is only at β-decays that $\approx$ 35 % of energy is lost due to neutrino emission, whereas there are no neutrino losses in (p,γ) and (α,p) reactions. Using the total measured burst energies from Kepler for a range of initial conditions, we have determined an approximation formula for the total energy per nucleon released during an X-ray burst, $Q_{\rm nuc} = (1.31 + 6.95\,\overline{X} - 1.92\,\overline{X}^2)$ MeV nucleon^{-1}, where $\overline{X}$ is the average hydrogen mass fraction of the ignition column, with an RMS error of 0.052 MeV nucleon^{-1}. We provide a detailed analysis of the nuclear energy output of a burst and find an incomplete extraction of mass excess in the burst fuel, with 14 % of the mass excess in the fuel not being extracted.

1. INTRODUCTION

Since the discovery of bright, energetic explosions from compact objects, known as thermonuclear X-ray bursts (Grindlay et al. 1976), observers have used these events as laboratories for nuclear physics experiments that cannot be replicated on Earth. Type I X-ray bursts are highly energetic ($\sim 10^{38}$ erg) thermonuclear flashes observed radiating from the surface of an accreting neutron star (e.g., Lewin et al. 1993). They are the most frequently observed thermonuclear-powered outbursts in nature and can be used to constrain fundamental information about matter of supernuclear density and the nuclear reactions and processes that can occur in extreme environments.

Thermonuclear X-ray bursts occur at high ($> 10^7$ K) temperatures. They are powered by nuclear reactions, with current theory suggesting five main nuclear reaction pathways involved in the burning in the lead up to a burst, as well as during a burst. These are: the (hot) CNO cycle, the 3α-process, the α-process, the αp-process, and the *rp*-process (e.g., Galloway & Keek 2017; Bildsten 1998).

The hot CNO cycle burns hydrogen into helium. The process involves two β-decays, releasing 2 neutrinos which carry away a total of $\sim$ 2 MeV, and is usually responsible for the steady hydrogen burning between bursts, and could be responsible for burst ignition at very low accretion rates (Fujimoto et al. 1981). The triple-α process is the pathway by which helium burns to carbon and is thought to be the primary cause of burst ignition (e.g., Joss 1978). The α-process forms heavier elements from the products of the previous two processes and occurs at temperatures $\gtrsim 10^9$ K (Fujimoto et al. 1981). The αp-process is similar to the α-process, but the reaction is catalysed by protons. The *rp*-process (rapid-proton capture process) is a chain of successive proton captures and β-decays, beginning with the products of the previous nuclear reaction chains, and quite easily producing elements beyond ^{56}Fe (see Wallace & Woosley 1981). Each β-decay releases a neutrino.

The primary source of neutrinos during a burst is the β-decays, where typically $\approx$ 35 % of energy is lost as neutrinos

Corresponding author: Adelle Goodwin
adelle.goodwin@monash.edu

(Fujimoto et al. 1987), depending on weak strength distribution, and can be quite different for electron captures. In recent X-ray burst literature, this is often misinterpreted to mean neutrino energy release for the entire *rp*-process is 35 % (e.g., in't Zand et al. 2017; Cumming & Bildsten 2000). To emphasise this point, again, it is only for the β-decays that 35 % of the energy is lost as neutrinos and β-decays do not dominate the total energy release.

Modelling of Type I thermonuclear X-ray bursts has played a significant role in our understanding of their observational properties. Understanding of Type I X-ray bursts must combine theory and observations to comprehensively predict observed burst parameters. Early models (e.g., Fujimoto et al. 1981; Taam 1980; van Paradijs et al. 1988; Cumming & Bildsten 2000), focus on the correlation between burst energies and recurrence times, to varying success, using an analytic or semi-analytic approach to integrate an ignition column using simple assumptions. More recent models (e.g., Woosley et al. 2004; Fisker et al. 2008, 2004) have a heavier focus on the nuclear physics driving the bursts, predicting fuel compositions and accretion rates by implementing a deeper understanding of the nuclear reactions that produce the observed energy generation rates. The most advanced of these models, KEPLER (Woosley et al. 2004), uses an adaptive nuclear reaction network to model the burning before, and during a burst in more detail.

Based on an incorrect expression for neutrino losses during the αp- and *rp*-process, the energy generation of Type I bursts ($Q_{\rm nuc}$) in simple models has often been given by the relation $Q_{\rm nuc} = (1.6{+}4\,\overline{X})$ MeV nucleon^{-1}, where $\overline{X}$ is the average hydrogen mass fraction of the ignition column (e.g., Cumming & Bildsten 2000). The formula accounts for helium burning to iron group with an energy release of 1.6 MeV nucleon^{-1} and hydrogen burning to iron group with an energy release of $4\,\overline{X}$ MeV nucleon^{-1}. $Q_{\rm nuc}$ is directly related to the energy of a burst by multiplying by the number of nucleons (mass) burnt in the burst. As such, this expression for $Q_{\rm nuc}$ can be used to infer the energy of a simulated burst, given some composition and accretion rate (and hence ignition depth) in simple analytic models (such as Cumming 2003). Observers also use this approximation to infer the average hydrogen fraction at ignition, and thus composition of the fuel burnt in the burst from observations of energy (e.g., Galloway & Cumming 2006; Chenevez et al. 2016; Galloway et al. 2008, 2004a).

In this work we measure the neutrino fluxes of Type I X-ray bursts based on the predictions of the advanced modelling code KEPLER (Woosley et al. 2004), and develop a new nuclear energy generation approximation using these neutrino estimates. We also examine the metallicity dependence on the neutrino losses and the incomplete burning of the burst fuel. In Section 2 we outline the methods and describe the KEPLER code used in this work, in Section 3 we present the results, giving the expected neutrino losses for Type I X-ray bursts and in Section 4 we discuss the results and provide a case study on the effect that overestimating the neutrino losses has had on composition predictions. Our conclusions are given in Section 5.

2. METHODS

KEPLER is a one-dimensional implicit hydrodynamics code that allows for a general mixture of radiation, ions, and degenerate or relativistic electrons (Woosley et al. 2004). It provides a detailed treatment of the nuclear physics and energy generation using a large nuclear reaction network. Reaction rates for nuclei in the mass range A = 44–63 are taken from shell model calculations by Fisker et al. (2001) and all other reaction rates are calculated using the Hauser-Fashbach code NON-SMOKER (Rauscher & Thielemann 2000). It is worth noting that there are some uncertainties inherent in the calculation of rates near the proton drip line, as discussed by Fisker et al. (2001). Calculations include electron capture, nuclear β^+-decays (positron emission) and neutrino energy losses (Woosley et al. 2004).

Neutrino losses during weak decays are significant, typically taking away $\approx$ 35 % of the energy available in a decay (Woosley et al. 2004). KEPLER estimates the energy taken away by neutrinos during a burst using the neutrino energy loss rates of weak decay reactions from Langanke & Martínez-Pinedo (2001) or Fuller et al. (1982), or using experimentally determined ground state weak strength distributions for a few light nuclei, or by taking the product of the weak decay rate and the average neutrino energy of predictions from a code from Petr Vogel (see Woosley et al. 2004). Woosley et al. (2004) note that since phase space heavily favours the transitions with the most energetic outgoing neutrinos, empirical strength distributions can do a fair job at estimating average neutrino energies despite the fact they cannot reliably reproduce ground state decay rates.

We computed 84 KEPLER models of a system that exhibits Type I X-ray bursts for initial hydrogen mass fractions of 0.2–0.8, metallicity mass fractions of 0.1, 0.02, and 0.005 and accretion rates of 0.3, 0.2, 0.1, and 0.01 $\dot{m}_{\rm edd}$, where $\dot{m}_{\rm edd}$ is the Eddington accretion rate, $8.8 \times 10^{-4} \frac{1.7}{(X+1)}$ g cm^{-2} s^{-1}. We use the same setup as in Johnston et al. (2018): a neutron star radius of 10 km, a neutron star mass of 1.4 $M_\odot$. We start accretion on top of an iron substrate of mass $2{\times}10^{25}$ g and use a base heating rate of 0.1 MeV nucleon^{-1}. Since the layer considered is thin compared to the neutron star radius ($\sim$ 10 m) and we are only interested in the gravity of the local frame, we just use Newtonian gravity. The local gravity corresponds to a general relativistic case of same gravitational mass but radius of 11.2 km. All accretion rates, time scales, energies, and luminosities in this paper are given in the local

Newtonian frame. For clarity, we have provided a table of key definitions of terms used in this paper in Table 1.

For simplicity we use a simplified composition setup that uses ^{14}N as the only metal plus ^{1}H and ^{4}He. That is, we use the ^{14}N mass fraction synonymous for "metallicity." The initial abundance of CNO isotopes is the key aspect of metals affecting the bursting behaviour. The reader may note that in solar composition there is other metals as well, and hence in such a mix the metallicity would need to be higher to have the same CNO number abundance as in the models presented here. Hydrogen fractions higher than 0.8 are not observed and hard to achieve due to Big Bang Nucleosynthesis, and so are not explored in this work. Likewise, metallicities lower than 0.005 and higher than 0.1 are unlikely in the systems studied here, with metallicity usually assumed to be around solar (0.02) so we do not explore metallicities outside those ranges.

The accretions rates explored in this grid correspond to Cases 2–4 burning (as defined by Keek & Heger 2016), or Case III and IV burning (as defined by Fujimoto et al. 1981). In these cases we expect to find hydrogen/helium rich bursts. This is discussed in Section 3.5. Each run produced multiple bursts. We calculated burst energies by taking the average of the simulated bursts, excluding the first. Uncertainties were taken as the standard deviation of the burst energies. We exclude any model runs that produces one or fewer bursts, as these cannot give a reliable energy estimate because the first burst does not have the "chemical inertia" (ashes layer) of the later burst in a sequence (Woosley et al. 2004). We measured the neutrino flux by taking the neutrino flux of every burst from KEPLER. Because the neutrino fluxes of bursts in individual runs varied from burst to burst, we did not just take an average for the entire run, but instead look at the results for each burst separately. To calculate energy generation per nucleon, the ignition column of the burst was found by assuming this was the accreted fuel since the last burst, though in our models ignition may occur above or below this point, in or above the ashes of the previous burst. The exact point of ignition of the thermonuclear runaway is difficult to extract from a multi-zone model as it depends on the exact definition of what ignition actually is: whether one defines a temperature, convection, luminosity threshold, or similar. Therefore we use this simple approach that is consistent with definitions used in other models which assumes that all the accreted fuel is burnt in the burst, and no residual ashes are accounted for. We calculated the total burst energy, i.e., nuclear energy release less neutrino losses, and the total neutrino energy release for a range of $\overline{X}$ values. And $\overline{X}$ was defined as the hydrogen present in the zones above the assumed ignition depth at ignition time.

3. RESULTS

3.1. *Neutrino Losses in Type I X-ray Bursts*

We extracted the neutrino losses for each run from our multi-zone calculations and find neutrino losses range from 6.7×10^{-3} % ($\overline{X} \approx 0$) to 14.2 % ($\overline{X} \approx 0.75$). See Figure 1.

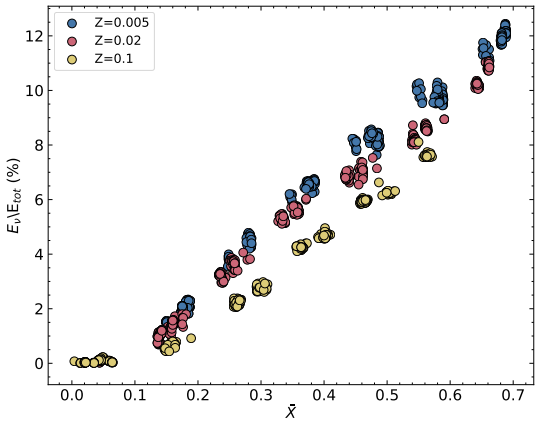

Figure 1. The ratio of neutrino energy (E_ν) to total burst energy ($E_{\rm tot}$ = $E_{\rm b}$ + E_ν) for a range of initial hydrogen fractions and metallicities (Z). $\overline{X}$ is the average hydrogen mass fraction of the ignition column. *Yellow points* correspond to Z = 0.1, *red points* to Z = 0.02 and *blue points* to Z = 0.005.

When more hydrogen is present, more *rp*-process burning occurs and thus more energy is lost in the form of neutrinos from β-decays. One can see clearly that there is never as much as 35 % energy lost as neutrinos for any amount of hydrogen present. There are differences in neutrino energy for the 3 different metallicities explored, as we discuss in Section 3.4 below.

3.2. *A New Nuclear Energy Generation Estimate*

In Figure 2 we show the nuclear energy generation of the bursts as a function of the average hydrogen fraction of the ignition column, $\overline{X}$. Both the burst energy (nuclear energy less neutrinos) and the neutrino energy deviate significantly from $Q_{\rm nuc} = (1.6 + 4\,\overline{X})$ MeV nucleon^{-1} due to the overestimation of the neutrino losses and reduced energy release (see Section 3.3 below).

Fitting the multi-zone model data points using a χ^2 minimisation method gives a new relation: $Q_{\rm nuc} = (1.31 + 6.95\,\overline{X} - 1.92\,\overline{X}^2)$ MeV nucleon^{-1}, with a reduced χ^2 value of 2.32 for 57 degrees of freedom ($n_{\rm obs} - 3$) and root mean square error (RMS) of 0.052 MeV nucleon^{-1}, as shown in Figure 2. We require a second order polynomial to account for a trend observed in the residuals of a first order fit, $Q_{\rm nuc} = (1.35 + 6.05\,\overline{X})$ MeV nucleon^{-1}, which has a reduced χ^2 value of 3.55 for 58 degrees of freedom and a RMS

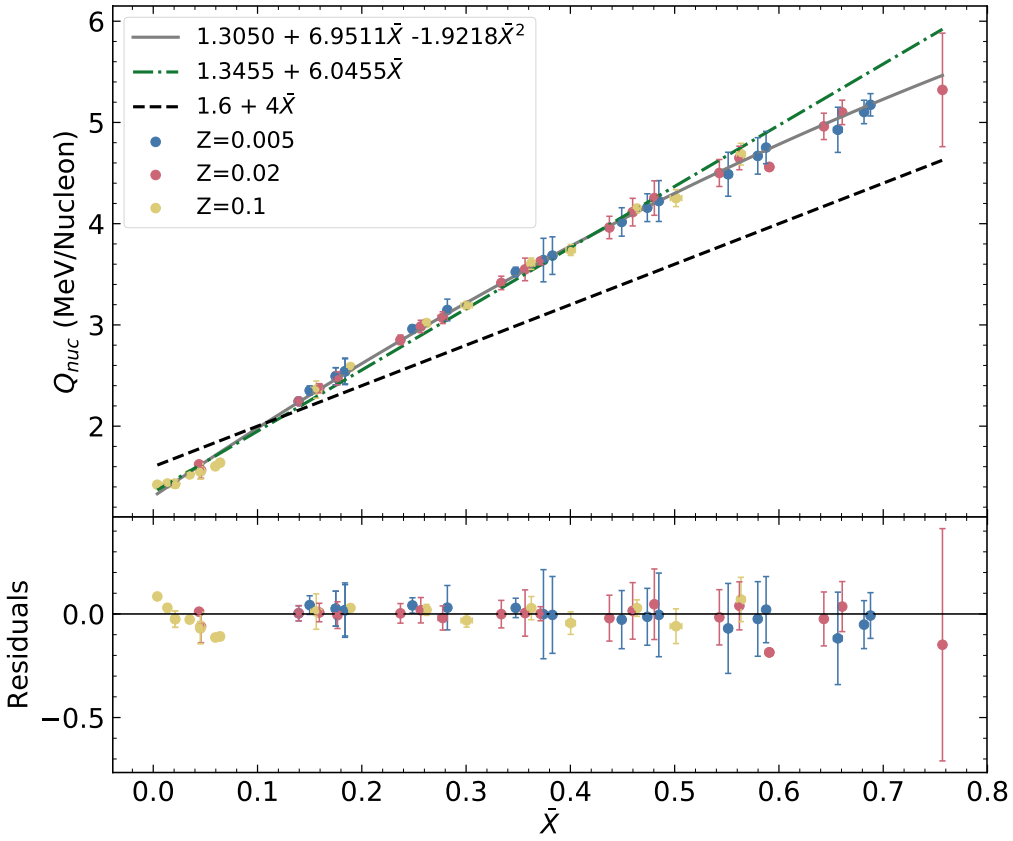

Figure 2. KEPLER $Q_{\rm nuc}$ predictions (*circles*) for a range of metallicities, Z, and initial hydrogen fractions, X, compared to the approximation $Q_{\rm nuc} = (1.6{+}4\,\overline{X})$ MeV nucleon^{-1} (*dashed black*). *Yellow points* correspond to $Z = 0.1$, *red points* to $Z = 0.02$ and *blue points* to $Z = 0.005$. The best fit to the KEPLER data is given by $Q_{\rm nuc} = (1.31{+}6.95\,\overline{X}{-}1.92\,\overline{X}^2)$ MeV nucleon^{-1} (*grey curve*). A first order approximation is given by $Q_{\rm nuc} = (1.35 + 6.05\,\overline{X})$ MeV nucleon^{-1} (*green line*). The residuals ($Q_{\rm nuc,obs} - Q_{\rm nuc,exp}$, where $Q_{\rm nuc,exp} = (1.31 + 6.95\,\overline{X} - 1.92\,\overline{X}^2)$ MeV nucleon^{-1}) are shown in the *bottom panel*.

of 0.15 MeV nucleon^{-1}. We find there is a statistical significance in going to a second order polynomial according to the F-test (Rawlings et al. 2001). We find there is no statistical significance in going to a 3$^{\rm rd}$ order polynomial according to the F-test.

The previous relation of $Q_{\rm nuc} = (1.6 + 4\overline{X})$ MeV nucleon^{-1} has a reduced χ^2 of 75.4 and RMS error of 0.5 MeV nucleon^{-1}, and so is a statistically poor fit to the energies predicted by our multi-zone model. Whilst the reduced χ^2 values of any of the fits are not close to 1, we note that the new relation is a marked improvement on the old relation, though still being an approximation to the true full calculation of a multi-zone model.

3.3. *Incomplete Burning of Burst Fuel*

This relation for $Q_{\rm nuc}$ corresponds to an energy release of 1.305 MeV nucleon^{-1} for fuel with no hydrogen. This value is lower than the expected value of 1.6 MeV nucleon^{-1}, which is the nuclear mass excess difference in burning ^{4}He all the way to ^{56}Fe. On examination of some runs with low hydrogen fraction of the ignition column we found that this discrepancy is caused by two factors: first, the reaction pathways do not burn just to ^{56}Fe but also produce other nuclei with larger mass excess; and second, some helium burns to carbon between bursts, reducing the total yield when the burst finally ignites.

Figure 3 shows the mass excess per nucleon just before (*dark blue curve*) and just after (*light blue curve*) a burst with low hydrogen content of the ignition column ($\overline{X} = 0.14$). The *dashed line* shows the mass excess per nucleon for ^{56}Fe. We find that the mass excess per nucleon in the ashes (*light*

Table 1. Definitions of key terms used in this paper

Symbol	Units	Definition
$Q_{\rm nuc}$	MeV nucleon^{-1}	**Nuclear energy generation per nucleon.** The energy released due to nuclear burning per nucleon burnt. It is computed from the difference in mass excess per nucleon between the start and end of a burst.
$\overline{X}$	1	**Average hydrogen fraction of the ignition column.** The hydrogen fraction of the material in the ignition column as measured just before the burst ignites.
$y_{\rm acc}$	g cm^{-2}	**Accretion Column.** Column of material that is accreted since the previous burst until the ignition of the current burst.
y	g cm^{-2}	**Ignition Column.** Column of material that is ignited in the burst. For the sake of comparison with one-zone models, in this paper we define the ignition column as the same column as the accretion column. In general, however, the ignition point may lie within the ashes from previous bursts. See discussion in Section 2.
$E_{\rm b}$	MeV	**Burst Energy.** Energy released in the form of photons from the surface of the neutron star during a burst.
E_ν	MeV	**Neutrino Energy.** Energy released during a burst in the form of neutrinos. Measured by summing the total neutrino energy released between the start and end of the burst.
$E_{\rm tot}$	MeV	**Total Burst Energy.** Energy released during a burst in the form of photons and neutrinos. $E_{\rm tot} = E_{\rm b} + E_\nu$.

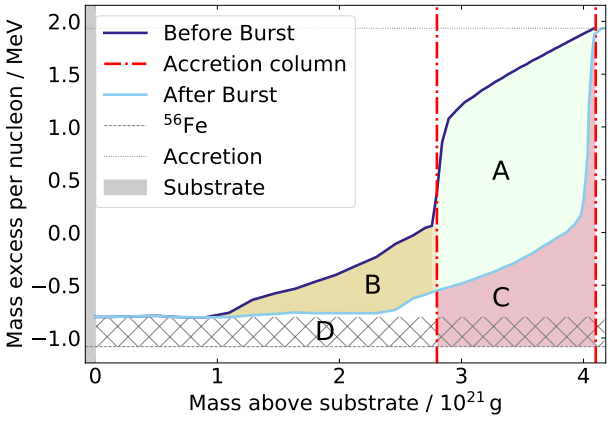

Figure 3. Mass excess per nucleon as a function of mass accreted on top of substrate just before and after a burst with very low hydrogen content in the ignition column ($\overline{X} = 0.14$). The dashed line corresponds to the mass excess of ^{56}Fe, the most stable nucleus. The labelled regions are as follows: *A*: Energy released in burst in the accretion column; *B*: Energy released in burst below the accretion column, in the ashes of the previous burst; *C*: Energy from fuel in the accretion column not released in this burst; *D*: Energy always missing in the ashes of bursts from not burning all the fuel to just ^{56}Fe (about 0.3 MeV nucleon^{-1}).

blue curve) is greater than that of ^{56}Fe, the nucleus with the lowest mass excess. Therefore the total energy produced in the burst is less than would be obtained for burning all the way to ^{56}Fe. Evaluating the area between the *light blue curve* and *dark blue curve*, Areas A + B in Figure 3, by integrating over the mass in the ignition column, gives us the actual total energy produced in the burst. For the case shown, we find ~ 2.2 MeV nucleon^{-1}, in agreement with the 2.2 MeV nucleon^{-1} of our multi-zone model. Note that for the total energy input to the model there is also a base heating of 0.1 MeV nucleon^{-1}, however, that is mostly released between the bursts.

Evaluating the area between the light blue curve and the ^{56}Fe line (Area C), we find the energy missing from not burning all the way to ^{56}Fe as 0.9 MeV nucleon^{-1} in the ignition column. In contrast, if we were burning H to ^{4}He and ^{4}He to ^{56}Fe we would expect to get $Q_{\rm nuc} = 1.6$ MeV nucleon^{-1} (helium burning to iron group) + 6.7 $\overline{X}$ MeV nucleon^{-1} (hydrogen burning to helium) = 2.54 MeV nucleon^{-1} for the material in the ignition column. Adding together the missing energy (Area C) and the energy released in the burst in the ignition column (Area A), we find $Q_{\rm nuc} \approx 1.5$ MeV nucleon^{-1} (burst energy) + 1.1 MeV nucleon^{-1} (missing energy) = 2.6 MeV nucleon^{-1}. This is very close to the expected value, but our numerical model will have had some extra burning, e.g., 3α reactions during the runaway phase of the burst at the base of the ignition layer.

The missing energy from not burning to iron group elements is due to two factors: 1) incomplete burning of fuel leaving elements lighter than ^{56}Fe after the burst; and 2) production of heavier elements with higher mass excess by the *rp*-process. In Figure 4 we show the mass excess relative to ^{56}Fe as a function of accretion mass and how it is distributed by nuclear mass number for the ashes of the same burst as in Figure 4. In this case the mass excess in the ashes is predominately in elements below ^{56}Fe, giving strong evidence that this missing energy is caused by incomplete consumption of mass excess of the fuel, rather than excessive *rp*-process burning.

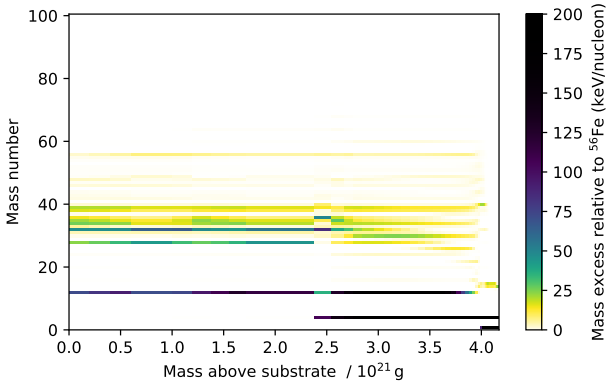

Figure 4. Mass excess per nucleon relative to ^{56}Fe (*colour coding*) as a function of mass accreted on top of substrate (*x-axis*) and how it is distributed by mass number (*y-axis*) for a snapshot taken just after a burst with low hydrogen fraction of the ignition column ($\overline{X} = 0.14$). This is the same model as the *light blue curve* in Figure 3. Mass excess has been truncated at 200 keV nucleon^{-1}.

Furthermore, we found that in the cases where most of the hydrogen had been burned to helium before ignition conditions for a burst were met, there was some evidence for helium burning to carbon before the burst. The resulting ignition column consists of up to ≈ 10 % ^{12}C, which would also reduce the total energy per nucleon available for the burst from the expected value for pure helium fuel burning to the iron group. Burning pure carbon produces 0.6 MeV nucleon^{-1}, so this would reduce the expected energy output, which could be significant for cases in which almost all the carbon burns prior to ignition (e.g., Keek & Heger 2016). In the specific modest case mentioned above, 0.06 MeV nucleon^{-1} were lost.

Interestingly, we find a significant fraction of the burst energy (0.6 MeV nucleon^{-1}, 40 % of the total burst energy) is released from fuel burning below the accretion column, in the ashes of the previous burst (Area B in Figure 3). We find that an even higher fraction of fuel (50 %) does not undergo significant burning in the burst (Area C), leaving some of this to be burnt in subsequent bursts (where it will become Area B). Finally, we find that in this case all bursts leave ~ 0.3 MeV nucleon^{-1} of mass excess in the ashes (14 % of

the energy released in the burst) that is not burnt in the burst, or any subsequent bursts (Area D). In general, there is an average of 15% mass excess of the material burnt in the burst in the ashes that is leftover, and not burnt in any bursts, since the average relation is 15% less than the expected value for burning ^{4}He to ^{56}Fe.

3.4. *Effect of Metallicity and Accretion Rate*

We ran models for 3 metallicites: $Z = 0.005$, 0.02, and 0.1 and find no significant deviation from the relation in Figure 2, with higher metallicities causing a larger variation in the $Q_{\rm nuc}$ value for constant $\overline{X}$. Likewise, for the 3 accretion rates explored, we find no significant deviation from the relation, with higher accretion rates causing a slightly larger scatter in the data. Whilst there is no significant deviation from the $Q_{\rm nuc}$ relation with different metallicities, we investigated the cause of the variations seen and found that bursts with lower metallicity have more *rp*-process burning, producing more neutrinos and higher $Q_{\rm nuc}$ values than bursts with higher metallicities at the same hydrogen fractions.

Bursts ignite with the same $\overline{X}$ but different metallicities and produce different neutrino losses as a fraction of total burst energy. We explored this further and found that, for 3 bursts with different initial metallicities, igniting with the same $\overline{X}$ but producing different neutrino losses, the distribution of heavy elements just after the burst were different, as seen in Figure 5.

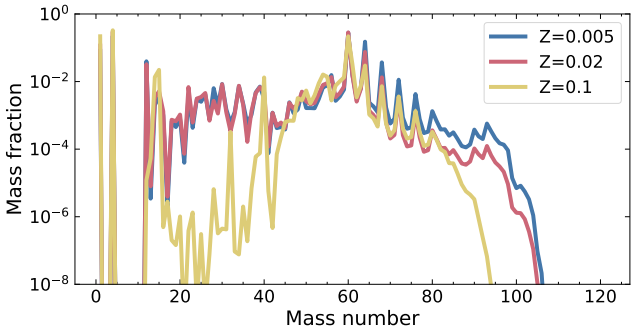

Figure 5. The mass fraction of isobars present just after a burst for 3 models with different metallicities (Z) but the same hydrogen content ($\overline{X}$) of the ignition column. The colours are the same as for Figures 1 and 2: the *yellow line* corresponds to $Z = 0.1$, the *red line* to $Z = 0.02$, and the *blue line* to $Z = 0.005$.

We find that for lower metallicity, more *rp*-process burning occurs, reaching a higher mass number, and ultimately producing more β-decays and so more neutrinos. Conversely, for higher metallicity, the *rp*-process burning stops at a lower mass number, resulting in less neutrinos produced in these cases. This result confirms that β-decays play an important role in the amount of neutrinos released during a burst, with more neutrinos released when the reaction pathways favour a greater number of β-decays, which corresponds to more prolonged *rp*-process burning.

For the purpose of this paper we note that whilst there is a trend observed with metallicity, the difference in neutrino losses is only $\approx 2\,\%$ (smaller than our percentage difference in the 3 metallicites we explored) and thus we do not include a metallicity component in any of our relations. As discussed above, this introduces some scatter to the $Q_{\rm nuc}$ relation we have derived, but it remarkably follows a tight relation, with factors such as accretion rate and Z causing slight shifts up or down the line.

3.5. *Burning Regimes*

Keek & Heger (2016) define 5 distinct burning regimes based on the accretion rate and type of burning that occurs before and during a burst. In different burning regimes there are different contributions to the energetics of bursts and a single formula for $Q_{\rm nuc}$ may not hold. In our model grid we explored three different burning regimes: 0.1–4 % $\dot{m}_{\rm Edd}$ corresponding to He flash (stable H burning), 4–8 % $\dot{m}_{\rm Edd}$ corresponding to stable H/He burning and 11–100 % $\dot{m}_{\rm Edd}$ corresponding to Mixed H/He flash. (For Fujimoto et al. (1981)'s burning regimes this corresponds to Case IV pure He bursts, $\dot{m} = 0.01$–$0.1\,\dot{m}_{\rm Edd}$, and Case III mixed H/He bursts, $\dot{m} = 0.1$–$1.0\,\dot{m}_{\rm Edd}$). Unfortunately, of the 24 runs with $\dot{m} < 1\,\%\,\dot{m}_{\rm Edd}$ we studied, only 4 were usable due to the low accretion rate and time cut off for the runs causing most of the runs to only produce one or less bursts, and thus not a reliable estimate of the energy. As expected, the 4 low accretion rate runs have very low $\overline{X}$ of the ignition column, despite having initially high hydrogen fraction. We have insufficient data to determine if this different burning regime causes a significant deviation from the $Q_{\rm nuc}$ relation we have developed and caution that this relation may only be valid for burning in the accretion rate range 0.1–$1.0\,\dot{m}_{\rm Edd}$.

4. DISCUSSION

We find that neutrino losses in Type I X-ray bursts are only significant (up to 14.2 %) when there is a large amount of hydrogen present in the ignition column of the burst (mass fraction > 0.5). We also find that lower metallicity of the accreted fuel results in more energy released in the form of neutrinos than higher metallicity compositions. We found that lower metallicity fuel results in more prolonged *rp*-process burning than higher metallicity fuel with the same hydrogen content, resulting in slightly more neutrinos produced. This confirms the obvious, namely that neutrino losses are only significant at β-decays of the *rp*-process as according to Wallace & Woosley (1981); Fujimoto et al. (1987).

The nuclear burning processes and the resulting energy release in Type I X-ray bursts are complex, with many non-linear interaction between burning and the structure. Therefore it

is not surprising that it may not be reproduced by a simple relation that depends only on the hydrogen fraction of the ignition column. There is no physical reason for the burst energies to be linearly proportional to the hydrogen present in the ignition column, and thus it is also unsurprising that we find a non-linear relation best fits the data. The energy deposited in the star cannot be easily estimated by the mass excess of hydrogen and helium alone: Depending on the reaction path different amounts of neutrinos will be carried away, and the ashes are not just pure ^{56}Fe but do contain both heavier and light nuclei, both with large mass excess (Figure 4). Our results depend on the nuclear data being used, affecting the reaction rates and the nuclear reaction flow, and on the details and physics of the multi-zone model used (KEPLER), affecting, e.g., mixing and transport processes.

4.1. *Effect on Composition Predictions: A Case Study*

We quantify the overall effect of using $Q_{\rm nuc} = (1.31 + 6.95\,\overline{X} - 1.92\,\overline{X}^2)$ MeV nucleon^{-1} instead of assuming 35 % neutrino losses with $Q_{\rm nuc} = (1.6 + 4\,\overline{X})$ MeV nucleon^{-1} with a case study of two of the most well known accretion powered millisecond pulsars: SAX J1808.4–3658 (in 't Zand et al. 1998) and GS 1826–24 (Galloway et al. 2004b). Galloway & Cumming (2006) find that the observed α values (where α is the ratio between nuclear burning energy and gravitational energy) of $\approx$ 150 for AX J1808.4–3658 imply that $Q_{\rm nuc} \approx 2$ MeV nucleon^{-1}. From that they infer an average hydrogen fraction of the ignition column of $\overline{X} \approx 0.1$. Using $Q_{\rm nuc} = (1.31 + 6.95\,\overline{X} - 1.92\,\overline{X}^2)$ MeV nucleon^{-1} ($Q_{\rm nuc} = (1.35 + 6.05\,\overline{X})$ MeV nucleon^{-1}) instead gives $\overline{X} \approx 0.102$ (0.107), corresponding to a maximum of 10 % increase in the predicted average hydrogen fraction of the ignition column for this source. For GS 1826–24, Galloway et al. (2004b) find the observed α values imply that $Q_{\rm nuc} \approx 3.8$ MeV nucleon^{-1} and infer an average hydrogen fraction of the ignition column of $\overline{X} \approx 0.55$. Using $Q_{\rm nuc} = (1.31 + 6.95\,\overline{X} - 1.92\,\overline{X}^2)$ MeV nucleon^{-1} ($Q_{\rm nuc} = (1.35 + 6.05\,\overline{X})$ MeV nucleon^{-1}) instead gives $\overline{X} \approx 0.403$ (0.405), corresponding to a $\approx$ 30% decrease in the predicted hydrogen content of the burst fuel.

We note that the old relation fits better for low hydrogen fractions but deviates more significantly from the new formula at higher H fractions (see Figure 2) so we expect to see a larger difference in fuel composition predictions for sources with higher H fraction, such as GS 1826–24. Overall, using the correct neutrino losses in the formula for $Q_{\rm nuc}$ corresponds to a maximum energy produced of 6.34 MeV nucleon^{-1} for pure hydrogen fuel, compared to 5.6 MeV nucleon^{-1} for the old relation. The theoretical Q value of hydrogen burning by the β-limited CNO cycle, less neutrinos, is 6.2 MeV nucleon^{-1}, so the new relation agrees better with classical theory.

5. CONCLUSION

We have shown that neutrino losses in Type I X-ray bursts range from 6.7×10^{-3}–14.2 % of the total burst energy, which is significantly less than the often-adopted value of 35 % during the *rp*-process. We find that by assuming there is $\sim$ 35 % neutrino losses in hydrogen burning during an Type I X-ray burst, the typically adopted estimate for nuclear energy generation in Type I X-ray bursts of $Q_{\rm nuc} = (1.6 + 4\,\overline{X})$ MeV nucleon^{-1} significantly overestimates the neutrino losses by up to a factor of 2. We find that $Q_{\rm nuc} = (1.31 + 6.95\,\overline{X} - 1.92\,\overline{X}^2)$ MeV nucleon^{-1}, or approximately $Q_{\rm nuc} = (1.35 + 6.05\,\overline{X})$ MeV nucleon^{-1}, more accurately approximates the nuclear energy generation for Case III burning (Fujimoto et al. 1981) as predicted by our multi-zone models. In our models the mass excess of the fuel is incompletely extracted, reducing the energy generation for pure helium fuel from 1.6 MeV nucleon^{-1} to 1.35 MeV nucleon^{-1} as it does not burn to pure ^{56}Fe as is classically assumed. For the specific case discussed in detail about 0.3 MeV nucleon^{-1} (14 % of the initial mass excess relative to iron) remains in the ashes. Interestingly, we found evidence for a significant fraction of energy ($\approx$ 40 %) released in a burst coming from burning below the accretion depth, in the ashes of the previous burst. We also found that the amount of energy carried away by neutrinos does noticeably depend on metallicity even for the same hydrogen fraction of the ignition column. This indicates that for lower metallicity there is stronger *rp*-process burning and so more neutrinos released by a larger number of β-decays or reaction pathways with higher-energetic neutrino emission, than for cases with the higher metallicity.

We thank Andrew Cumming and Ed Brown for helpful discussions. AG acknowledges support by an Australian Government Research Training (RTP) Scholarship. AH has been supported, in part, by the Australian Research Council through a Future Fellowship (FT120100363) and by TDLI though a grant from Science and Technology Commission of Shanghai Municipality (Grants No.16DZ2260200) and National Natural Science Foundation of China (Grants No.11655002).

Software: KEPLER (Woosley et al. 2004), NONSMOKER (Rauscher & Thielemann 2000)

REFERENCES

Bildsten, L. 1998, in NATO Advanced Science Institutes (ASI) Series C, Vol. 515, NATO Advanced Science Institutes (ASI) Series C, ed. R. Buccheri, J. van Paradijs, & A. Alpar, 419

Chenevez, J., Galloway, D. K., in 't Zand, J. J. M., et al. 2016, ApJ, 818, 135, doi: 10.3847/0004-637X/818/2/135

Cumming, A. 2003, ApJ, 595, 1077, doi: 10.1086/377446

Cumming, A., & Bildsten, L. 2000, The Astrophysical Journal, 544, 453

Fisker, J. L., Rembges, F., Barnard, V., & Wiescher, M. C. 2001, in Astrophysics and Space Science Library, Vol. 264, The Influence of Binaries on Stellar Population Studies, ed. D. Vanbeveren, 569

Fisker, J. L., Schatz, H., & Thielemann, F.-K. 2008, ApJS, 174, 261, doi: 10.1086/521104

Fisker, J. L., Thielemann, F.-K., & Wiescher, M. 2004, ApJL, 608, L61, doi: 10.1086/422215

Fujimoto, M. Y., Hanawa, T., & Miyaji, S. 1981, ApJ, 247, 267, doi: 10.1086/159034

Fujimoto, M. Y., Sztajno, M., Lewin, W. H. G., & van Paradijs, J. 1987, ApJ, 319, 902, doi: 10.1086/165507

Fuller, G. M., Fowler, W. A., & Newman, M. J. 1982, ApJS, 48, 279, doi: 10.1086/190779

Galloway, D. K., & Cumming, A. 2006, ApJ, 652, 559, doi: 10.1086/507598

Galloway, D. K., Cumming, A., Kuulkers, E., et al. 2004a, ApJ, 601, 466, doi: 10.1086/380445

—. 2004b, ApJ, 601, 466, doi: 10.1086/380445

Galloway, D. K., & Keek, L. 2017, ArXiv e-prints. https://arxiv.org/abs/1712.06227

Galloway, D. K., Muno, M. P., Hartman, J. M., Psaltis, D., & Chakrabarty, D. 2008, ApJS, 179, 360, doi: 10.1086/592044

Grindlay, J., Gursky, H., Schnopper, H., et al. 1976, ApJL, 205, L127, doi: 10.1086/182105

in 't Zand, J. J. M., Heise, J., Muller, J. M., et al. 1998, A&A, 331, L25

in't Zand, J. J. M., Visser, M. E. B., Galloway, D. K., et al. 2017, A&A, 606, A130, doi: 10.1051/0004-6361/201731281

Johnston, Z., Heger, A., & Galloway, D. K. 2018, MNRAS, 477, 2112, doi: 10.1093/mnras/sty757

Joss, P. C. 1978, ApJL, 225, L123, doi: 10.1086/182808

Keek, L., & Heger, A. 2016, MNRAS, 456, L11, doi: 10.1093/mnrasl/slv167

Langanke, K., & Martínez-Pinedo, G. 2001, Atomic Data and Nuclear Data Tables, 79, 1, doi: 10.1006/adnd.2001.0865

Lewin, W. H., Van Paradijs, J., & Taam, R. E. 1993, Space Science Reviews, 62, 223

Rauscher, T., & Thielemann, F.-K. 2000, Atomic Data and Nuclear Data Tables, 75, 1, doi: 10.1006/adnd.2000.0834

Rawlings, J. O., Pantula, S. G., & Dickey, D. A. 2001, Applied regression analysis: a research tool (Springer Science & Business Media)

Taam, R. E. 1980, ApJ, 241, 358, doi: 10.1086/158348

van Paradijs, J., Penninx, W., & Lewin, W. H. G. 1988, MNRAS, 233, 437, doi: 10.1093/mnras/233.2.437

Wallace, R., & Woosley, S. 1981, The Astrophysical Journal Supplement Series, 45, 389

Woosley, S., Heger, A., Cumming, A., et al. 2004, ApJS, 151, 75

3.2 X-RAY BURST IGNITION LOCATION ON THE SURFACE OF ACCRETING PULSARS: CAN BURSTS IGNITE AT THE HOTSPOT?

Studies of X-ray burst ignition location on the surface of accreting neutron stars in general do not consider the effect that a asymmetries in the surface temperature on the surface may have on the ignition location. It has been shown that burst ignition should preferentially occur at the equator due to the effect that the fast rotation of the neutron star has on reducing the surface gravity at the equator (Spitkovsky, Levin and Ushomirsky, 2002). Hotspots have been observed as persistent pulsations in the lightcurves of the accreting X-ray pulsars, however it has not been determined if the hotspot can induce heating down to the depth at which X-ray bursts may ignite, possibly moving the ignition location of bursts from the equator to the location of the hotspot. In the second study in this chapter we present 2D model calculations of the accreted layers and ignition location of bursts, taking into account the hotspot and lower surface gravity at the equator.

Submitted to Monthly Notices of the Royal Astronomical Society:
A. J. Goodwin et al. (Oct. 2020b). 'X-ray burst ignition location on the surface of accreting X-ray pulsars: Can bursts preferentially ignite at the hotspot?' *MNRAS* submitted

MNRAS **000**, 1–13 (2020) Preprint 6 October 2020 Compiled using MNRAS LATEX style file v3.0

X-ray burst ignition location on the surface of accreting X-ray pulsars: Can bursts preferentially ignite at the hotspot?

A. J. Goodwin,[1,2]★ A. Heger,[1–4] F. R. N. Chambers,[5] A. L. Watts,[5] and Y. Cavecchi[2,6]
[1]*School of Physics and Astronomy, Monash University, Clayton, 3800, Australia*
[2]*Joint Institute for Nuclear Astrophysics, 1 Cyclotron Laboratory, National Superconducting Cyclotron Laboratory, Michigan State University, East Lansing, MI 48824-1321, USA*
[3]*Australian Research Council Centre of Excellence for Gravitational Wave Discovery (OzGrav), Clayton, VIC 3800, Australia*
[4]*Center of Excellence for Astrophysics in Three Dimensions (ASTRO-3D), Australia*
[5]*Anton Pannekoek Institute for Astronomy, University of Amsterdam, Postbus 94249, 1090 GE Amsterdam, The Netherlands*
[6]*Mathematical Sciences and STAG Research Centre, University of Southampton, SO17 1BJ, UK*

Accepted XXX. Received YYY; in original form ZZZ

ABSTRACT
Hotspots on the surface of accreting neutron stars have been directly observed via pulsations in the lightcurves of X-ray pulsars. They are thought to occur due to magnetic channelling of the accreted fuel to the neutron star magnetic poles. Some X-ray pulsars exhibit burst oscillations during Type I thermonuclear X-ray bursts which are thought to be caused by asymmetries in the burning. In rapidly rotating neutron stars, it has been shown that the lower gravity at the equator can lead to preferential ignition of X-ray bursts at this location. These models, however, do not include the effect of accretion hotspots at the the neutron star surface. There are two accreting neutron star sources in which the burst oscillations track exactly the neutron star spin period, but only when the local accretion rate is high. We analyse whether this could be due to the X-ray bursts igniting at the magnetic pole of the neutron star, because of heating in the accreted layers under the hotspot causing ignition conditions to be reached earlier. We investigate heat transport in the accreted layers using a 2D model and study the prevalence of heating down to the ignition depth of X-ray bursts for different hotspot temperatures and sizes. We perform calculations for accretion at the pole and at the equator, and infer that ignition could occur away from the equator at the magnetic pole for hotspots with temperature $T_{\rm HS} \gtrsim 1 \times 10^8$ K.

Key words: pulsars: general – X-rays: binaries – X-rays: bursts

1 INTRODUCTION

Accretion-powered X-ray pulsars (AXPs) are neutron stars in close binary orbits ($P \lesssim 1$ d) that accrete from their companion via Roche-Lobe overflow (e.g., White et al. 1983; Nagase 1989; Chakrabarty 2005). In some cases the accretion flow from the accretion disk may be channelled by the magnetic field of the neutron star to the magnetic poles, causing hotspots to form on the surface. These hotspots give rise to X-ray pulsations that are observed in the outburst lightcurves of these systems (e.g., Wijnands & van der Klis 1998). Detailed timing studies of the pulsations in AXPs provide insight into the neutron star spin period, spin evolution, the binary orbit, and the dense equation of state through mass constraints (e.g., Chakrabarty & Morgan 1998). Some AXPs rotate very rapidly, at millisecond spin periods ($\nu \gtrsim 100$ Hz), and thus are known as accretion-powered millisecond pulsars (AMXPs) (see Patruno & Watts 2012, for a review). AMXPs are pulsars that have been spun up through the process of accretion over time (Tauris & van den Heuvel 2006).

Currently, there are 19 known AMXPs that exhibit persistent pulsations in their X-ray lightcurves during outburst, and an additional ∼10 AXPs with spin periods between 0.1–11 Hz (for a review see Patruno & Watts 2012). Observationally, AXPs all exhibit relatively faint outburst luminosities, indicating they accrete at low rates ($\dot{m} \lesssim 0.1$; $\dot{m}_{\rm Edd}$ is the Eddington accretion rate, given by $\dot{m}_{\rm Edd} \approx 1.75 \times 10^{-8}\,{\rm M}_\odot\,{\rm yr}^{-1}$ for hydrogen-accreting sources), small donor companion stars ($M_{\rm c} \lesssim 0.2\,{\rm M}_\odot$), and short orbital periods ($P \lesssim 1$ d). They are all transient systems and accrete into an accretion disk around the pulsar for long periods (∼years). AXPs exhibit sudden outbursts that last ∼1 month, during which time they become active in X-rays as material is transferred from the disk to the neutron star.

In some AXPs, when the accreted fuel builds up on the surface of the neutron star during outburst, it can ignite unstably, producing

★ E-mail: ajgoodwin.astro@gmail.com

a bright ($L \sim 10^{38}$ erg s^{-1}) thermonuclear explosion known as a Type I X-ray burst (for a review see Galloway & Keek 2017). The conditions that produce an X-ray burst in the accreted layer depend primarily on the temperature, composition of the fuel, and the accretion rate. These basic conditions can be simulated in simple one-dimensional analytic calculations of the accretion column (e.g., Bildsten 1998; Cumming & Bildsten 2000).

Some AXPs exhibit thermonuclear burst oscillations, which are strong oscillations observed in the lightcurve of an X-ray burst (e.g., Watts 2012). The first observation of this phenomenon was in 1996 in bursts from 4U 1728–34, where a strong 363 Hz signal was observed in 6 X-ray bursts (Strohmayer et al. 1996). There was an upwards drift in the frequency of these oscillations, and they appeared to disappear near the peak of the burst. Strohmayer et al. (1996) concluded that these oscillations could be caused by rotational modulation of a bright spot on the surface of the neutron star. We have now observed burst oscillations in many sources and the prevalent theory is that they are caused by highly asymmetric bright patches in the surface layers of a burning neutron star (Watts 2012). Most burst oscillations observed exhibit a frequency drift during the burst, which could be explained by the brighter-patches location moving over the star (for examples due to travelling waves/modes in the ocean). There are 2 known sources (XTE 1814–338 and IGR J17480–2446), however, in which the burst oscillations during the burst rise are phase locked with the accretion-powered pulsations (Watts et al. 2008; Cavecchi et al. 2011).

Under the assumption that the observed hotspots are caused by channelled accretion onto the surface of the neutron star at the magnetic pole, the phase locking of burst oscillations with accretion-powered pulsations could be explained by burst ignition occurring at the magnetic pole, and burning being confined to this location during the phase-locking. This is contrary to the assumption that ignition should preferentially occur at the equator due to the effect of fast rotation on reducing the effective gravity at the equator (Spitkovsky et al. 2002; Cooper & Narayan 2007).

It has been demonstrated that the magnetic fields of XTE 1814–338 and IGR J17480–2446 are most likely not strong enough to confine material at the magnetic pole, with magnetic confinement requiring $B \gtrsim 4\times10^9 - 3\times10^{10}$ G (Brown & Bildsten 1998; Cavecchi et al. 2011) and the magnetic fields of XTE 1814–338 and IGR J17480–2446 having been estimated to be $0.16\times10^8 - 7.8\times10^8$ and $\sim 2\times10^8 - 2.4\times10^{10}$ G, respectively (e.g., Mukherjee et al. 2015; Papitto et al. 2012). Even taking into account dynamical strengthening of the magnetic field (Heng & Spitkovsky 2009), confinement could still be difficult due to the occurrence of instabilities like the "ballooning" instability (e.g. Litwin et al. 2001). What has not been explored, however, is whether the presence of a hotspot at the surface could induce heating down to the ignition depth of a burst, even after the magnetic confinement has washed out, first suggested as a possibility by Watts et al. (2008). Furthermore, in models of the ignition location of bursts on the surface of accreting neutron stars, the presence of a hotspot in AXPs is often neglected (Spitkovsky et al. 2002; Cooper & Narayan 2007; Cavecchi et al. 2017).

In this first paper we investigate the plausibility of heating caused by a hotspot or accretion stripe (Figure 1) reaching down to the ignition depth of an X-ray burst, focussing on the case of hydrogen-free accretion as the effect of external heating is likely the most prominent there. We analyse whether this could cause bursts to preferentially ignite under the hotspot in the accreted layers. We model the surface layers by solving a 2D heat diffusion equation and exploring the heat transport inside the accretion column, to determine at what hotspot temperature X-ray bursts would preferentially ignite under the hotspot. In Section 2 we describe the numerical set up and equations used to describe the surface layers of the neutron star, in Section 3 we present the results for different hotspot temperatures and geometries, in Section 4 we discuss the limitations of this study, and in Section 5 we provide concluding remarks.

2 METHODS

We solve the heat diffusion equation in 2D to describe the heat conduction and transport mechanisms in the gaseous accreted layers on the surface of the neutron star. To derive the diffusive flux we begin with the general diffusive flux for a photon

$$j = -D\,\nabla n \tag{1}$$

where D is the diffusion coefficient and n is the number density.

We estimate the diffusion coefficient from a random walk approximation

$$D = \frac{1}{3}\,v\,l_{\rm ph} \tag{2}$$

where the velocity, v for a photon may be replaced by the speed of light, c, and the mean free path of a photon is $l_{\rm ph} = 1/(\rho\kappa)$, where ρ is the density and κ is the opacity of the gas.

∇n can be calculated using the energy density of a photon gas, $U = aT^4$, where a is the radiation constant and T is the temperature. Differentiating gives:

$$\nabla U = a\,\nabla T^4 \tag{3}$$

Thus the total diffuse flux, F is given by

$$F = \frac{a\,c}{3\,\kappa\,\rho}\,\nabla T^4 \tag{4}$$

The heat diffusion equation for this flux is thus

$$\nabla\left(\frac{a\,c}{3\,\kappa\,\rho}\,\nabla T^4\right) = \epsilon(T,\rho)\,\rho \tag{5}$$

where $\epsilon(T,\rho)$ is the heat source term (specific energy generation rate), which in this case corresponds to the heating due to nuclear burning. We assume the simplest case for nuclear burning in accreting neutron stars, in which the accreted fuel is almost pure ^{4}He and $\epsilon(T,\rho)$ is given by (Bildsten 1998)

$$\epsilon_{3\alpha} = 5.3\times10^{21}\,\frac{\rho_5^2\,Y^3}{T_8^3}\,\exp\left(-\frac{44}{T_8}\right) \tag{6}$$

where T_8 is the temperature in 10^8 K, ρ_5 is the density in 10^5 g cm^{-3}, and Y is helium mass fraction. For the accreted material we assume a helium mass fraction of $Y = 0.99$ and metallicity of $Z = 0.01$ and that the metals do to not contribute to the nuclear energy generation. There is no nuclear burning in the substrate below the accreted layers.

We choose to use the triple-α energy generation rate to represent the heating due to nuclear burning in our model since it has been shown that thermally unstable helium burning is likely responsible for the thermonuclear runaway that begins an X-ray burst (e.g., Bildsten 1998). We note that there would be additional energy due to CNO burning if hydrogen was present, as well as nuclear burning beyond carbon that we do not account for because it is not significant before runaway in pure helium accretors.

For the opacity and the density we assume κ is a function of T and ρ, and ρ is a function of the radial coordinate, r only. We extract a density distribution, opacity grid, and initial temperature distribution from a KEPLER model, and pre-compute an opacity table for given T and ρ, using the mass fractions $Y = 0.99$, $Z = 0.01$ (0.009 ^{14}N and 0.001 ^{56}Fe) for the accreted layers and ^{56}Fe = 1.0 for the substrate, where the substrate is a thick layer below the accreted layers consisting of a non-reactive substance (^{56}Fe in this case).

KEPLER is a 1D multi-zone model of Type I X-ray bursts that integrates the time-dependent equations of conservation of momentum, mass, and energy, in spherical symmetry (see Woosley et al. 2004). KEPLER allows for a general mixture of radiation, ions, and degenerate or relativistic electrons, and implements a complex nuclear reaction network. For each set of parameters we extract the temperature and density distributions in a snapshot 1 minute before a burst commences, where we define burst commencement as the first timestep in which convection appears in the accreted layer. For the KEPLER model and for the case study of XTE J1814–338 (Model A), we set the global accretion rate, $\dot{m} = 0.1\,\dot{M}_{\rm Edd}$, hydrogen mass fraction, $X = 0.0$, helium mass fraction, $Y = 0.99$, metallicity $Z = 0.01$ (0.009 as ^{14}N and 0.001 as ^{56}Fe), and the base heating $Q_{\rm b} = 0.1\,\mathrm{MeV\,nucleon^{-1}}$ and $0.15\,\mathrm{MeV\,nucleon^{-1}}$. We note that in our simulations we set the global accretion rate across the simulation domain to be constant, at the value expected from the X-ray luminosity of the system. We then place a hot region at the top to mimic the additional effect of a local higher accretion rate (and heating from the accretion shock above). An example opacity distribution for the accreted layers and substrate is shown in Figure 3. For the case study of IGR J17480–2446 (Model B), we use a similar KEPLER model but set $\dot{m} = 0.038\,\dot{M}_{\rm Edd}$. Here we infer the accretion rate of the system from observations of the X-ray luminosity, $L_{\rm X}$ using the relation from Galloway et al. (2008)

$$\dot{m} = \frac{L_X(1 \quad z)}{4\pi R^2 Q_{\rm grav}} \tag{7}$$

where z is the gravitational redshift (which we assume is 0.259 for a $1.4\,\mathrm{M}_\odot$ neutron star), R is the radius of the neutron star (which we assume is 11.2 km), and $Q_{\rm grav}$ is the energy released per nucleon during accretion, for which we approximate $Q_{\rm grav} = GM/R$.

To model a hot-stripe at the equator we use a KEPLER model with the same parameters as the magnetic pole but set the gravity to be 75 %, to emulate the effect of the fast rotation of the neutron star on the effective surface gravity (Model C). Spitkovsky et al. (2003) suggest that the surface gravity at the equator could be up to 25 % less than at the poles.

The KEPLER distributions of ρ and T with radial coordinate, r, and column depth, y, for the accreted layers are shown in Figure 2. For comparison, we have plotted a range of $\dot{m}$ and $Q_{\rm b}$ to demonstrate how these distributions change under the assumed parameters. When the accretion rate is higher, the accreted layer is thinner and hotter than when the accretion rate is lower. Likewise, when $Q_{\rm b}$ is higher, the entire layer is slightly hotter than when $Q_{\rm b}$ is lower. In our models, we ran all cases for the two values of $Q_{\rm b}$ (0.1 and $0.15\,\mathrm{MeV\,nucleon^{-1}}$) but found that since the effect of increasing $Q_{\rm b}$ uniformly increased the temperature over the entire layer, there was no significant difference in the results.

2.1 2D Transport Code

We solve Equation 5 using a finite volume method to discretise the equation in PYTHON, and set up a two-dimensional grid. We choose to use a finite volume method over a finite difference method to ensure conservation of energy.

For simplicity and numerical stability, we solve for $\tau := T^4$ instead of solving for T. To discretise the equations, we integrate over the finite volume of each cell on the grid and apply Gauss's theorem to convert the left-hand term into a surface integral, such that Eq. 5 becomes

$$\int_{\Delta A} -\frac{a\,c}{3}\frac{\nabla\tau}{\kappa\rho}\,\mathrm{d}A - \int_{\Delta V}\rho\,\epsilon(T,\rho)\,\mathrm{d}V = 0 \tag{8}$$

where ΔA is the surface area of the cell and ΔV its volume.

The total energy flow into a cell at coordinates (x, y, z) (or corresponding cylindrical or polar coordinates) with indices (i, j, k) is given by the sum of the flows at each of the cell interfaces

$$\begin{aligned} F_{i,j,k} \quad &= \quad \mathcal{F}_{i-1/2,j,k} - \mathcal{F}_{i-1/2,j,k} \quad \mathcal{F}_{i,j\ 1/2,k} \\ &- \quad \mathcal{F}_{i,j-1/2,k} \quad \mathcal{F}_{i,j,k\ 1/2} - \mathcal{F}_{i,j,k-1/2} \end{aligned} \tag{9}$$

where the half indices correspond to the zone interfaces. The flows are centred using the scheme

$$\begin{aligned} &\mathcal{F}_{i-1/2,j,k} = \\ &-\frac{a\,c\,\Delta A_{i-1/2,j,k}}{3\,\kappa(\rho_{i-1/2,j,k},\tilde{\tau}_{i-1/2,j,k})\,\rho_{i-1/2,j,k}}\frac{\tau_{i,j,k}-\tau_{i-1,j,k}}{x^{\rm c}_{i,j,k}-x^{\rm c}_{i-1,j,k}} \end{aligned} \tag{10}$$

where $x^{\rm c}_{i,j,k}$ denotes the zone centre of zone (i, j, k),

$$\tilde{\tau}_{i-1/2,j,k} = \frac{1}{2}\left(\tau_{i,j,k} \quad \tau_{i-1,j,k}\right)$$

and $\Delta A_{i-1/2,j,k}$ is the surface area in the negative i-direction, and $\rho_{i-1/2,j,k}$ is the density at the centre of that surface. In the calculations presented here, the densities are pre-defined and only depend on z coordinate.

With

$$\int_{\Delta V}\rho\,\mathrm{d}V = m\ ,$$

the mass of the zone, the source term from nuclear burning becomes just $m\,\epsilon(T,\rho)$ and our equation to solve becomes

$$F_{i,j,k} - m_{i,j,k}\,\epsilon(\tau_{i,j,k},\rho_{i,j,k}) = 0\ . \tag{11}$$

To model a hotspot on the surface we use a 2D cylindrical coordinate system, such that $\Delta A = 2\pi h R_{\rm in}$ in the $i - 1$ direction, $\Delta A = 2\pi h R_{\rm out}$ in the $i \quad 1$ direction, and $\Delta A = \pi\,(R^2_{\rm out} - R^2_{\rm in})$ in the k-directions, where h is the height, $h = \Delta r$. To model a hot-stripe along the equator we use a Cartesian coordinate system, such that $\Delta A = \Delta r\,\Delta x$ in the i directions and $\Delta A = \Delta x\,\Delta r$ in the k-directions. The reason for the choice of these two coordinates systems is due to the assumed symmetry in modelling in 2D. For a cylindrical coordinate system, symmetry is assumed about the angle coordinate, going around the neutron star, thus simulating a hotspot, and there is rotational symmetry in j-direction (see Figure 1). Whereas, in a Cartesian coordinate system, translational symmetry is assumed in j-direction (i.e., the y direction), and thus heat cannot diffuse in this direction (rather it is constant), which simulates a stripe along the equator, allowing us to just model a cross-section of this stripe.

We solve for τ by relaxation of an initial guess. We define a coefficient matrix, A such that $A\tau = b$, where b is a matrix consisting of the source terms and A is the Jacobian matrix. We use the sparse matrix solver of the SciPy PYTHON package (Virtanen et al. 2020).

The grid is uniformly separated in x and non-uniform in r, for which we use the zone-width from the KEPLER snapshots, which

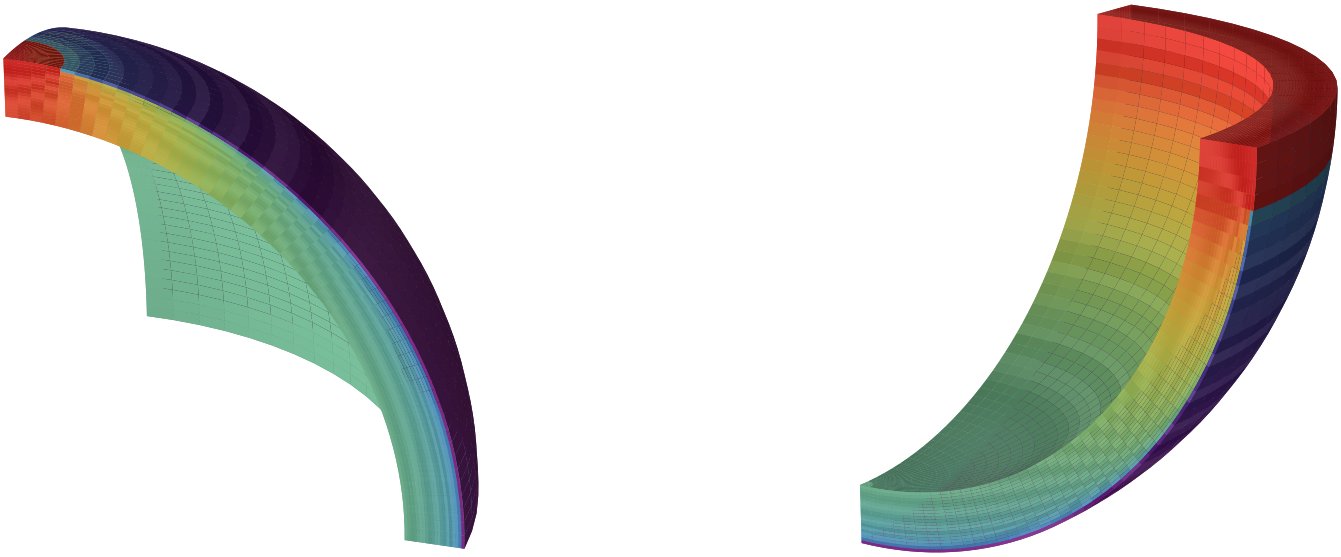

Figure 1. Geometrical setup of polar (*left*) and equatorial (*right*) accretion. These figures are for a simplified setup using a 3D version of our code. These models are to visualise the geometry only and are not to scale (using 10 m neutron star radius) nor covering full depths range (outer 1.5 m shown). The grid size is $50 \times 20 \times 20$ in $\vartheta \times \varphi \times r$. In both cases the width of the "hot" region (distance from pole or equator, respectively) is 2 % of the circumference. Shown is one octant; assume rotational symmetry around the z-axis and mirror symmetry about the equator. Colour coding indicates temperature with the *red colour* at the hot spot corresponding to 100 MK (8.6 keV) and the coolest dark purple colour at the unheated surface having about 0.6 MK (5.1 keV). The base heat flux is 10^{19} erg s^{-1} cm^{-2}.

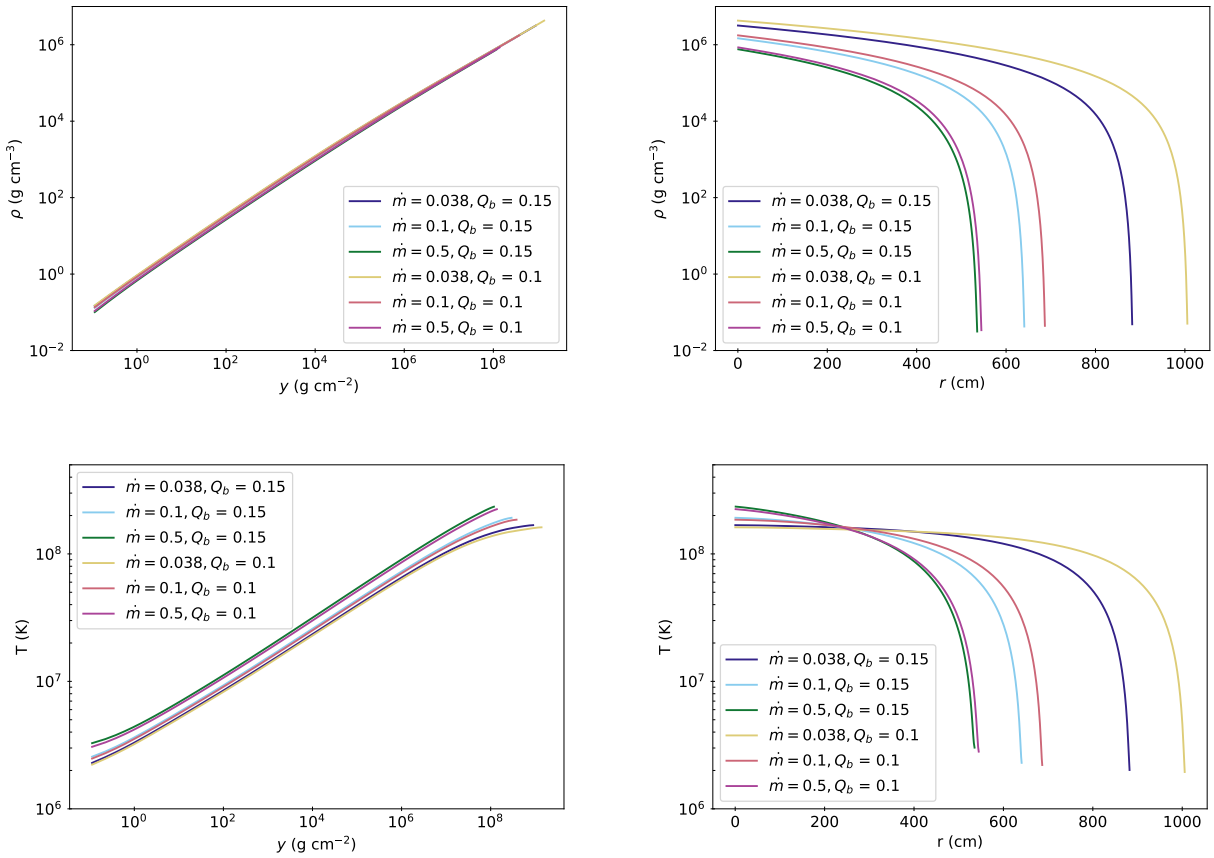

Figure 2. *Top Panels:* KEPLER model distributions of density (ρ) for column depth (y) and radial coordinate (r) for different initial accretion rates ($\dot{m}$) and base fluxes (Q_b). *Bottom Panels:* KEPLER model distributions of temperature (T) for column depth (y) and radial coordinate (r) for different initial accretion rates ($\dot{m}$) and base fluxes (Q_b). All distributions are taken from a snapshot 1 minute before a burst commences.

results in higher resolution close to the surface. For all models we use a grid of $x \times r = 280 \times (220-280)$, where the number of r zones depends on the specific KEPLER model parameters. We ran tests with lower and higher resolution and found no significant changes in the results.

2.1.1 *Boundary Conditions and Initial Conditions*

The proper choice of boundary conditions significantly affects our results. On the sides perpendicular to i we use reflective boundary conditions. We simulate the hotspot on top on one side of the box, since the reflective boundary conditions ensure symmetry in the cylindrical radial coordinate. For the surface boundary we use a blackbody with temperature corresponding to the surface temperature of the KEPLER model. The surface temperature in the model depends on how far into the neutron star atmosphere we wish to model. Since we extract the density distribution from KEPLER, we set the surface at an optical depth of 2/3, the photosphere of the star. The surface at this location has a density of $\sim 1\,\mathrm{g\,cm^{-3}}$, and temperature of $\sim 10^6$ K. Modelling into the photopshere of the neutron star aids in modelling a hotspot due to the accretion shock, rather than a hotspot deep within the neutron star atmosphere. For the base boundary we use both a constant flux condition, where the base flux is set by our choice of Q_b, for which we use the commonly used value of 0.1 MeV nucleon^{-1} (but also tested 0.15 MeV nucleon^{-1} in all cases), or a constant temperature condition. We found no significant difference in the depth of heating induced by the hotspot between models with a constant flux base boundary and a constant temperature base boundary, but we found the models with a constant flux base boundary reached runaway in general a couple of seconds earlier than those with a constant temperature boundary. The reason for such a little difference between the runs with the two kinds of base boundary conditions is the fact that we simulate a substrate of Iron at the bottom of the domain, which sets the boundary deep, and far enough from the region we are interested in modelling. We do not model the core of the neutron star, however, we expect some heat to diffuse lower into (or upwards out of) the neutron star than our simulation bounds. Thus, we find a constant flux base boundary is more physically motivated, as this allows heat to move into or out of our simulated domain. For all models presented in the results, we use a constant flux boundary at the bottom of our domain.

2.2 Physical sizes of heating regions

The size of the hotspot can be approximated by the size of the polar cap (e.g., Bogdanov 2016)

$$R_\mathrm{pc} = \sqrt{\frac{2\pi R^3}{Pc}} \tag{12}$$

where R is the radius of the star, P is the spin period, and c is the speed of light.

The hotspot may be smaller than the polar cap. For IGR J17480–2446, assuming $R = 11.2\,\mathrm{km}$[1] and $P = 0.0909\,\mathrm{s}$ ($\nu = 11\,\mathrm{Hz}$), we find $R_\mathrm{HS} \lesssim R_\mathrm{pc} \approx 0.57\,\mathrm{km}$. For XTE J1814–338, assuming $R = 11.2\,\mathrm{km}$ and $P = 0.00318\,\mathrm{s}$ ($\nu = 314\,\mathrm{Hz}$), we find $R_\mathrm{HS} \lesssim R_\mathrm{pc} \approx 3.04\,\mathrm{km}$. Thus we set the width of our simulation to 4 km, and the size of the hotspot to be the relevant polar cap size (R_pc). We note that it is extremely likely that the hotspot size in these two systems is smaller than these polar cap estimates, especially due to the high fractional amplitude of the accretion-powered pulsations in XTE J1814–338. However, in section 3.4 we demonstrate that once the hotspot is larger than $\sim 100\,\mathrm{m}$, the size of the hotspot no longer affects the base temperature of the stationary solution, so the size of the domain, and the size of the hotspot once it exceeds 100 m, do not affect the results.

Since the ocean and atmosphere layer depth is of the order $H \sim 10\,\mathrm{m}$, there is at least a factor of 100 difference between the size of the spot and the depth needed to be considered in the ocean. For the depth of our box, we use the entire accreted layer, extracted from the KEPLER simulations of the accretion column up to the point just before runaway occurs, which extends down to a column depth of $y \approx 3 \times 10^8\,\mathrm{g\,cm^{-2}}$, as well as the substrate that the accreted material is accreted onto, which extends down to $y \sim 10^{12}\,\mathrm{g\,cm^{-2}}$.

For the hotspot temperature, we explore a range of temperatures, noting that for the AMXP SAX J1808.4–3658, the hotspot temperature has been inferred to be 0.9×10^7 K (Poutanen & Gierliński 2003). The hotspot in XTE 1814–338 and IGR J17480–2446 should theoretically be slightly hotter than SAX J1808.4–3658 as these sources have slightly stronger magnetic fields and so could more strongly channel the accretion, producing a hotter hotspot. The temperature of the hotspot, however, also depends on the size of the hotspot, and the accretion rate. Spectral modelling of X-ray emission from IGR J17480–2446 in outburst has estimated temperatures of $\approx 4 \times 10^7$ K – 1.7×10^8 K (Papitto et al. 2011). For XTE J1814–338, Bhattacharyya et al. (2005) find that a hotspot temperature of $\sim 2.3 \times 10^7$ K is reasonable for this system, and spectral modelling has estimated the X-ray emission to have a temperature of $2-3.5 \times 10^7$ K (Strohmayer et al. 2003). Here we explore a range of hotspot temperatures from 2×10^7 K to 1.2×10^8 K.

We initialise the model with the temperature distribution from the relevant KEPLER model, shown in Figure 3, except the cells along the top boundary where the hotspot is placed, and solve for the steady-state solution. In reality, a static solution for temperature does not exist at the time of a burst, due to the nature of thermonuclear runaway. However, including time-dependence and modelling a full runaway is outside the scope of this work and so we solve for a static solution as close to runaway as possible. Thus we are able to examine the depth to which heating persists during accretion just prior to a burst, and operate under the assumption that the conditions just prior to a burst will not be significantly different to the conditions at the time of a burst.

2.3 Ignition Depth

We use three different approaches to independently verify the ignition properties of the model calculations. First, to infer the ignition depth via temperature of a burst, we assume the radial coordinate, r, is related to the column depth, y, by $\mathrm{d}y = \rho\,\mathrm{d}r$ (e.g., Bildsten 1998; Cumming & Bildsten 2000). One may estimate the temperature of the ignition depth using the simple model of Bildsten (1998) for pure helium burning:

$$T_\mathrm{ign} = 1.83 \times 10^8\,\mathrm{K} \cdot \kappa_0^{-1/10} Y^{-3/10} \mu_0^{-1/5} g_{14}^{-1/5} y_8^{-2/5} \tag{13}$$

where g_{14} is the surface gravity in $10^{14}\,\mathrm{cm\,s^{-2}}$, y_8 is the column depth in $10^8\,\mathrm{g\,cm^{-2}}$, κ_0 is the opacity in $\mathrm{cm^2\,g^{-1}}$, Y is the helium mass fraction of the accreted material, and μ_0 is the mean molecular

[1] Throughout this work we consistently assume $R_\mathrm{NS} = 11.2\,\mathrm{km}$. We base this value off the ranges predicted by Steiner et al. (2013) for accreting neutron star sources, but note that the actual neutron star radius in each of these systems is likely different (see e.g., Riley et al. 2019, for a millisecond pulsar radius measurement).

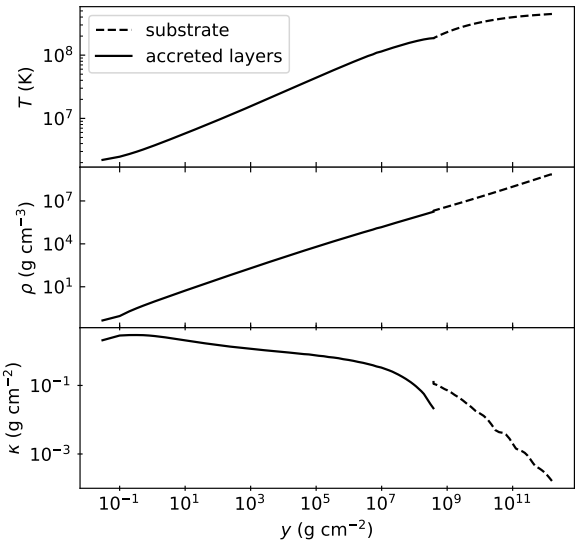

Figure 3. Initial distribution of temperature (top), density (middle) and opacity (bottom) with column depth y. The temperature and density distributions are extracted directly from a KEPLER model with parameters $\dot{m} = 0.1\,\dot{M}_{\rm Edd}$, $Q_{\rm b} = 0.1$, $Y = 0.99$, and $Z = 0.01$, 1 minute before a burst begins. The opacity is extracted from our opacity grid for given T and ρ. The dashed line indicates the substrate and the solid line indicates the accreted layers. The jump in opacity curve at the substrate boundary is due to discontinuous change in composition from He to Fe.

weight of the accreting gas in g mol^{-1}. This model only provides a crude guidance; the KEPLER model did not experience runaway for these conditions, and our models find stationary solutions well beyond that point; a stationary solution is only possible when there is no runaway.

Thus we also independently infer when runaway occurs by calculating the stationary solution using our 2D heat transport code for a sequence of KEPLER dumps consecutively closer to the start of the burst (when convection begins in KEPLER). When there is no stationary solution, the model should not converge. We compare the time before the start of convection at which no stationary solution is found for a model with no hotspot to the same time for models with hotspots of varying temperatures. If a model with hotspot fails to find a stationary solution before a model without hotspot fails, this may indicate that heating from the hotspot has induced runaway earlier. Obviously, it is difficult to assess that no solution could be found with a different numerical scheme, so our inferred times form the 2D models have to be considered upper limits on the change in runaway time. To optimise out search for a stationary solution, we set the initial guess temperature distribution for the hotter hotspots to be the solution for a slightly cooler hotspot, which in some cases allows the code to find a solution. At some point, however, ignition conditions are met and a static solution is not possible to find with our approach, which is the time we report. The equations may still have a solution, the fully-activated burning, but that may lie outside the physics domain of our burning physics and tabulated opacity tables.

Finally, we independently infer when runaway occurs under the influence of a hotspot by carrying out modified KEPLER calculations of the lead up to a burst. For each set of parameters, we explore a range of hotspot temperatures by setting the surface boundary to the hotspot temperature (since KEPLER is 1D it does not model horizontal diffusion as in the 2D heat transport code), we set the surface boundary pressure to be $3P_{\rm rad}$, where $P_{\rm rad} = \sigma T^4$ is the radiation pressure, and lower the surface resolution to allow convergence (see Footnote *b*, Table 1). We define the commencement of thermonuclear runaway as the time at which convection first begins. All other model parameters are the same as described for the 2D transport code. As we show later, for sufficiently large (realistic) hotspots, the centre of the hotspot is not affected by heat loss at the edges, and therefore these KEPLER simulations are an adequate approximation for the core of the hotspot or stripe.

Table 1. The time before convection at which a stationary solution is no longer found for different accretion rates, geometries, and hotspot temperatures.

Model Case	$\dot{m}$ ($\dot{m}_{\rm Edd}$)	$T_{\rm HS}$ (MK)	Time[a] (s)	KEPLER[a] (s)
A	0.1	No hotspot	0	(-17.7)[b]
pole	0.1	20	0	20.0
	0.1	50	0	103
	0.1	100	0	3,009
	0.1	115	5	5,122
	0.1	120	> 60	5,949
B	0.038	No hotspot	0	(-1.0)[b]
pole	0.038	20	0	47.5
	0.038	50	0	4,554
	0.038	100	7–8	9.31×10^4
	0.038	115	39–58	1.30×10^5
	0.038	120	> 60	1.41×10^5
C	0.1	No hotspot	76–80	(-27.8)[b]
equator	0.1	20	81–106	4.9
(0.75 g)	0.1	50	81–106	34.0
	0.1	100	> 107	955
	0.1	115	> 107	1,782
	0.1	120	> 107	2,101

[a] measured as time before KEPLER model in which convection first appears that stationary solution is no longer found.
[b] due to adjusted boundary condition there is a small offset relative to base model for 2D runs; all other KEPLER values in this column are measured relative to this reference. Total time to burst is 2.527×10^4 s, 2.459×10^5 s, and 1.490×10^4 s for Models A–C, respectively.

3 RESULTS

A summary of the time before ignition in the KEPLER models without hotspot is reached for the three different models explored is shown in Table 1.

3.1 The case of XTE J1814–338

The observed and inferred system parameters for XTE J1814–338 are shown in Table 2. Based on these observed parameters, we set up our model such that $R_{\rm HS} = 3$ km, $\dot{m} = 0.1\dot{m}_{\rm Edd}$, and explored a range of hotspot temperatures, and call the models with this set of parameters Model A.

The time before convection at which no stationary solution was found for KEPLER dumps sequentially closer to runaway is shown in Table 1 (Model A) for different hotspot temperatures. For the 2D code we found that only for hotspot temperatures $T_{\rm HS} \gtrsim$

Table 2. Observed and inferred parameters for XTE J1814–338

Parameter	Value	Units	Ref.
P	314	Hz	[1]
F_X	2.64×10^{-8}	ergs s^{-1} cm^{-2}	[2]
d	8	kpc	[2]
$\dot{m}$	0.11	$\dot{M}_{\rm Edd}$	Eq. 7
$R_{\rm pc}$	3.04	km	Eq. 12
$k_{\rm B}T$	1.7–3	keV	[2]
B	$0.16 \times 10^8 - 7.8 \times 10^8$	G	[1], [4]

$k_{\rm B}$ is the Boltzmann constant. Ref.: [1] Papitto et al. (2007), [2] Strohmayer et al. (2003) , [3] Bhattacharyya et al. (2005) , [4] Mukherjee et al. (2015)

Table 3. Observed and inferred parameters for IGR J17480–2446

Parameter	Value	Units	Ref.
P	11	Hz	[1]
L_X	7×10^{37}		[1]
$\dot{m}$	0.038	$\dot{M}_{\rm Edd}$	Eq. 7
$R_{\rm pc}$	0.57	km	Eq. 12
$k_{\rm B}T$	3–15	keV	[1]
B	$\sim 2 \times 10^8 - 2.4 \times 10^{10}$	G	[1, 2]

Ref.: [1] Papitto et al. (2012), [2] Ootes et al. (2019)

1.15×10^8 K did runaway occur earlier than the case with no hotspot, and we found that runaway occured 5 seconds earlier for a hotspot of 1.15×10^8 K and more than 60 seconds earlier for a hotspot of 2×10^8 K. In the KEPLER calculation under the same conditions, however, we found that a hotspot of just 2×10^7 K was sufficient to induce runaway 20 s earlier than the case with no hotspot. Given the timescales that X-ray bursts usually operate on (~ 60 s), we deduce that an X-ray burst igniting 5–20 s earlier at the hotspot would be sufficient to induce burning located at the magnetic pole.

The 2D temperature distributions and temperature profiles for the XTE J1814–338 models 1 minute before convection are shown in Figure 4. We found that there was no difference in temperature at the burst ignition depth for $T \lesssim 1.0 \times 10^8$ K. According to the Bildsten (1998) ignition formula (Eq. 13), in these cases ignition would be reached at all locations on the star at the same time, however, we note that this is a very simple formula and since we were able to obtain a stationary solution, runaway could not have commenced in these models. Qualitatively, in Figure 4, it is clear that the hotter the hotspot, the deeper the heating penetrates, and closer to a burst the hotspot could indeed provide enough heating to trigger burst ignition shallower than the rest of the star.

3.2 The case of IGR J17480–2446

The observed and inferred system parameters for IGR J17480–2446 are shown in Table 3. Based on these observed parameters, we set up our model such that $R_{\rm HS} = 0.5$ km, $\dot{m} = 0.038\,\dot{m}_{\rm Edd}$, and explored a range of hotspot temperatures, and call the models with this set of parameters Model B.

The time before convection at which no stationary solution was found for KEPLER dumps sequentially closer to runaway is shown in Table 1 (Model B) for different hotspot temperatures. We found that for the 2D code runaway only occured earlier for hotspot temperatures $T_{\rm HS} \gtrsim 1 \times 10^8$ K, and we found that runaway occured at least 7 seconds earlier; considerably earlier than the comparable case for XTE J1814–338. Similarly, for the KEPLER calculations with the same parameters, we found that a hotspot of just $T_{\rm HS} \gtrsim 2 \times 10^7$ K was sufficient to induce runaway 47.5 s earlier than the case with no hotspot. Again, this is considerably earlier than the comparable case for XTE J1814–338.

The 2D temperature distributions and temperature profiles for IGR J17480–2446 are shown in Figure 4. Similar to the models for XTE J1814–338 we found that there was no difference in temperature at the burst ignition depth for any of the models for the Bildsten (1998) ignition criterion, however this ignition criterion does not agree with the location of runaway for the KEPLER models. Qualitatively, as for XTE J1814–338, in Figure 4, it is clear that the hotter the hotspot, the deeper the heating penetrates, and closer to a burst the hotspot could indeed provide enough heating to trigger burst ignition shallower than the rest of the star.

On comparison of the temperature profiles for XTE J1814–338 and IGR J17480–2446 we find qualitatively very similar results for both accretion rates explored, excepting that for the lower accretion rate, the accreted layer is thicker and cooler, and ignition occurs deeper at cooler temperatures. In both cases we required a hotspot temperature $\gtrsim 1.0 \times 10^8$ K to see any difference in the ignition depth between the column under the hotspot and the column with no heated area on the surface.

3.3 More general models: Hotspot at magnetic pole vs hot-stripe at equator

Here we consider the effect that the fast rotation of the pulsar might have on the ignition location at the equator compared to the magnetic poles.

The time before convection at which no stationary solution was found for KEPLER dumps sequentially closer to runaway is shown in Table 1 (Model C) for different hotspot temperatures with reduced gravity and Cartesian geometry. Using the 2D code we found that runaway occured earlier than the case with no hotspot for the models with much lower hotspot temperatures than at the pole, with runaway occuring 1–10 s earlier than the no hotspot case for $T_{\rm HS} = 2 \times 10^7$ K. This is considerably lower than the hotspot temperature required for earlier runaway at the pole, of $T_{\rm HS} = 1.15 \times 10^8$ K, however, if there was a hot-stripe along the equator due to accretion it is not clear how thick this stripe might be. Here we have set the stripe to just 1 km thick. For the KEPLER calculations with the same parameters, we found that runaway occurred earlier for all hotspot temperatures simulated, with runaway occurring 4.9 s earlier for $T_{\rm HS} = 2 \times 10^7$ K.

Next we consider the two sets of models, Model A and Model C (which are the same except Model C has 25 % reduced gravity), and use cylindrical coordinates to simulate the pole for Model A and Cartesian coordinates to simulate the equator for Model C. We consider two hotspot temperatures at the pole, of $T_{\rm HS} = 5 \times 10^7$ K and 1×10^8 K, and set the radius of the hotspot to be 1 km. The temperature profiles for these models are plotted in Figure 5.

In Figure 5 it is clear that if the star was uniformly at the same temperature, for rapidly rotating neutron stars (where we have assumed the surface gravity at the equator is reduced by 25%) ignition would preferentially occur at the equator, as the temperature of the entire accreted column is slightly hotter (yellow line) than at the pole (red line). This result is in agreement with previous studies on ignition location by Spitkovsky et al. (2002); Cooper & Narayan (2007). The effect of the hot-stripe at the equator is quantitatively the same as the effect of a hotspot at the pole, however due to the higher temperature at the equator, runaway occurs for a much colder hotspot.

Interestingly, we found that for a 1×10^8 K hotspot, ignition is

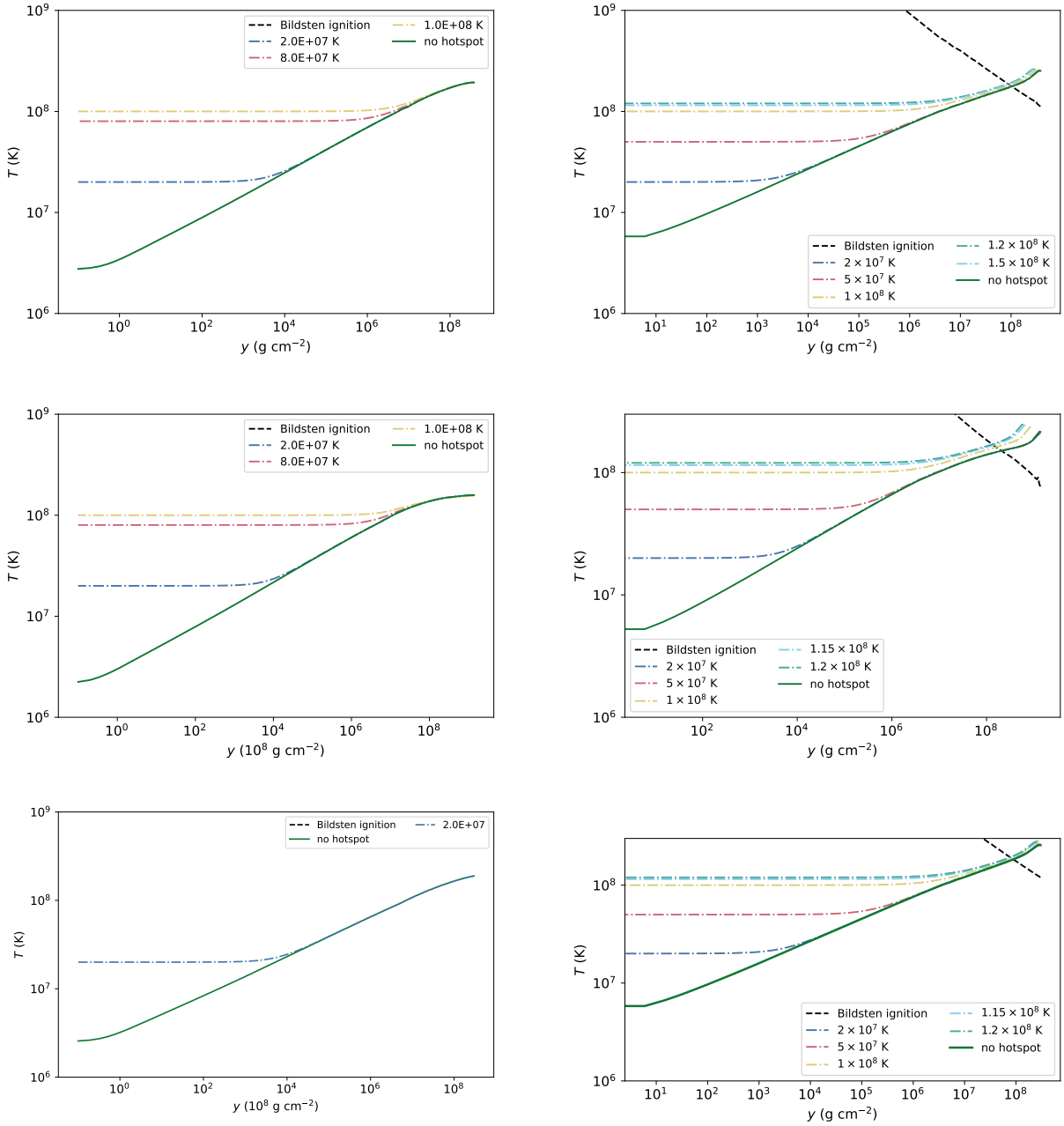

Figure 4. *Left panels:* Individual radial columns under the hotspot for each temperature (dashed-dotted lines) and a radial column far from the hotspot location (solid line). The $T - y$ conditions for X-ray burst ignition (Eq. 13) are plotted (dashed black line). Since the temperature profile is not different from the KEPLER run without hotspot near the ignition depth, it is clear that ignition is not reached in any of the models, as expected since these models are 1 minute before ignition. *Right panels:* The temperature distribution at ignition for different hotspot temperatures for the KEPLER calculations. *Top panels:* Model A; *Middle panels:* Model B; *Bottom panels:* Model C.

likely reached underneath the hotspot at the pole before the equator (with no hotter area). In Figure 5, the temperature profiles are plotted 2 minutes before a burst (when convection begins in KEPLER), and closer to the burst all columns would be hotter, and ignition would be reached under the 1×10^8 K hotspot prior to the no hotspot column at the equator. *This suggests that for a sufficiently hot hotspot, ignition could occur away from the equator at the magnetic pole, despite the lower surface gravity at the equator.*

3.4 Influence of hotspot size and geometries

We explored the effect that different hotspot sizes and the geometries of our models had on the diffusion and heating induced in deeper layers by the hotspot. For a very small hotspot, it is expected that the temperature of deeper layers would not be affected. As the hotspot increases in size, the deeper layers will become increasingly more affected. If we increase the size of the hotspot above a certain radius, the temperature in the column below the center asymptotes to a constant value (set by the temperature of the hotspot). Due to

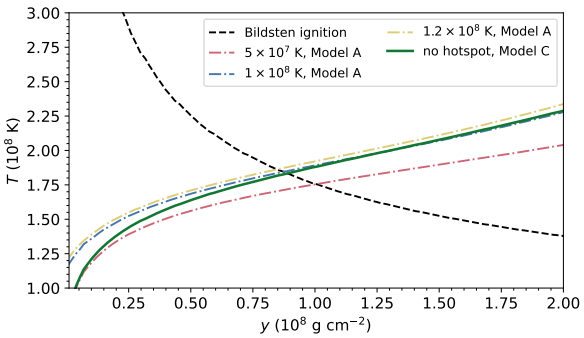

Figure 5. Comparison of temperature profiles for a hotspot at the magnetic pole (dashed-dotted, Model A) and the no hotspot case at the equator (solid line, Model C) for the KEPLER calculations. In our models the gravity at the equator is reduced by 25 % to account for the effect of fast rotation. The dashed black line shows the location of burst ignition (Eq. 13). Ignition is reached earlier (shallower) for Model C at the equator except when the hotspot at the pole (Model A) is $T_{\rm HS} \gtrsim 1 \times 10^8$ K.

the 2D nature of our code, we were able to investigate the relevant hotspot sizes that induce this behaviour. We consider models of different hotspot sizes (from 1 cm–2 km) for cylindrical and Cartesian geometries and with $T_{\rm HS} = 8 \times 10^7$ K, and we set the length of the domain in x to be 4 times larger than the hotspot size (we set the number of zones in x-direction to 200 to ensure that we could measure the extent reached by dissipation). We note that for the purposes of analysing the effect that the model geometry has on the results we did not reduce the gravity at the equator by 25 % for these models.

The 2D temperature distribution and temperature profiles by radial depth for hotspots with radius 1 m, 10 m and 1 km and hotspot temperature 8×10^7 K are plotted in Figure 6. The 2D temperature distributions demonstrate how the heat diffuses outwards when the hotspots have smaller radii, which is not visible for the bigger hotspots due to the temperature saturation. For the 1 m case (top panels) it is evident that the temperature under the hotspot is not saturated, and horizontal diffusion is visible. Due to the scale at which horizontal diffusion occurs, there is no such diffusion visible in the 1 km case (bottom panels).

In Figure 7 the 2D distributions of opacity and nuclear burning are plotted for a hotspot size of 10 m. The opacity at the bottom of the accreted layer is very low ($\sim 10^{-2}$ cm^2 g^{-1}), and the nuclear burning is very low near the surface, and comes mostly from the deeper accreted layers.

In Figure 8 we have plotted the temperature at the bottom of the accreted layer ($T_{\rm base}$) for all hotspot sizes and the two geometries for the stationary solution 2 min before a burst, in hotspot size steps of 0.1 dex. Figure 8 demonstrates that for hotspot sizes less than 1 m, the heating does not penetrate to the bottom of the accreted layer, as there is no difference in temperature under the hotspot (dashed-dotted lines) and not under the hotspot (solid lines). Between 1 m and 100 m the temperature near the bottom of the accreted layer under the hotspot gradually becomes saturated. For hotspots bigger than ~100 m, i.e., *hotspots much larger than the layer thickness*, the centre temperature of the hotspot is saturated, and the boundary between the hotspot and the cooler columns drops on a scale shorter than the hotspot size. This, however, is not as trivial a result as it may naively seem. This is because the opacity in the deeper accretion layers and in the substrate is orders of magnitude smaller than at the surface (Figure 3), and hence heat could spread rather efficiently. In fact, in some preliminary time-dependent simulations not further discussed here, we have seen a broad runaway up to several times the layer height for hotspots with widths of the order of the layer height. Realistic hotspots, however, have sizes of ~ 1 km (see below), i.e., a factor 200 larger than the layer height, so that the centre of the hotspot is no longer affected by its boundary.

For a hot-stripe, simulated in Cartesian plane-parallel geometry, the accreted layers are consistently hotter as the ratio of the perimeter to the interior is smaller in the case of a stripe, and heat can less easily escape. We found, however, that the relevant size at which the hot-stripe could affect deeper layers is very similar to the cylindrical coordinate case. The centres of wide stripes hence behave the same way as the centre of large hotspots.

It is very unlikely that a hotspot caused by magnetic channelling in an AXP could be less than 10 m in size, given the size of the polar cap (Eq. 12). Therefore we are always operating in the regime where the accreted column under the hotspot is saturated, and heat diffusion horizontally from the hotspot is not important. Thus, both in the case of a wide hotspot and a wide equatorial stripe the centre can be well studied using a 1D code such as KEPLER.

4 DISCUSSION

Our findings reveal that a hotspot on the surface of an accreting pulsar could influence the ignition location of X-ray bursts if the hotspot has a temperature $\gtrsim 2 \times 10^7$ K. We reproduce previous studies that find that due to the lower surface gravity expected at the equator, ignition will almost always occur at this location. We find that hotspots with a temperature less than 1×10^8 K are unlikely to affect ignition location, but hotspots hotter than this could induce burst ignition at the magnetic pole, even when accounting for the expected lower surface gravity at the equator. Furthermore, when magnetic channelling is in place we do not expect a hot stripe to develop at the equator as in the case of pure disc accretion, so that ignition at the magnetic pole is even more likely.

Our results suggest that a hotspot with temperature $\gtrsim 1 \times 10^8$ K is required for X-ray burst ignition location to move from the equator to the magnetic pole. Whether hotspots on the surface can actually get this hot is uncertain, especially since spectral modelling of the X-ray emission from AXPs usually infers temperatures in the range 1–5$\times 10^7$ K or less. However, we cannot separate the hotspot emission from the rest of the neutron star or the accretion disk in the spectra obtained in observations of these sources, and thus these temperatures may not provide a reliable estimate of the hotspot temperature. An alternative (whilst simple) method of obtaining the hotspot temperature is by estimating the blackbody temperature of an emitting area with radius $R_{\rm HS}$, radiating with the accretion luminosity $L_{\rm acc}$ (Frank et al. 2002)

$$T_{\rm bb} = \left(\frac{L_{\rm acc}}{4\pi R_{\rm HS}^2 \sigma} \right)^{1/4} \tag{14}$$

where σ is the Stefan-Boltzmann constant.

Assuming an accretion luminosity of 1×10^{38} erg and $R_{\rm HS} = 0.5$ km this gives $T_{bb} \approx 8.7 \times 10^7$ K. Alternatively, we could consider the thermal energy released if the gravitational potential energy were entirely converted into thermal energy (Frank et al. 2002)

$$T_{\rm th} \approx \left(\frac{GMm_{\rm p}}{3\, k_{\rm B}\, R_\star} \right) \tag{15}$$

where $m_{\rm p}$ is the mass of a proton, M is the mass of the neutron star,

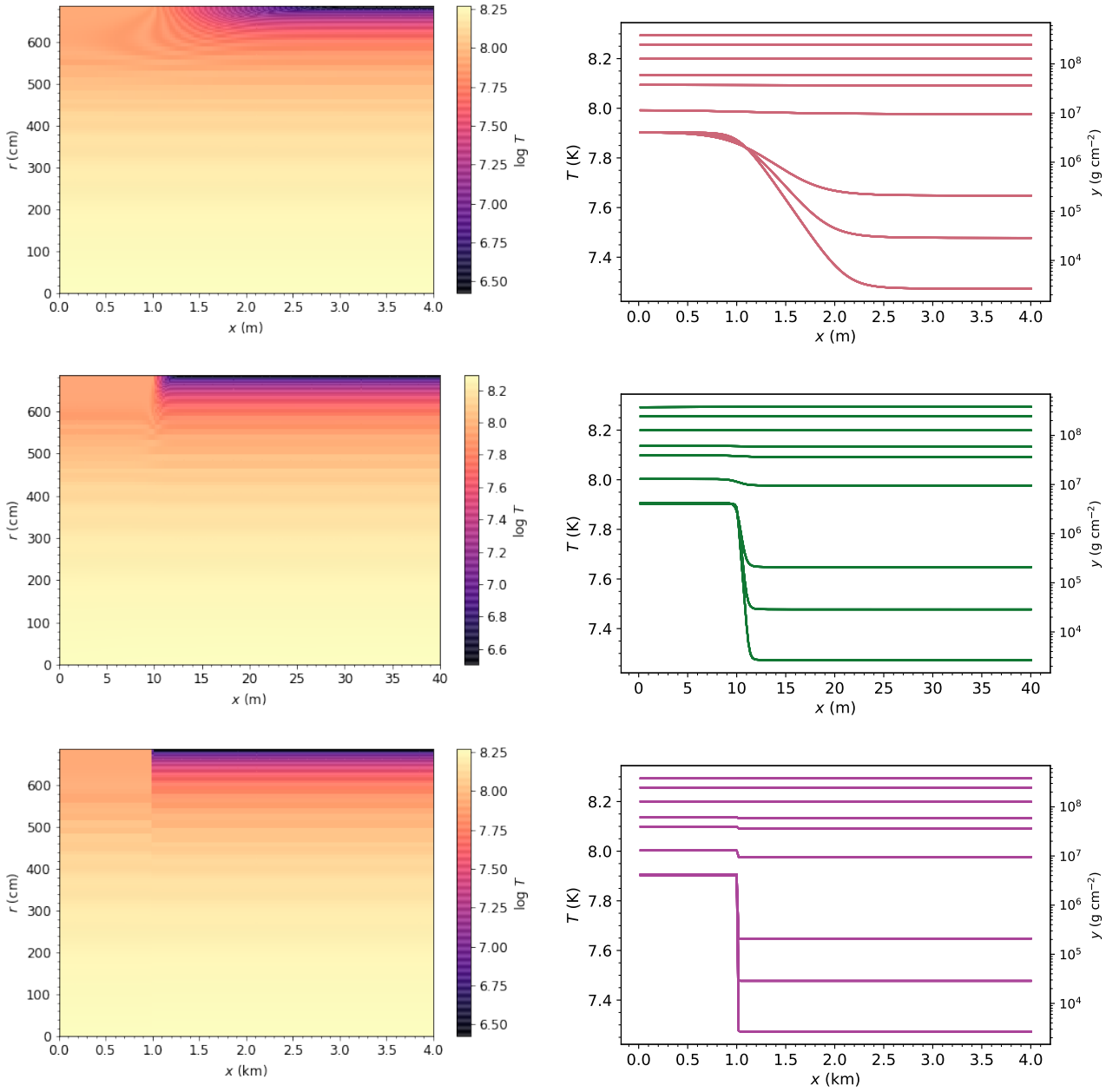

Figure 6. *Top Left panel:* 2D temperature distribution for a hotspot radius of 1 m with cylindrical geometry. *Top Right panel:* Temperature profiles for different radial depths for a hotspot of 1 m showing how the heat from the hotspot disperses into the accreted layers. *Middle Left panel:* 2D temperature distribution for a hotspot radius of 10 m with cylindrical geometry. *Middle Right panel:* Temperature profiles for different radial depths for a hotspot of 10 m showing how the heat from the hotspot disperses into the accreted layers. *Bottom Left panel:* 2D temperature distribution for a hotspot radius of 1 km with cylindrical geometry. *Bottom Right panel:* Temperature profiles for different radial depths for a hotspot of 1 km showing how the heat from the hotspot disperses into the accreted layers. The model has parameters $\dot{m} = 0.1\,\dot{m}_{\rm Edd}$, $Q_{\rm b} = 0.1{\rm MeVnuc}^{-1}$, and $T_{\rm HS} = 8 \times 10^7$ K, for a snapshot 1 min before a burst begins. All temperatures are reported in log10.

and $R_\star$ is the radius of the neutron star. For a $1.4\,{\rm M}_\odot$ neutron star and an emitting area with radius 0.5 km, we find $T_{\rm th} \approx 2.4 \times 10^8$ K.

Thus the likelihood that the hotspot in XTE J1814–338, IGR J17480–2446, or AXPs in general could be as hot as 1×10^8 K is uncertain. It is expected that the true radiation temperature should lie between the blackbody temperature and the thermal temperature (Frank et al. 2002). In spectral modelling of IGR J17480–2446, Papitto et al. (2012) found blackbody temperatures varied drastically between observations and instruments, and found temperatures as high as 3.5×10^8 K. Thus we find it unlikely, but not impossible, that the hotspot in AXPs could be as hot as 1×10^8 K.

If a hotspot can be as hot as 1×10^8 K, the scenario in which bursts ignite at the magnetic pole could be a plausible explanation for the burst oscillations observed in IGR J17480–2446 and XTE J1814–338 that are coincident with the spin period of the pulsar in each of these systems. Cavecchi et al. (2011) suggested that the burst oscillations at the same frequency as the spin period of the pulsar in IGR J17480–2446 could be explained by a hotspot confined by

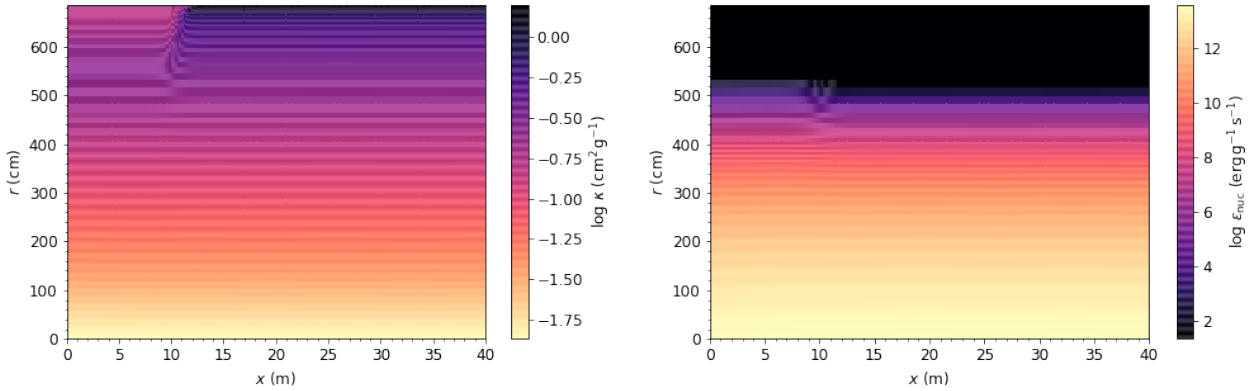

Figure 7. *Left panel:* 2D opacity distribution for a hotspot radius of 10 m with cylindrical geometry. *Right panel:* 2D distribution of nuclear energy generation for a hotspot radius of 10 m with cylindrical geometry. The model has parameters $\dot{m} = 0.1\,\dot{m}_{\rm Edd}$, $Q_{\rm b} = 0.1{\rm MeVnuc}^{-1}$, and $T_{\rm HS} = 8 \times 10^7$ K, for a snapshot 1 min before a burst begins.

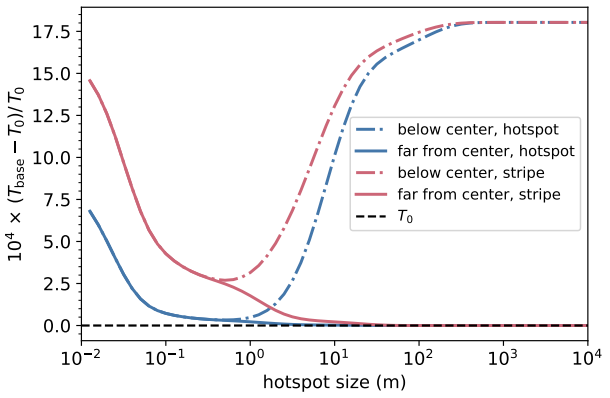

Figure 8. The temperature at the base of the accreted layer for a column under the hotspot (dashed-dotted line) and one far from the hotspot (solid line), for cylindrical (red) and Cartesian (blue) geometries and a range of hotspot sizes (in 0.1 dex steps). T_0 is the temperature at the base for a simulation with no hotspot. The model has parameters of Model A ($\dot{m} = 0.1\,\dot{m}_{\rm Edd}$, $Q_{\rm b} = 0.1{\rm MeVnuc}^{-1}$), and $T_{\rm HS} = 8 \times 10^7$ K, for a snapshot 2 min before a burst begins in the KEPLER simulation. Note that in this case we have not reduced the gravity in the Cartesian coordinate system simulations in order to analyse the effect of geometry alone. For hotspot sizes $\lesssim 1$ m the domain is so small that the heat from the hotspot spreads evenly by the time it reaches the bottom. This is an artifact of the code, but it would not be possible to resolve for the smallest sizes. We find the temperature under the hotspot asymptotes to a constant value for hotspots $\gtrsim 100$ m.

hydromagnetic stresses to the magnetic pole. They argue that due to tension induced by the compression of magnetic field lines, the strength of the magnetic field required for magnetic confinement is only $\sim 4 \times 10^9$ G (Heng & Spitkovsky 2009). This, combined with the ability to preferentially ignite X-ray bursts under the hotspot could well be a plausible explanation for these puzzling observations of IGR J17480–2446. The case of XTE J1814–338, however, is a little different, as the magnetic field in this system does not appear to be as strong as in IGR J17480–2446. Observations cannot rule out a magnetic field as strong as 4×10^9 G (Bhattacharyya et al. 2005), however, the magnetic field must be $\lesssim 10^9$ G in order for the magnetic propeller effect not to disrupt accretion (Rappaport et al. 2004). Watts et al. (2008) deduced that in the scenario in which magnetic confinement of the fuel is not possible, the effect of the higher temperature at the accretion impact point may induce burst ignition at this point. In this case, in order to explain the continued phase locking of the burst oscillations with the accretion hotspot, the burning front of the burst would need to stall, perhaps due to the rate of heat transfer of the burning front. In this work we deduce that it is plausible that the temperature asymmetries due to the accretion hotspot could cause bursts to ignite at the hotspot, however we need to include hydrodynamics and time-dependence in our simulations in order to assess if burst front stalling is possible. Regardless, the fact that the phase-locking of the burst oscillations with the persistent pulsations in XTE J1814–338 happen only when the accretion rate is inferred to be higher (Watts et al. 2008), supports our finding that only when the hotspot is sufficiently hot can bursts ignite under the hotspot.

In the results we report there are significant discrepancies between the 1D KEPLER calculations of the influence of the hotspot on the ignition time, and the 2D heat transport code we developed. These discrepancies can be attributed to a couple of things. Firstly, the influence of thermal inertia is clearly very important in calculations such as these, and the time-independent 2D heat transport code cannot account for this. Secondly, heating causes advection, which the 2D heat transport code does not model as it does not include hydrodynamics. KEPLER solves the full time-dependent equations of conservation of mass, momentum, and energy, and thus can track the movement of material as it is being heated. We deduce that it is most likely for this reason that there is such a discrepancy between the static 2D heat transport code and the KEPLER model predictions for the runaway times in Table 1. Thirdly, the ignition time inferred using the 2D heat transport code is heavily dependent on the numerical accuracy of the code, as we define ignition to be when the code no longer converges to a static solution. Whilst we mitigated this effect as much as possible by using static solutions for slightly cooler hotspots as the initial guess temperature, there is still some uncertainty introduced due to the numerical accuracy. In Section 3.4, however, we demonstrated the utility of the 2D heat transport code over KEPLER, as it enables the horizontal diffusion length scale to be determined. We find that the temperature diffuses horizontally on a length scale ~ 10 m, significantly smaller than the expected radius of the hotspot based on the polar-cap size. Thus we deduce that the 1D KEPLER models of the runaway time are

reasonable approximations to the 2D case, since the hotspots are sufficiently large that any horizontal diffusion is negligible.

The 2D model of heat transport inside the accreted layers on the surface of a neutron star that we have developed is by no means exhaustive, and our results are dependent on numerous assumptions.

Firstly, we assumed that the accreted material is almost pure helium, and only accounted for helium burning via the triple-α reaction for the energy released due to nuclear burning. Since it is thought that the triple-α reaction should be the main trigger of thermonuclear runaway at the onset of a burst (e.g., Bildsten 1998), this assumption is the simplest case for the nuclear burning, but excludes energy released due to burning via other pathways, and would neglect heating due to burning of hydrogen to helium in case of helium-rich accretors. In the latter case, the influence of the hotspot may be much reduced. This case may be studied in the future.

Secondly, we only solve for the steady-state solution and do not solve the equations including time-dependence. Under this assumption, our models cannot reach thermonuclear runaway as there is no static solution during runaway, and thus we can only model the conditions in the accreted layers up to just before a burst occurs. Indeed, on comparison with the equivalent time-dependent KEPLER calculations, there is a discrepancy in the time of runaway for the different model cases.

Finally, in this model we only address heat transport mechanisms and do not include hydrodynamical effects. This assumption is perhaps the most important limitation of our model to discuss, as the effect of the temperature gradient on the movement of material in the accreted layer is important to consider. For example, the heated material may rise in the hotspot, inducing mixing in the hotter layers and movement of the fuel. This would be complicated by composition gradients that could stabilise against rise of material. Our static model cannot account for this, and it may have an effect on the prevalence of a temperature gradient in deeper layers, or the depth at which ignition conditions are reached first (see, e.g., Malone et al. 2011, 2014).

In favour of our approach, however, is that in a hotspot we may expect strong magnetic fields, strong enough to funnel the accretion flow, and these same magnetic fields may also prevent fluid flow unless there was significant ambipolar diffusion. For the other case, accretion in a stripe at the equator, Coriolis forces may prevent fluid motions away from the equator due to angular momentum conservation. A detailed study of these effects is beyond the scope of this paper, but see Spitkovsky et al. (2002); Cavecchi et al. (2015).

In future, the model should be upgraded to include hydrodynamical affects in order to conclusively examine the effect that a hotspot has on the deeper layers and location at which ignition conditions are reached first. A more realistic nuclear reaction network that accounts for energy released by reactions other than the triple-α reaction and time-dependence should also be included so that the full thermonuclear runaway can be modelled.

5 CONCLUSIONS

In this study we have presented 2D calculations of X-ray burst ignition location on the surface of accreting pulsars, taking into account the effect of temperature asymmetries caused by a hotspot on their surface. We found that heating persisted down to the approximate column depth of X-ray burst ignition for a hotspot temperature $\sim (2) \times 10^7$ K and independent of the size of the hotspot (assuming the hotspot radius is $\gtrsim 100$ m). In models of accretion at the equator and in models where the accreted fuel spreads evenly over the neutron star before ignition, we found that due to the lower surface gravity at the equator for rapidly rotating neutron stars, burst ignition will always preferentially ignite here unless the hotspot at the magnetic pole is hotter than $\gtrsim (1) \times 10^8$ K. At this temperature ignition would preferentially occur under the hotspot at the magnetic pole, providing a scenario in which off-equator ignition could occur in an accreting pulsar. However, we find it unlikely, but not impossible, that the hotspot in XTE J1814–338, IGR J17480–2446, or any AXP could be as hot as 1×10^8 K. We conclude that the ignition of bursts at the hotspot combined with magnetohydrodynamic effects leading to hotter and colder patches associated with the magnetic pole (for example hydromagnetic modes) could explain the phase locking of burst oscillations with the accretion-powered pulsations in the two AXPs XTE J1814–338 and IGR J17480–2446. Whilst this scenario is promising, in order to comprehensively assess if it is possible we would need to include a full treatment of hydrodynamics in the 2D heat transport code, time-dependence in our simulations, as well as a more robust nuclear reaction network.

ACKNOWLEDGEMENTS

The authors thank Duncan Galloway, Bernhard Müller and Andrew Cumming for helpful discussions. AJG acknowledges support by an Australian Government Research Training Program scholarship. This work benefited from support, in part, by the National Science Foundation under Grant No. PHY-1430152 (JINA Center for the Evolution of the Elements); by the Australian Research Council Centre of Excellence for Gravitational Wave Discovery (OzGrav), through project number CE170100004; by the Australian Research Council Centre of Excellence for All Sky Astrophysics in 3 Dimensions (ASTRO 3D); and from discussions at the Lorentz center workshop *"Bursting the Bubble: Connecting Thermonuclear Burst Research to a Wider Community"* held in Leiden, June 2019. FRNC and ALW acknowledge support from ERC Starting Grant No. 639217 CSINEUTRONSTAR (PI Watts).

This research made use of Matplotlib, a community-developed core PYTHON package (Hunter 2007) and NASA's Astrophysics Data System Bibliographic Services.

DATA AVAILABILITY

The software written for the purpose of this work is publicly available on Github at `https://github.com/adellej/ignition-calculations`

REFERENCES

Bhattacharyya S., Strohmayer T. E., Miller M. C., Markwardt C. B., 2005, ApJ, 619, 483

Bildsten L., 1998, in Buccheri R., van Paradijs J., Alpar A., eds, NATO Advanced Science Institutes (ASI) Series C Vol. 515, NATO Advanced Science Institutes (ASI) Series C. p. 419 (arXiv:astro-ph/9709094)

Bogdanov S., 2016, European Physical Journal A, 52, 37

Brown E. F., Bildsten L., 1998, ApJ, 496, 915

Cavecchi Y., et al., 2011, ApJ, 740, L8

Cavecchi Y., Watts A. L., Levin Y., Braithwaite J., 2015, MNRAS, 448, 445

Cavecchi Y., Watts A. L., Galloway D. K., 2017, ApJ, 851, 1

Chakrabarty D., 2005, in Rasio F. A., Stairs I. H., eds, Astronomical Society of the Pacific Conference Series Vol. 328, Binary Radio Pulsars. p. 279 (arXiv:astro-ph/0408004)

Chakrabarty D., Morgan E. H., 1998, Nature, 394, 346
Cooper R. L., Narayan R., 2007, ApJ, 657, L29
Cumming A., Bildsten L., 2000, ApJ, 544, 453
Frank J., King A., Raine D. J., 2002, Accretion Power in Astrophysics: Third Edition
Galloway D. K., Keek L., 2017, arXiv e-prints, p. arXiv:1712.06227
Galloway D. K., Muno M. P., Hartman J. M., Psaltis D., Chakrabarty D., 2008, ApJS, 179, 360
Heng K., Spitkovsky A., 2009, ApJ, 703, 1819
Hunter J. D., 2007, Computing in Science & Engineering, 9, 90
Litwin C., Brown E. F., Rosner R., 2001, ApJ, 553, 788
Malone C. M., Nonaka A., Almgren A. S., Bell J. B., Zingale M., 2011, ApJ, 728, 118
Malone C. M., Zingale M., Nonaka A., Almgren A. S., Bell J. B., 2014, ApJ, 788, 115
Mukherjee D., Bult P., van der Klis M., Bhattacharya D., 2015, MNRAS, 452, 3994
Nagase F., 1989, PASJ, 41, 1
Ootes L. S., et al., 2019, MNRAS, 487, 1447
Papitto A., di Salvo T., Burderi L., Menna M. T., Lavagetto G., Riggio A., 2007, MNRAS, 375, 971
Papitto A., et al., 2011, A&A, 535, L4
Papitto A., et al., 2012, MNRAS, 423, 1178
Patruno A., Watts A. L., 2012, arXiv e-prints, p. arXiv:1206.2727
Poutanen J., Gierliński M., 2003, MNRAS, 343, 1301
Rappaport S. A., Fregeau J. M., Spruit H., 2004, ApJ, 606, 436
Riley T. E., et al., 2019, ApJ, 887, L21
Spitkovsky A., Levin Y., Ushomirsky G., 2002, ApJ, 566, 1018
Spitkovsky A., Ushomirsky G., Levin Y., 2003, in AAS/High Energy Astrophysics Division #7. AAS/High Energy Astrophysics Division. p. 17.31
Steiner A. W., Lattimer J. M., Brown E. F., 2013, ApJ, 765, L5
Strohmayer T. E., Zhang W., Swank J. H., Smale A., Titarchuk L., Day C., Lee U., 1996, ApJ, 469, L9
Strohmayer T. E., Markwardt C. B., Swank J. H., in't Zand J., 2003, ApJ, 596, L67
Tauris T. M., van den Heuvel E. P. J., 2006, Formation and evolution of compact stellar X-ray sources. pp 623–665
Virtanen P., et al., 2020, Nature Methods, 17, 261
Watts A. L., 2012, ARA&A, 50, 609
Watts A. L., Patruno A., van der Klis M., 2008, ApJ, 688, L37
White N. E., Swank J. H., Holt S. S., 1983, ApJ, 270, 711
Wijnands R., van der Klis M., 1998, Nature, 394, 344
Woosley S. E., et al., 2004, ApJS, 151, 75

This paper has been typeset from a TEX/LATEX file prepared by the author.

4

OBSERVATIONS OF ACCRETING NEUTRON STARS

Observations of accreting neutron stars are a crucial component in advancing our understanding of these systems. In the case of accreting neutron stars, often observations are limited to a few intermittent snapshots of when a source goes into outburst. Usually observations are primarily taken with X-ray instruments aboard satellite telescopes. In this chapter we present two observational studies of accreting neutron star systems.

4.1 ENHANCED OPTICAL ACTIVITY 12 DAYS BEFORE X-RAY ACTIVITY, AND A 4 DAY X-RAY DELAY DURING OUTBURST RISE, IN A LOW-MASS X-RAY BINARY

When transient accreting neutron stars go into outburst, often they are not observed until the X-ray flux has reached a level detectable by all-sky monitors aboard X-ray satellite telescopes ($F \sim 10^{-8}\,\mathrm{erg\,s^{-1}\,cm^{-2}}$). In the first study of this chapter, we present unprecedented observations we obtained of the rise to outburst of the accretion-powered millisecond pulsar SAX J1808.4–3658 in August 2019. We observed the system with multiple telescopes across optical, UV, and X-ray wavelengths from before the outburst began, to the initial signs of outburst, through to the commencement of accretion onto the neutron star and the outburst in its entirety. These observations are the first, detailed observations of a transient accreting neutron star switching on to date, and provide important constraints on the optical to X-ray delay that is expected by the disk instability model.

Published in:
A. J. Goodwin et al. (June 2020a). 'A 12 day delay between optical and X-ray activity during outburst rise in a low-mass X-ray binary'. *arXiv e-prints*, arXiv:2006.02872, arXiv:2006.02872. arXiv: 2006.02872 [astro-ph.HE]

MNRAS **000**, 1–12 (2020) Preprint 6 October 2020 Compiled using MNRAS LATEX style file v3.0

Enhanced optical activity 12 days before X-ray activity, and a 4 day X-ray delay during outburst rise, in a low-mass X-ray binary

A. J. Goodwin,[1]★ D. M. Russell,[2] D. K. Galloway,[1] M. C. Baglio,[2,3] A. S. Parikh,[4] D. A. H. Buckley,[5] J. Homan,[6,7] D. M. Bramich,[2] J. J. M. in 't Zand,[6] C. O. Heinke,[8] E. J. Kotze, [5,9] D. de Martino, [10] A. Papitto,[11] F. Lewis,[12,13] and R. Wijnands[4]

[1]*School of Physics and Astronomy, Monash University, Clayton, 3800, Australia*
[2]*Center for Astro, Particle and Planetary Physics, New York University Abu Dhabi, PO Box 129188, Abu Dhabi, UAE*
[3]*INAF, Osservatorio Astronomico di Brera, Via E. Bianchi 46, I-23807 Merate (LC), Italy*
[4]*Anton Pannekoek Institute for Astronomy, University of Amsterdam, Postbus 94249, NL-1090 GE Amsterdam, The Netherlands*
[5]*South African Astronomical Observatory, PO Box 9, Observatory 7935, Cape Town, South Africa*
[6]*Eureka Scientific, Inc., 2452 Delmer Street, Oakland, CA 94602, USA*
[7]*SRON Netherlands Institute for Space Research, Sorbonnelaan 2, 3584 CA, Utrecht, The Netherlands*
[8]*Department of Physics, University of Alberta, CCIS 4-183, Edmonton, AB T6G 2E1, Canada*
[9]*Southern African Large Telescope Foundation, PO Box 9, Observatory 7935, Cape Town, South Africa*
[10]*INAF – Osservatorio Astronomico di Capodimonte, Salita Moiariello 16, 80131 Napoli, Italy*
[11]*INAF – Osservatorio Astronomico di Roma, via Frascati 33, 00040 Monte Porzio Catone (Roma), Italy*
[12]*Faulkes Telescope Project, School of Physics and Astronomy, Cardiff University, The Parade, Cardiff, CF24 3AA, Wales, UK*
[13]*Astrophysics Research Institute, Liverpool John Moores University, 146 Brownlow Hill, Liverpool L3 5RF, UK*

Accepted 2020 August 20. Received 2020 August 20; in original form 2020 June 4

ABSTRACT

X-ray transients, such as accreting neutron stars, periodically undergo outbursts, thought to be caused by a thermal-viscous instability in the accretion disk. Usually outbursts of accreting neutron stars are identified when the accretion disk has undergone an instability, and the persistent X-ray flux has risen to a threshold detectable by all sky monitors on X-ray space observatories. Here we present the earliest known combined optical, UV, and X-ray monitoring observations of the outburst onset of an accreting neutron star low mass X-ray binary system. We observed a significant, continuing increase in the optical i'-band magnitude starting on July 25, 12 days before the first X-ray detection with *Swift*/XRT and NICER (August 6), during the onset of the 2019 outburst of SAX J1808.4–3658. We also observed a 4 day optical to X-ray rise delay, and a 2 day UV to X-ray delay, at the onset of the outburst. We present the multiwavelength observations that were obtained, discussing the theory of outbursts in X-ray transients, including the disk instability model, and the implications of the delay. This work is an important confirmation of the delay in optical to X-ray emission during the onset of outbursts in low mass X-ray binaries, which has only previously been measured with less sensitive all sky monitors. We find observational evidence that the outburst is triggered by ionisation of hydrogen in the disk.

Key words: accretion, accretion discs – X-rays: binaries – X-rays: individual: SAX J1808.4-3658

1 INTRODUCTION

Transient accreting neutron stars in low mass X-ray binaries (LMXBs) are in close binary orbits with a main sequence, white dwarf, or other low mass star. The neutron star accretes from the companion via Roche Lobe overflow, forming an accretion disk, and emitting energetic radiation in the form of X-rays when material transfers from the accretion disk onto the neutron star (e.g. White & Mason 1985; Lewin & van der Klis 2006). Outbursts in transient accreting neutron stars are characterised by an abrupt increase in X-ray luminosity of several orders of magnitude over a few days, typically followed by a decay on a timescale of a month or several months, before the system returns to its low luminosity quiescent state (e.g. Frank et al. 1987).

Optical emission in these systems is generally thought to arise

★ E-mail: ajgoodwin.astro@gmail.com

from the outer accretion disk, companion star, and at higher luminosity X-ray reprocessing in the disk, in some cases with a contribution from synchrotron emission from jets (e.g. Russell, Fender & Jonker 2007). Whereas X-rays are thought to originate from close to the neutron star, at the inner disk from the hot accretion flow (Lasota 2001), or from the neutron star surface. Thus, we can use multiwavelength observations of LMXBs to follow the progression of an outburst, and separate the activity of the accretion disk, jet, companion star, and neutron star.

SAX J1808.4–3658 was the first accretion-powered millisecond pulsar (AMSP) to be discovered (in 't Zand et al. 1998; Wijnands & van der Klis 1998), and goes into outburst every few years (Bult et al. 2019; Del Santo et al. 2015; in't Zand et al. 2013; Markwardt et al. 2011a; Markwardt & Swank 2008; Markwardt et al. 2002; Wijnands et al. 2001). The outbursts of SAX J1808.4–3658 have been occurring with progressively longer recurrence times (e.g. Galloway & Cumming 2006), which is a puzzling phenomenon. The system consists of a 401 Hz pulsar (Wijnands & van der Klis 1998) in a close binary orbit (P=2.01 hr; Chakrabarty & Morgan 1998), with a very low mass ($M = 0.03 - 0.11\,\mathrm{M}_{\odot}$; Deloye et al. 2008; Elebert et al. 2009; Wang et al. 2013) companion star that is likely hydrogen depleted (Goodwin et al. 2019a; Johnston et al. 2018; Galloway & Cumming 2006). During outburst, the system exhibits type-I thermonuclear X-ray bursts (e.g. Galloway & Cumming 2006) with burst oscillations at the pulsar frequency (in't Zand et al. 2001; Chakrabarty et al. 2003).

The exact mechanism that causes the onset of an outburst in LMXBs is unknown. The disk instability model (DIM) is the prevalent theory that describes a mechanism for outburst: a thermal-viscous disk instability (see Dubus et al. 2001, for a review). The theory was first proposed in the 1970s to explain similar outbursts observed in dwarf novae systems (a subset of cataclysmic variables (CVs); Smak 1971; Hōshi 1979; Osaki 1974). The DIM was extended to encompass LMXBs around 20 years later when the similarity in the fast-rise and exponential-decay behaviour between outbursts in CVs and transient LMXBs was recognised (van Paradijs & Verbunt 1984; Cannizzo et al. 1985; van Paradijs 1996). There have been some significant and important modifications to the DIM necessary to explain the variations in, and general observational behaviour of, LMXBs. These include the effects of irradiation of the accretion disk and the donor star by the LMXB primary; inner disk truncation, if the compact object has a strong ($> 10^8$ G) magnetic field or due to evaporation; variations in mass transfer; and the existence of winds and outflows and the torque they exert on the accretion disk (e.g., Hameury 2019). Nevertheless, the single underlying mechanism that describes the cause of outburst in an accretion disk has remained constant since the theory was first proposed; a thermal-viscous disk instability.

According to the DIM, the outburst-quiescence cycle of an LMXB may proceed as follows: first, during quiescence, the cold disk accumulates mass via Roche-lobe overflow from the companion until the disk reaches a critical density, and the disk temperature rises to the critical value required to ionise hydrogen. This event causes a heating front to propagate through the disk, bringing it to a hot, bright state, and commencing the outburst (e.g. Menou et al. 1999). The outburst lasts on the order of a month, during which accretion onto the compact object gives rise to high energy X-ray emission. The outburst then decays in luminosity as the disk depletes, and the system returns to quiescence to begin building up mass in the disk for the next outburst (e.g. Lasota 2001). This picture is a very simplified rendition of what is happening during an outburst of an LXMB, and there is variation observed in the behaviour of many systems. One such key variation includes the time delay between when the disk instability first occurs, and the heating front begins to propagate in the disk; and when the outburst commences, and accretion onto the compact object is observed as an increase in X-ray luminosity.

Dubus et al. (2001) describe two different kinds of outburst, depending on how long it takes for the heating front to propagate in to the inner disk. Two heating fronts are formed at the point of ignition in the disk, and they propagate both inwards and outwards from the ignition radius (Menou et al. 1999). For "inside-out" outbursts, the ignition occurs at a small radius, and the inward propagating front reaches the inner disk much faster than the outward propagating front reaches the outer disk. In "outside-in" outbursts, the ignition occurs at a larger disk radius, and it can take much longer for the heating front to reach the inner disk. Dubus et al. (2001) describe the primary difference between "inside-out" and "outside-in" outbursts. During quiescence, the density profile of the disk is approximately linearly proportional to its radius, which implies that "outside-in" heating fronts always progress through regions of decreasing surface density. Whereas, in "inside-out" outbursts, the outward front can encounter regions of higher densities, and if the heating front cannot raise the density of the front above the higher density, it stalls and a cooling front can develop. "Inside-out" outburst fronts propagate slowly, and it can take much longer to bring the disk to the hot state than in "outside-in" outbursts. When irradiation is accounted for, it does not change the structure of the heating front, but it does change the maximum radius to which an "inside-out" outburst can propagate. The ignition radius depends on the mass transfer rate from the secondary and the size of the disk. (Smak 1984; Hameury et al. 1998). For low mass transfer rates, the accreted matter will drift inwards in the cold disk, and the maximum surface density will accumulate in the inner disk, giving rise to inside-out outbursts. If the mass transfer rate is high, the mass accumulation time at the outer radius can become lower than the drift time, and an outside-in outburst will be triggered by the higher surface density in the outer disk. Dubus et al. (2001) found that the mass transfer rate required for an outside-in outburst to occur in their model of a soft X-ray transient was higher than the accretion rate for which the disk was stable, thus indicating that inside-out outbursts are more likely for this kind of system. However, an outside-in outburst is theoretically possible if the accretion disk has a small radius.

Observations, especially over multiple wavelengths, of the rise to outburst in LMXB systems are rare, as the rise occurs rather quickly (on the order of a few days), and outbursts are not usually detected until the flux has risen above the detection threshold of all-sky monitors aboard X-ray space observatories. The X-ray Binary New Early Warning System (XB-NEWS; Russell et al. 2019a) was developed with the goal of producing light curves in real time for long-term optical monitoring of LMXBs (Lewis et al. 2008, and other sources) with Las Cumbres Observatory network telescopes. One of the main aims of this pipeline is to be able to identify new outbursts of LMXBs from an early optical rise, in real time, which will increase the number of sources that have observationally constrained optical to X-ray delays. There are a few systems in which the optical to X-ray delay has been constrained using observations from X-ray all sky monitors. These include: a < 7 d delay in V404 Cyg (Bernardini et al. 2016), a < 6 d delay in GRO J1655–40 (Orosz et al. 1997; Hameury et al. 1997), a < 9 d delay in XTE J1550–564 (Jain et al. 2001), a < 10 d delay in XTE J1118+480 (Wren et al. 2001; Zurita et al. 2006), a < 5 d delay in 4U 1543–47, and a < 7 d delay in ASASSN–18ey (Tucker et al. 2018), which are all black hole low mass X-ray binaries. There is one neutron star X-ray

binary, Aql X–1, in which a < 3–8 d optical to X-ray delay has been inferred (Shahbaz et al. 1998; Russell et al. 2019a), but again this constraint was only obtained with an X-ray all sky monitor. Prior to this work, to date, there are no observations of the rise to outburst of an LMXB that conclusively constrain the delay time using an X-ray telescope more sensitive than an all sky monitor.

In this work we present the earliest multiwavelength observations of the rise to outburst of the accreting neutron star SAX J1808.4–3658. In Section 2, we outline the observations and data processing of the 2019 outburst we obtained. In Section 3 we present the multiwavelength light curve, including an optical spectrum obtained on the day of the first X-ray detection, and the disk temperature evolution inferred from the optical V-i' color. In Section 4, we discuss the implications of a 12 day delay between the first optical and X-ray detections of the source, and relate these observations to the theoretical expectations from the disk instability model.

2 METHODS AND OBSERVATIONS

We monitored the accretion-powered millisecond pulsar SAX J1808.4–3658 during the lead-up to its 2019 outburst using the Neil Gehrels Swift Observatory (*Swift*), the 2-m Faulkes Telescope South (at Siding Spring, Australia), the Las Cumbres Observatory (LCO) network of 1-m robotic telescopes, and the South African Large Telescope (SALT).

Our monitoring program was motivated by the prediction of a phenomenological (quadratic) model for the times of the previous 8 outbursts, since the first in 1996. The model predicted the next outburst in 2019 May, but no activity was seen either in that month or the following. We began our observing program on 2019 July 17, and observed a statistically significant (> 5-σ) increase from the quiescent level in the optical i'-band magnitude on July 25 (MJD 58689). We first detected X-ray activity with the *Swift* X-ray Telescope (XRT) on August 6.44 (MJD 58701.44; Goodwin et al. 2019b), 12 days after the first sign of increased optical activity. The X-ray flux subsequently increased over the next 2 days, indicating the beginning of accretion onto the neutron star, and the onset of outburst.

The 2019 outburst occurred 85 d later than the time predicted by the phenomenological model, after a quiescent interval of 4.3 yr. This interval is the longest separating any two outbursts of SAX J1808.4−3658, by almost a year. The outburst interval has increased after every outburst, up from 1.6 yr between the first two, in 1996 September and 1998 April. As noted by Galloway (2008), the continuing trend of increasing outburst interval contributed to a decline in the long-term averaged accretion rate. Provided the quadratic model holds for the next outburst, we expect it to occur no earlier than MJD 60260 (2023 November 12), another 4.3 yr after the 2019 outburst. The likely uncertainty on this prediction is as for the present outburst, ≈ 90 d.

We present below a description of the optical observations, as well as the X-ray observations with *Swift* and the Neutron Star Interior Composition Explorer (NICER) instrument; the NICER observations have already been reported in Bult et al. (2019).

2.1 Optical observations

2.1.1 *LCO monitoring*

SAX J1808.4–3658 was extensively monitored throughout the 2019 outburst from the very beginning with the Las Cumbres Observatory (LCO) network including the 2-metre Faulkes Telescope South. The LCO observations are part of an ongoing monitoring campaign of∼50 low-mass X-ray binaries (Lewis et al. 2008) co-ordinated by the Faulkes Telescope Project. Observations were performed with the B, V, R Bessell filters and the SDSS u',i',z' filters (354–870 nm). For the purposes of this paper, we include the B, V, R, i', and z'-band measurements of the first part of the outburst. The full data set in all filters will be published in Baglio et al. (submitted) and Russell et al. (in preparation). Aperture photometry was performed by a new data analysis pipeline, the "X-ray Binary New Early Warning System (XB-NEWS)", developed with the aim of automatically analysing any image of a specific list of targets that is acquired with the LCO network telescopes, including new images in real-time. The pipeline first computes an astrometric solution on each image using Gaia DR2[1] positions, then performs accurate aperture photometry of all the stars in the field of view. Zero-point calibrations between epochs are solved for using the method described in Bramich & Freudling (2012), and finally the pipeline flux calibrates all the stars on a standard magnitude scale using the ATLAS-REFCAT2 catalogue (Tonry et al. 2018)[2] (which includes PanSTARRS DR1, APASS, and other catalogues). XB-NEWS also performs multi-aperture photometry (similar to the DAOGROW algorithm by Stetson 1990) which is effectively azimuthally-averaged PSF profile fitting photometry. This method is optimised for point sources in fields that are not too crowded, and it was used to extract the magnitudes of SAX J1808.4–3658 for this paper.

For images in which the source was not formally detected above the detection threshold, forced multi-aperture photometry at the known location of the source was performed, and magnitudes with errors > 0.25 mag were excluded as these are only very marginal detections, or non-detections. SAX J1808.4–3658 lies in a very crowded field of the Galactic plane, with a few stars within 1″ of the source position (e.g. Deloye et al. 2008). These stars can contribute to the quiescent flux measurements, but this does not affect the date of the early rise into outburst since these stars are unchanging and the rise does not correlate with seeing.

The result of the pipeline process is a calibrated light curve for each object in the field of view. For further details see Russell et al. (2019a); Pirbhoy et al. (2020). We also extinction corrected the V and i' magnitudes using $A_V = 0.510$ mag, where we have inferred A_V given the relationship between $N_{\rm H}$ and A_V for our Galaxy, reported in Foight et al. (2016) and using the measured $N_{\rm H}$ for the 2019 outburst of SAX J1808.4–3658 of $(1.5 \pm 0.1) \times 10^{21}$ cm^{-2} (Di Salvo et al. 2019). Using the Cardelli et al. (1989) extinction law, we infer $A_{i'} = 0.340$ mag.

The LCO monitoring of SAX J1808.4–3658 was crucial to detect the first flux enhancement; the early precursor of the new outburst, on July 25 (MJD 58689.48; Russell et al. 2019b) in i'-band.

2.1.2 *SALT Spectroscopy*

We took optical spectroscopic observations of SAX J1808.4–3658 with the Southern African Large Telescope (SALT; Buckley et al. 2006), on August 2, 3 and 6 (MJD 58697, 58698, and 58701). We covered the region 4060–7120 Å at a mean resolution of 4.7 Å using the Robert Stobie Spectrograph (RSS; Burgh et al. 2003) with the PG900 VPH grating in frame transfer mode with 200 s exposures

[1] https://www.cosmos.esa.int/web/gaia/dr2
[2] https://archive.stsci.edu/prepds/atlas-refcat2/

and a slitwidth of 1.5″. No spectral trace was detected on August 2 in an accumulated 2400 s exposure, although there was a focus issue. A weak spectral trace was detected on August 3 in an accumulated 2200 s exposure. On August 6 a spectrum of the object was obtained with 12 repetitions of 200 s exposures, revealing Balmer absorption lines and strong interstellar NaD absorption. The seeing on August 6 was 1.8″. We also obtained follow up spectra on August 22, 25, and September 26 (MJD 58717, 58720, and 58752), which will be presented in a follow up paper (Russell et al., in preparation).

The spectroscopic data reductions were done using the PySALT version 0.47, the PyRAF-based software package for SALT data reductions (Crawford et al. 2010)[3], which includes gain and amplifier cross-talk corrections, bias subtraction, amplifier mosaicing, and cosmetic corrections. Spectral reductions (object extraction, wavelength calibration and background subtraction) were all done using standard IRAF[4] routines, as was the relative flux calibration, as absolute flux calibration is not possible with SALT due to its unusual design (Buckley et al. 2017). Low frequency bumps are artefacts from the imperfect flux calibration.

2.2 *Swift* observations

2.2.1 *XRT*

The XRT aboard *Swift* is sensitive in the 0.2–10 keV energy range, has an effective area of 100 cm^2, a 23.6×23.6′ field of view, and an 18″ resolution at half-power diameter (Burrows et al. 2005). We obtained a total of 14 observations between July 21 and August 9 (MJD 58685 to 58705), with an average exposure time of 0.5 ks, and a cadence of 2 days. The 8 observations between July 21 and August 4 were carried out with the XRT in Windowed Timing (WT) mode, the observation on August 6 with the XRT in Photon Counting (PC) mode, and the remaining observations from August 8 with the XRT in Auto mode. WT mode provides 1 dimensional imaging at the orientation of the roll angle of the spacecraft, with a sensitivity limit of approximately 2.4×10^{-11} erg cm^{-2} s^{-1}. Photon counting mode permits full spectral and spatial information to be obtained for sources, capable of accurately measuring fluxes down to 2×10^{-14} erg cm^{-2} s^{-1} in 10^4 s. To extract the X-ray flux measured by the XRT, we examined all 14 observations (OBSID 00030034120–00033801025, July 21–August 9) using the *Swift* online XRT product builder (Evans et al. 2009). The observations prior to Aug 6 (OBSID 00030034120–00030034127) could not be processed with the online XRT product builder, so we manually extracted upper limits using a box of 20 by 5 pixels (aligned to match the data) to extract the source flux, and a larger region (typically > 40 pixels by 5 pixels) to extract the background. In none of these observations was the source clearly visible to the eye. Exposure maps and ancillary response functions were generated, with the appropriate RMF file from the *Swift* calibration website. The upper limits obtained are 90% (two-sided) confidence levels. Two instances where the FOV of *Swift* missed the target (OBSID 00030034122 and 00030034128), and one instance where the observation was only 40 s long (OBSID 00030034128) were excluded.

2.2.2 *UVOT*

The UltraViolet and Optical Telescope (UVOT) aboard *Swift* is a 30 cm Ritchey-Chrétien reflector with a 17×17′ field of view, sensitive to wavelengths in the range 1700–6500 Å, and operates in photon counting mode. It has 7 filters, 4 of which were used in this project. The UVW1 filter has a peak sensitivity at 2600 Å, the UVW2 filter at 1928 Å, the UVM2 filter at 2245 Å and the U filter at 3465 Å (Roming et al. 2005). To extract the UV flux for each filter we examined the observations between July 19 and August 10 (MJD 58683 to 58705). We re-aligned the images, used a circular source region of 5″ and background region consisting of 3×5″ apertures (due to the field being very crowded in UV it is not possible to find a bigger background region). We used the HEAsoft Swift software tools[5] UVOTSOURCE task to carry out the aperture photometry and construct the light curve. The error bars and upper limits correspond to 1-σ. Two instances of very low exposure images leading to unconstrained upper limits have been rejected (OBSID 30034125 with the UVW2 filter, the only filter used during this observation, and 00030034140 with the UVW1 filter, one of three filters used during this observation with the others being UVM2 and UVW2). To extinction correct the UV magnitudes we used the relation with A_V described in Mathis (1990) to infer that $A_U = 0.82$, $A_{W1} = 1.08$, $A_{M2} = 1.49$, $A_{W2} = 1.36$.

2.3 NICER observations

The NICER X-ray Timing Instrument (Gendreau et al. 2016) consists of 56 concentrators that are each coupled to a silicon drift detector that is housed in a Focal Plane Module (FPM). At the time of the SAX J1808.4–3658 observations, 52 of the 56 FPMs were functional, providing an effective area of ∼1750 cm^2 in the 0.2–12 keV band. We analysed 69 *NICER* ObsIDs of SAX J1808.4–3658 (2050260101–2584014301), corresponding to observations made between July 30 and October 13. The source was often observed multiple times per day, resulting in dense coverage of the pre-outburst phase and the rise.

We used the `nicerl2` task in HEAsoft version 6.27.2 to reprocess all observations, applying gain solution 'optmv7he' and using the default filter criteria. We extracted spectra from all active FPMs, except #14 and #34, which often show excessive noise; and for all good-time-intervals (GTIs) longer than 100 s. Since NICER is a non-imaging instrument, the background needs to be estimated. We used the tool `nibackgen3C50` (R. Remillard et al, in prep.) which predicted background rates generally below 3 counts s^{-1} in the 0.5–10 keV band. The extracted spectra were grouped to a minimum of 25 counts per bin. They were background subtracted and analysed in the 0.5-10 keV band with XSPEC 12.11.0 (Arnaud 1996), with the appropriate response files for gain solution 'optmv7he', and using χ^2 statistics. The extracted-spectra and model background spectra were also used to construct a background-subtracted 0.5–10 keV light curve, with one data point per GTI (pink symbols in Figure 1).

The first clear detection of SAX J1808.4–3658 with NICER during the rise was made on August 6, 22:00 UTC, when the net (background-subtracted) count rate was 9.16±0.16 counts s^{-1}. We fit the spectrum of that GTI with an absorbed power-law (`tbnew` × `pegpwrlw` in XSPEC), with the photoionization cross section set to `vern` and the abundances set to `wilm`. Our best fit (χ^2=88 for 108 degrees of freedom) yields an N_H of 0.33±0.03 atoms cm^{-2}, a

[3] https://astronomers.salt.ac.za/software/pysalt-documentation/
[4] https://iraf.noao.edu/
[5] https://heasarc.nasa.gov/lheasoft/

power-law photon index of 2.43±0.07, and an unabsorbed 0.5–10 keV flux of $(2.91\pm0.11)\times10^{-11}$ erg cm^{-2} s^{-1}.

A potential detection was made one GTI earlier, on August 5 22:46 UTC, when the net count rate (1.44±0.06 counts s^{-1}) was higher than during all observations preceding it (maximum of 0.85 counts s^{-1}). However, comparison to contemporaneous background measurements indicated that the flux was still background dominated, and there was no statistically significant detection.

Between July 30 and August 5 the net count rates varied between -0.22 and 1.44 counts s^{-1}, with an average of 0.402 ± 0.003 counts s^{-1}. This rate is significantly above zero, possibly due to contaminating sources in NICER's ∼30 arcmin^2 field-of-view. The variations in the pre-outburst net count rate are likely due to limitations of the background model (which is still being refined). The 1-σ standard deviation in the net count rate before the first detection is 0.32 counts s^{-1}. We consider the average pre-outburst net count rate plus three times the 1-σ standard deviation, 1.37 counts s^{-1}, to be a good general estimate of the NICER detection limit of SAX J1808.4–3658. Using the best-fit model to the spectrum of the first detection, this count rate corresponds to an unabsorbed 0.5–10 keV flux of $\sim 4\times10^{-12}$ erg cm^{-2} s^{-1}.

3 RESULTS

The multiwavelength light curve of the 2019 rise to outburst of SAX J1808.4–3658 is shown in Fig. 1. Activity of the source was first noticed in the optical i'-band observations, beginning July 25 (MJD 58689), as the i'-band magnitude fluctuated between 0.7–1.0 mag brighter than the quiescent level of approximately 19.8 mag. Then, between August 3.85 and 5.98 (MJD 58698.85 and 58700.98), the i'-band intensity increased to approximately 2 mag brighter than the quiescent level, and continued to increase over the coming days as the outburst progressed. The peak of the 2019 outburst was reached at around August 10 (MJD 58705) in optical, and August 14 (MJD 58709) in X-ray (Fig. 1).

The first *Swift*/UVOT detection occurred on August 4 (MJD 58699.71), 10 days after the first sign of increased optical activity in the source, and 2 d before the first X-ray detection. The UV magnitude in all bands rose sharply by approximately 3 mag over the next 4 days until the outburst peak was reached. We note that prior to August 4 there were 7 UV observations in which an upper limit only was obtained with *Swift*/UVOT, which had a sensitivity of ≈ 21.5 mag for our observations given the short exposure times of the images, and so we cannot rule out low-level UV activity prior to August 4.

There was no detection of the source in the 8 *Swift*/XRT observations between July 17–August 1 (MJD 58685–58697), with upper limits of $0.8-3\times10^{-12}$ erg cm^{-2} s^{-1} (0.2–10 keV). There was a marginal detection of the source on August 2 (MJD 58697.85). However, the Aug. 2 *Swift*/XRT data do not show a clear source in visual inspection, leading us to suspect a spurious detection. We note that the *Swift*/XRT observations between July 17–August 4 were carried out with the XRT in WT mode, which is less sensitive than the XRT in PC mode, and thus we cannot rule out low-level X-ray activity ($< 1\times10^{-12}$ erg cm^{-2} s^{-1}) during this time.

On August 6.44 (MJD 58701.44) the source was first detected with the XRT in PC mode, with a count rate of 4.55×10^{-2} count s^{-1} in the 614 s exposure time. We estimate an unabsorbed X-ray flux (0.2–10 keV) of 2.5×10^{-12} erg cm^{-2} s^{-1}, for a power law spectrum with photon index of 1.73 and neutral hydrogen column of 1.46×10^{21} cm^{-2} (Di Salvo et al. 2019). Later that day, NICER first detected the source on Aug 6.92 (MJD 58701.92), at a 0.5–10 keV count rate of 9.07 count s^{-1}. For this observation and the same spectral parameters, we estimate an unabsorbed (0.5–10 keV) flux of $(2.91\pm0.11)\times10^{-11}$ erg cm^{-2} s^{-1}.

This first *Swift* X-ray detection on August 6 corresponds to a flux ≈50 times greater than the X-ray quiescent flux of SAX J1808.4–3658, of 5×10^{-14} erg cm^{-2} s^{-1} (0.5–10 keV, Heinke et al. 2009). This flux is the lowest the source has been detected in the early part of any outburst to date (previously the lowest flux the source had been detected at early in outburst was in 2011 at a flux of 0.2 mCrab, which is ≈100 times the quiescent X-ray flux; Markwardt et al. 2011b). We estimate the possible observed delay between the first optical activity to the first X-ray detection above the Swift flux sensitivity limit to be 10–15 d, based on the cadence of the optical and X-ray observations. The fact that we detected the source at such low X-ray flux likely indicates that the 12 day delay between the first optical and the first X-ray activity detected is close to the actual time it takes for the disk to completely ionise from an initial instability, and for the accretion outburst to begin.

3.1 Optical quiescence and the first signs of activity in 2019

We examined LCO i'-band observations of SAX J1808.4–3658 from approximately 500 d before the 2019 outburst in order to determine the quiescent level of optical activity, and the significance of the optical activity we saw on July 25 (MJD 58689, Fig. 2).

The quiescent light curve shown in Fig. 2 indicates significant variations in the i'-band magnitude on a range of timescales. Assuming the source is in quiescence during these 500 days, we thus measure an optical i'-band quiescent level of 19.8–20.2 mag. Deloye et al. (2008) measured a de-reddened quiescent i'-band magnitude range of 20.05–20.55 for SAX J1808.4–3658, fainter than our inferred range. We suspect the discrepancy could be due to orbital variations, and confusion in the LCO observations. Alternatively, the optical quiescent level of the source could have evolved since the 2008 outburst, and the source could now appear slightly brighter in quiescence. Nevertheless, we see no evidence for optical activity above the LCO observed quiescent level prior to July 25, which is when we infer the optical activity began.

3.2 Spectral evolution and disk temperature

The linearised optical and X-ray light curves are shown in Fig. 3. It is clear the V-band rose more quickly than and before the i'-band, with limited early observations in the B, R, and z bands. The B-band appears to rise the quickest, and reach the peak earlier than the other bands. Interestingly, the V-band was also observed to rise first and the B-band was observed to rise the fastest in observations of the dwarf Nova WX Hydri (Kuulkers et al. 1991). In the 1996 outburst of GRO J1655–40, the B-band was observed to rise after the V, R and i bands (Hameury et al. 1997).

We determined an optical 2-band V-i' temperature using the V and i'-band LCO observations, shown in Figure 4. To obtain a temperature from the V-i' colour, we approximate the optically emitting part of the disk by a blackbody with time-variable temperature to model the relationship between colour and magnitude. We adopted the model of Maitra & Bailyn (2008), described in detail in Russell et al. (2011). The blackbody model depends on the intrinsic colour, and thus the assumed extinction.

How well the blackbody model fits the data depends on the uncertainties in the system parameters, as well as the disk geometry,

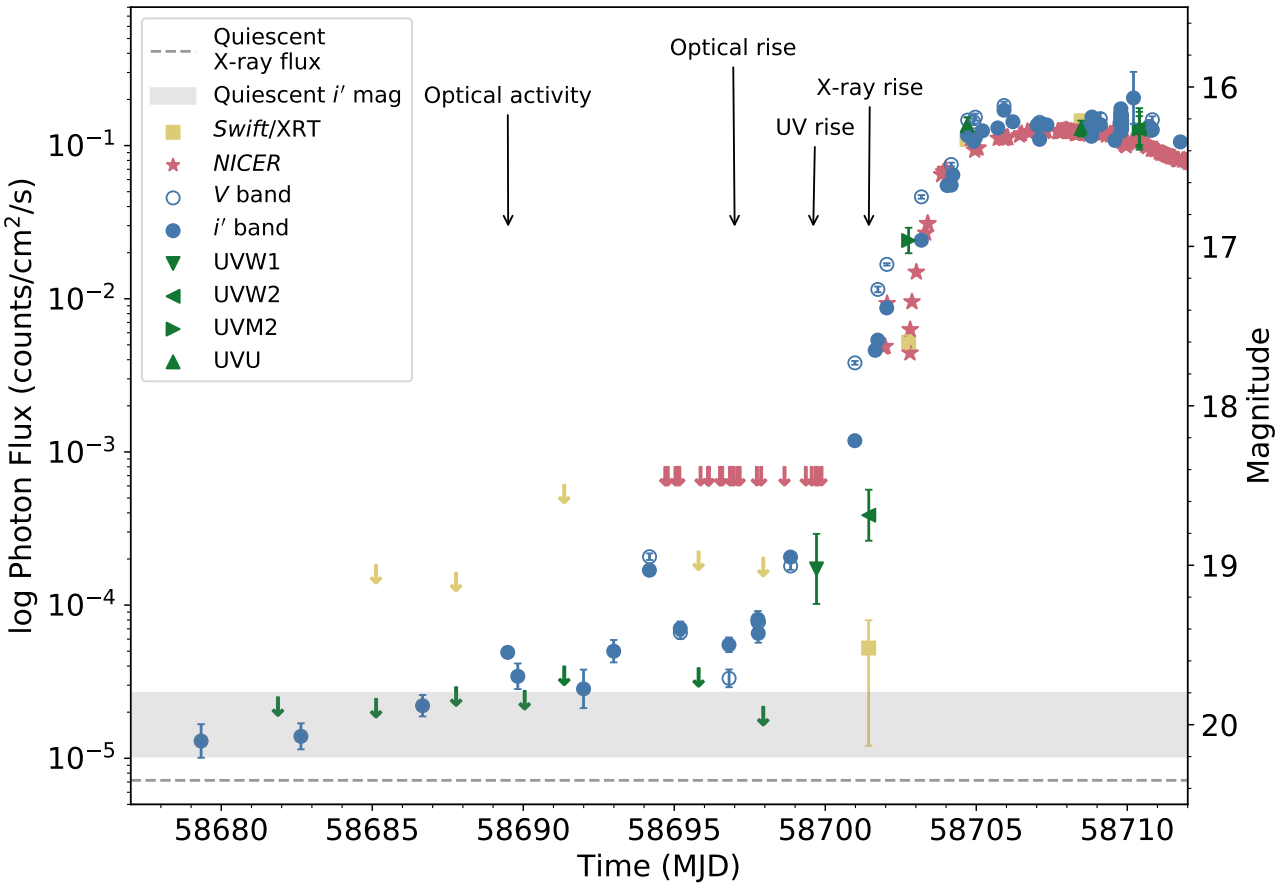

Figure 1. The multiwavelength light curve of the 2019 outburst rise in SAX J1808.4–3658. Optical V and i'-band observations (blue circles) were obtained with the 2-m Faulkes Telescope South (at Siding Spring, Australia), and the Las Cumbres Observatory(LCO) network of 1-m robotic telescopes. *Swift*/XRT 0.2–10 keV and *Swift*/UVOT UV observations are shown in yellow squares and green triangles respectively. NICER 0.2–10 keV observations are shown in red stars. '↓' symbols indicate UV and X-ray upper limits. Error bars and upper limits correspond to 1-σ. UV and optical observations are plotted on the RHS axis (Magnitude) and the *Swift* and NICER X-ray observations are plotted on the LHS axis, in log 0.2–10 keV counts/cm^2/s, where the effective area of the XRT and NICER were taken as 110 cm^2 and 1900 cm^2 respectively. The optical and UV magnitudes have been de-reddened.

so we do not fit the model to the data but use a normalisation parameter to approximately overlap the model with the data. This approach allows us to estimate the approximate disk temperature, and to infer the general trend in the temperature during the onset of outburst.

We observed the disk transitioning through the temperature at which hydrogen ionises in the 12 d of optical activity, before X-ray emission was observed. In Figure 4 the disk begins at a temperature of ≈10,000 K, 5 days after the first sign of increased optical activity on July 25, and decreases in temperature to ≈7,000 K on Aug 2, then spends approximately 2 d at a temperature of ≈ 8,000 − 9,500 K, and finally increases to a temperature of > 15,000 K, coincident with the first X-ray detection of the source on Aug 6. After Aug 6, the V-i' band colour begins to increase again, and our simple blackbody disk model breaks down as the optical spectrum now likely has contributions from the outer irradiated disk as well as a jet component (Baglio et al., submitted). Thus, after Aug 6 we cannot infer the disk temperature using our model, so it is unlikely that the accretion disk temperature began decreasing again, and more likely that the jet component of the optical emission is contributing to the V-i' colour, which our disk model does not include.

We note that we do not have exactly simultaneous V and i' magnitude measurements to infer the temperatures in Fig. 4 from the V-i' colour, which would cause larger uncertainties in temperature at the brighter magnitudes, or hotter temperatures. The fainter magnitude points earlier in the rise are less affected by this uncertainty, as 0.1 mag corresponds to < 1000 K at these lower fluxes. The error bars we plot are statistical only, and do not take into account systematic uncertainties in the V-i' colour. The colour-magnitude diagram of the whole outburst, and the model fit of the data, are presented in (Baglio et al., submitted).

The range of temperatures we inferred from the beginning of optical activity to the first X-ray detection corresponds to the range of ionisation temperatures of hydrogen, with hydrogen likely being completely neutral below 5,000 K, and completely ionised at 10,000 K (Lasota, Dubus & Kruk 2008). This observation is crucial in confirming the role of hydrogen ionisation in the DIM, and triggering outbursts in LMXBs.

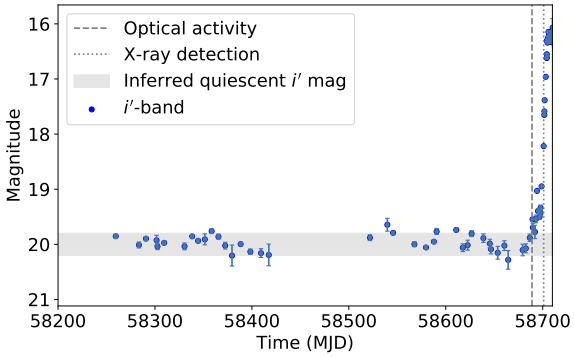

Figure 2. LCO observations of the optical i'-band light curve of SAX J1808.4–3658 from 500 d before the 2019 outburst commenced. The vertical dashed line indicates the first statistically significant increase in the optical magnitude (July 25), and the vertical dotted line indicates the time of the first X-ray detection with *Swift* (August 6). The horizontal grey bar indicates our inferred optical i'-band quiescent magnitude range, based on these observations. The magnitudes have been de-reddened.

3.3 Optical spectrum

The summed optical spectrum from 2019 August 6 (MJD 58701), shown in Figure 5, is consistent with an optically thick accretion disk viewed at low-intermediate inclination. The spectrum is similar to that taken by Cornelisse et al. (2009) during the 2008 outburst, with strong Hα, Hβ, and Hγ absorption lines, but with weak HeII emission and no Bowen complex emission visible. Central emission reversals are evident in the Hα and Hβ absorption lines, almost filling in the former. A strong HeII emission line was observed later in the outburst in additional spectra obtained with SALT (Russell et al., in preparation), and is present in the spectrum obtained by Cornelisse et al. (2009) during the 2008 outburst, but no Bowen complex emission was detected in any of the spectra obtained with SALT during this outburst.

The accretion disk in SAX J1808.4–3658 is likely composed of ≈50 % helium, inferred from properties of the type I X-ray bursts observed from the source (Goodwin et al. 2019a; Galloway & Cumming 2006; Johnston et al. 2018). The spectrum observed on Aug 6 coincides with an inferred accretion disk temperature of ≈10,000 K (Section 3.2), right at the temperature that helium in the disk would begin to be ionised. The fact that only weak HeII emission was observed in the spectrum, and much stronger HeII emission was observed later in the outburst implies that the accretion disk was not yet hot enough at this time to have ionised much of the helium in the disk, and later in the outburst more helium in the disk was ionised.

4 DISCUSSION

Our findings reveal a 10–15 d delay between the optical and X-ray activity at the onset of outburst in the accretion-powered millisecond pulsar SAX J1808.4–3658, as well as a 4 d optical to X-ray rise delay. This work presents the first observational measurement of the X-ray delay time in an LMXB using an X-ray instrument more sensitive than an all sky monitor, and provides important observational constraints for the disk instability model. Our first X-ray detection at ≈50 times the quiescent X-ray level confirms that X-ray activity

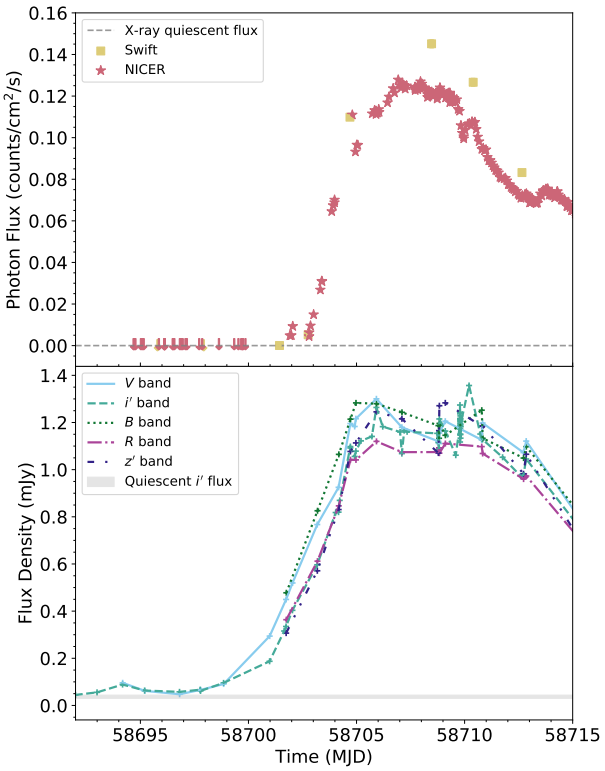

Figure 3. *Bottom:* The linear X-ray and optical light curves of the 2019 outburst rise of SAX J1808.4–3658. Optical V, i', B, R, and z-band observations were obtained with the 2-m Faulkes Telescope South (at Siding Spring, Australia), and the Las Cumbres Observatory (LCO) network of 1-m robotic telescopes. '+' symbols indicate time of observations. The optical magnitudes have been de-reddened. *Top: Swift*/XRT 0.2–10 keV and NICER 0.2–10 keV observations are shown in yellow squares and red stars. '↓' symbols indicate X-ray upper limits. Error bars and upper limits correspond to 1-σ. The *Swift* and NICER X-ray observations are plotted in 0.2–10 keV counts/cm^2/s, where the effective areas of the XRT and of NICER were taken as 110 cm^2 and 1900 cm^2 respectively. The optical observations indicate the V-band rose before the i'-band, and the fastest increase was seen in the B-band.

before this detection was either non-existent or very low level. The 12 d delay (possible range of 10–15 d) between the X-ray and optical activity we observed is indicative of the time between the initial beginnings of activity in the system, to the triggering of the outburst through a disk instability, to the onset of accretion onto the neutron star.

SAX J1808.4–3658 is a very well-studied source, and has precisely measured orbital constraints, listed in Section 1. These observational constraints imply the accretion disk in SAX J1808.4–3658 is small ($R < 3 \times 10^{10}$ cm), and the inner disk is likely truncated by the neutron star magnetic field (Papitto et al. 2009) at the neutron star magnetospheric radius (see e.g. Frank et al. 2002). These are important considerations to take into account when assessing the possibility of the outburst being explained by the DIM.

There was no radio detection coincident with the position of SAX J1808.4−3658 before the first X-ray detection on August 6, in an observation by MeerKAT on July 31 (Williams et al. 2019a), but there was a radio detection by MeerKAT at approximately the peak of the outburst, on August 10 (Williams et al. 2019b). Since radio

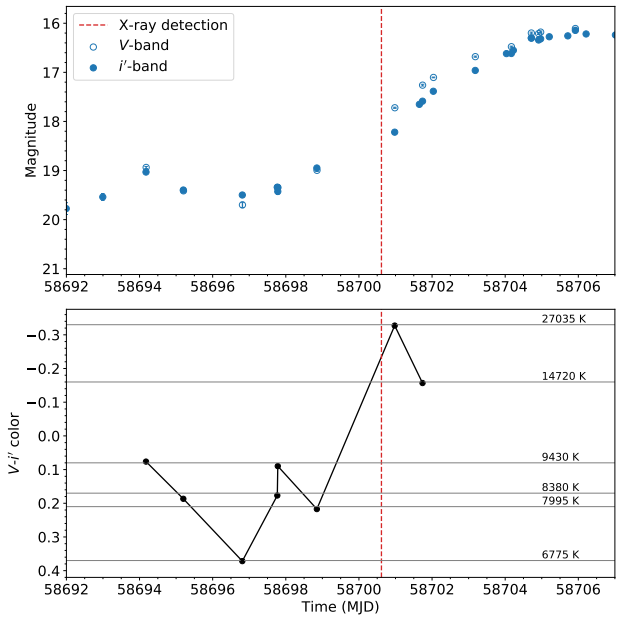

Figure 4. *Top:* Optical V- and i'-band observations of the 2019 outburst of SAX J1808.4–3658 obtained with the LCO. *Bottom:* The evolution of the V-i' colour during the rise to the 2019 outburst of SAX J1808.4–3658. The grey horizontal lines correspond to the temperature (K) inferred from our simple blackbody disk model. The vertical red line indicates the time of the first *Swift* X-ray detection. Statistical error bars are plotted for the V-i' colour, but are too small to see, and do not take into account systematic uncertainties such as orbital modulations.

emission is generally thought to come from a jet component of the system, the nondetection on July 31 indicates that there was not yet a jet present, which would be consistent with the disk not yet filling in the truncated inner edge to reach the neutron star. In addition, the first indication of a jet at optical wavelengths (i.e. when the jet power was relatively high) occurred after August 8 (Baglio et al., submitted).

The temperature of the accretion disk we inferred during the optical rise, of 7000 K increasing to $\gtrsim$ 20000 K at the time of the first X-ray detection, corresponds exactly to the ionisation temperature range of hydrogen. Furthermore, in the spectrum obtained on August 6 (Figure 5), the strong Balmer absorption lines present are a clear indication that hydrogen was ionised in the disk. These inferred temperatures and level of hydrogen ionisation thus support the prevalent theory of the disk instability model: that the initial instability that triggers an outburst is caused by ionisation of hydrogen in the accretion disk (e.g. Lasota 2001; Dubus et al. 2001).

4.1 The disk instability model

We now discuss whether the observations we present are consistent with the DIM theory, and if there is evidence for an outside-in or inside-out type outburst. Classically, there is a general understanding that there would be no X-ray delay observed for an inside-out type outburst, and there would be an X-ray delay for an outside-in type outburst. However, Menou et al. (1999) and Lasota (2001) are careful in asserting that an X-ray delay observed during an LMXB rise to outburst is not evidence of an outside-in outburst, as this delay is theoretically possible for an inside-out type outburst if the disk is truncated. In this scenario, ignition would occur at the truncated inner edge of the accretion disk, which is still far from the compact object, but technically is classified as an inside-out type outburst. Theoretically, inside-out outbursts are expected for LMXBs, primarily due to the slower rise times, larger disks, and the observed shape of the outburst light curves in these systems (Lasota 2001). However, due to a lack of comprehensive multiwavelength observations of the rise to outburst of LMXBs, there is no compelling evidence that they exhibit either outside-in or inside-out outbursts.

The most important determining parameters of the location of the maximum surface density in the accretion disk, and thus the type of outburst that will occur in an LMXB are the mass transfer rate to the disk, the size of the accretion disk, and if the disk is truncated. According to Lasota (2001), the mass transfer rate criterion for outside-in outbursts to occur is given by,

$$\dot{M}_{\rm tr} \gtrsim \dot{M}_{\rm A} = 2\times10^{15}\delta^{-1/2}\left(\frac{M_{\rm NS}}{M_\odot}\right)^{-0.85}\left(\frac{R}{10^{10}{\rm cm}}\right)^{2.65}\ {\rm g\,s^{-1}} \quad (1)$$

where typically $\delta \leq 2$.

Thus, for SAX J1808.4–3658, where the quiescent accretion rate has been inferred to be 5.7×10^{14} g s^{-1} (Heinke et al. 2009), the critical mass transfer rate for an outside-in outburst to occur is reached if the disk is smaller than $\approx 7\times10^9$ cm. However, this criterion was developed for a CV system, and while it is likely that this criterion applies equally well to a neutron star LMXB such as SAX J1808.4–3658, there may be some important differences. Including irradiation (or heating of the outer disk) lowers the critical mass transfer rate due to additional heating of the outer disk region, lowering the maximum surface density, shortening the distance between the maximum and minimum surface densities, and allowing an outside-in outburst to occur for a slightly larger disk for SAX J1808.4–3658 (Lasota 2001). A thermal instability is easier to be triggered close to the outer disk radius when irradiation is accounted for. Thus, the system parameters in SAX J1808.4–3658 appear to be quite similar to the critical mass transfer rate for an outside-in outburst to occur, and since it is not clear how much irradiation might affect these calculations, we cannot deduce if the system theoretically should exhibit inside-out or outside-in type outbursts from Equation 1 alone.

There are a few different observationally constrained rise times important to consider when understanding the occurrences in the disk that lead to this outburst. First, the optical timescale, from the initial optical brightening on July 25 (MJD 58689), to the clear beginning of the optical rise on August 1 (MJD 58696), to the peak of the optical light curve on August 10 (MJD 58705), indicates a maximum optical rise time of 16 days for the disk in SAX J1808.4–3658, but it is more likely the true optical rise time is shorter than this (closer to 10 d) and the low-level optical activity between July 25 and August 1 is due to precursor activity before the onset of the outburst. Next, the UV delay time, between the initial optical activity on July 25 to the first UV detection above the sensitivity of *Swift*/UVOT on August 4 (MJD 58699), of 10 d, as well as the optical to UV rise delay time of 2 d. Next, the X-ray rise time from the first X-ray detection on August 6 (MJD 58701) to the peak of the X-ray light curve on August 14 (MJD 58709), of 8 days. Finally, the X-ray delay, between the commencement of the optical rise and the X-ray rise of 4 d, and between the optical brightening and the X-ray brightening, of 12 days. We note that these inferred timescales are heavily dependent on the sensitivity of the instruments used, and

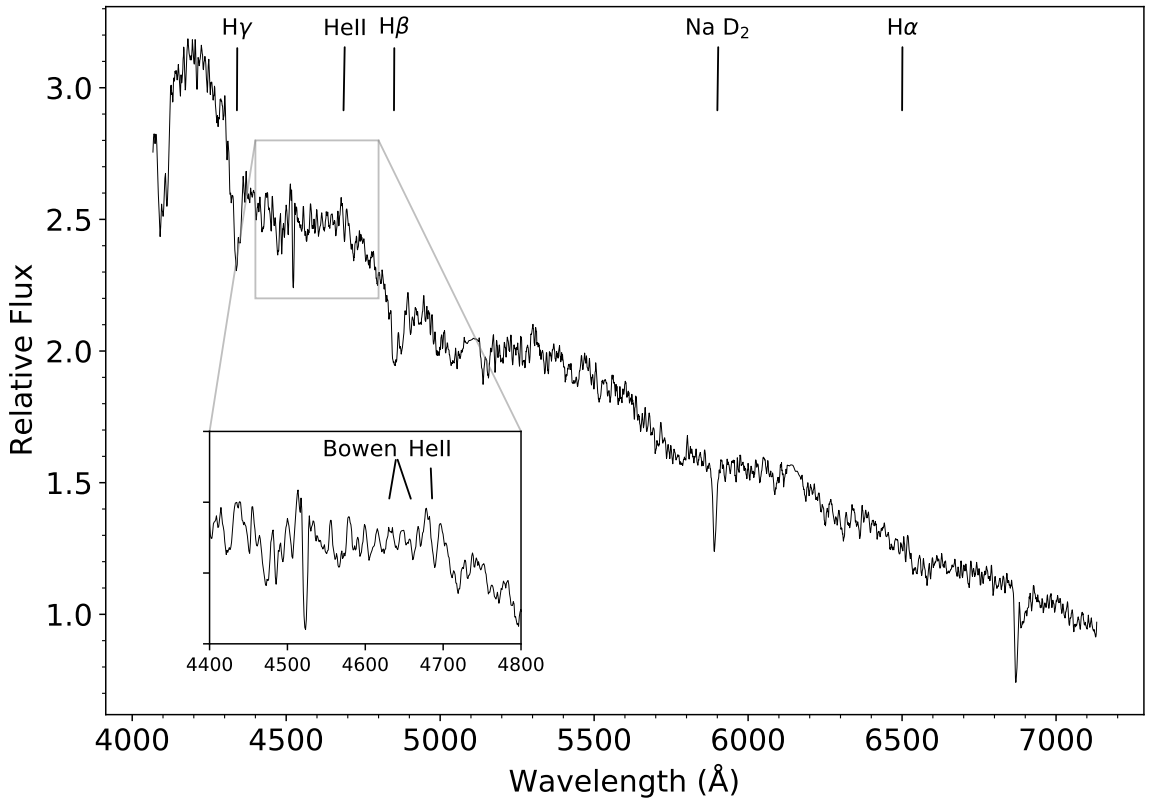

Figure 5. SALT summed (2400 s) optical spectrum of SAX J1808.4–3658 taken on 2019 August 6 (MJD 58701). There are clear Balmer absorption features and weak HeII emission present.

there is the possibility that there was low level activity in UV and X-ray before statistically significant detections were obtained.

4.2 The viscous timescale

According to Lasota (2001), the UV and X-ray flux will rise when the temperature has grown sufficiently high, when the heating front arrives at the inner disk. One may expect the inner disk to arrive close to the neutron star's surface in the viscous time, which is given by,

$$t_{\rm visc} = \frac{R\Delta R}{\nu} \tag{2}$$

where R is the inner disk radius (i.e. the truncation radius), ΔR is the typical scale of the density gradient, $\Delta R \approx \sqrt{HR}$, and ν is the viscosity, which is described by the α-prescription (Shakura & Sunyaev 1973),

$$\nu = \alpha c_{\rm s} H \tag{3}$$

where α is the artificial viscosity coefficient, c_s is the sound speed, and H is the scale height.

For SAX J1808.4–3658, the inner disk radius is less than the Roche lobe radius of 3.87×10^{10} cm, the neutron star mass is $\approx 1.4\,{\rm M}_{\odot}$, the neutron star radius is ≈ 11.2 km, and the accretion rate into the disk in quiescence is $\dot{M}_{tr} = 5.7 \times 10^{14}\,{\rm g\,s^{-1}}$ (Heinke et al. 2009). Using the Shakura-Sunyaev disk solution outlined in Frank et al. (2002) and assuming an inner disk radius of $5 \times 10^8 < R < 2 \times 10^{10}$ cm, in order for the viscous time of the disk to be ≈ 12 d, $0.0009 < \alpha < 0.1$. For this disk solution we find $H/R \approx 0.01$ and $c_{\rm s} \approx 20$ km/s. Alternatively, for a viscous time scale of ≈ 4 d, which is coincident with the delay between the first X-ray detection and the beginning of the optical rise we observed, we infer $0.0035 < \alpha < 0.9$ for the same disk size. Shakura & Sunyaev (1973) assert that $\alpha \leq 1$, Tetarenko et al. (2018) inferred that $\alpha \sim 0.2 - 1$ in models of LMXBs, and that the typical range for a hot disk is $\alpha \approx 0.1 - 1$. We find a reasonable range for α and the truncation radius of the disk if the viscous timescale is coincident with the 4 d day delay. If a 12 d day delay is assumed, we find a very limited range of alpha and disk truncation radii ($R \approx 1 \times 10^{10}$ and $\alpha \approx 0.1$). Thus this inferred artificial viscosity coefficient suggests alternative activity in the system during the 8 d of extended optical activity in the lead up to the outburst.

The viscous timescale has been inferred in a few black hole LMXBs, all with much longer orbital periods than SAX J1808.4–3658, from measurements of X-ray delays later in the outbursts. These include: LMC X–3, of 5–14 d (Torpin et al. 2017; Steiner et al. 2014; Brocksopp et al. 2001); GX 339–4, of 15–20 d (Homan

et al. 2005); 4U 1957+11, of 2–14 d (Russell et al. 2010); and Swift 1910.2–0546, of ≈ 6 d (Degenaar et al. 2014). Since these systems likely have much larger disks than in SAX J1808.4–3658, and the viscous time depends so heavily on disk radius (Eq. 3), it is unlikely that the viscous timescale for SAX J1808.4–3658 is as long as 12 d.

4.3 The optical precursor

We observed the optical magnitude fluctuating by ∼1 mag around July 29 (MJD 58693), before the onset of the clear optical rise of the outburst on August 1. Since it is unlikely that the viscous timescale in SAX J1808.4–3658 is as long as 12 d, the 8 d of increased optical activity we observed between July 25–August 1 is unlikely to be due to heating fronts propagating in the disk, and more likely can be attributed to other activity in the system in the leadup to outburst. This activity could include a number of different phenomena.

The first possibility is that there was enhanced mass transfer from the companion, which would help trigger the outburst. With no (or low-level) X-ray activity during this period, there is no evidence of increased mass transfer onto the neutron star, but this does not rule out increased mass transfer to the disk.

Another explanation is that the emission could have arose from instabilities due to geometric effects in the outer disc, involving spiral waves and/or the accretion stream impact point, interacting with the increasing density of the outer disk. This could lead to enhanced optical activity from these instabilities in the outer disk, and eventually leading to heating fronts propagating through the entire disk, and commencing the outburst.

Alternatively, it could have been due to a small unstable branch in the thermal stability curve as the density was close to, but not quite at, the critical density at which the outburst could begin in full (e.g. Menou et al. 2000, Fig. 7). However, this kind of unstable activity would occur at lower temperatures than the ionisation temperature of hydrogen, and we observed the disk to be above 6,000 K during this period (Fig. 4).

An additional possible scenario is that the level of irradiation of the companion was fluctuating caused by changes in the pulsar radiation pressure. It has been proposed that during quiescence SAX J1808.4–3658 switches on as a radio pulsar (e.g. Burderi et al. 2003), and the optical emission during quiescence is due to reprocessed emission from the companion being heated by the pulsar wind. However, there is no physical motivation for the pulsar wind to fluctuate on this kind of timescale. Nevertheless, SAX J1808.4–3658 has been proposed to be a "hidden" black widow system (di Salvo et al. 2008), in which it is possible that the accretion flow from the companion is swept away by the pulsar radiation pressure, ejecting a significant amount of mass at the inner Lagrangian point during quiescence. This shock emission would then irradiate the companion star, which would reprocess the shock emission photons and emit them in the optical band. Since the shock properties, and thus level of irradiation of the companion star, depend on the pulsar wind and the mass flow, fluctuations could be observed. Burderi et al. (2003) inferred the temperature of the companion star to be approximately 5500 K, which is similar to the temperature of the optical emission we measured of 6,000–7,000 K, so it is not impossible that the optical fluctuations were caused by fluctuations in the level of irradiation of the companion star. This scenario could lead to fluctuations in the inner disk radius, which would help to trigger the outburst.

We thus conclude that the most likely cause of the 8 d optical precursor is either mass transfer fluctuations from the companion, instabilities due to geometric effects in the outer accretion disk, or due to effects of the pulsar radiation pressure.

4.4 The outburst rise

We propose that, once the thermal instabilities in the accretion disk had caused heating fronts to begin propagating, since the thin disk in this system is likely truncated during quiescence at the neutron star magnetospheric radius, the increased pressure due to the rising accretion rate in the disk pushed the magnetospheric radius inwards, and the disk extended inwards towards the neutron star. The time taken to fill in the inner depleted region of the disk is the viscous timescale, of ≈ 4 d.

We conclude that based on the observations we obtained, it took approximately 4 d from the initial instability in the disk for the heating fronts to propagate inwards, through the truncated disk region, and the mass accretion rate to begin rising at the inner disk. It then took a further 8 d for the accretion rate at the inner disk to rise to its maximum rate. This scenario is similar to the models of GRO J1655–40 of Hameury et al. (1997), in which the heating front arrives at the inner disk quickly, and propagates through the cavity of the truncated disk on the viscous time of 6 d.

Without detailed DIM models applicable to this system, which are outside the scope of this work, we find it difficult to conclusively deduce the type of outburst observed during the 2019 outburst. Detailed models of a system like SAX J1808.4–3658 are necessary in order to fully understand if these observations can be reconciled with the DIM, or if there is additional physics that we are missing that needs to be accounted for.

5 CONCLUSIONS

We have presented the first measurement of the X-ray delay in an LMXB using an X-ray instrument more sensitive than an all sky monitor that we are aware of, and the earliest comprehensive multiwavelength observations of the rise to outburst of an accreting neutron star system. The inferred optical disk temperature during the rise to outburst from the V-i' color supports the DIM theory that LMXB outbursts are initiated by hydrogen ionisation in the disk. We found a delay of 12 d between the first sign of increased optical activity in the source, and the first X-ray detection. We observed the optical rise to occur first, then the UV rise 2 d later, then finally the X-ray rise a further 2 d later. We interpret the 8 d of optical activity prior to the commencement of the outburst to be due to either increased mass transfer from the companion star, geometric effects in the outer accretion disk, or fluctuations in the pulsar radiation pressure, causing changes in the irradiation of the companion star, and perhaps the inner disk radius. We deduce that the viscous timescale of the disk in SAX J1808.4–3658 is approximately 4 d, consistent with the optical to X-ray rise delay we observed. This is coincident with the time taken for the truncated disk to fill in to the surface of the neutron star, releasing UV and X-ray emission. Detailed modelling of the disk in SAX J1808.4–3658 is required in order to conclusively determine if these observations can be reconciled with the DIM, and if this source exhibits inside-out or outside-in type outbursts.

ACKNOWLEDGEMENTS

We thank the referee, Guillaume Dubus, for insightful and constructive comments that improved the manuscript and for contributing

interesting discussion points. AJG acknowledges support by an Australian Government Research Training Program scholarship. The authors thank Daniel Price and Alexander Heger for helpful discussions, and the Swift team for approving the monitoring observations via a ToO proposal prior to the start of the outburst. Some of the observations reported in this paper were obtained with the Southern African Large Telescope (SALT), as part of the Large Science Programme on transients 2018-2-LSP-001 (PI: Buckley). Polish participation in SALT is funded by grant no. MNiSW DIR/WK/2016/07. DAHB thanks the National Research Foundation (NRF) of South Africa for research funding. DMR and DMB acknowledge the support of the NYU Abu Dhabi Research Enhancement Fund under grant RE124. DdM acknowledges funding from ASI-INAF n.2017-14-H.0 and from INAF 70/2016 and 43/2018. COH is supported by NSERC Discovery Grant RGPIN-2016-04602. The Faulkes Telescope Project is an education partner of Las Cumbres Observatory (LCO). The Faulkes Telescopes are maintained and operated by LCO.

DATA AVAILABILITY

The *Swift*/XRT and UVOT observations are publicly available via the *Swift* data center: `https://swift.gsfc.nasa.gov/sdc/`. The NICER observations are publicly available via the NICER data archive: `https://heasarc.gsfc.nasa.gov/docs/nicer/nicer_archive.html`. All optical data are available on request.

REFERENCES

Arnaud K. A., 1996, in Jacoby G. H., Barnes J., eds, Astronomical Society of the Pacific Conference Series Vol. 101, ASP Conf. Ser.. p. 17
Bernardini F., Russell D. M., Shaw A. W., Lewis F., Charles P. A., Koljonen K. I. I., Lasota J. P., Casares J., 2016, ApJ, 818, L5
Bramich D. M., Freudling W., 2012, MNRAS, 424, 1584
Brocksopp C., Groot P. J., Wilms J., 2001, MNRAS, 328, 139
Buckley D. A. H., Swart G. P., Meiring J. G., 2006, in Society of Photo-Optical Instrumentation Engineers (SPIE) Conference Series. p. 62670Z, doi:10.1117/12.673750
Buckley D. A. H., et al., 2017, Monthly Notices of the Royal Astronomical Society: Letters, 474, L71
Bult P., Chakrabarty D., Arzoumanian Z., Gendreau K. C., Guillot S., Malacaria C., Ray P. S., Strohmayer T. E., 2019, arXiv e-prints, p. arXiv:1910.03062
Burderi L., Di Salvo T., D'Antona F., Robba N. R., Testa V., 2003, A&A, 404, L43
Burgh E. B., Nordsieck K. H., Kobulnicky H. A., Williams T. B., O'Donoghue D., Smith M. P., Percival J. W., 2003, in Iye M., Moorwood A. F. M., eds, Proc. SPIEVol. 4841, Instrument Design and Performance for Optical/Infrared Ground-based Telescopes. pp 1463–1471, doi:10.1117/12.460312
Burrows D. N., et al., 2005, Space Sci. Rev., 120, 165
Cannizzo J. K., Wheeler J. C., Ghosh P., 1985, Accretion Instability Models for Dwarf Novae and X-Ray Transients. D. Reidel Publishing Co. (Astrophysics and Space Science Library), p. 307, doi:10.1007/978-94-009-5319-2_36
Cardelli J. A., Clayton G. C., Mathis J. S., 1989, ApJ, 345, 245
Chakrabarty D., Morgan E. H., 1998, Nature, 394, 346
Chakrabarty D., Morgan E. H., Muno M. P., Galloway D. K., Wijnands R., van der Klis M., Markwardt C. B., 2003, Nature, 424, 42
Cornelisse R., et al., 2009, A&A, 495, L1
Crawford S. M., et al., 2010, in Observatory Operations: Strategies, Processes, and Systems III. p. 773725, doi:10.1117/12.857000
Degenaar N., et al., 2014, ApJ, 784, 122
Del Santo M., et al., 2015, The Astronomer's Telegram, 7380, 1
Deloye C. J., Heinke C. O., Taam R. E., Jonker P. G., 2008, MNRAS, 391, 1619
Di Salvo T., Sanna A., Burderi L., Papitto A., Iaria R., Gambino A. F., Riggio A., 2019, MNRAS, 483, 767
Dubus G., Hameury J. M., Lasota J. P., 2001, A&A, 373, 251
Elebert P., et al., 2009, MNRAS, 395, 884
Evans P. A., et al., 2009, MNRAS, 397, 1177
Foight D. R., Güver T., Özel F., Slane P. O., 2016, ApJ, 826, 66
Frank J., King A. R., Lasota J. P., 1987, A&A, 178, 137
Frank J., King A., Raine D. J., 2002, Accretion Power in Astrophysics: Third Edition. Cambridge University Press
Galloway D. K., 2008, in 40 Years of Pulsars: Millisecond Pulsars, Magnetars and More. AIP; arXiv:0711.4420, Melville, NY
Galloway D. K., Cumming A., 2006, ApJ, 652, 559
Gendreau K. C., et al., 2016, in Proc. SPIE. p. 99051H, doi:10.1117/12.2231304
Goodwin A. J., Galloway D. K., Heger A., Cumming A., Johnston Z., 2019a, MNRAS, 490, 2228
Goodwin A. J., Russell D. M., Galloway D. K., in't Zand J. J. M., Heinke C., Lewis F., Baglio M. C., 2019b, The Astronomer's Telegram, 12993, 1
Hameury J.-M., 2019, arXiv e-prints, p. arXiv:1910.01852
Hameury J. M., Lasota J. P., McClintock J. E., Narayan R., 1997, ApJ, 489, 234
Hameury J.-M., Menou K., Dubus G., Lasota J.-P., Hure J.-M., 1998, MNRAS, 298, 1048
Heinke C. O., Jonker P. G., Wijnands R., Deloye C. J., Taam R. E., 2009, ApJ, 691, 1035
Homan J., Buxton M., Markoff S., Bailyn C. D., Nespoli E., Belloni T., 2005, ApJ, 624, 295
Hōshi R., 1979, Progress of Theoretical Physics, 61, 1307
Jain R. K., Bailyn C. D., Orosz J. A., McClintock J. E., Remillard R. A., 2001, ApJ, 554, L181
Johnston Z., Heger A., Galloway D. K., 2018, MNRAS, 477, 2112
Kuulkers E., Hollander A., Oosterbroek T., van Paradijs J., 1991, A&A, 242, 401
Lasota J.-P., 2001, New Astron. Rev., 45, 449
Lasota J. P., Dubus G., Kruk K., 2008, A&A, 486, 523
Lewin W. H. G., van der Klis M., 2006, Compact Stellar X-ray Sources. Cambridge Astrophysics Series Vol. 39, Cambridge University Press
Lewis F., Roche P., Russell D. M., Fender R. P., 2008, in Bandyopadhyay R. M., Wachter S., Gelino D., Gelino C. R., eds, American Institute of Physics Conference Series Vol. 1010, A Population Explosion: The Nature & Evolution of X-ray Binaries in Diverse Environments. pp 204–206 (`arXiv:0712.2751`), doi:10.1063/1.2945042
Maitra D., Bailyn C. D., 2008, ApJ, 688, 537
Markwardt C. B., Swank J. H., 2008, The Astronomer's Telegram, 1728, 1
Markwardt C. B., Miller J. M., Wijnands R., 2002, The Astronomer's Telegram, 110, 1
Markwardt C. B., et al., 2011a, The Astronomer's Telegram, 3733, 1
Markwardt C. B., et al., 2011b, The Astronomer's Telegram, 3733, 1
Mathis J. S., 1990, ARA&A, 28, 37
Menou K., Hameury J.-M., Stehle R., 1999, MNRAS, 305, 79
Menou K., Hameury J.-M., Lasota J.-P., Narayan R., 2000, MNRAS, 314, 498
Orosz J. A., Remillard R. A., Bailyn C. D., McClintock J. E., 1997, ApJ, 478, L83
Osaki Y., 1974, PASJ, 26, 429
Papitto A., Di Salvo T., D'Aì A., Iaria R., Burderi L., Riggio A., Menna M. T., Robba N. R., 2009, A&A, 493, L39
Pirbhoy S. F., Baglio M. C., Russell D. M., Bramich D. M., Saikia P., Yazeedi A. A., Lewis F., 2020, The Astronomer's Telegram, 13451, 1
Roming P. W. A., et al., 2005, Space Sci. Rev., 120, 95
Russell D. M., Fender R. P., Jonker P. G., 2007, MNRAS, 379, 1108
Russell D. M., Lewis F., Roche P., Clark J. S., Breedt E., Fender R. P., 2010, MNRAS, 402, 2671

Russell D. M., Maitra D., Dunn R. J. H., Fender R. P., 2011, MNRAS, 416, 2311
Russell D. M., et al., 2019a, Astronomische Nachrichten, 340, 278
Russell D. M., Goodwin A. J., Galloway D. K., in't Zand J. J. M., Lewis F., Baglio M. C., 2019b, The Astronomer's Telegram, 12964, 1
Shahbaz T., Bandyopadhyay R. M., Charles P. A., Wagner R. M., Muhli P., Hakala P., Casares J., Greenhill J., 1998, MNRAS, 300, 1035
Shakura N. I., Sunyaev R. A., 1973, A&A, 500, 33
Smak J., 1971, Acta Astron., 21, 15
Smak J., 1984, Acta Astron., 34, 161
Steiner J. F., McClintock J. E., Orosz J. A., Buxton M. M., Bailyn C. D., Remillard R. A., Kara E., 2014, ApJ, 783, 101
Stetson P. B., 1990, PASP, 102, 932
Tetarenko B. E., Lasota J. P., Heinke C. O., Dubus G., Sivakoff G. R., 2018, Nature, 554, 69
Tonry J. L., et al., 2018, ApJ, 867, 105
Torpin T. J., Boyd P. T., Smale A. P., Valencic L. A., 2017, ApJ, 849, 32
Tucker M. A., et al., 2018, ApJ, 867, L9
Wang Z., Breton R. P., Heinke C. O., Deloye C. J., Zhong J., 2013, ApJ, 765, 151
White N. E., Mason K. O., 1985, Space Sci. Rev., 40, 167
Wijnands R., van der Klis M., 1998, Nature, 394, 344
Wijnands R., Méndez M., Markwardt C., van der Klis M., Chakrabarty D., Morgan E., 2001, ApJ, 560, 892
Williams D., Motta S., Fender R., Woudt P., Miller-Jones J., 2019a, The Astronomer's Telegram, 12982, 1
Williams D., Motta S., Fender R., Woudt P., Miller-Jones J., 2019b, The Astronomer's Telegram, 13026, 1
Wren J., et al., 2001, ApJ, 557, L97
Zurita C., et al., 2006, ApJ, 644, 432
di Salvo T., Burderi L., Riggio A., Papitto A., Menna M. T., 2008, MNRAS, 389, 1851
in 't Zand J. J. M., Heise J., Muller J. M., Bazzano A., Cocchi M., Natalucci L., Ubertini P., 1998, A&A, 331, L25
in't Zand J. J. M., et al., 2001, A&A, 372, 916
in't Zand J. J. M., et al., 2013, A&A, 553, A83
van Paradijs J., 1996, ApJ, 464, L139
van Paradijs J., Verbunt F., 1984, in Woosley S. E., ed., American Institute of Physics Conference Series Vol. 115, American Institute of Physics Conference Series. pp 49–62, doi:10.1063/1.34556

This paper has been typeset from a TEX/LATEX file prepared by the author.

4.2 XMMU J181227.8–181234: A NEW ULTRACOMPACT X-RAY BINARY CANDIDATE

Ultracompact X-ray binaries are a rare type of accreting neutron star system in which the neutron star is in a close orbit with a white dwarf. In the second study in this chapter, we present observations of X-ray bursts we discovered in archival *RXTE* data of the accreting neutron star XMMU J181227.8–181234. Through the use of the X-ray burst energy-composition relation we presented in Chapter 3, we are able to infer that the accreted fuel in this system is probably pure helium, indicating that the companion star is most likely a white dwarf.

Published in:
A. J. Goodwin et al. (July 2019b). 'XMMU J181227.8-181234: a new ultracompact X-ray binary candidate'. *MNRAS* 486.3, pp. 4149–4157. DOI: 10.1093/mnras/stz1094. arXiv: 1904.10970 [astro-ph.HE]

MNRAS **000**, 1–9 (2019) Preprint 6 October 2020 Compiled using MNRAS LATEX style file v3.0

XMMU J181227.8–181234: a new ultracompact X-ray binary candidate

A. J. Goodwin,[1,2]★ D. K. Galloway,[1,2] J. J. M. in 't Zand,[3] E. Kuulkers,[4] A. Bilous[5] and L. Keek[6]

[1] *School of Physics and Astronomy, Monash University, Clayton, Victoria, Austalia, 3800*
[2] *also Monash Centre for Astrophysics*
[3] *SRON Netherlands Institute for Space Research, Sorbonnelaan 2, 3584 CA Utrecht, The Netherlands*
[4] *ESA/ESTEC, Keplerlaan 1, 2201, AZ Noordwijk, The Netherlands*
[5] *Anton Pannekoek Institute for Astronomy, University of Amsterdam, Science Park 904, 1098 XH Amsterdam, The Netherlands*
[6] *Department of Astronomy, University of Maryland, College Park, MD 20742, USA*

Accepted 2019 April 15. Received 2019 April 13; in original form 2018 December 20

ABSTRACT

We report the discovery of Type I (thermonuclear) X-ray bursts from the transient source XMMU J181227.8–181234 = XTE J1812–182. We found 7 X-ray bursts in *Rossi X-ray Timing Explorer* observations during the 2008 outburst, confirming the source as a neutron star low mass X-ray binary. Based on the measured burst fluence and the average recurrence time of $1.4^{+0.9}_{-0.5}$ hr, we deduce that the source is accreting almost pure helium ($X \leq 0.1$) fuel. Two bursts occurred just 18 minutes apart; the first short waiting time bursts observed in a source accreting hydrogen-poor fuel. Taking into consideration the effects on the burst and persistent flux due to the inferred system inclination of $30 \pm 10°$, we estimate the distance to be 14 ± 2 kpc, where we report the statistical uncertainty but note that there could be up to 20% variation in the distance due to systematic effects discussed in the paper. The corresponding maximum accretion rate is 0.30 ± 0.05 times the Eddington limit. Based on the low hydrogen content of the accreted fuel and the short average recurrence time, we classify the source as a transient ultracompact low-mass X-ray binary.

Key words: XTE J1812–182 – XMMU J181227.8–181234 – Stars: neutron – X-rays: binaries – X-rays: bursts

1 INTRODUCTION

Low mass X-ray binaries are neutron stars or black holes accreting from a companion star in a close binary orbit (e.g. White et al. 1995). As hydrogen/helium accretes onto a neutron star (NS), the hydrogen may burn steadily via the (hot) CNO cycle. If the accreting material condenses and heats enough, reaching a high enough pressure to cause a thermonuclear runaway, a Type I X-ray burst is produced (see Lewin et al. 1993; Galloway & Keek 2017, for comprehensive reviews). There are two types of emission that can be observed: the usually fainter, persistent emission that is produced by the accretion process onto the NS, and the short, bright flares that are X-ray bursts.

Observations of Type I X-ray bursts can constrain the composition of fuel via the nuclear energy generation of the bursts, the recurrence time of the bursts and the accretion rate at which the material is piling onto the NS. The distance and inclination of the source can be constrained if photospheric radius expansion is observed (e.g Galloway et al. 2008). The ratio of gravitational energy to nuclear burning energy is higher for sources that burn more helium during a burst, as helium burns via the triple alpha process, producing less energy per nucleon than hydrogen, which burns via the hot CNO cycle and *rp* process (Wallace & Woosley 1981). Helium-fueled bursts are also observed to have faster rise times than hydrogen bursts (e.g. Galloway et al. 2008). The composition of the accreted fuel gives insight into the burning processes that are occurring in the system as well as the evolutionary history of the binary system. For example, a low mass binary with a companion star that donates almost pure helium to the NS must be significantly evolved, as a young, low mass star does not accumulate helium in its core on short timescales.

XMMU J181227.8–181234 = XTE J1812–182 was first discovered on March 20, 2003 by *XMM-Newton* when it went into outburst, as reported by Cackett et al. (2006). Initially it was only detected with XMM, and not with the *Rossi X-ray Timing Explorer (RXTE) All Sky Monitor* (ASM). However, upon reprocessing of the *RXTE* data, it was detected. No pulsations or X-ray bursts were originally detected. Cackett et al. (2006) found a very high absorption along the line of sight to the source ($N_{\rm H}$ of $12.8 \pm 0.3 \times 10^{22}$ cm^{-2}).

★ E-mail: adelle.goodwin@monash.edu

They could not conclusively identify if the source was a high mass X-ray binary characteristic of the color and absorption of the source, or low mass X-ray binary characteristic of the steep power law index that fit its spectrum.

On 2008 August 21 *RXTE* detected XMMU J181227.8–181234 in outburst again, in proportional counter array (PCA) scans of the Galactic ridge region (Markwardt et al. 2008). Twenty-six follow-up observations were performed with the PCA between MJD 54699 and 54758 (August 21 and October 19, 2008).

In this paper, we report on the discovery and analysis of bursts of XMMU J181227.8–181234 in these 2008 follow-up observations. An initial report was given by in 't Zand et al. (2017). Throughout this paper we report the 1-σ confidence intervals when uncertainties are presented, unless otherwise noted. In Section 2 we describe the data extraction and telescope observations; in Section 3 we analyse the burst and persistent emission and deduce the source properties, providing a full treatment of the anisotropy factors and thus inclination of the accretion disk. Finally, in Section 4 we conclude by classifying the source as a transient ultracompact low mass X-ray binary.

2 DATA REDUCTION

We analysed archival *RXTE* observations of XMMU 181227.8–181234 from its 2008 outburst (Cackett et al. 2006; Markwardt et al. 2008; Torres et al. 2008). We used archival *RXTE* ASM and Proportional Counter Array (PCA) data available via the Multi-Instrument Burst Archive (MINBAR[1]) and in the publicly available online *RXTE* archive. The PCA (Jahoda et al. 2006) consists of five proportional counter units (PCUs), each with approximately 1600 cm^2 of photon-sensitive area, and a bandpass of 2–60 keV at a spectral resolution of about 20% full width at half maximum (FWHM). The PCUs are co-aligned with a collimator delimiting the field of view to 1° (FWHM).

There were a total of 26 dedicated PCA observations between MJD 54699 and 54758, with a total exposure time of 45 ks that the source is visible. There were a further 49 PCA bulge scan observations between MJD 54420 and 55890 during which the source was in quiescence. There were 4043 archival ASM measurements covering the 2–10 keV energy band between MJD 50137 and 55825. For the persistent flux observations in Section 3.2 we also used *Swift* Burst Alert Telescope (BAT) daily average light curve data from the online publicly available archive (Krimm et al. 2008). There were 4049 daily BAT observations between MJD 53415 and 58015 in the 15–50 keV energy band. Finally, we used *BeppoSAX* Wide Field Camera (WFC; Jager et al. 1997) data from MINBAR in the 2–28 keV energy band. There is 4.5 Msec of WFC data between MJD 50310 and 52380 (1996–2002).

2.1 Position and History

Markwardt et al. (2008) reported the *RXTE* detection of a transient source in PCA scans of the Galactic ridge region in an observation on 2008 August 21. They determined the position of this source in a follow up scanning observation to be (RA,Dec) = 273.117, -18.26 (J2000) with an error radius of 2.1 arcmin (95% confidence), making it likely to be renewed activity of XMMU 181227.8–181234. This position translates to Galactic coordinates $(l^{\rm II}, b^{\rm II}) = (12.^{\circ}3577, +0.^{\circ}0337)$. The bursting transient source XTE J1810-189 is 0.996 degrees away from this location (Krimm et al. 2008), just within the PCA field of view. However, the last significant detection of XTE J1810-189 with the PCA during the Galactic bulge scans was on 2008 June 10, when it concluded its most recent outburst (Weng et al. 2015). Since no activity of XTE J1810-189 was detected for the three months following, up to the time of the bursts we detected, we can confidently exclude this source as the source of the detected photons and attribute them to XMMU J181227.8–181234 = XTE J1812–182.

Cackett et al. (2006) noticed that XMMU J181227.8–181234 lies ~40″ from the 95% confidence-level 2.′1 by 1.′8 error box of the source 1H1812–182, which was detected in 1977 during the Large Area Sky Survey Experiment with the HEAO-1 Satellite (Wood et al. 1984). They concluded that although the centroid position of 1H1812–182 is ~0.7° from that of XMMU J181227.8–181234, the large extended error box makes it possible that the HEAO 1 source is a detection of XMMU J181227.8–181234 during a previous outburst. Wood et al. (1984) reported that 1H1812–182 was detected with a flux of 0.1470 ± 0.0025 counts cm^{-2} s^{-1} in the 0.5–25 keV band, corresponding to an unabsorbed flux of approximately 9.7 × 10^{-10} ergs cm^{-2} s^{-1} and absorbed flux of approximately 4.0 × 10^{-10} ergs cm^{-2} s^{-1} in the 2–25 keV range, assuming a power law persistent spectrum with parameters in Table 1. We measured a range of (0.079–1.551) × 10^{-9} ergs cm^{-2} s^{-1} in the 2–25 keV band with the *RXTE* PCA telescope (see below), which means the flux of 1H1812–182 is within the ranges observed for XMMU J181227.8–181234. Interestingly, Fleischman (1985) reported the observation of a single X-ray burst in August 1977 from either GX 13+1 or 1H1812-182, with the Horizontal Tube Detector aboard SAS-3. The detector had a 3.4° diameter so the author could not discern if the X-ray burst came from GX 13+1 or 1H1812-182. Matsuba et al. (1995) reported the observations of bright bursts from GX 13+1, with similar characteristics to the burst observed by Fleischman (1985), making it plausible this X-ray burst came from GX 13+1. However, there is a chance this burst came from 1H1812-182 = XMMU J181227.8–181234, or, in the case they are not the same source, this X-ray burst could even have come from XMMU J181227.8–181234, before it was a known source.

3 ANALYSIS AND RESULTS

3.1 Light Curve and Persistent Spectrum

When XMMU J181227.8–181234 was first detected in outburst by *RXTE* on 2008-08-21 (MJD 54699) (Markwardt et al. 2008), the flux rose over 24 days to reach a peak on 54723, before dropping and returning to quiescent levels on 2008-10-19 (MJD 54758). The outburst lasted a total of approximately 60 days, similar to the 2003 outburst that lasted 60-100 days (Cackett et al. 2006). The persistent flux observations for both the outbursts are plotted in Figure 1. The conversion factors from count s^{-1} to Crab for each telescope were used as follows: for ASM data 1 Crab = 75 count s^{-1} and for PCA data 1 Crab = 2000 count s^{-1} PCU^{-1}. The reader may note that there is some uncertainty associated with these conversion factors due to the variable nature of the Crab Nebula (variations of up to 7%; e.g. Wilson-Hodge et al. 2011) and different telescope calibrations. The source was not detected by IBIS/ISGRI observations from the *INTEGRAL* Galactic bulge monitoring program (Kuulkers et al. 2007), with a typical 3σ upper limit of 6-10 mCrab in 18-40 keV for each one of 69 3.5 hr observations during the outburst.

[1] https://burst.sci.monash.edu/minbar/

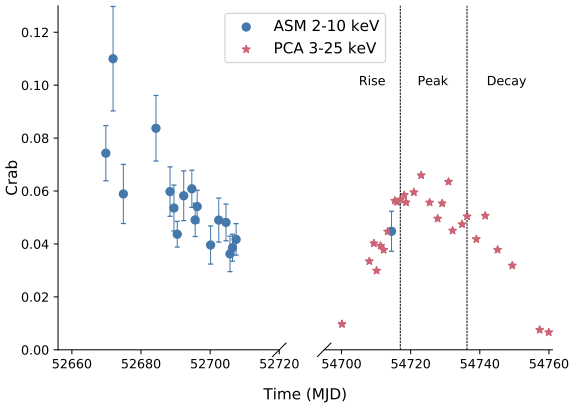

Figure 1. Persistent flux observations of XMMU J181227.8–181234 for the 2003 and 2008 outbursts from *RXTE*. ASM is all sky monitor dwell-by-dwell sum band intensity (2-10 keV) with a 5σ cut applied, and PCA is the proportional counter array mean flux (3-25 keV). Observations have been normalised to the Crab flux for the relevant instruments, assuming a Crab like spectrum. The rise, peak, and decay of the outburst as used in Figure 2 are indicated.

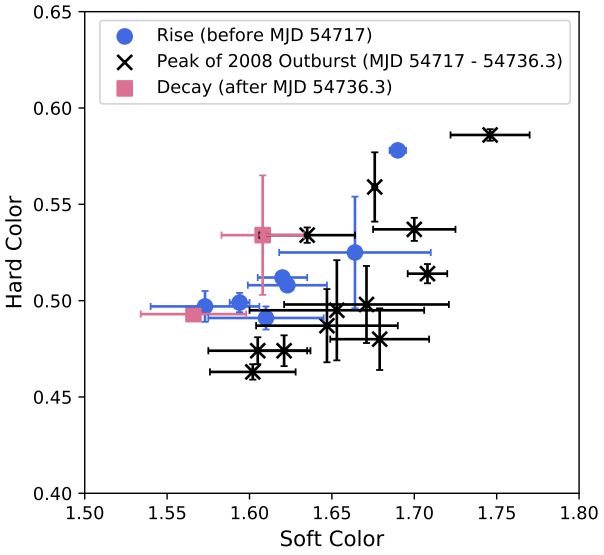

Figure 2. Evolution of the hard and soft colours of the source for the *RXTE* PCA persistent flux observations. Observations begin at 54420.10115 and end at 55890.14174 so do not include the 2003 outburst of the source. Only detections are plotted, which are during the 2008 outburst. There is no broad evolution of the colour during the different phases of the outburst for this source.

We measured a peak persistent intensity of 97±3 c s^{-1} PCU^{-1} in the 2-25 keV energy band from the PCA, which translates to approximately 65 mCrab (or 1.3×10^{-9} erg s^{-1}cm^{-2} for a Crab-like spectrum). For this outburst we adopted a bolometric correction ($c_{\rm bol}$) of 2.522, calculated based on the assumed $N_{\rm H}$ of 12.8×10^{22} cm^{-2} (Cackett et al. 2006), and a Comptonisation model fit to the spectrum, outlined below. Spectral variations outside of the PCA band might contribute errors of up to ≈ 40% (e.g. Thompson et al. 2008) to the bolometric correction, but these cannot be measured and are not taken into account.

We chose 3 observations near the peak of the outburst (Obs IDs 93044-11-04-01, 93044-11-04-02, 93044-11-05-00) to analyse for a high signal-to-noise persistent spectrum. We fit the three spectra simultaneously with two choices for the continuum model, first a blackbody and powerlaw, and second a Comptonisation model (`compTT` in XSPEC; Titarchuk 1994). Only the normalisation was allowed to vary between the three observations, to account for variations in the accretion rate between the different epochs.

In both cases we included a multiplicative component to model the effects of neutral absorption along the line of sight using the absorption model from Morrison & McCammon (1983) (model 'tbabs' in XSPEC). Hydrogen column density was fixed at $N_{\rm H} = 12.8 \times 10^{22}$ cm^{-2} (Cackett et al. 2006); and a Gaussian component was included to account for an excess around 6.4 keV, likely arising from Fe Kα emission local to the binary or across the FOV. We also adopted a systematic error of 0.5% channel to channel as recommended by the PCA instrument team (Shaposhnikov et al. 2012).

The persistent spectrum was equally well fit with the Comptonisation model as a blackbody plus power-law model. The persistent spectrum was soft, with a plasma temperature of kT = 2.73±0.05 keV for a Comptonisation model with a Gaussian component, with a reduced chi-squared value of 1.00 for 111 degrees of freedom (DOF). The Gaussian component was centered at 6.63 keV with a 1-σ width of 1.1 keV, most likely due to an iron emission line in the spectrum. While a Comptonisation model is a more physically motivated fit to the data, we also found that a blackbody plus powerlaw model with a Gaussian component fits nearly equally as well to the 3 observations, with a reduced chi-squared value of 1.04 and a blackbody temperature of 1.78±0.02 keV. The Gaussian was fit at 6.5 keV with a 1-σ width of 0.3 keV, again attributed to an iron emission line from somewhere in the field of view. The model fit parameters are listed in Table 1. The quoted error for the persistent unabsorbed flux is statistical, including the contribution from uncertainty in the absorption column, but does not include systematic contributions from the absorption model, bolometric correction, continuum model, or absolute calibration.

We analysed the spectral evolution by looking at the soft and hard colours for the 2008 outburst. The soft and hard colours were found by following the approach used in (Galloway et al. 2008), by calculating the ratios of fluxes in different bands rather than the usually adopted method for RXTE data that calculates the ratio of the counts in different bands. Galloway et al. (2008) chose 4 bands: 2.2–3.6 keV, 3.6–5.0 keV, 5.0–8.6 keV and 8.6–18.6 keV, and calculated the soft and hard colour as the ratio of integrated fluxes in each pair of low and high energy fluxes. We found no significant evolution of the colour or temperature of the source over the observations, as seen in Figure 2, and could not deduce if the source is an atoll source on the banana branch or a Z source (Hasinger & van der Klis 1989). The kT and taup values listed in Table 1, model 2 are consistent with a soft persistent spectrum, so if the source was an atoll source this would imply it is on the banana branch.

3.2 Quiescent Behaviour

We explored the possibility of low-level activity from XMMU J181227.8–181234 outside of its known outbursts in order to properly classify the source. We analysed archival *RXTE*/ASM

Table 1. Spectral fit parameters for the 2 different models used for 3 observations near the peak of the 2008 outburst of XMMU J181227.8–181234

Model 1: Blackbody + Gaussian + Powerlaw Model							
N_H (cm^{-2})	Constant	kT (keV)	Gauss. line (keV)	Gauss. σ (keV)	Powerlaw PhoIndex	red. χ^2	Flux[a]
12.8×10^{22}	1, 0.96, 0.94	1.78±0.02	6.50±0.08	0.3±0.2	3.03±0.03	1.04 for 111 D.O.F.	1.69±0.04
Model 2: Comptonisation Model + Gaussian							
N_H (cm^{-2})	Constant	T_0, kT (keV)	Gauss. line (keV)	Gauss. σ (keV)	taup	red. χ^2	Flux
12.8×10^{22}	1, 0.96, 0.94	0.4±0.3, 2.76±0.05	7.1±0.4	1.1±0.2	5.2±0.2	0.96 for 111 D.O.F.	1.71±0.06

[a] Average unabsorbed 3-25 keV flux in 10^{-9}ergs/cm^2/s

taken from 1996 to 2012, *Swift*/BAT (2004–current) and *BeppoSax*/WFC (1996–2002) long-term observations of XMMU J181227.8–181234. In none of the data did we find any clear evidence for a third outburst, with a typical 3-sigma upper limit of 12 mCrab over a 1-week time scale in the 3–20 keV bandpass for the ASM and 24 mCrab on a 1-day time scale in the 15-50 keV bandpass for *Swift*/BAT. Furthermore, we combined all WFC data (exposure time 4.5 Msec) into single images for the mission duration in 2–5, 5–10, 10–30 keV and combinations thereof. No point source is apparent at the location of XMMU J181227.8–181234 in these combined data with a 5-sigma upper limit of 2 mCrab in 2–30 keV. A 500 s *Swift*/XRT observation (Obs ID 00043947001) from 2012 September 29 centered just 1' from the position of XMMU J181227.8–181234 did not yield any detection, with a 3-σ count rate of 0.012 count s^{-1}, a factor of 340 times fainter than the count rate observed by *Swift* during its last outburst. This confirms in the 0.2-10 keV range it was not persistently active. There are many bright sources in the neighbourhood of XMMU J181227.8–181234 (it lies between GX 9+1 and GX 13+1), which causes a lot of noise in the light curve of the source. We thus concluded that the low level persistent flux we observed from the source is attributed to this, and is not as a result of persistent activity from XMMU J181227.8–181234. Therefore, we classify XMMU J181227.8–181234 as a transient X-ray binary with episodes of high luminosity outbursts.

3.3 Type I X-ray Bursts

We detected 7 X-ray bursts in the data of the 26 follow-up observations with the PCA. Figure 3 shows the light curves of these bursts. As the instrumental vignetting factor for the off-axis burster XTE J1810-189 would give a peak intensity that is roughly consistent with the measured peak intensity, the bursts could in principle come from that source. However, XTE J1810-189 was shown by the PCA bulge scans to be already in an off state for three months (see § 2) and this possibility can be safely excluded. This leaves only XMMU J181227.8-181234 as the possible origin of the bursts.

The follow-up data have a total exposure time of 45 ks. The light curves of the burst events show rise times shorter than 2 s, durations above the noise of about 20 s, e-folding decay times of about 5 s and net peak intensities of up to 180±10 c s^{-1} PCU^{-1}.

3.3.1 Search for Burst Oscillations

We searched for burst oscillations in all of the bursts observed, using Science Event files (E-125us-64M-0-1s), which have a time resolution of 122 μs and employ 64-channels to read out photon energies between 2 and 60 keV. For each burst, we extracted photon sequences in the 20-s intervals starting 4 s before the burst onset. Photon sequences were binned matching the time resolution and the Fourier transform was taken in 1-s sliding windows shifted by 0.5 s with respect to each other. Real and imaginary Leahy-normalized coefficients (Leahy et al. 1983) were saved for the harmonics between 1 and 2001 Hz.

Overall, we found no strong oscillation signal or clustering of oscillation candidates at any particular frequency down to the threshold Leahy-normalized power of 13.816. This power was converted to the background-corrected upper limit on fractional amplitudes (Watts et al. 2005):

$$A = \left(\frac{P_s}{N_m}\right)^{1/2} \frac{N_m}{N_m - N_{bkg}} \quad (1)$$

where P_s is the Leahy-normalized power of signal in the absence of noise, N_m is the number of photons in the given time window and N_{bkg} is the number of background photons in the same time window, estimated as an average of the count rate in a minute-long region prior to burst onset. For unknown P_s, we used the median value of $P_s = P_m + 1$ from the distribution of P_s given P_m (Groth 1975; Watts 2012), where P_m is the power spectrum of noise + signal. The best upper limits on the fractional amplitude (at burst peaks) range from 24% to 43%. This is higher than all burst oscillation amplitudes measured thus far with RXTE (e.g. Bilous & Watts 2018).

3.3.2 Time-resolved Spectral Analysis

The burst spectra were modelled by black body radiation, slicing each burst in a number of time intervals to allow studying the spectral evolution. The number of time intervals varied from 3 to 20 for each burst, with the duration and number of the time intervals depending on the burst duration and data quality. The non-burst spectrum was assumed to be constant during the bursts as a first-order approximation since the data are of insufficient quality to probe changing accretion spectra during the burst (e.g., Worpel et al. 2013; in't Zand et al. 2013; Worpel et al. 2015). The results of this time-resolved spectral analysis of all bursts except burst 4, which does not have a high quality spectrum, are plotted in Figure 4.

We found the spectrum to be consistent with black body radiation, with a typical reduced χ^2 value of 0.95. The peak temperature is kT = (2.4 ±0.1) keV for burst 1 with a peak bolometric unabsorbed flux of $(3.5 \pm 0.3) \times 10^{-9}$ erg s^{-1} cm^{-2}. We found significant evidence for cooling of the spectrum of the bursts, with the blackbody temperature decreasing from kT ≈ 2–2.5 keV at the peak to kT ≈ 1 keV after the peak for all bursts, as seen in Figure 4. This confirms the bursts are Type I thermonuclear X-ray bursts. The radius variations of the bursts are not significant (< 3σ) and so we found no evidence for photospheric radius expansion in any of the bursts. There are distinct double peaks in the bolometric flux of bursts 1 and 3, with the second peak being slightly smaller in both cases. Similar double-peaked events have been observed in other

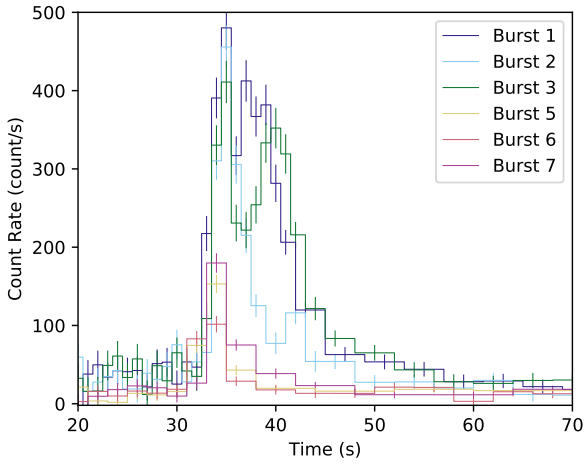

Figure 3. The light curves of 6 of the Type I X-ray Bursts observed during the 2008 outburst of XMMU J181227.8–181234. Observations are from the PCA aboard *RXTE* and the onset of the burst was set to 33 seconds. The count rates have not been corrected for number of active PCUs. Bursts 5 and 6 are clear candidate SWT bursts, with significantly lower fluxes than the other observed bursts.

burst sources without radius expansion, most notably 4U 1636−536 (e.g. Sztajno et al. 1985).

3.3.3 *Burst Properties*

The observed and inferred burst properties are listed in Table 2. We generally inferred burst properties based on the methods outlined in Galloway et al. (2008). α is the ratio of observed integrated persistent flux to observed burst fluence:

$$\alpha = \frac{F_{\rm pers} c_{\rm bol} \Delta t}{E_{\rm b}} \quad (2)$$

where $c_{\rm bol}$ is the bolometric correction factor, $F_{\rm pers}$ is the persistent flux, Δt is the recurrence time and $E_{\rm b}$ is the burst fluence. Fluence is the observed bolometric integrated burst flux.

We estimated the average burst recurrence time using Poisson statistics by dividing the 45 ks (0.3446-day) exposure time by the number of the observed bursts, excluding burst 6, as we identified this as a candidate short waiting time (SWT) burst (see §3.3.4). Since SWT bursts are caused by a different mechanism to 'normal' bursts, we think it is appropriate to exclude the second SWT burst when inferring the recurrence time. We found the most likely recurrence time to be $1.4^{+0.9}_{-0.5}$ hours. We adopted a recurrence time of 18.0 ± 0.1 minutes for bursts 5 and 6 when calculating the α values.

We estimated the nuclear energy generation of the bursts, $Q_{\rm nuc}$ as

$$Q_{\rm nuc} = \frac{Q_{\rm grav}(1+z)}{\alpha} = \frac{218}{\alpha} \quad {\rm MeV/nucleon} \quad (3)$$

where $1 + z = 1.259$ is the assumed gravitational redshift, $Q_{\rm grav} = c^2 z/(1+z) \approx {\rm GM_{NS}/R_{NS}}$, is the gravitational energy, G is the gravitational constant and we use fiducial values of $M_{\rm NS} = 1.4\,M_\odot$ and $R_{\rm NS} = 11.2$ km (e.g. Steiner et al. 2018) for the neutron star. The true value of $Q_{\rm nuc}$ thus depends linearly on the unknown neutron star mass, and must also be corrected for possible anisotropy of the burst and persistent X-ray emission to find the true value in the NS frame (see Section 3.4). The anisotropy correction requires multiplication by $\frac{\xi_b}{\xi_p}$, and explains why the $Q_{\rm nuc}$ values reported in Table 2 are significantly less than the minimum expected value of 1.35 MeV nucleon^{-1}.

3.3.4 *Short Recurrence Time Bursts*

Upon testing for regularity in the burst times we found that bursts 5 and 6 were just 18 minutes apart, while the other bursts were observed days apart. We thus identified bursts 5 and 6 as candidates for short recurrence time bursts (or short waiting time (SWT) bursts). SWT bursts are Type I X-ray bursts that have short ($\lesssim$ 1 hour) recurrence times and occur in groups of 2 or more (doubles, triplets or quadruplets) (e.g. Linares et al. 2009; Keek et al. 2010; Keek & Heger 2017; Boirin et al. 2007). Keek et al. (2010) provided a comprehensive assessment of this phenomenon using a preliminary version of the MINBAR catalog of 3387 bursts observed with the *BeppoSAX*/WFCs and *RXTE*/PCA X-ray instruments. They found 136 SWT bursts with recurrence times of less than one hour, from 15 sources. Overall, they concluded that SWT bursts consistently have α values less than 40, lower peak luminosity, fluence, and temperature than 'normal' bursts and lack the longer decay component from the rp-process in their decay profiles. Those authors also found that of the 15 sources found to exhibit SWT bursts, all were fast spinning (>500 Hz) and of the sources where the accreted composition was known, they all had a high hydrogen fraction. SWT bursts have not been observed from ultra-compact X-ray binaries.

Due to the low duty cycle of the observations of 1.78%, we could not rule out burst 5 being the second or third burst in a triplet or quadruplet of SWT bursts and its lower fluence indicates this might be the case. Bursts 5 and 6 were observed in the same 0.6 hours telescope observation, with burst 5 occurring 0.24 hours from the start of the observation and burst 6 occurring 0.54 hours from the start of the observation. Since the average recurrence time of these bursts is 0.3 hours, we cannot rule out any bursts occurring after burst 6, as the observation continues for only 0.06 hours after burst 6 was observed. We also cannot rule out bursts occurring before burst 5, as the observation started 0.24 hours before burst 5 was observed, and the previous observation ended 1.147 days before this one began. We have plotted the raw lightcurve of the observation in which bursts 5 and 6 occurred in Figure 5.

Bursts 5 and 6 in this outburst have α values significantly lower than the other bursts in the outburst, burst 6 has a short (18 minute) recurrence time, and we cannot rule out burst 5 also having a short recurrence time from the observations. The observations cannot constrain if these two bursts are part of a triplet or even quadruplet of SWT bursts. Both bursts have significantly shorter decay times than the other bursts in the outburst, which is typical of SWT bursts since they have been found to lack the longer decay component from the rp process in their decay profiles (Keek et al. 2010).

The light curves of the two SWT bursts observed are plotted in Figure 3 and the time resolved spectroscopy of the bursts are plotted in Figure 4. In these Figures it is clear that the SWT bursts (bursts 5 and 6) registered significantly lower fluence than the other bursts observed during this outburst, excluding burst 7, which we also cannot rule out as being an SWT burst from the duty cycle of the observations. The low fluence of bursts 5 and 6 provides strong evidence that these are SWT bursts. Bursts 5, 6 and 7 have fluences ranging from 8–15 $\times 10^{-9}$ ergs cm^{-2}, on average a factor of 2.5 times smaller than the average fluence of the other bursts observed

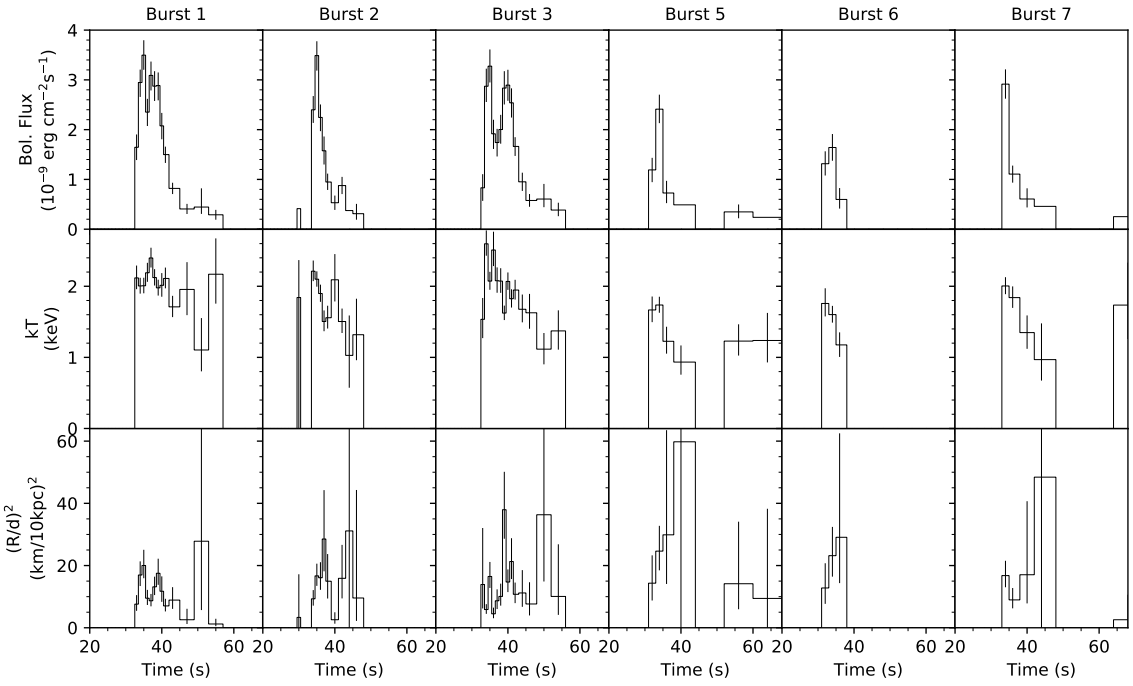

Figure 4. The time resolved spectroscopy of the four highest quality Type I X-ray bursts (bursts 1, 2, 3 and 7) and the two short waiting time bursts (bursts 5 and 6), from data taken with the the PCA aboard the *RXTE*. Note the significant difference in flux of the SWT bursts compared to the normal bursts. There is signifcant evidence for cooling of the spectrum in all observed burst spectra, indicating these are Type I X-ray bursts. There is no evidence for radius expansion in any of the burst spectra.

Table 2. Observed and inferred burst properties for the 7 Type I X-ray bursts detected during the 2008 outburst of XMMU J181227.8–181234.

Burst	MJD	OBSID [a]	F_p [b] (10^{-9} ergs cm^{-2})	E_b [c] (10^{-9} ergs cm^{-2})	F_{pers} [d] (10^{-9} ergs cm^{-2}s^{-1})	α [e]	Q_{nuc} [f] (MeV/nucleon)	τ [g] (s)
1	54717.02685	93044 11 03 02	3.5±0.3	35±2	-	-	-	5.0±0.4
2	54718.13443	93044 11 03 03	3.5±0.3	20±5	1.16±0.03	700^{+500}_{-300}	$0.3^{+0.2}_{-0.1}$	4.5±0.7
3	54720.94267	93044 11 03 05	3.3±0.3	37±4	1.30± 0.03	400^{+300}_{-200}	$0.5^{+0.3}_{-0.2}$	8.6±1.0
4	54723.04537	93044 11 04 00	-	-	1.45±0.03	-	-	-
5	54732.12320	93044 11 05 02	2.4±0.3	15±2	1.23±0.03	230^{+30}_{-30}	$1.0^{+0.1}_{-0.1}$	1.3±0.2
6	54732.13572	93044 11 05 02	1.6±0.3	8±1	0.98±0.03	320^{+40}_{-40}	$0.7^{+0.1}_{-0.1}$	2.1±0.8
7	54736.33460	93450 01 01 00	2.9±0.3	15±2	1.03±0.03	900^{+600}_{-300}	$0.3^{+0.2}_{-0.1}$	4.9±0.9

Note: All values reported in this table are the observed quantities and so are not corrected for anisotropy of emission.

[a] Active PCUs: Bursts 1 and 2: PCU1 and PCU2, Burst 3: PCU2 and PCU3, Bursts 4, 5, 6 and 7: PCU2
[b] Peak bolometric burst flux. Note that we do not have flux measurements for burst 4, as the data quality was not good enough for this burst.
[c] Bolometric burst fluence. The values given in this table are the observed quantities and so are not corrected for anisotropy factors. See section 3.4 for an explanation of the anisotropies.
[d] 3-25 keV persistent flux
[e] α is calculated between bursts using Equation 2. For bursts 5 and 6, α was calculated assuming $\Delta t = 0.3^{+0.002}_{-0.002}$ hours and for all other bursts α was calculated assuming $\Delta t = 1.4^{+0.9}_{-0.5}$ hours.
[f] Inferred nuclear energy generation
[g] Decay time

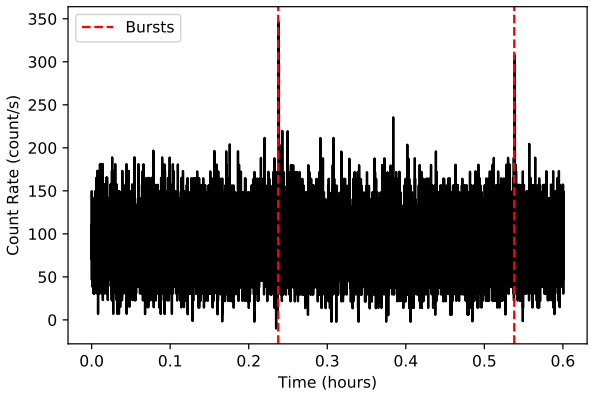

Figure 5. Raw *RXTE* PCA lightcurve of the observation OBSID: 93044-11-05-02 in which the two SWT bursts (bursts 5 and 6) were observed. We cannot rule out SWT bursts occurring before or after these two bursts due to the length of the observation and the 0.3 hour recurrence time.

during the outburst, (20–37) $\times 10^{-9}$ ergs cm^{-2}. However, we cannot confirm burst 7 as a SWT burst as it has a decay time around the same as the non-SWT bursts in this outburst, and it is a combination of short recurrence time, low fluence, short decay time and low alpha values that characterises SWT bursts. The time resolved spectral analysis of bursts 5 and 6 showed significant evidence for cooling of the spectrum, confirming that these are also Type I X-ray bursts (Figure 4).

3.4 Distance, Accretion Rate and Anisotropy Factors

Here we estimate the system parameters based on the burst measurements described above. The persistent and burst emission detected from LMXBs are both subject to projection effects due to the inclination angle of the accretion disk and its inclination-dependent obscuration of the NS. He & Keek (2016) describe the angular distribution of radiation from low mass X-ray binaries for 4 different disk shapes. Anisotropy in the observed persistent emission is caused by scattering in the extended inner disk, collimating radiation from the boundary layer in the direction perpendicular to the disk plane. Anisotropy in the observed burst emission is caused by reflection of photons incident upon the disk surface, enhanced in the same direction as the persistent emission, as well as anisotropic emission from the burst itself. The simplest model (labeled 'model A') assumes an optically thick, geometrically thin disk in the vicinity of the neutron star.

It is plausible that this flat disk scenario is only applicable for sources in a soft spectral state, and a different disk geometry needs to be assumed for sources in a hard spectral state (e.g., Done et al. 2007). Sources in the hard spectral state may instead have a truncated disk that would require different assumptions about the anisotropy factors. Since XMMU J181227.8–181234 remains in the soft state for the duration of this outburst (see Figure 2) we can safely use the calculations of He & Keek (2016) to infer the anisotropy factors.

We used the disk anisotropy model 'A' geometry and the burst properties to place constraints on the inclination. From the recurrence time, average fluence (excluding the SWT candidate bursts 5 and 6) of (24±7) $\times 10^{-9}$ erg cm^{-2}, and persistent flux of (1.19±0.16)$\times 10^{-9}$ erg cm^{-2} s^{-1} we calculated the average α-value of the bursts as 620^{+280}_{-160}.

We then drew samples from the α distribution and calculated the corresponding $Q_{\rm nuc}$ values from equation 3. For each sample we adopted a random value for the inclination θ drawn from an a priori isotropic distribution (i.e. uniform in $\cos\theta$). We calculated the anisotropy factors ξ_b, ξ_p, using the value for θ and the model of He & Keek (2016), and then estimated the H-fraction at ignition (adopting the $Q_{\rm nuc}$ value corrected for anisotropy) by inverting the relation suggested by Goodwin et al. (2018):

$$Q_{\rm nuc}\frac{\xi_b}{\xi_p} = 1.35 + 6.05\bar{X}\,{\rm MeV/nucleon} \quad (4)$$

We retained only those samples with $\bar{X} > 0$, excluding the unphysical values.

The H-fraction in the accreted fuel, X_0 can then be estimated based on the recurrence time and the estimated time to burn H prior to ignition (Lampe et al. 2016):

$$t_{\rm cno} = 9.8\,{\rm hr}\frac{X_0}{0.7}\frac{0.02}{Z} \quad (5)$$

The implied H-fraction in the accreted fuel is $X_0 \leq 0.1071$ (95% confidence), calculated using Equation 5.

Only the smallest inclination values in the low tail of the α-distribution satisfied our constraint on $\bar{X}$, indicating a likely range of $\theta = 30 \pm 10°$ (1-σ confidence). Although only ≈3% of samples were retained, this fraction also depends on the CNO abundance. The fraction of samples accepted increases with lower metallicity, which might suggest that the metallicity in this source is lower than solar. Similarly, increased redshift also results in an increased acceptance fraction of samples. We note that this inclination is only correct under the assumption that the flat disk geometry assumed by He & Keek (2016) Model A reflects the actual geometry of this system.

Based on the possible range of inclination values derived above, we calculated the distance of XMMU J181227.8–181234. The accretion rate was inferred using the models of Lampe et al. (2016) (Figure 1 in their paper) that relate recurrence time to accretion rate for different compositions. Given a recurrence time of 1.4 hours, the inferred $\dot{m}$ is (0.30 ± 0.05) $\dot{m}_{\rm Edd}$ [2] for solar metallicity. No photospheric radius expansion was detected so we found an upper limit for the distance of d$\sqrt{\xi_{\rm b}}$ = 25 kpc, d = 35 kpc for ξ_b = 0.5, using the peak bolometric burst flux. Note the burst anisotropy factor inherent in the observations of the burst peak flux.

We inferred the distance using the anisotropy factors and Equation 6, modified from Galloway et al. (2008):

$$d^2 = \frac{G\dot{m}M_{\rm NS}R_{\rm NS}}{F_{\rm pers}\xi_{\rm p}c_{\rm bol}(1+z)}{\rm cm}^2 \quad (6)$$

We found a distance to the source given by the distribution in Figure 6, with a median of 14.4 kpc and 68th percentile limits of +1.8 -1.6 kpc, for an accretion rate of 0.30±0.05 $\dot{m}_{\rm Edd}$. Note that this distance estimate is dependent on the assumption that the NS mass is 1.4 $M_\odot$ and radius is 11.2 km. Recent works such as Antoniadis et al. (2016) or Steiner et al. (2018) have attempted to constrain the NS mass and radius for X-ray binary systems as well as millisecond pulsars. Antoniadis et al. (2016) found evidence that the birth mass

[2] For simplicity we use $\dot{m}_{\rm Edd}$ = 8.8 $\times 10^4$ g cm^{-2} s^{-1}, but we note this Eddington accretion rate is assuming the hydrogen mass fraction of the fuel is X=0.7. In this paper this accretion rate is used merely as a reference point.

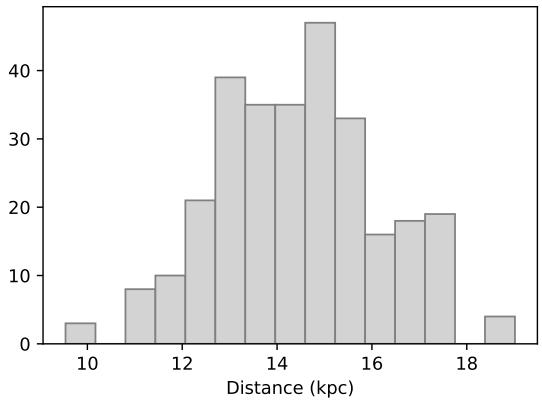

Figure 6. The distribution of distances to XMMU J181227.8–18123 calculated using Equation 6 based on the allowed anisotropy factors. The *y*-axis corresponds to the number of samples meeting our selection criteria (see Section 3.4).

of the NS in these systems could vary significantly, indicating that the NS constraints are highly system dependent, so the mass of the NS in XMMU J181227.8–181234 may not be well constrained by their, or other's observations. However, they find strong indication of a maximum NS mass of 2.018 $M_\odot$. This corresponds to a 40% more massive NS than we have assumed, which would increase our distance estimate by up to 20%. Likewise, for a minimum NS mass of 1.1 $M_\odot$ (e.g. Antoniadis et al. 2016), which is a 20% less massive NS, there would be a 10% decrease in the distance (which is within the statistical uncertainty of 15%). Steiner et al. (2018) analysed observations of low mass X-ray binaries in quiescence and found that the NS radius for a 1.4 $M_\odot$ is most likely between 10 and 14 km. These limits correspond to a 25% increase or 10% decrease in the radius, which would cause a 12.5% increase or 5% decrease in the distance. These radius effects are within the range of the statistical uncertainty on the distance of 15%. Similarly, the bolometric correction could vary by up to 40% due to systematic effects (see Section 3), which would cause a 20% change in the predicted distance. These systematic effects cannot be quantified and so we have not included them in the statistical uncertainty on the distance. We thus conclude the distance to XMMU J181227.8–181234 is 14±2 kpc.

A distance of 16 kpc agrees with the typical distance of a Type I X-ray burst with peak luminosity of about 10^{38} erg s^{-1} (Kuulkers et al. 2003) for the peak bolometric burst flux for this source of $(3.5\pm0.3) \times 10^{-9}$ erg $s^{-1}cm^{-2}$. This is within 1-σ of the distance we predict.

4 DISCUSSION AND CONCLUSIONS

The discovery of Type I thermonuclear X-ray bursts observed from XMMU J181227.8–181234 confirms that the compact object is a neutron star in this system. The bursts have relatively short recurrence times and short decay times that indicate they lack the extended tail that results from rp-process burning in bursts with hydrogen. They also have low nuclear energy generation, low $\bar{X}$ and high α values, which all are properties found in (pure) helium bursts. Therefore, we deduce that the bursts ignite with almost pure helium fuel as the source of the thermonuclear burning. The short recurrence time requires the accreted fuel to be almost pure helium ($X_0 \leq 0.082$) as there is not sufficient time between bursts for a significant amount of hydrogen to burn to helium.

We also observed several candidate short waiting time bursts. SWT bursts are usually observed in systems with high hydrogen fraction, so we have discovered SWT bursts with helium fuel for the first time. We tentatively classify XMMU J181227.8–181234 as an ultracompact X-ray binary due to the strong evidence that it is accreting almost pure helium fuel, despite the fact that SWT bursts have not been observed in ultracompact systems. We thus deduce that the companion star in the system is extremely evolved. We note that this kind of inference of an ultracompact nature (frequent short bursts at high accretion rates) is novel and adds to the methods of orbital period measurement, relatively faint optical counterparts and persistent accretion at very low levels ($\lesssim$1% of Eddington, e.g. in't Zand et al. 2007; van Haaften et al. 2012).

XMMU J181227.8–181234 has previously been tentatively classified as a transient high-luminosity distant low-mass X-ray binary (Cackett et al. 2006). To further understand the behaviour of XMMU J181227.8–181234 we searched for some parallels with other known systems. We found 4 known helium bursters in the burst catalogue of Galloway et al. (2008) with frequent, short bursts and a moderate to high accretion rate. These sources include Ser X-1, 4U 1728-34, 4U 1702-429 and 4U 1916-053. 4U 1728-34 and 4U 1916-053 are ultracompact systems, like XMMU J181227.8–181234. 4U 1916-053 and 4U 1702-429 are persistently active at low accretion rates, unlike XMMU J181227.8–181234. 4U 1728-34, 4U 1702-429 and 4U 1916-053 all have observed alpha values < 150, making them unlike XMMU J181227.8–181234, which has alpha values of 450-850. Ser X-1 is the only other source to exhibit high alpha values (as high as 1600), but this source also has irregular recurrence time bursts. SWT bursts have not been observed from any of these sources. Seemingly, none of the similar sources we found exactly match the behaviour of XMMU J181227.8–181234, making it an unusual source.

Keek et al. (2012) modelled superbursts in a helium accretor at ≈ 30% Eddington. After a superburst, the helium bursts evolve as the atmosphere cools. In the absence of a superburst and during a transient outburst, as in XMMU J181227.8–181234, similar bursting regimes may appear. Interestingly, the predicted recurrence times of the helium accreting model from Keek et al. (2012) exhibited two bursting modes: one with shorter and one with longer recurrence times. The longer recurrence time is similar to the average recurrence time of the bursts from XMMU J181227.8–181234, 80 ± 30 minutes. The peak luminosity of the modelled bursts is around 5×10^{38} erg s^{-1}, larger than the observed peak flux of the normal bursts from XMMU J181227.8–181234, but on the same order of magnitude. The shorter recurrence times are slightly longer than the 18 minutes of the SWT bursts from XMMU J181227.8–181234, at ≈45 minutes, and the peak flux is significantly smaller at $\approx4\times10^{37}$ erg s^{-1}. Nevertheless, this kind of bursting regime is similar to what we have observed in XMMU J181227.8–181234 and future work could tune the model parameters to replicate this kind of behaviour, and explore further what kind of bursting regimes are possible when accreting helium at high rates.

XMMU J181227.8–181234 is a very frequent burster and so should be actively monitored at a higher duty cycle in its next outburst (perhaps within the next couple of years) as it will likely produce a large number of X-ray bursts for analysis.

ACKNOWLEDGEMENTS

This paper utilizes preliminary analysis results from the Multi-INstrument Burst ARchive (MINBAR), which is supported under the Australian Academy of Science's Scientific Visits to Europe program, and the Australian Research Council's Discovery Projects (project DP0880369) and Future Fellowship (project FT0991598) schemes. The MINBAR project has also received funding from the European Union's Horizon 2020 Programme under AHEAD project (grant agreement n. 654215). AG acknowledges support by an Australian Government Research Training (RTP) Scholarship. We thank the anonymous referee for their detailed comments on the manuscript.

REFERENCES

Antoniadis J., Tauris T. M., Ozel F., Barr E., Champion D. J., Freire P. C. C., 2016, arXiv e-prints,
Bilous A. V., Watts A. L., 2018, arXiv e-prints,
Boirin L., Keek L., Méndez M., Cumming A., in't Zand J. J. M., Cottam J., Paerels F., Lewin W. H. G., 2007, A&A, 465, 559
Cackett E. M., Wijnands R., Remillard R., 2006, MNRAS, 369, 1965
Done C., Gierliński M., Kubota A., 2007, A&ARv, 15, 1
Fleischman J. R., 1985, A&A, 153, 106
Galloway D. K., Keek L., 2017, preprint, (arXiv:1712.06227)
Galloway D. K., Muno M. P., Hartman J. M., Psaltis D., Chakrabarty D., 2008, ApJS, 179, 360
Goodwin A. J., Galloway D. K., Heger A., 2018, preprint, (arXiv:1808.02225)
Groth E. J., 1975, ApJS, 29, 285
Hasinger G., van der Klis M., 1989, A&A, 225, 79
He C.-C., Keek L., 2016, ApJ, 819, 47
Jager R., et al., 1997, A&AS, 125, 557
Jahoda K., Markwardt C. B., Radeva Y., Rots A. H., Stark M. J., Swank J. H., Strohmayer T. E., Zhang W., 2006, ApJS, 163, 401
Keek L., Heger A., 2017, ApJ, 842, 113
Keek L., Galloway D. K., in't Zand J. J. M., Heger A., 2010, ApJ, 718, 292
Keek L., Heger A., in't Zand J. J. M., 2012, ApJ, 752, 150
Krimm H. A., Kennea J., Tueller J., 2008, The Astronomer's Telegram, 1432
Kuulkers E., den Hartog P. R., in't Zand J. J. M., Verbunt F. W. M., Harris W. E., Cocchi M., 2003, A&A, 399, 663
Kuulkers E., et al., 2007, A&A, 466, 595
Lampe N., Heger A., Galloway D. K., 2016, ApJ, 819, 46
Leahy D. A., Elsner R. F., Weisskopf M. C., 1983, ApJ, 272, 256
Lewin W. H. G., van Paradijs J., Taam R. E., 1993, Space Sci. Rev., 62, 223
Linares M., et al., 2009, The Astronomer's Telegram, 1979
Markwardt C. B., Pereira D., Swank J. H., 2008, The Astronomer's Telegram, 1685
Matsuba E., Dotani T., Mitsuda K., Asai K., Lewin W. H. G., van Paradijs J., van der Klis M., 1995, PASJ, 47, 575
Morrison R., McCammon D., 1983, ApJ, 270, 119
Shaposhnikov N., Jahoda K., Markwardt C., Swank J., Strohmayer T., 2012, ApJ, 757, 159
Steiner A. W., Heinke C. O., Bogdanov S., Li C. K., Ho W. C. G., Bahramian A., Han S., 2018, MNRAS, 476, 421
Sztajno M., van Paradijs J., Lewin W. H. G., Trumper J., Stollman G., Pietsch W., van der Klis M., 1985, ApJ, 299, 487
Thompson T. W. J., Galloway D. K., Rothschild R. E., Homer L., 2008, ApJ, 681, 506
Titarchuk L., 1994, ApJ, 434, 570
Torres M. A. P., Steeghs D., Kennea J. A., Homan J., Miller J. M., 2008, The Astronomer's Telegram, 1696
Wallace R. K., Woosley S. E., 1981, ApJS, 45, 389
Watts A. L., 2012, ARA&A, 50, 609
Watts A. L., Strohmayer T. E., Markwardt C. B., 2005, ApJ, 634, 547
Weng S.-S., Zhang S.-N., Yi S.-X., Rong Y., Gao X.-D., 2015, MNRAS, 450, 2915
White N. E., Nagase F., Parmar A. N., 1995, X-ray Binaries, pp 1–57
Wilson-Hodge C. A., et al., 2011, ApJ, 727, L40
Wood K. S., et al., 1984, ApJS, 56, 507
Worpel H., Galloway D. K., Price D. J., 2013, ApJ, 772, 94
Worpel H., Galloway D. K., Price D. J., 2015, ApJ, 801, 60
in 't Zand J. J. M., Galloway D. K., Kuulkers E., Goodwin A., 2017, The Astronomer's Telegram, 10567
in't Zand J. J. M., Jonker P. G., Markwardt C. B., 2007, A&A, 465, 953
in't Zand J. J. M., et al., 2013, A&A, 553, A83
van Haaften L. M., Voss R., Nelemans G., 2012, A&A, 543, A121

This paper has been typeset from a TEX/LATEX file prepared by the author.

5

COMBINING MODELS OF ACCRETING NEUTRON STARS WITH OBSERVATIONS

Whilst much effort has been put into developing advanced models of accreting neutron star systems, it is also important that we determine how well these models can predict observed parameters, as well as using observations to better inform our models.

5.1 A BAYESIAN APPROACH TO MATCHING THERMONUCLEAR X-RAY BURST OBSERVATIONS WITH MODELS

In this Chapter we present a case study of SAX J1808.4–3658, in which we use a Markov Chain Monte Carlo approach to predict system parameters we cannot measure, by matching observations of a burst train with the `Settle` model. To predict the total burst energy, we use the energy generation rate presented in Chapter 3. The software we present, called `BEANS`, is publicly available and can now be used to infer parameters we cannot observe for additional accreting neutron star systems with observations of burst trains. The model we present is powerful as it can predict system parameters such as neutron star mass, radius, distance, inclination, accreted fuel composition, and more. However, we must note that the software is only as good as the model, and the model we use is relatively basic when compared to more advanced models such as `Kepler` or `MESA` (for more detail on the `Settle` model see Chapter 2).

Published in:
A. J. Goodwin et al. (Dec. 2019a). 'A Bayesian approach to matching thermonuclear X-ray burst observations with models'. *MNRAS* 490.2, pp. 2228–2240. DOI: 10.1093/mnras/stz2638. arXiv: 1907.00996 [astro-ph.HE]

MNRAS **000**, 1–12 (2019) Preprint 6 October 2020 Compiled using MNRAS LATEX style file v3.0

A Bayesian Approach to Matching Thermonuclear X-ray Burst Observations with Models

A. J. Goodwin[1,2,⋆] D. K. Galloway[1,2], A. Heger[1,2,3], A. Cumming[4], and Z. Johnston[1,2]
[1]*School of Physics & Astronomy, Monash University, Clayton VIC 3800, Australia*
[2]*also Monash Centre for Astrophysics (MoCA)*
[3]*Tsung-Dao Lee Institute, Shanghai 200240, China*
[4]*Department of Physics and McGill Space Institute, McGill University, 3550 rue University, Montreal, QC, H3A 2T8, Canada*

Accepted 2019 September 16. Received 2019 September 05; in original form 2019 July 01

ABSTRACT

We present a new method of matching observations of Type I (thermonuclear) X-ray bursts with models, comparing the predictions of a semi-analytic ignition model with X-ray observations of the accretion-powered millisecond pulsar SAX J1808.4−3658 in outburst. We used a Bayesian analysis approach to marginalise over the parameters of interest and determine parameters such as fuel composition, distance/anisotropy factors, neutron star mass and neutron star radius. Our study includes a treatment of the system inclination effects, inferring that the rotation axis of the system is inclined $\left(69^{+4}_{-2}\right)^{\circ}$ from the observers line of sight, assuming a flat disc model. This method can be applied to any accreting source that exhibits Type I X-ray bursts. We find a hydrogen mass fraction of $0.57^{+0.13}_{-0.14}$ and CNO metallicity of $0.013^{+0.006}_{-0.004}$ for the accreted fuel is required by the model to match the observed burst energies, for a distance to the source of $3.3^{+0.3}_{-0.2}$ kpc. We infer a neutron star mass of $1.5^{+0.6}_{-0.3}\,M_{\odot}$ and radius of $11.8^{+1.3}_{-0.9}$ km for a surface gravity of $1.9^{+0.7}_{-0.4} \times 10^{14}$ cm s^{-2} for SAX J1808.4−3658.

Key words: X-rays: bursts – X-rays: binaries – pulsars: individual: SAX J1808.4−3658

1 INTRODUCTION

Accretion-powered millisecond pulsars (AMSPs) are neutron stars with weak ($\sim 10^8$ G) magnetic fields that are accreting matter from a low mass companion star (e.g., Lewin et al. 1993; Chakrabarty & Morgan 1998; Wijnands & van der Klis 1998; Patruno & Watts 2012; Galloway & Keek 2017). These systems are typically transient X-ray sources, and exhibit coherent X-ray pulsations as well as Type I thermonuclear X-ray bursts periodically (e.g., Wijnands 2004). A source goes into outburst when the accretion disc around the neutron star, formed by accretion of matter onto the companion star, reaches a critical state that causes matter to transfer directly onto the neutron star and ignites thermonuclear bursts (e.g., Strohmayer & Bildsten 2006; Galloway & Keek 2017). Type I X-ray bursts are the most frequently observed thermonuclear powered outbursts in nature and provide a unique insight into the nuclear reactions that can occur in extreme environments. They are characterised by a sudden increase in the X-ray flux of a source in outburst (e.g., Galloway et al. 2008). They can be observed from neutron stars in binary systems, and are thought to be caused by unstable ignition of hydrogen or helium on the surface of an accreting neutron star (e.g., Strohmayer & Bildsten 2006).

The challenge inherent in understanding low-mass neutron star binary systems is estimating system parameters, including the composition of the fuel that drives the thermonuclear burst; and the distance/inclination of the source, which cannot be directly observed as they are kilometre-sized objects at kilo-parsec distances. These parameters are an essential ingredient in modelling and understanding the dense matter of neutron stars and the physical processes behind thermonuclear bursts. Applications range from stellar evolution (with fuel composition of the bursts enabling constraints on the evolution of the companion star and population synthesis) to constraining proton- and carbon-rich nuclear reactions that are difficult to replicate in Earth-bound laboratories.

Neutron stars are the densest directly observable stellar objects known. The study of neutron stars through various electromagnetic bands has seen much progress in recent years, furthering the understanding of high-density cold matter and the dense equation of state (e.g. Miller et al. 2019; Degenaar & Suleimanov 2018; Özel & Freire 2016) The recent observation of gravitational waves from merging neutron stars (Abbott et al. 2017) has also seen an increase in efforts to constrain neutron star properties, such as the neutron star mass, radius, spin, and equation of state (e.g., Abbott et al. 2018; Annala et al. 2018; Radice et al. 2018). Constraining these properties is fundamental in the understanding of ultra-dense matter, such as the material that makes up a neutron star, as well as

⋆ E-mail: ajgoodwin.astro@gmail.com

providing additional constraints in the search for more gravitational waves.

Observations of AMSPs that exhibit Type I X-ray bursts are becoming increasingly more accessible, with the Multi-INstrument Burst Archive (MINBAR)[1] providing an extensive collection of processed and anlaysed X-ray burst data. Observations are limited to the X-ray activity of these sources, providing measurements of the accretion flux, burst flux, and recurrence time of bursts.

Efforts to model burst sources have evolved from early models (e.g., Fujimoto et al. 1987; Taam 1980; van Paradijs et al. 1988) that focused on the correlation between burst energies and recurrence times, to varying success, to more recent models (e.g., Cumming 2003; Galloway et al. 2004; Woosley et al. 2004) which have a heavier focus on the nuclear physics driving the bursts, predicting fuel compositions and accretion rates by implementing more detailed models of the nuclear reaction rates that produce the observed energy generation rates.

These observations and models motivate an effort to combine the data obtained from both, to obtain a deeper understanding of the thermonuclear processes that occur during an X-ray burst, as well as identifying where current models are failing to predict observed properties (e.g., Galloway et al. 2017). The most well-studied transients, such as the accretion-powered millisecond pulsar SAX J1808.4−3658, provide crucial test cases for numerical models of thermonuclear bursts and can be used as standard cases in modelling studies.

Galloway & Cumming (2006) showed that the bursts from SAX J1808.4−3658 were consistent with ignition in an almost pure He environment. The long recurrence times of ≈1 day allow enough time for hydrogen to be depleted by thermally-stable hot CNO burning between bursts. By modelling the burst properties, they were able to constrain the hydrogen fraction in the accreted layer, and showed that the observed recurrence times imply a relation between the hydrogen fraction and fraction of CNO elements. As such, SAX J1808.4−3658 provides the best example of pure helium ignited bursts, and validates the theory in which hydrogen depletes before ignition of the X-ray burst in a helium environment.

In this study we develop a new method for matching burst observations with a semi-analytic ignition model, extending the previous work of Galloway & Cumming (2006), to determine system parameters such as fuel composition, neutron star mass and radius, distance, and inclination. We use a Markov Chain Monte Carlo approach to find the best-fitting system parameters, with uncertainties. In Section 2 we describe the semi-analytic model used in this study, compare it to detailed time-dependent simulations, and describe the MCMC implementation. In Section 3 we report the parameter limits predicted by the model, and describe how well our model matches the observations. Finally, in Section 4, we summarise the results and give our conclusions.

2 METHODS

We used the ignition model of Cumming & Bildsten (2000) (hereafter called SETTLE) to generate burst sequences, which were then compared to *Rossi X-ray Timing Explorer* (RXTE) Proportional Counter Array (PCA) telescope observations of the 2002 outburst of SAX J1808.4−3658 using a Markov Chain Monte Carlo (MCMC) algorithm. We obtained the 'best' model run that matched the observations, providing predictions for parameters such as fuel composition, distance, anisotropies, neutron star mass and radius, that cannot be measured otherwise. We used the python implementation of MCMC, EMCEE (Foreman-Mackey et al. 2013). RXTE observations were obtained from archival data available in MINBAR and shown in Table 1, updated since the initial analysis of this outburst by Galloway & Cumming (2006). Observed properties of the bursts include times, persistent flux, burst fluence and α values. Here, α is defined as the ratio of integrated persistent flux to the fluence, given by

$$\alpha = \frac{F_{\rm p} c_{\rm bol} \Delta t}{E_{\rm b}} \tag{1}$$

where $E_{\rm b}$ is the burst fluence, Δt is the recurrence time, $F_{\rm p}$ is the persistent flux, and $c_{\rm bol}$ is the bolometric correction. For $c_{\rm bol}$ we adopted a constant value of 2.12, as in Galloway & Cumming (2006).

In order to determine the accretion rate at the time of a burst, we used persistent flux measurements of the outburst from the PCA and linearly interpolated the values between measurements either side of the burst. This enabled us to obtain a value at the time of each burst, from which an accretion rate was inferred using

$$\dot{m} = c_{\rm bol} F_{\rm p} r_{\rm l} \tag{2}$$

where $F_{\rm p}$ is the persistent flux, $\dot{m}$ is the accretion rate, and $r_{\rm l}$ is the scaling factor between the accretion rate and the persistent flux, described in Section 2.3.

Table 1. Observations of the 2002 October outburst of SAX J1808.4−3658

No.	Burst start time (MJD)	Peak Flux (10^{-9} erg cm^{-2} s^{-1})	Fluence (10^{-6} erg cm^{-2})	α
1	52562.4136	163±3	2.62±0.02	–
2	52564.3051	177±3	2.65±0.01	107±2
3	52565.1843	179±3	2.99±0.01	118±2
4	52566.4268	177±3	3.46±0.02	128±2

Notes: The α values are calculated between bursts using Equation 1, assuming 2 bursts occurring between Bursts 1 and 2. Fluxes reported are bolometric fluxes and uncertainties are 1σ confidence levels.

2.1 SETTLE

SETTLE is a semi-analytic ignition model developed by Cumming & Bildsten (2000) that integrates the thermal profile of a settling atmosphere to find ignition conditions for a single burst, from which the burst train can be predicted. It applies a one-zone ignition criterion to simple models of the accumulating layer, which allows a survey of parameter space whilst also enabling estimation of the ignition depth. Researchers have applied SETTLE to observations of regular Type I bursters, such as 4U 1820−30 (Cumming 2003), GS 1826−24 (Cumming 2003), and SAX J1808.4−3658 (Galloway & Cumming 2006). The SETTLE model assumes the accumulating fuel layer is heated by hot CNO hydrogen burning within the layer, and a constant flux from deeper layers. It does not include heating from energy released in a previous burst, or the possibility of ignition of unburnt fuel within the ashes of a previous burst (commonly referred to as thermal and compositional inertia; Woosley et al. 2004; see Section 2.2 for corrections we applied to SETTLE to account for some of these simple assumptions). Assuming spherical symmetry,

[1] https://burst.sci.monash.edu/minbar/

SETTLE does not address complex physics that is currently poorly understood, such as how the burning front spreads across the star after ignition occurs, what determines the number of hotspots on the surface of the star, or the cause of asymmetry near the end of bursts as the material is cooling (e.g., Cavecchi & Spitkovsky 2019).

SETTLE adopts a neutron star mass and radius (e.g., $M_{\rm NS} = 1.4\,{\rm M}_\odot$ and $R_{\rm NS} = 11.2\,{\rm km}$) which then sets the gravitational redshift and surface gravity, where the surface gravity, g, in the X-ray burst layer is given by

$$g = \frac{GM_{\rm NS}}{R_{\rm NS}^2} \cdot (1+z) \tag{3}$$

where G is the Gravitational constant, z is the gravitational redshift, $M_{\rm NS}$ is the gravitational neutron star mass and $R_{\rm NS}$ is the neutron star radius in the observer frame.

An X-ray burst is triggered when helium burning becomes unstable at the base of the accumulated layer, at a temperature of $\approx 2\times10^8$ K and a density range of $\sim 10^5$–$10^6\,{\rm g\,cm^{-3}}$. The temperature profile of the accumulating layer of hydrogen and helium is calculated given the accretion rate, and the accumulating layer is allowed to build up until the one-zone condition for a thermal runaway is satisfied at the base of the layer. This condition is met when $d\epsilon_{3\alpha}/dT > d\epsilon_{\rm cool}/dT$, where $\epsilon_{3\alpha}$ is the energy production rate of helium burning (via the triple alpha reaction) and $\epsilon_{\rm cool}$ is the effective local cooling rate. At this point, a thermal instability occurs and the conditions for thermonuclear runaway are met. The temperature profile at ignition is determined such that $d\epsilon_{3\alpha}/dT = d\epsilon_{\rm cool}/dT$ at the base of the ignition column.

The composition of the ignition column at ignition depends on how much hydrogen has burned before the ignition conditions were met, during the accumulation of the fuel. The amount of hydrogen burned is determined by the local accretion rate, since hydrogen is assumed to burn steadily at a constant rate via the hot CNO cycle. The rate at which hydrogen burns is thus given by

$$\frac{dY_{^1{\rm H}}}{dt} = \frac{4\ln 2\, Y_{\rm CNO}}{t_{\frac{1}{2},{\rm CNO}}}\,, \tag{4}$$

where $Y_{\rm CNO}$ is the parts per nucleon of CNO elements and $t_{\frac{1}{2},{\rm CNO}}$ is the cycle half life, i.e., the sum of the half lives of the isoptopes limiting the cycle. In SETTLE, we assume the CNO elements are the β-limited CNO cycle isotopes, ^{14}O and ^{15}O, in their cycle equilibrium abundance values and $Y_{\rm CNO}$ can be computed from

$$Y_{\rm CNO} = \frac{Z_{{\rm CNO},\beta}}{\bar{A}_{{\rm CNO},\beta}} \tag{5}$$

where $\bar{A}_{{\rm CNO},\beta}$ is the average mass number of the CNO isotopes in the β-limited CNO cycle, given by

$$\bar{A}_{{\rm CNO},\beta} = \frac{t_{\frac{1}{2},^{15}{\rm O}} A_{^{15}{\rm O}} + t_{\frac{1}{2},^{14}{\rm O}} A_{^{14}{\rm O}}}{t_{\frac{1}{2},^{15}{\rm O}} + t_{\frac{1}{2},^{14}{\rm O}}}\,, \tag{6}$$

where A_i is the mass number of species i, $t_{\frac{1}{2},^{15}{\rm O}} = 122\,{\rm s}$ and $t_{\frac{1}{2},^{14}{\rm O}} = 71\,{\rm s}$.

The ratio of the parts per nucleon of ^{14}O to ^{15}O is given by the ratio of their half lives. Thus the mass fractions $Z_{14} = 0.352\,Z_{\rm CNO}$ and $Z_{15} = 0.648\,Z_{\rm CNO}$, giving $\bar{A}_{{\rm CNO},\beta} = 14.653\,{\rm g\,mol^{-1}}$.

The energy production rate of hydrogen burning via the CNO cycle, $\epsilon_{\rm H}$, is given by

$$\epsilon_{\rm H} = \frac{\rm d}{{\rm d}t} Y_{^1{\rm H}}\, E_{\rm H}\,,$$

where $E_{\rm H}$ is the energy produced from burning 4 ^{1}H to ^{4}He. $E_{\rm H}$ is given by the change in mass excess less the energy carried away by neutrinos, $E_{\rm H} = 6.03\times10^{18}\,{\rm erg\,g^{-1}}$. Thus, $\epsilon_{\rm H}$ is given by

$$\epsilon_{\rm H} = 5.94\times10^{13}\,\frac{Z_{{\rm CNO},\beta}}{0.01}\quad {\rm erg\,g^{-1}\,s^{-1}}\,, \tag{7}$$

where $Z_{{\rm CNO},\beta}$ is the mass fraction of CNO nuclei in the β-limited CNO cycle, computed as outlined above.

We also compare to the Sun as a reference point with its own, different, distribution of the CNO isotopes, with $\bar{A}_{{\rm CNO},\odot} = 14.688$, such that a given CNO metallicity translates into a slightly different value of $Y_{\rm CNO}$. Using the solar abundance ratios for CNO isotopes from Lodders et al. (2009), one obtains:

$$\epsilon_{\rm H} = 5.93\times10^{13}\,\frac{Z_{{\rm CNO,scaled}\,\odot}}{0.01}\quad {\rm erg\,g^{-1}\,s^{-1}} \tag{8}$$

which is remarkably similar to the value using the β-limited Z value reference, though only by coincidence, not by design.

Throughout the remainder of this paper all values of metallicity refer exclusively to the β-limited CNO metallicity, which is the relevant value for SETTLE. The reference value of 0.01 used here is indeed very close to the solar mass fraction of CNO isotopes given by Lodders et al. (2009) as 0.01001.

Summarising, the time to burn all of the hydrogen ($t_{\rm H}$) is dependent only on the metallicity and initial hydrogen abundance. The time to burn hydrogen is thus

$$t_{\rm H} = \frac{Y_{^1{\rm H}}}{Y_{\rm CNO}}\,\frac{t_{\frac{1}{2},^{15}{\rm O}} + t_{\frac{1}{2},^{14}{\rm O}}}{4\ln 2} = 20.45\left(\frac{X_0}{0.7}\right)\left(\frac{0.01}{Z_{\rm CNO}}\right)\,{\rm h} \tag{9}$$

where X_0 is the initial hydrogen mass fraction of the accreted fuel. This sets the minimum recurrence time required for pure helium bursts. Note that we have updated this equation from the original work of Cumming & Bildsten (2000), and it is the time to burn hydrogen locally on the neutron star surface, for the observer this timescale is longer by a redshift factor $1+z$. For higher accretion rates ($\dot{m} \gtrsim 0.04\,\dot{m}_{\rm Edd}$[2]) helium burning becomes unstable before sufficient time has passed for all of the hydrogen to be burned, resulting in ignition occurring in a hydrogen rich environment. For lower ($\dot{m} \lesssim 0.04\,\dot{m}_{\rm Edd}$) accretion rates, there is sufficient time for all of the hydrogen to be burned before ignition, allowing a pure helium layer to accumulate before ignition, and a helium rich environment for the burst.

The column depth at which hydrogen runs out ($y_{\rm d}$) is given by:

$$y_{\rm d} = 6.9\times10^8\left(\frac{\dot{m}}{0.01\dot{m}_{Edd}}\right)\left(\frac{0.01}{Z_{\rm CNO}}\right)\left(\frac{X_0}{0.7}\right)\quad {\rm g\,cm^{-2}} \tag{10}$$

If helium ignites at a column depth $y < y_{\rm d}$, a mixed H/He burst occurs; and if helium ignites at a column depth $y > y_{\rm d}$, a pure helium layer has time to accumulate and ignition occurs in a pure helium environment.

Once ignition conditions are met, the burst parameters are calculated based on the total mass in the ignition column and its composition. The burst energy is calculated by assuming complete

[2] $\dot{m}_{\rm Edd}$ is the Eddington accretion rate, given by $\dot{m}_{\rm Edd} = 1.75\frac{0.7}{1+X}\times10^{-8}\,{\rm M_\odot\,yr^{-1}}$, where X is the H mass fraction

burning of the H/He layer, and the accreted material is assumed to cover the whole surface of the neutron star. The thickness of the accumulated layer at ignition determines the recurrence time of the bursts.

2.1.1 *Updates to* SETTLE

When hydrogen remains at the time of ignition, and bursts ignite in a mixed H/He environment, there is extra energy released by the triple-alpha process due to proton capture by ^{12}C. To avoid a discontinuity in accretion rate–recurrence time parameter space at the transition zone between mixed H/He bursts and pure He bursts, we gradually switched on the factor that multiplies the triple alpha reaction energy generation rate to account for the ^{12}C(p, γ) reaction when protons begin running out at the critical H fraction of $X = 1/7$ (since the ratio of protons to alpha particles is 2 : 3). The gradual switch on of this multiplicative factor was not a feature of Cumming & Bildsten (2000)'s original code.

We updated some of the energy and rate values used in SETTLE. We corrected the energy generation of hydrogen burning via the CNO cycle such that $\epsilon_{\rm H} = 5.94 \times 10^{15}\,{\rm erg\,g^{-1}\,s^{-1}}$ (used to be $5.8 \times 10^{15}\,{\rm erg\,g^{-1}\,s^{-1}}$). We also used an updated version for the total nuclear energy released per unit mass in an X-ray burst as calibrated by Goodwin et al. (2018) using KEPLER models, $Q_{\rm nuc} = 1.35 + 6.05\,\bar{X}$ MeV/nucleon, where $\bar{X}$ is the average hydrogen mass fraction of the ignition column. The ignition depth correction we applied due to differences between SETTLE and KEPLER is described in Section 2.2

Using KEPLER models with fully time-dependent accretion rates, Johnston et al. (2018) found that using constant accretion rates (averaged between bursts) can systematically underestimate the burst recurrence times when the slope of the accretion rate is negative (see Figure 4 of that paper). Because SETTLE implicitly uses averaged accretion rates, we accounted for this effect by multiplying each predicted recurrence time by a correction factor, as determined by the linear approximation from Johnston et al. (2018). These correction factors ranged from approximately 0.9–1.0 for our modelled bursts. The correction factors we adopted are specific to SAX J1808.4–3658 and will either need to be recalculated or made more generally applicable if this method is applied to a different system. To rigorously test the influence of these correction factors we ran the code without the scaling factors and found that while the central value of the distance, hydrogen fraction, metallicity, and base flux shifted, the parameters still agreed within 1-σ uncertainty of the model run with the scaling factors.

2.2 Code Verification

A simple code such as SETTLE can be run in seconds, enabling multiple instances of the code to be run, and a marginalising method such as MCMC possible. Other codes, such as KEPLER (Woosley et al. 2004), use bigger nuclear reaction networks and a more complex treatment of the neutron star atmosphere during outburst, at the cost of computational expense and runtime. KEPLER solves the full time-dependent stellar structure equations, following the evolution of temperature and composition at each depth in the neutron star envelope over many cycles of bursts. To assess the limitations of SETTLE, we ran a comparison with some KEPLER models, and implemented corrections to SETTLE to account for some of the differences we found. Woosley et al. (2004) provided a limited comparison between some SETTLE and KEPLER models, and found that, in general, the agreement was good, although with SETTLE consistently

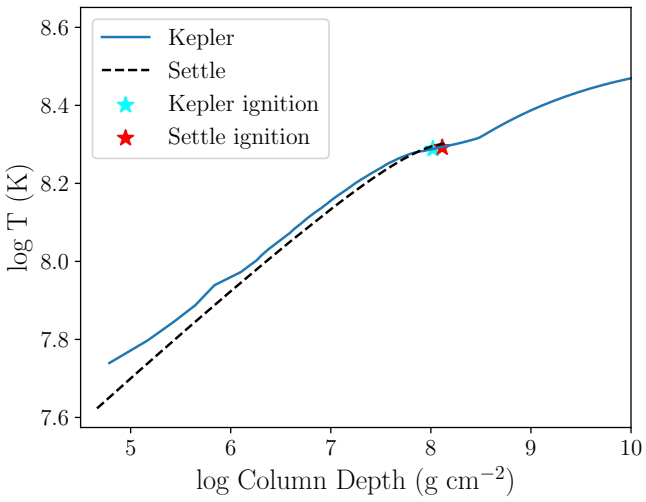

Figure 1. Comparison of the temperature profile of SETTLE (black dashed) and KEPLER (blue solid) models at the ignition of a burst. Stars indicate the ignition depth of the burst for each model. Model conditions: $X = 0.2$, $z = 0.02$, $\dot{m} = 0.2\,\dot{m}_{\rm Edd}$, $Q_{\rm b} = 0.1$ Mev/nucleon.

overestimating the burst energies and recurrence times. The authors attribute the discrepancy between the SETTLE and KEPLER models to the lack of compositional inertia in the SETTLE models.

We compared the predicted fluences ($E_{\rm b}$) and recurrence times (Δt) of the two codes for a range of hydrogen mass fractions (X), CNO mass fractions (Z), accretion rates ($\dot{m}$) and base fluxes ($Q_{\rm b}$). In order to allow meaningful comparison, we redshifted the KEPLER recurrence times by multiplying by $1+z$, as KEPLER calculates recurrence time in the reference frame of the neutron star, whereas SETTLE calculates recurrence time in the reference frame of a distant observer. In both codes we fixed $M_{\rm NS} = 1.4\,{\rm M}_\odot$ and $R_{\rm NS} = 11.2$ km. We also increased the SETTLE $Q_{\rm b}$ value by 0.1 MeV/nucleon when comparing to KEPLER to account for thermal inertia (Cumming & Bildsten 2000).

On initial comparison we found the SETTLE recurrence times and fluences were at least ~ 30% higher than the KEPLER predictions. We compared the temperature profiles of the ignition column for each code, shown in Figure 1.

We found the temperature profile of SETTLE was overall cooler than KEPLER, causing a longer recurrence time, deeper ignition, and thus brighter bursts. Since KEPLER provides a more complex analysis of the underlying physics, we decided to correct the ignition depth of SETTLE such that it matched the KEPLER ignition depth. To do this we multiplied the SETTLE ignition depth by a factor of 0.65. Reducing the ignition depth reduced the recurrence time and fluences of the SETTLE bursts and produced the comparison shown in Figure 2.

In Figure 2 for higher hydrogen fractions ($X = 0.6$ and 0.7) there is a significant difference between the predicted fluences and recurrence times of the SETTLE and KEPLER bursts across all accretion rates. There is much better agreement at lower hydrogen fractions ($X < 0.5$) and lower accretion rates ($\dot{m} < 0.1\,\dot{m}_{\rm Edd}$ between the two codes. For the purpose of this paper we note that for the source we are investigating, `SAX J1808.4-3658`, observations indicate that is has a slightly depleted hydrogen fraction and low ($\approx 4\%$ Eddington) accretion rate, so it is within the parameter space that SETTLE agrees well with KEPLER.

Fundamental differences between the two models can be attributed primarily to the fact that SETTLE has a one-zone ignition

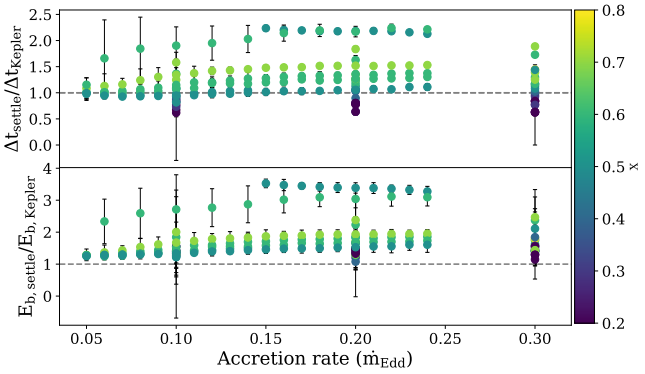

Figure 2. Comparison of the predicted recurrence times (top) and burst fluences (bottom) for the SETTLE and KEPLER models for a range of accretion rates ($\dot{m}$, expressed as a fraction of $\dot{m}_{\rm Edd}$), after the ignition depth in SETTLE has been reduced by 45%. The dashed line shows the one-one relation between the two predictions. Some of the models have different CNO metallicities and base heating, causing some variances in the predictions for the same accretion rate and hydrogen mass fraction.

criterion which uses a local approximation for the cooling, whereas KEPLER follows the detailed cooling as a function of depth. Other differences could arise due to the fact that SETTLE assumes there is no triple-alpha burning during the accumulation of fuel, SETTLE assumes that all of the accreted fuel is burnt in a single burst, and the burst train is generated without accounting for subsequent bursts occurring in the ashes of previous bursts. Finally, SETTLES uses an approximate formula for the nuclear energy generation of the bursts, that has been calibrated to KEPLER predictions, but still is not the same as calculating the full nuclear reaction network, with thermal inertia included. As a caveat we note that calibrating to KEPLER introduces a different kind of model bias. Since there have been no comprehensive studies done between KEPLER and other similar codes, we do not understand how accurately KEPLER models the true physics of these systems.

2.3 MCMC

We used a Python implementation of MCMC (EMCEE; Foreman-Mackey et al. 2013) to estimate posterior distributions of the properties predicted by SETTLE, based on the known values of the observed properties of the burst train (time, $E_{\rm b}$ and α). We defined a likelihood function, given by Equation 11, and prior ranges for each parameter. We used a simple Gaussian likelihood function where the variance was underestimated by some fractional amount, f, and the overall likelihood is the sum of the individual likelihoods for each parameter i,

$$L(x_i|\theta, \text{model}) = \frac{1}{\sigma_i f_i \sqrt{2\pi}} \exp\left[\frac{-(x_i - \text{model})^2}{2 f_i \sigma_i}\right] \tag{11}$$

where σ_i is the observed uncertainty, x_i is the observed parameter value (time, fluence, and alpha), model is the parameter value predicted by the model, and θ are our parameters of interest. The parameters of interest we defined are hydrogen mass fraction X, metallicity Z, which is defined as the mass fraction of CNO elements (all in ^{14}O and ^{15}O), base flux $Q_{\rm b}$, neutron star mass M, neutron star radius R and three scaling factors, r_1, r_2, and r_3.

The 3 scaling factors, r_1, r_2, and r_3 are defined as in Galloway & Cumming (2006), given in Equations 12, 13, and 14,

$$r_1 = \frac{\dot{m}_i}{c_{\rm bol} F_{{\rm p},i} \xi_{\rm p}} \tag{12}$$

where $\dot{m}_i$ is the accretion rate between burst $i-1$ and burst i, $\xi_{\rm p}$ is the persistent anisotropy (defined in Section 3.1, $F_{{\rm p},i}$ is the mean $2-25$ keV persistent flux between burst $i-1$ and i (in units of 10^{-9} erg cm^{-2} s^{-1}, from interpolation) and $c_{\rm bol}$ is the bolometric flux correction.

$$r_2 = \frac{\alpha}{\alpha_{\rm pred}} \tag{13}$$

where α is the observed value (Equation 1) and $\alpha_{\rm pred} = 290/Q_{\rm nuc,pred}$.

$$r_3 = \frac{E_{\rm b}/10^{-9}}{L_{\rm b,pred}\,\xi_{\rm b}} \tag{14}$$

where $L_{\rm b,pred}$ is the predicted burst luminosity in units of 10^{39} erg s^{-1} and $E_{\rm b}$ is the observed burst fluence.

We initialised the parameters in a tiny ($\sim 10^{-3}$) Gaussian ball around the initial value. We ran the MCMC chains with 300 walkers for 2,000 steps, and discarded the first 200 steps in each chain to account for burn-in. See Section 3.4 for information on the tests we ran to ensure the MCMC chains were fully converged and independent of initial walker positions.

2.4 Priors

For each parameter except metallicity, mass and radius, we used a uniform prior, where we chose an acceptable range based on observations or theoretical assumptions. For metallicity ($Z_{\rm CNO}$) we chose a more informed prior, using a synthetic survey of the Milky Way in the location of `SAX J1808.4-3658` at 2–4 kpc generated by the Galaxia code (Sharma et al. 2011) to determine a likely distribution of the metallicity, given by Equation 15 and shown in Figure 3.

$$[\text{Fe/H}] \sim \phi(3 + \frac{3}{4}) - 3 \tag{15}$$

where $\phi \sim \mathcal{B}(10, 3)$ is a Beta distribution with $\alpha = 10$ and $\beta = 3$, and the linear translation limits the metallicity prior to have support between [Fe/H] $= -3$ and $+0.75$ (i.e., $0.00001 < Z_{\rm CNO} < 0.056$).

For mass and radius we also imposed a more informed prior based on the models of Steiner et al. (2018), who used observations of eight quiescent low mass X-ray binaries in globular clusters to determine the neutron star mass–radius curve and the equation of state. Steiner et al. (2018) used a fixed mass grid and varied radius according to their chosen equation of state and observations of radii. We chose the simplest of their models ('baseline') and used the probability distribution given in Figure 2.4 for the relationship between mass and radius. We also constrained mass and radius to: $1.15\,{\rm M}_\odot < M < 2.5\,{\rm M}_\odot$ and $9\,{\rm km} < R < 17\,{\rm km}$. This prior effectively checks if the masses and radii predicted by the model are consistent with the expected mass-radius relation of low mass X-ray binaries in globular clusters. It provides a probability of the predicted radius given the predicted mass.

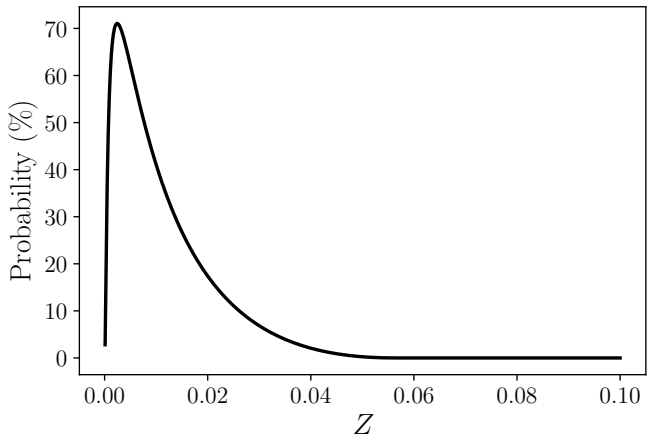

Figure 3. The probability distribution assumed for metallicity (Z), based on a simple model of the Galaxy in the location of SAX J1808.4−3658 at 2–4 kpc.

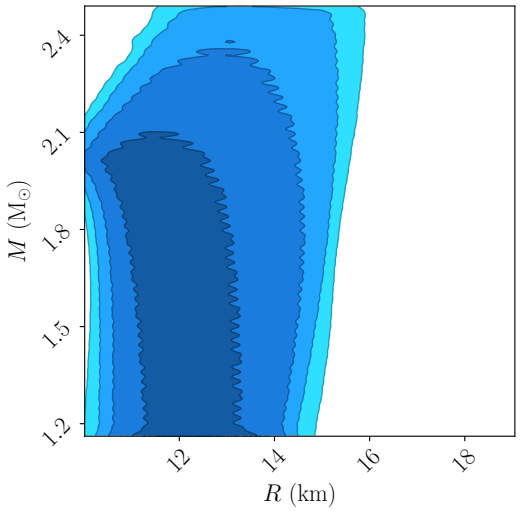

Figure 4. Steiner et al. (2018) probability distribution for NS radius as a function of mass based on observations of low mass X-ray binaries in globular clusters. Contour levels shown are 1σ intervals up to 5σ.

3 RESULTS

We report the posterior limits for the predicted system parameters in Table 2, reporting the mean value and the 68th percentile limits of the distributions for the uncertainties. Additional model runs are shown in the Appendix, including one that replicates Galloway & Cumming (2006) with fixed mass and radius and one with a uniform prior in mass and radius.

The times and fluences of the 6 predicted bursts are plotted in Figure 5, as well as the 4 observed bursts. We predict 3 bursts that were not observed, but that cannot be ruled out by observations, since they occur during periods that the telescope was not observing. The two bursts predicted between the first and second observed bursts were also predicted by Galloway & Cumming (2006) and Johnston et al. (2018). The predicted burst properties agree reasonably well with the predictions from Johnston et al. (2018), who used Kepler to model this outburst without doing an exhaustive parameter space exploration such as we have done in this work.

Table 2. SAX J1808.4−3658 derived neutron star parameters

Parameter	Value	Units
X	$0.58^{+0.13}_{-0.14}$	
Z	$0.013^{+0.006}_{-0.004}$	
Q_b	$0.4^{+0.3}_{-0.2}$	MeV/nucleon
M	$1.5^{+0.6}_{-0.3}$	$M_\odot$
R	$11.8^{+1.3}_{-1.0}$	km
$\dot{m}_{max}$	$0.037^{+0.002}_{-0.002}$	$\dot{m}_{Edd}$
g	$1.9^{+0.7}_{-0.4}$	10^{14} cm s^{-2}
$1+z$	$1.27^{+0.13}_{-0.05}$	
d	$3.3^{+0.3}_{-0.2}$	kpc
ξ_b	$0.74^{+0.10}_{-0.10}$	
ξ_p	$0.87^{+0.12}_{-0.10}$	
$\cos i$	$0.36^{+0.07}_{-0.04}$	

Notes: g and $1+z$ are calculated based on the M and R values, using Equation 3. $\dot{m}_{max}$ is the maximum inferred accretion rate using Equation 2.

Table 3. SAX J1808.4−3658 predicted burst parameters

Burst	$\bar{X}$	α	Δt (hours)
2	$0.20^{+0.06}_{-0.06}$	108^{+12}_{-9}	14.7
3	$0.20^{+0.06}_{-0.06}$	107^{+12}_{-9}	14.4
4*	$0.19^{+0.05}_{-0.06}$	110^{+11}_{-9}	16.1
5*	$0.16^{+0.04}_{-0.04}$	117^{+10}_{-9}	19.4
6*	$0.12^{+0.03}_{-0.03}$	126^{+9}_{-7}	31.2
7	$0.07^{+0.02}_{-0.02}$	139^{+6}_{-5}	56

Notes: "*" indicates this burst was observed by *RXTE*. Burst 1 is excluded as it was used as a reference burst and we did not infer properties for this burst. $\bar{X}$ is the average hydrogen mass fraction of the ignition column.

Interestingly, Johnston et al. (2018) also predict a very bright burst at late time, ≈ 7 days after the first observed burst.

Burst properties for individual bursts inferred by the model are listed in Table 3. The recurrence time for each burst is predicted to fall in the range 14 – 56 hours. The time to exhaust hydrogen and ignite bursts in a pure helium environment is 13.0 hours at this accreted fuel composition (Equation 9). These predicted recurrence times and their respective accretion rates indicate that sufficient time passes between each burst for the accreted hydrogen to be completely burned by the hot CNO cycle, and we have ignition occurring in a pure helium environment, as has been previously concluded by Galloway & Cumming (2006); Johnston et al. (2018). The low $\bar{X}$ values for each burst confirms this, with $\bar{X} < 0.2$ for all bursts.

The probability contours and posterior distributions for X, Z, Q_b, d, ξ_b, and ξ_p are plotted in Figure 6. There is a positive correlation between X and Z, which was also found by Galloway & Cumming (2006). This correlation is due to the relationship between recurrence time and fuel composition, since provided all of the H is exhausted before ignition, there are multiple combinations of X and Z that reproduce the observed recurrence time.

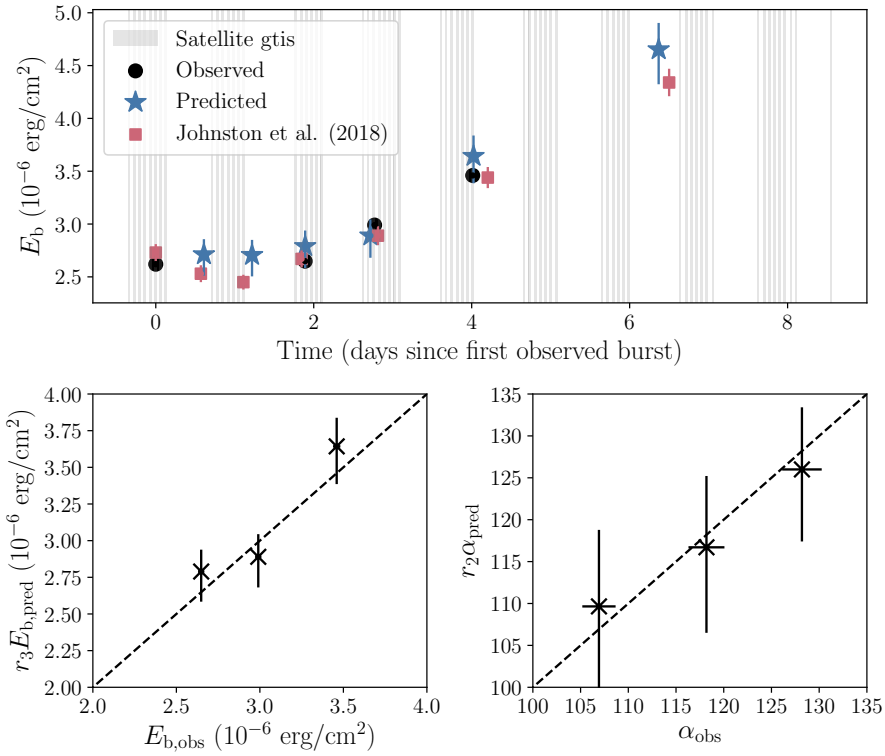

Figure 5. Top: predicted burst times and fluences (blue stars), observed bursts times and fluences (black circles) and predicted burst times and fluences from Johnston et al. (2018) (red squares). The grey regions show the satellite observing periods ('good time intervals'). Bottom left: r_3 times the predicted burst fluences vs observed burst fluences. Dashed line is the one-to-one relation. Bottom right: r_2 times the predicted alphas vs observed alphas. Dashed line is the one-to-one relation.

3.1 Distance and Anisotropies

We used the scaling parameters r_1, r_2, and r_3 to obtain posterior distributions for the distance and emission anisotropies of the source, and thus the inclination, shown in Figure 6. Relating the scaling parameters to their corresponding physical parameters gives:

$$r_2 = 0.74816 \left(\frac{M_{NS}}{1.4\,M_\odot}\right)\left(\frac{R_{NS}}{11.2\,km}\right)^{-1}\left(\frac{Q_{nuc}}{Q_{nuc,pred}}\right)^{-1}\left(\frac{\xi_p}{\xi_b}\right) \quad (16)$$

$$r_3 = 63.23 \left(\frac{d}{10\,kpc}\right)^{-2}\left(\frac{R_{NS}}{11.2\,km}\right)^{2}\left(\frac{1+z}{1.258}\right)^{-1}\left(\frac{Q_{nuc}}{Q_{nuc,pred}}\right)\xi_b \quad (17)$$

Assuming $Q_{nuc} = Q_{nuc,pred}$, this gives the following set of equations which enable calculation of d, ξ_b and ξ_p using the three scaling factors.

$$\xi_p = r_1 \left(\frac{10}{d}\right)^2 \quad (18)$$

$$\xi_b = \frac{r_2 \xi_p}{0.74816} \quad (19)$$

$$d = 10\sqrt{\frac{63.23\xi_b}{r_3}}\ \text{kpc} \quad (20)$$

Using these equations, we obtained posteriors on distance (d), burst anisotropy (ξ_b) and persistent anisotropy (ξ_p), shown in Figure 6 and values reported in Table 2. He & Keek (2016) modelled the relationship between anisotropy factors and inclination in low mass binaries with different disc shapes. They considered 4 different disc geometries, motivated by an effort to match observations of high reflection fractions observed in a couple of superbursts. Since `SAX J1808.4-3658` has never shown evidence of such high reflection fractions, we chose the simplest disc geometry described by He & Keek (2016), Model A, corresponding to a flat disc. He & Keek (2016) Model A is approximated by Equation 21, which we used to also obtain a posterior distribution for cos i, based on the inferred anisotropy factors.

$$\frac{\xi_p}{\xi_b} = \frac{0.5 + |\cos i|}{2|\cos i|} \quad (21)$$

where i is the inclination of the system, the angle between the rotation axis and the direction from which the system is viewed by an observer.

For this disc Model A, we infer a distance to `SAX J1808.4-3658` of $3.3^{+0.3}_{-0.2}$ kpc, which agrees within uncertainty of the predictions of Galloway & Cumming (2006) of 3.1–3.8 kpc. We note that Galloway & Cumming (2006) did not account for the anisotropy of emission when inferring their distance estimate. Applying our predicted anisotropy factors to their distance estimate reduces their estimate to 2.7–3 kpc, still within our predicted distance range.

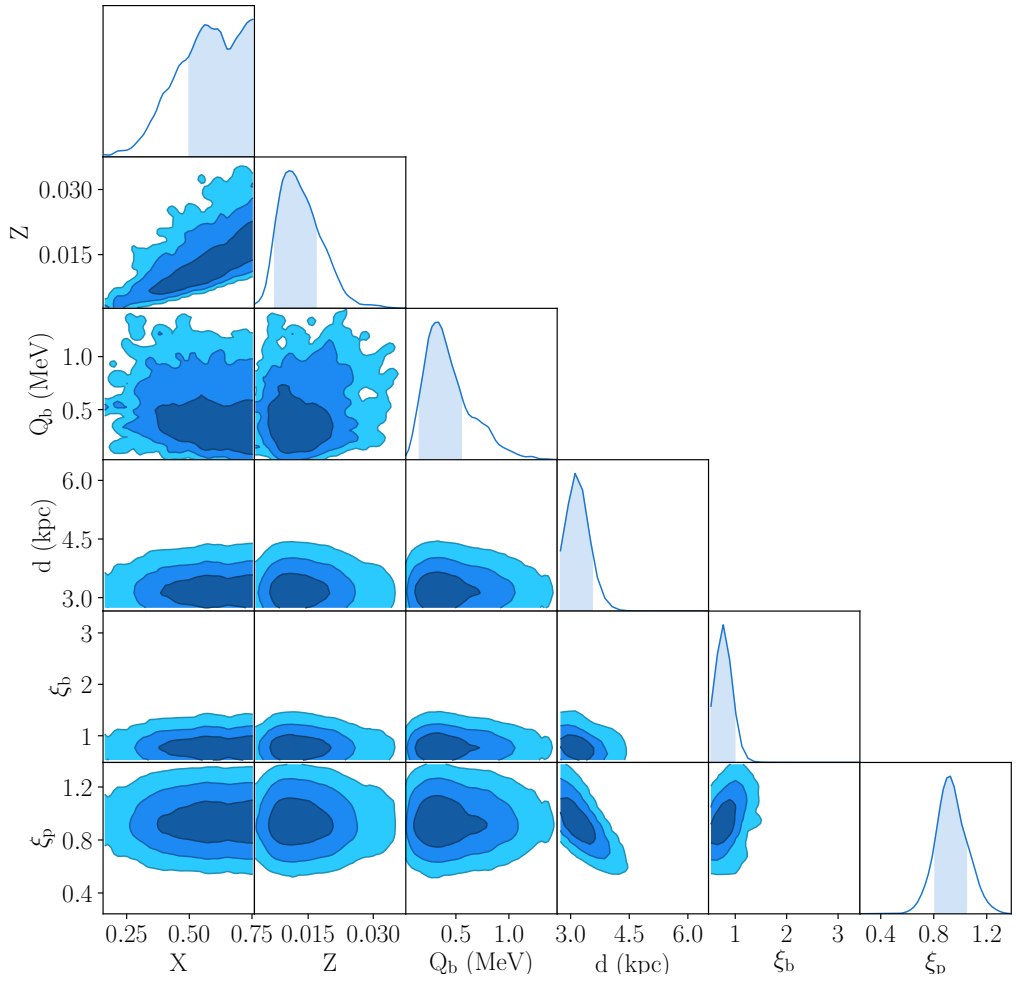

Figure 6. 2-dimensional projection of the posterior probabilities of hydrogen mass fraction (X), metallicity (Z), base heating rate (Q_b), distance (d) and anisotropy factors (ξ_b and ξ_p) of `SAX J1808.4-3658`. Histograms along the diagonal show the marginalised probabilities of the individual parameters. Contour levels are the 1, 2, and 3 σ bounds.

3.2 Neutron Star Mass and Radius

We infer a neutron star mass of $M_{\rm NS} = 1.5^{+0.6}_{-0.3}\,{\rm M}_\odot$ based on the gravity and gravitational redshift required by the model that gives the best match to the observations. Since the neutron star in this system has been accreting matter periodically, we expect it to be more massive than a single non-binary neutron star (e.g. Kiziltan et al. 2013). Canonically, the neutron star mass is assumed to be $M_{\rm NS} = 1.4\,{\rm M}_\odot$, and recent works constraining NS mass and radii have found the NS mass could be between 1.1–2.2 $\rm M_\odot$ (e.g., Antoniadis et al. 2016). There has been extensive work in trying to estimate the mass of `SAX J1808.4-3658` with no consensus on the value, but the general finding that it is more massive than the canonical value of $1.4\,{\rm M}_\odot$ (e.g. Heinke et al. 2009; Elebert et al. 2009; Morsink & Leahy 2011). If the NS mass is larger than the usually assumed NS mass, this could indicate that some of the accreted matter is not burned in the observed X-ray bursts, as was modelled by Goodwin et al. (2018), however, due to the uncertainty of our mass prediction this result is not significant.

The posterior distributions and probability contours for mass and radius are plotted in Figure 7, coloured by surface gravity. The prior we used for mass and radius is plotted in red.

From Figure 7 it appears that there is a preferred surface gravity loosely driving the correlation between mass and radius, with the preferred surface gravity being $1.9 \times 10^{14}\,{\rm g\,cm^{-2}}$. Interestingly, the radius posterior peaks at a radius lower than the peak radius of the prior distribution, indicating that the model fit prefers a smaller radius. The model is thus sensitive to changes in radius. We explore this further in Section 4, in which we compare model runs with fixed mass and radius and flat mass and radius priors.

3.3 Binary System Parameters and Inclination

The mass function of the binary orbit is given by

$$f_x = \frac{(M_{\rm c}\sin i)^3}{(M_{\rm NS}+M_{\rm c})^2} = \frac{4\pi^2 (a_x \sin i)^3}{G P_{\rm orb}^2} \tag{22}$$

where i is the binary inclination, $M_{\rm c}$ is the companion star mass and $M_{\rm NS}$ is the neutron star mass (e.g., Chakrabarty & Morgan 1998; Bildsten & Chakrabarty 2001).

Setting the projected semi-major axis, $a_x \sin i = 62.809\,{\rm light-ms}$ (Chakrabarty & Morgan 1998) and orbital period, $P_{\rm orb} = 2.01\,{\rm h}$ gives $f_x = 3.8 \times 10^{-5}\,{\rm M}_\odot$. This leaves $M_{\rm NS}$, i, and $M_{\rm c}$. Our MCMC algorithm uses SETTLE to find $M_{\rm NS} = 1.5^{+0.6}_{-0.3}\,{\rm M}_\odot$.

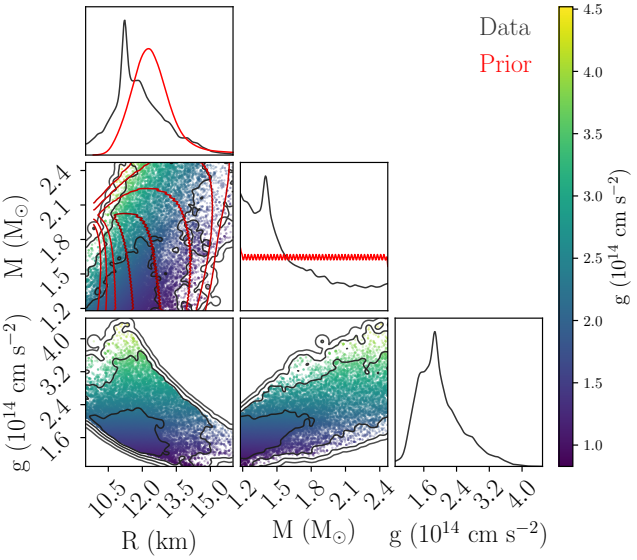

Figure 7. 2-dimensional projection of the posterior probabilities of NS mass (M), NS radius (R) and surface gravity (g) of `SAX J1808.4-3658` (black and coloured by g) and the NS mass and radius prior probability distribution from Steiner et al. (2018) (red). Histograms along the diagonal show the marginalised probabilities of the individual parameters and contour levels are 1 σ intervals up to 5 σ.

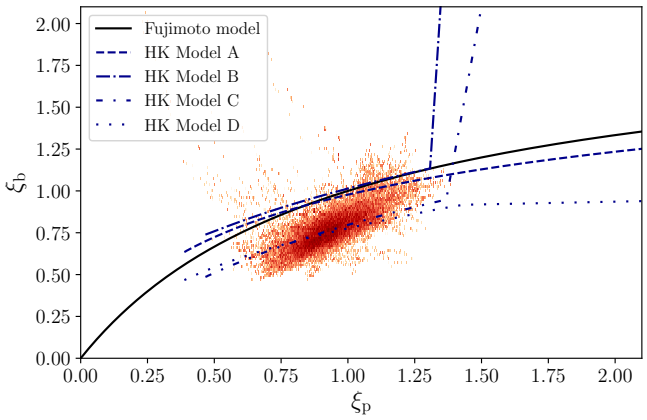

Figure 8. The distribution of the 1 σ MCMC predictions for the anisotropy factors, ξ_p and ξ_b (orange) and the relationship between ξ_p and ξ_b as predicted by the He & Keek (2016) (HK) and Fujimoto (1988) models for different disc shapes.

Given estimates of $M_c = 0.02 - 0.011\,M_\odot$ (e.g., Bildsten & Chakrabarty 2001) and using Equation 22, the mass function gives $\cos i = 0.62^{+0.09}_{-0.08}$ ($i = \left(64^{+37}_{-20}\right)^\circ$).

Lack of deep X-ray eclipse rules out $i > 82°$ ($\cos i < 0.15$) (Chakrabarty & Morgan 1998). There is a 2% modulation in X-ray intensity at the orbital period, which suggests that i must be large enough to allow partial X-ray blockage from some circumbinary material (Bildsten & Chakrabarty 2001). Those authors rule out face on inclination due to the 2 hour single-peaked modulation in the optical intensity, confirmed by Homer et al. (2001). The flux minimum occurs when the neutron star is behind the companion, implying that the X-ray heating of the companion is the origin of the modulation, which would have no effect in a face on system. Our best estimate gives $\cos i = 0.36^{+0.07}_{-0.04}$ ($i = \left(69^{+4}_{-2}\right)^\circ$), which agrees within 3 σ of $\cos i = 0.62^{+0.09}_{-0.08}$ found using the mass function, and is within the ranges predicted by Bildsten & Chakrabarty (2001) and Wang et al. (2001). More recently, Wang et al. (2013) and Cackett et al. (2009) have attempted to constrain the inclination through optical modelling and iron line modelling respectively. Wang et al. (2013) found $i = \left(50^{+6}_{-5}\right)^\circ$ and Cackett et al. (2009) found $i = \left(55^{+8}_{-4}\right)^\circ$ (1 σ uncertainties). The Cackett et al. (2009) estimate agrees within 2 σ of our best estimate, and the Wang et al. (2013) estimate agrees within 3 σ.

Since the anisotropy factors are determined independently in this method, we checked the self consistency of these factors with the relationships predicted by the Fujimoto (1988) and He & Keek (2016) models in Figure 8.

`SAX J1808.4-3658` is in the hard spectral state during its outbursts and due to its nature as an accreting pulsar, it is predicted to have a truncated disc (e.g., Psaltis & Chakrabarty 1999). The Fujimoto et al. (1981) and He & Keek (2016) models do not model for a truncated disc, and thus we do not expect any of them to match our predictions perfectly. We could not decisively conclude which of the models matched our predictions best, as they all pass through the 1 σ confidence area in Figure 8, motivating us to use the simplest model, He & Keek (2016) Model A.

3.3.1 *Wind loss*

Recent research has found that a significant amount ($\approx$ 30%) of the nuclear energy of a Type I X-ray burst could be used to unbind matter from the neutron star surface, ejected in a wind. Yu & Weinberg (2018) found that wind losses can cause up to 30% loss of nuclear energy in ejecting material from the system. We do not correct for wind loss in our models as upon testing it simply reduced the predicted distance by $\approx$ 7%, with mass loss causing the source to be predicted closer due to fainter bursts being predicted.

3.4 Chain Convergence and MCMC performance

The convergence of MCMC chains is notoriously difficult to assess. Goodman & Weare (2010) recommend using the integrated autocorrelation time (τ) to quantify the effects of sampling error on the results. The autocorrelation time provides a measure of the large time error of the Monte Carlo estimator, and so is a reliable indicator of the accuracy of the sampler by measuring the asymptotic variance in the limit of long chains. This essentially measures the effective number of independent samples, and enables estimation of the number of samples required to reduce the relative error on the target integral to a few percent. Foreman-Mackey et al. (2013) recommend running the chains for at least 50 τ samples (or conservatively 100 τ samples).

In Figure 9 the autocorrelation time of each parameter we varied is plotted as a function of the number of samples. The autocorrelation time is not reliably estimated early on, as there are not enough samples. As more samples are taken, the autocorrelation time estimate becomes more accurate, and after $\approx$ 500 samples, the autocorrelation time converged on a single value for all of the parameters. By 2,000 samples, all of the autocorrelation estimates are well below the $\tau = N/100$ line, indicating this is an accurate estimate of the autocorrelation time. The largest autocorrelation time is <10 so the chains should be converged according to this conver-

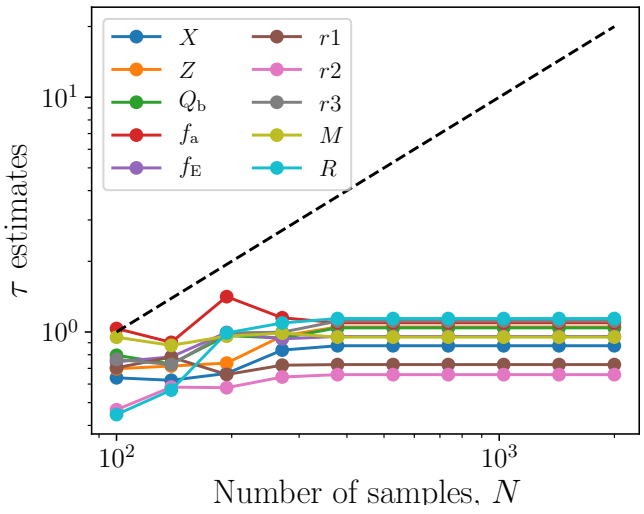

Figure 9. The evolution of the autocorrelation time (τ) with the number of samples taken for the 10 parameters varied with MCMC. The black dashed line is the $\tau = N/100$ line.

gence test after 1,000 steps. We ran the chains for 2,000 steps and 300 walkers to ensure they would be fully converged.

The acceptance fraction of the samples is a widely used measure to check the performance of MCMC. The acceptance fraction is the number of proposed steps that are accepted, and will be small if too many steps are rejected and large if too many steps are accepted (Foreman-Mackey et al. 2013). The general consensus is that the acceptance fraction should be between 0.2–0.5 (e.g., Gelman et al. 1996), however, it depends on the model and situation. The acceptance fraction of our final run was 0.14, which is lower than 0.2 but not unreasonably low. As a test, we ran the MCMC code returning only the prior (excluding the likelihood and thus model call) and found an acceptance fraction of 0.11. We can thus conclude that the prior limits are constraining parameter space and causing a larger than usual amount of steps to be proposed outside the allowed domain and be rejected.

A final test we ran to ensure the end walker positions were independent of the initial positions was to change the size of the Gaussian ball the walkers were initialised around by a factor of 100. This did not affect the marginalised posterior distributions of each parameter.

4 DISCUSSION AND CONCLUSIONS

We have used a Bayesian approach to successfully match observed burst fluence, alpha, and recurrence times with the SETTLE model to infer system parameters of an accreting millisecond pulsar in outburst. The properties of the bursts observed from `SAX J1808.4-3658` indicate they arrive in helium rich fuel, given the relatively short length, low flux, and high alpha values (e.g., Galloway & Cumming 2006). We inferred $\bar{X} < 0.2$ for all bursts, as expected for helium rich bursts. Overall, we matched the observed burst fluences, alphas, and recurrence times to within the $1\,\sigma$ uncertainty of the model.

Based on the agreement between the observed burst properties, we then inferred and modelled composition, base flux, neutron star mass, neutron star radius, distance, and inclination. We set the prior for metallicity to the expected distribution of metallicities based on the location of `SAX J1808.3-3658` in the Galaxy, and deduced the most likely CNO mass fraction (metallicity) of the source to be between 0.009–0.019. This range covers the expected value for solar CNO metallicity, which recent work puts at 0.01 (Lodders et al. 2009). We inferred a slightly depleted hydrogen mass fraction of the accreted fuel, of $0.58^{+0.13}_{-0.14}$, indicating that the companion star in this system could be significantly evolved.

We inferred a base flux of 0.25–0.7 MeV/nucleon, which gives an indication of the base heating of the neutron star. We used the constraints on the relationship between NS mass and radius calculated by Steiner et al. (2018) for neutron stars in low mass X-ray binaries in globular clusters as an informed prior for the distribution of acceptable mass and radius combinations and inferred a NS mass between 0.9–1.8 $M_\odot$ and a radius between 10.8–13.1 km. The mass is constrained to within 40% ($1\,\sigma$ limit) and the radius is constrained to within 11% ($1\,\sigma$ limit), indicating that this method cannot constrain neutron star mass and radius to a high precision. This is most likely due to degeneracies in some of the other model parameters, such as base heating (Q_b), that can adjust to produce the same burst energies and recurrence time when the mass, radius, and thus surface gravity and redshift are varied.

Finally, we used the scaling factors we defined and the posterior distributions of the parameters to infer a distance and inclination of `SAX J1808.4-3658`, based on He & Keek (2016) disc Model A. We found a distance range of 3.1–3.6 kpc for an inclination from the rotation axis of 67°–73°. Galloway & Cumming (2006) used the fact that the observed bursts showed photospheric radius expansion to infer an upper limit of the distance to the source of 3.6 kpc, just within our $1\,\sigma$ upper limit on the distance. An inclination of 69°, implies both the observed burst and persistent fluxes are artificially increased by reflection from the disc and by the disc itself, bringing the source closer when compared to distance estimates such as Galloway & Cumming (2006) that do not account for inclination.

We have reported the median value and 68th percentile limits of the predicted posterior distributions to give an indication of the parameter values. While this is a representation of the data, the true solutions are the posterior distributions that were calculated by the MCMC algorithm. Parameters estimated using this technique are limited to the accuracy of the SETTLE model predictions. The benefit of using such a simple model is that it can be used in a MCMC algorithm to effectively sample parameter space.

We have demonstrated that we can infer system parameters of a bursting source using observations of an outburst and the SETTLE model. Future work could apply this method of matching observed properties with models to the other known bursting AMSPs with observations of burst trains, or any accreting neutron star with observations of burst trains. This method enables initial exploration of parameter space, to determine an estimate for the range of parameters for each source. These ranges could then be used in more advanced, computationally expensive models such as KEPLER to narrow down the parameter limits.

ACKNOWLEDGEMENTS

We thank Andrew Casey for his contribution of the metallicity prior we used. We thank Andrew Steiner for helpful discussions regarding the neutron star mass-radius prior. This paper utilizes preliminary analysis results from the Multi-INstrument Burst ARchive (MINBAR), which is supported under the Australian Academy of Science's Scientific Visits to Europe program, and the Australian Research Council's Discovery Projects and Future Fellowship funding

schemes. AG and ZJ acknowledge support by an Australian Government Research Training (RTP) Scholarship. AH was supported by a grant from Science and Technology Commission of Shanghai Municipality (Grant No. 16DZ2260200) and National Natural Science Foundation of China (Grant No. 11655002). This work benefited from support by the National Science Foundation under Grant No. PHY-1430152 (JINA Center for the Evolution of the Elements). We thank the anonymous referee for constructive and insightful comments that helped to improve the manuscript.

REFERENCES

Abbott B. P., et al., 2017, Physical Review Letters, 119, 161101
Abbott B. P., et al., 2018, Physical Review Letters, 121, 161101
Annala E., Gorda T., Kurkela A., Vuorinen A., 2018, Physical Review Letters, 120, 172703
Antoniadis J., Tauris T. M., Ozel F., Barr E., Champion D. J., Freire P. C. C., 2016, arXiv e-prints, p. arXiv:1605.01665
Bildsten L., Chakrabarty D., 2001, The Astrophysical Journal, 557, 292
Cackett E. M., Altamirano D., Patruno A., Miller J. M., Reynolds M., Linares M., Wijnands R., 2009, ApJ, 694, L21
Cavecchi Y., Spitkovsky A., 2019, arXiv e-prints, p. arXiv:1905.13735
Chakrabarty D., Morgan E. H., 1998, Nature, 394, 346
Cumming A., 2003, ApJ, 595, 1077
Cumming A., Bildsten L., 2000, ApJ, 544, 453
Degenaar N., Suleimanov V. F., 2018, arXiv e-prints, p. arXiv:1806.02833
Elebert P., et al., 2009, MNRAS, 395, 884
Foreman-Mackey D., Hogg D. W., Lang D., Goodman J., 2013, PASJ, 125, 306
Fujimoto M. Y., 1988, ApJ, 324, 995
Fujimoto M., Hanawa T., Miyaji S., 1981, ApJ, 247, 267
Fujimoto M. Y., Sztajno M., Lewin W. H., Van Paradijs J., 1987, ApJ, 319, 902
Galloway D. K., Cumming A., 2006, ApJ, 652, 559
Galloway D. K., Keek L., 2017, arXiv e-prints, p. arXiv:1712.06227
Galloway D. K., Cumming A., Kuulkers E., Bildsten L., Chakrabarty D., Rothschild R. E., 2004, ApJ, 601, 466
Galloway D. K., Muno M. P., Hartman J. M., Psaltis D., Chakrabarty D., 2008, ApJS, 179, 360
Galloway D. K., Goodwin A. J., Keek L., 2017, Publ. Astron. Soc. Australia, 34, e019
Gelman A., Roberts G., Gilks W., 1996, Oxford University Press, 16, 17
Goodman J., Weare J., 2010, Communications in Applied Mathematics and Computational Science, Vol.~5, No.~1, p.~65-80, 2010, 5, 65
Goodwin A. J., Galloway D. K., Heger A., 2018, preprint, (arXiv:1808.02225)
He C.-C., Keek L., 2016, ApJ, 819, 47
Heinke C. O., Jonker P. G., Wijnands R., Deloye C. J., Taam R. E., 2009, ApJ, 691, 1035
Homer L., Charles P., Chakrabarty D., Van Zyl L., 2001, Monthly Notices of the Royal Astronomical Society, 325, 1471
Johnston Z., Heger A., Galloway D. K., 2018, MNRAS, 477, 2112
Kiziltan B., Kottas A., De Yoreo M., Thorsett S. E., 2013, ApJ, 778, 66
Lewin W. H., Van Paradijs J., Taam R. E., 1993, Space Science Reviews, 62, 223
Lodders K., Palme H., Gail H.-P., 2009, Landolt Börnstein, p. 712
Miller M. C., Chirenti C., Lamb F. K., 2019, arXiv e-prints, p. arXiv:1904.08907
Morsink S. M., Leahy D. A., 2011, ApJ, 726, 56
Özel F., Freire P., 2016, ARA&A, 54, 401
Patruno A., Watts A. L., 2012, arXiv e-prints,
Psaltis D., Chakrabarty D., 1999, ApJ, 521, 332
Radice D., Perego A., Zappa F., Bernuzzi S., 2018, ApJ, 852, L29
Sharma S., Bland-Hawthorn J., Johnston K. V., Binney J., 2011, ApJ, 730, 3
Steiner A. W., Heinke C. O., Bogdanov S., Li C. K., Ho W. C. G., Bahramian A., Han S., 2018, MNRAS, 476, 421
Strohmayer T., Bildsten L., 2006, New views of thermonuclear bursts. pp 113–156
Taam R. E., 1980, ApJ, 241, 358
Wang Z., et al., 2001, ApJ, 563, L61
Wang Z., Breton R. P., Heinke C. O., Deloye C. J., Zhong J., 2013, ApJ, 765, 151
Wijnands R., 2004, Nuclear Physics B Proceedings Supplements, 132, 496
Wijnands R., van der Klis M., 1998, Nature, 394, 344
Woosley S., et al., 2004, ApJS, 151, 75
Yu H., Weinberg N. N., 2018, ApJ, 863, 53
van Paradijs J., Penninx W., Lewin W. H. G., 1988, MNRAS, 233, 437

Table A1. SAX J1808.4−3658 derived neutron star parameters for a fixed mass and radius

Parameter	Value
X	$0.57^{+0.13}_{-0.15}$
Z	$0.012^{+0.004}_{-0.003}$
$Q_{\rm b}$ (MeV/nucleon)	$0.6^{+0.1}_{-0.1}$
M ($M_\odot$)	1.4
R (km)	11.2
$\dot{m}_{\rm max}$ ($\dot{m}_{\rm Edd}$)	$0.035^{+0.002}_{-0.001}$
g (10^{14} cm s^{-2})	1.86
$1+z$	1.26
d (kpc)	$2.9^{+0.1}_{-0.1}$
$\xi_{\rm b}$	$0.9^{+0.1}_{-0.1}$
$\xi_{\rm p}$	$1.04^{+0.05}_{-0.04}$
$\cos i$	$0.35^{+0.08}_{-0.05}$

Table A2. SAX J1808.4−3658 derived neutron star parameters

Parameter	Value
X	$0.58^{+0.13}_{-0.15}$
Z	$0.013^{+0.006}_{-0.004}$
$Q_{\rm b}$ (MeV/nucleon)	$0.4^{+0.2}_{-0.2}$
M ($M_\odot$)	$1.6^{+0.5}_{-0.3}$
R (km)	$11.9^{+1.4}_{-1.2}$
$\dot{m}_{\rm max}$ ($\dot{m}_{\rm Edd}$)	$0.037^{+0.002}_{-0.002}$
g (10^{14} cm s^{-2})	$1.95^{+0.6}_{-0.4}$
$1+z$	$1.29^{+0.1}_{-0.06}$
d (kpc)	$3.3^{+0.2}_{-0.2}$
$\xi_{\rm b}$	$0.74^{+0.1}_{-0.10}$
$\xi_{\rm p}$	$0.87^{+0.1}_{-0.10}$
$\cos i$	$0.37^{+0.07}_{-0.05}$

APPENDIX A: ADDITIONAL MODEL RUNS

In this section we provide the results of additional model runs carried out in order to robustly test the MCMC code, as well as to replicate past works.

A1 Fixed mass and radius

We held mass and radius constant at $M = 1.4\,{\rm M}_\odot$ and $R = 11.2$ km to replicate the analysis of Galloway & Cumming (2006). The parameter predictions are presented in Table A1 and the probability contours for X, Z, $Q_{\rm b}$, d, $\xi_{\rm p}$ and $\xi_{\rm b}$ are presented in Figure A1.

The predicted hydrogen mass fraction in Table A1 matches within uncertainty of those predicted by Galloway & Cumming (2006) ($X_0 = 0.54$ for $Z = 0.02$, or $X_0 = 0.5$ for $Z = 0.016$). Galloway & Cumming (2006) inferred a base flux of $Q_{\rm b} = 0.325$ and a distance of 3.1–3.8 kpc which is just outside the lower limit of our 1-σ range of predictions for these parameters. Galloway & Cumming (2006) used a chi-squared minimisation approach to determine the parameters of interest given a fixed grid of parameters in X, Z and $Q_{\rm b}$ space to find the best fit burst fluence, recurrence times and alpha values. We used a more robust approach to determine the parameters of interest, and vary more parameters than just X, Z, and $Q_{\rm b}$ and so we do not expect our results to match exactly with those of Galloway & Cumming (2006). The composition constraints and distance estimate broadly agree with those found by Galloway & Cumming (2006) for a fixed NS mass and radius.

A2 Flat priors on mass and radius

Here we show the parameter limits when assuming a flat prior for mass and radius, rather than the Steiner et al. (2018) probability distribution. The parameter limits are reported in Table A2 and posterior distributions are plotted in Figure A2.

When assuming a flat prior range in mass and radius compared to assuming a more informative prior, we find that the mass is equally well constrained in both cases but that the radius is better constrained for the more informative prior run. Otherwise, all parameters remain approximately the same, except for surface gravity, with a stronger surface gravity required by the flat prior run.

This paper has been typeset from a TEX/LATEX file prepared by the author.

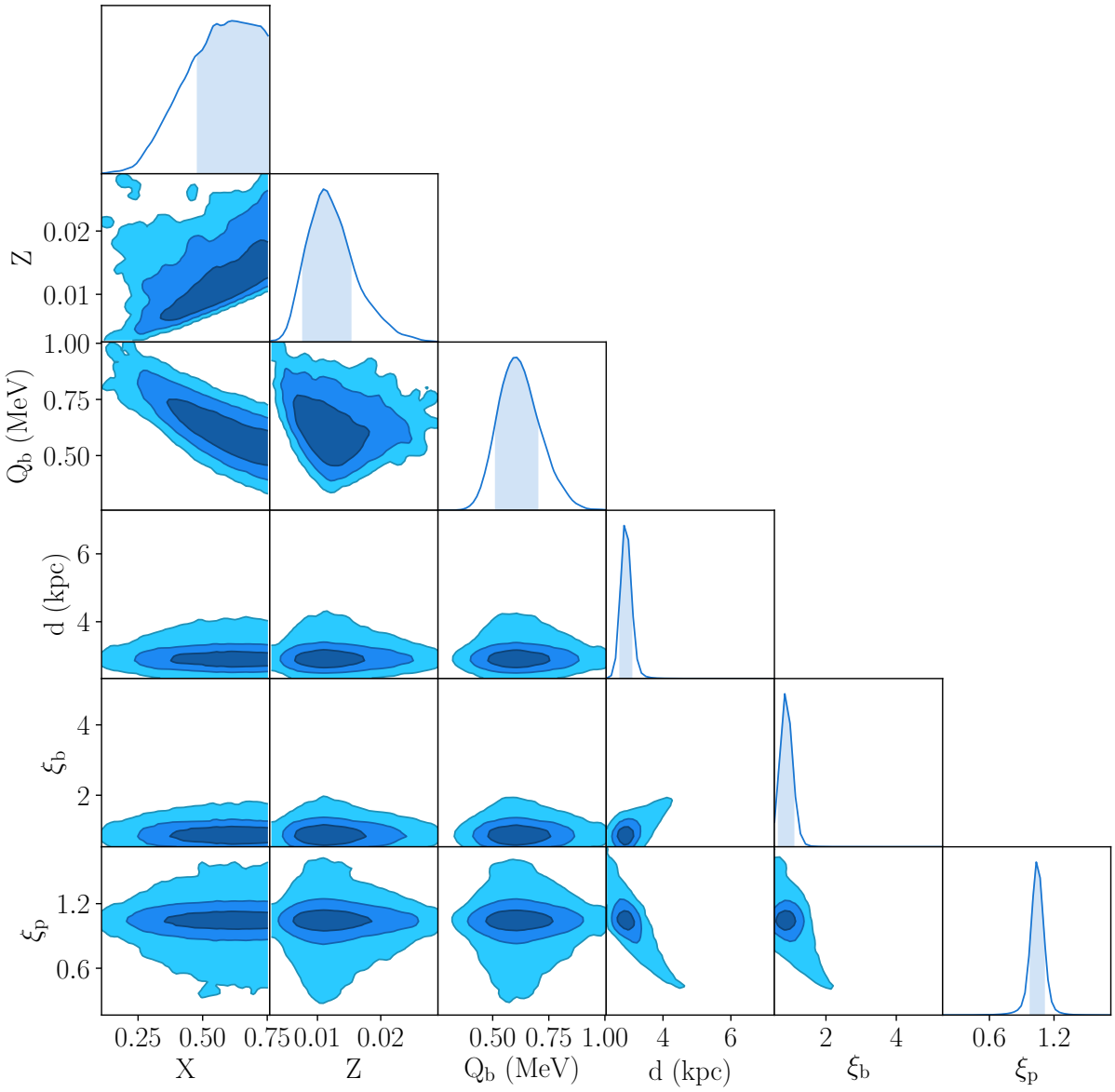

Figure A1. Marginalised probability distributions for hydrogen fraction X, CNO metallicity Z, base flux Q_b, distance d and anisotropy factors ξ_p and ξ_b for the MCMC run with fixed NS mass of 1.4 $M_\odot$ and radius of 11.2 km.

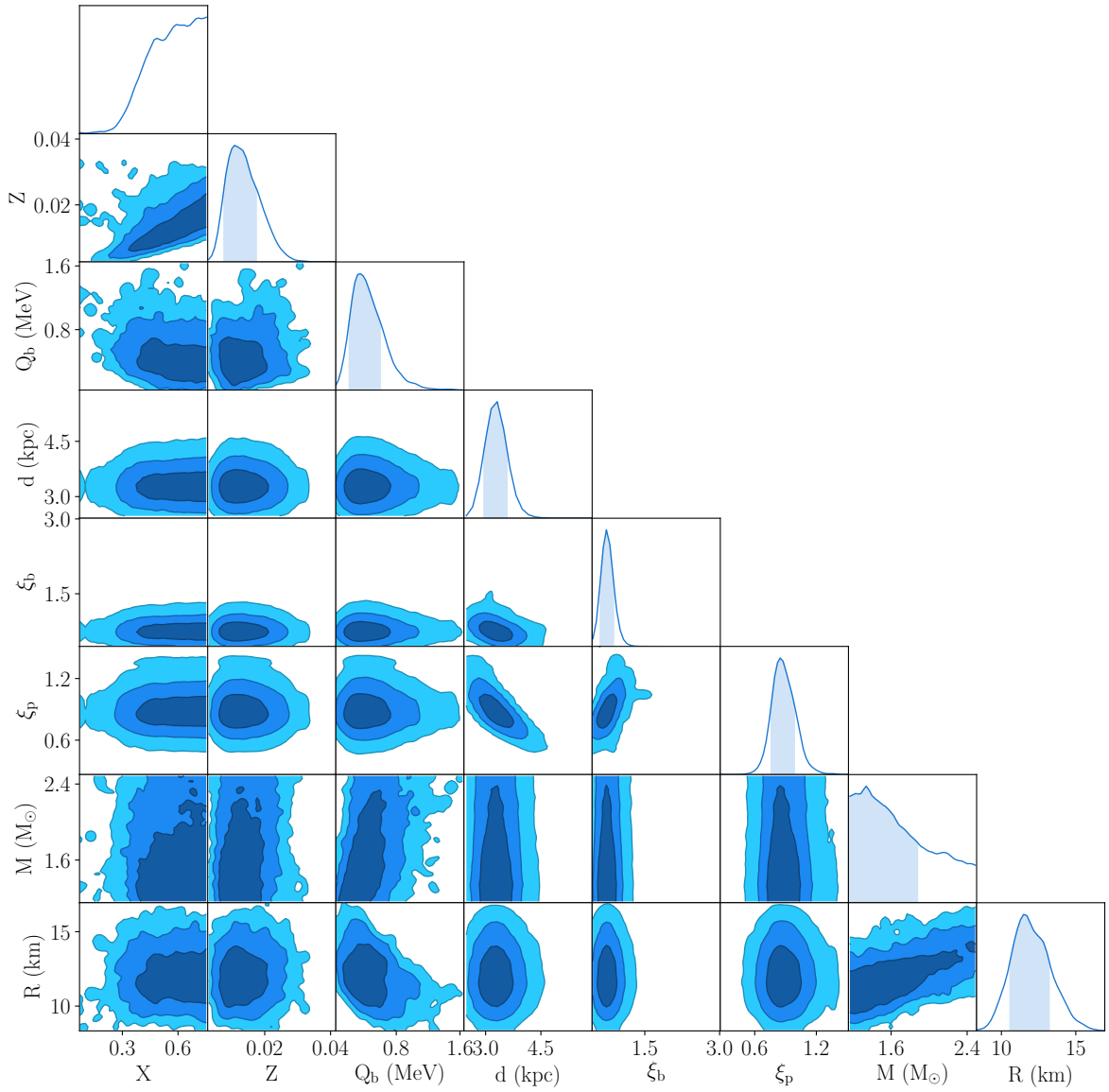

Figure A2. Marginalised probability distributions for hydrogen fraction X, CNO metallicity Z, base flux $Q_{\rm b}$, distance d and anisotropy factors $\xi_{\rm p}$ and $\xi_{\rm b}$, NS mass M, and NS radius R for the MCMC run with flat prior ranges for M and R.

6

TOWARDS THE EVOLUTION AND PROGENITORS OF ACCRETING NEUTRON STARS

The evolution and progenitors of accreting neutron star systems has been puzzling for many years, primarily due to the close orbital periods of many of these systems, as well as the phenomenon of recycled pulsars. Furthermore, most evolutionary studies do not take full advantage of constraints obtained from other types of models of these systems, such as X-ray burst models.

6.1 THE BINARY EVOLUTION OF SAX J1808.4−3658: IMPLICATIONS OF AN EVOLVED DONOR STAR

In this chapter, we use `MESA` (Paxton et al., 2011) and present a case study of the binary evolution of the accreting neutron star SAX J1808.4–3658, that has observationally well constrained parameters. Studies that have modelled the binary evolution of this system previously do not account for the fact that the donor star in this system is likely evolved, as we discovered in Chapter 5 through estimation of the accreted fuel composition. If the accreted fuel from the donor star is indeed approximately 50% helium, then the donor star must have once been much more massive than it is now (at $\approx 0.05\,M_\odot$), as stars that are $\lesssim 0.7\,M_\odot$ do not deplete hydrogen in their cores within the age of the Universe. In this study we also include a treatment of the effects of donor irradiation and evaporation from the pulsar and X-ray accretion luminosity on the overall evolution of the system.

Published in:
A. J. Goodwin and T. E. Woods (May 2020). 'The binary evolution of SAX J1808.4-3658: implications of an evolved donor star'. *MNRAS* 495.1, pp. 796–805. DOI: 10.1093/mnras/staa1234. arXiv: 2003.02970 [astro-ph.HE]

MNRAS **000**, 000–000 (2020) Preprint 6 October 2020 Compiled using MNRAS LATEX style file v3.0

The binary evolution of SAX J1808.4–3658: Implications of an evolved donor star

A. J. Goodwin[1]★ and T. E. Woods[2]

[1]*School of Physics and Astronomy, Monash University, Clayton, Victoria, Australia, 3800*
[2]*National Research Council of Canada, Herzberg Astronomy & Astrophysics Research Centre, 5071 West Saanich Road, Victoria, BC V9E 2E7, Canada*

Accepted 2020 April 28. Received 2020 April 15; in original form 2020 February 12

ABSTRACT

Observations of the accretion powered millisecond pulsar SAX J1808.4–3658 have revealed an interesting binary evolution, with the orbit of the system expanding at an accelerated rate. We use the recent finding that the accreted fuel in SAX J1808.4–3658 is hydrogen depleted to greatly refine models of the progenitor and prior evolution of the binary system. We constrain the initial mass of the companion star to 1.0–1.2 $M_\odot$, more massive than previous evolutionary studies of this system have assumed. We also infer the system must have undergone strongly non-conservative mass transfer in order to explain the observed orbital period changes. Following Jia & Li (2015), we include mass loss due to the pulsar radiation pressure on the donor star, inducing an evaporative wind which is ejected at the inner Lagrangian point of the binary system. The resulting additional loss of angular momentum resolves the discrepancy between conservative mass transfer models and the observed orbital period derivative of this system. We also include a treatment of donor irradiation due to the accretion luminosity, and find this has a non-negligible effect on the evolution of the system.

Key words: (stars:) binaries, neutron – X-rays: binaries

1 INTRODUCTION

Accretion powered millisecond pulsars (AMSPs) are rapidly spinning neutron stars in binary orbits that are thought to be the progenitors of radio millisecond pulsars (e.g., Tauris & van den Heuvel 2006). Pulsars are born with strong ($\approx 10^{12}$ G) magnetic fields, and their rotation periods spin down over time due to rotational loss of energy (e.g., Bhattacharya & van den Heuvel 1991). The peculiar observation of fast-spinning radio pulsars with weak ($\approx 10^8$ G) magnetic fields in the 1980s motivated the theory that these are "recycled" pulsars that have been spun up through accretion of mass from a binary companion star and now appear as radio millisecond pulsars (e.g., Bhattacharya & van den Heuvel 1991). Further evidence for this theory was that a large fraction of radio millisecond pulsars were observed to be in binary systems (Bhattacharya & van den Heuvel 1991). It was not until 1998 that this "recycling scenario" theory was confirmed by the observation of an actively accreting millisecond pulsar (AMSP) in a binary system, SAX J1808.4–3658 (Chakrabarty & Morgan 1998; Wijnands & van der Klis 1998). Since this discovery, more than 17 other AMSP systems have been discovered (see e.g., Patruno & Watts 2012, for a review). Now, more than 20 years after the first AMSP was discovered, it is thought that millisecond pulsars go through an accretion phase, in which they are spun up and X-ray emission is observed. Then, when the mass transfer rate reduces, they switch on as rotation-powered radio millisecond pulsars. This theory is supported by the observation of swings between rotation and accretion power in the millisecond binary pulsar IGR J18245–2452 (Papitto et al. 2013), which provides direct evidence that a rotation powered radio millisecond pulsar can switch on during periods of low mass inflow in an AMSP system, demonstrating an evolutionary pathway for AMSPs to evolve into radio pulsars.

Numerical studies of the formation channels of AMSP systems have been successful in modelling their population as a whole, but individual systems are often insufficiently constrained to reliably determine their prior evolutionary history (e.g., Podsiadlowski et al. 2002; Nelson & Rappaport 2003). Recent efforts have used state of the art models com-

★ E-mail: ajgoodwin.astro@gmail.com

bined with accreting neutron star observations, specifically those that exhibit Type I (thermonuclear) X-ray bursts, to constrain system parameters such as the accreted fuel's composition, the accretion rate, and the neutron star mass and radius (Goodwin et al. 2019a). These new constraints enable more precise, system dependent, models of the binary evolution to be obtained, potentially clearing the way to constraining the mass transfer history and efficiency of these systems.

SAX J1808.4–3658 goes into outburst approximately every 4 years (Goodwin et al. 2019b; Del Santo et al. 2015; Markwardt et al. 2011; Markwardt & Swank 2008; Markwardt et al. 2002), and is the most well studied and observationally constrained AMSP of its kind. The orbital period evolution of SAX J1808.4–3658 has proven consistently puzzling, as its orbital period derivative was measured to be an order of magnitude larger than expected by conservative mass transfer models (di Salvo et al. 2008). The currently prevailing theory for the unusually rapid orbital evolution of SAX J1808.4–3658 is the radio-ejection model, in which a significant amount of matter is ejected from the inner Lagrangian point of the system during quiescence. In the radio-ejection model, the radiation pressure from the pulsar on the infalling accreted matter stops the matter at the inner Lagrangian point, and ejects it from the system (e.g. Burderi et al. 2002). This evolutionary phase occurs during the pulsar's transition from an AMSP to a rotation-powered radio millisecond pulsar, in a semi-detached binary.

SAX J1808.4–3658 is one of the few individual AMSPs whose evolution has been extensively modelled, due to the large amount of observational data available. However, none of these evolutionary studies have accounted for the fact that the donor star in this system has been shown to be significantly evolved, as evidenced from model constraints on the accreted fuel composition during X-ray outbursts (Goodwin et al. 2019a; Johnston et al. 2018; Galloway & Cumming 2006). An evolved donor increases the required initial mass of the donor star, since small (<0.7 $M_\odot$) donors could not have depleted hydrogen in their cores within the Hubble time.

Tailo et al. (2018) simulated evolutionary tracks for SAX J1808.4–3658 using the stellar evolution code ATON 2.0 (Ventura et al. 2008). They followed the binary evolution of the system beginning with an orbital period of ≈6.6 hr and modelled evolution driven by angular momentum losses via magnetic braking, gravitational radiation, and mass loss. They accounted for effects of irradiation of the donor by the X-ray emission and the spin-down luminosity of the pulsar, but did not include evaporation in their models. They included a treatment of radio ejection, in which the system ejects mass lost from the donor, as well as its angular momentum, if the period of the system exceeds the critical period predicted. They start with a companion mass of 0.75 $M_\odot$, NS mass of 1.33 $M_\odot$ and P=6.6 hrs, assuming a NS radius of 10 km.

Chen (2017) also simulated evolutionary tracks of SAX J1808.4–3658 using MESA, where the evolution of the binary system was driven by angular momentum losses from gravitational wave radiation, magnetic braking, and mass loss. They included evaporation driven by the spin-down luminosity of the pulsar and irradiation driven by the high X-ray luminosity during transient outburst phases. These processes induce a high wind-loss rate ($\sim 10^{-9}$ $M_\odot$ yr^{-1}, eventually resulting in a detached binary system, motivating the authors to conclude that SAX J1808.4–3658 would evolve into a black widow-like system.

Both of these studies required that magnetic braking continues to be active once the companion star becomes fully convective, with Tailo et al. (2018) arguing that due to effects of irradiation on the internal structure of the companion star, it would not be completely convective even at its very small presently observed mass. These studies found that a mass loss rate of $\sim 10^{-9}$ $M_\odot$ yr^{-1} from the inner Lagrangian point is required in order to match the observed orbital period derivative of this system. Neither of the best evolutionary tracks of these studies included an evolved companion star, however, with approximately 50% helium at the surface at the current evolutionary phase of the system being required by the observed bursting behaviour. Tailo et al. (2018) do not discuss the H mass fraction at the surface of the donor star for their best model, but it is assumed to be somewhere between 0.7–0.75, and Chen (2017) found that the current H mass fraction at the surface of the donor star was 0.68 in their best model. Neither of these H mass fractions support the evidence for a depleted H mass fraction (X≈ 0.57) of the accreted fuel during X-ray outbursts found by Goodwin et al. (2019a), Johnston et al. (2018) as well as Galloway & Cumming (2006).

In particular, using a Markov Chain Monte Carlo method to match observations of accreting neutron stars in outburst with a semi-analytic ignition model, Goodwin et al. (2019a) obtained constraints on the neutron star mass, radius, accretion rate, accreted fuel composition and distance to the AMSP SAX J1808.4–3658. They found that a present neutron star mass of approximately 1.6 $M_\odot$ (higher than the traditionally adopted value of 1.4 $M_\odot$ (e.g. Steiner et al. 2018) and a H fraction of approximately 0.57 for the accreted fuel were required in order to match burst observations. This result implies that not only has the neutron star gained mass through accretion, but that the companion star has undergone significant hydrogen-burning, placing a strong lower bound on its initial mass. In this work we calculate the binary evolution pathway of SAX J1808.4–3658 starting after the neutron star has formed, and taking into account the hydrogen depletion in the core of the donor star, in order to gain insight into the evolution of this system and its progenitor.

In Section 2 we describe the methods and physics used to model the evolutionary tracks of SAX J1808.4–3658. In Section 3 we present our results, providing evolutionary tracks including the effects of evaporation and without the effects of evaporation. Finally in Section 4 we discuss the implications of our results and present our conclusions.

2 METHODS

We calculated possible binary evolution pathways for SAX J1808.4–3658 using the Modules for Experiments in Stellar Astrophysics stellar evolution binary program version 9575 (MESA; Paxton et al. 2011, 2013, 2015, 2019). We explored a range of initial donor star masses (0.6–2.0 $M_\odot$) and orbital separations (0.4–3 d), with a fixed initial neutron star point mass of 1.4 $M_\odot$. We initialised the donor star as a zero-age

main sequence star with a hydrogen mass fraction of X=0.7 and metallicity of Z=0.02. We used the Ritter mass transfer scheme (Ritter 1988) and the Eggleton Roche Lobe Overflow scheme (Eggleton 1983) with Eddington limited accretion.

The rate at which angular momentum is lost from the system is dependent on gravitational radiation, mass loss, and magnetic braking, with the total change in angular momentum given by

$$\dot{J} = \dot{J}_{\rm GR} + \dot{J}_{\rm ML} + \dot{J}_{\rm MB} \tag{1}$$

For the rate of angular momentum loss due to gravitational radiation, $\dot{J}_{\rm GR}$, we used the default MESA implementation of the Peters formulae (Peters 1964) assuming zero initial eccentricity, as described in Paxton et al. (2015),

$$\dot{J}_{\rm GR} = -\frac{32}{5c^5}\left(\frac{2\pi G}{P_{\rm orb}}\right)^{7/3}\frac{(M_{\rm NS}M_{\rm d})^2}{(M_{\rm NS}+M_{\rm d})^{2/3}} \tag{2}$$

where c is the speed of light, $M_{\rm d}$ is the donor star mass, $M_{\rm NS}$ is the neutron star mass, G is the gravitational constant, and $P_{\rm orb}$ is the orbital period.

For the angular momentum changes due to magnetic braking, $\dot{J}_{\rm MB}$, we used the default MESA prescription, following Rappaport et al. (1983),

$$\dot{J}_{\rm MB} = -3.8\times10^{-30}M_1R_\odot^4\left(\frac{R_{\rm d}}{R_\odot}\right)^{\gamma_{mb}}\omega^3 \tag{3}$$

where ω is the rotational angular frequency of the donor star, $R_{\rm d}$ is the radius of the donor star, and γ_{mb} is the magnetic braking index, which we fixed at the default MESA value of 3.[1] We did not switch magnetic braking off once the donor star has sufficiently reduced in mass to (in isolation) become fully convective ($\sim 0.3M_\odot$). As discussed in Tailo et al. (2018), due to the effects of irradiation on the internal structure of the donor star, it may not be fully convective at these very low masses, and magnetic braking could still be active in the system.

The final contribution to orbital angular momentum evolution is mass loss, which can cause different amounts of angular momentum loss depending on where the mass is ejected from the system. By default, MESA includes mass loss prescriptions for mass ejected via a fast isotropic wind from either star, or a circumbinary coplanar toroid. Here, we include mass loss due to the radiation pressure of the pulsar on the donor star, causing an evaporative wind to blow that is ejected at the inner Lagrangian point of the binary system. The default MESA mass transfer efficiency, $f_{\rm mt}$, is given by

$$f_{\rm mt} = 1 - \alpha_{\rm mt} - \beta_{\rm mt} - \delta_{\rm mt} \tag{4}$$

where $\alpha_{\rm mt}$ is the efficiency of mass loss from the vicinity of the donor, $\beta_{\rm mt}$ from the accretor, and $\delta_{\rm mt}$ from the circumbinary coplanar toroid. We assumed there is no mass lost from the immediate vicinity of the donor or the circumbinary coplanar toroid, and chose an arbitrary $\beta_{\rm mt} = 0.5$ for mass lost from the vicinity of the accretor. Upon testing, using different values of $\beta_{\rm mt}$ did not significantly affect the evolutionary tracks of our calculations. The results for the models we calculated using only the angular momentum losses outlined above are presented in Section 3.3.

In addition to the standard MESA mass loss implementation, we also defined an evaporation efficiency, $f_{\rm ev}$, which is the efficiency by which mass is ejected via the evaporative wind at the inner Lagrangian point of the binary system. This is implemented via an extras routine in MESA, as the prescription is not included in the standard version of the software. As in Jia & Li (2015), we assumed the pulsar radiation causes evaporation of the donor star during quiescence, when the mass transfer is temporarily interrupted, driving a wind which is given by (van den Heuvel & van Paradijs 1988; Stevens et al. 1992)

$$\dot{M}_{\rm d,evap} = -\frac{f_{\rm ev}}{2v_{\rm d,esc}^2}L_p\left(\frac{R_{\rm d}}{a}\right)^2 \tag{5}$$

where $v_{\rm d,esc}$ is the escape velocity of the donor star, a is the orbital separation, and L_p is the spin-down luminosity of the pulsar, $L_p = 4\pi^2 I\dot{P}/P^3$, where I is the pulsar moment of inertia. This evaporative wind is then added to the total wind mass transfer from the donor star, which is ejected at the inner Lagrangian point, adding to the angular momentum losses of the system. For the pulsar properties, we assume the pulsar spin evolution follows the standard magnetic dipole radiation model described by Shapiro & Teukolsky (1983), assuming $P_0 = 3$ ms (and in our calculations $P_f = 3.1$ ms), $\dot{P} = 1\times10^{-20}$ ss^{-1}, $B \sim 10^8$ G, and $I = 10^{45}$ gcm^{-2}. The evolution of the pulsar spin period we adopt thus neglects spin-up due to accretion, however, on comparison of a model calculation with a faster initial spin period pf $P_0 = 2.4$ ms (and $P_f = 2.5$ ms), the evolutionary tracks were very similar, and the best fit model remained the same.

The total angular momentum changes due to mass loss in our calculations are thus given by

$$\dot{J}_{\rm ML} = (\beta_{\rm mt}\dot{M}_{\rm d,RLOF} + \dot{M_{\rm d,w}})L_1a^2\omega \tag{6}$$

where $\omega = 2\pi/P$ and L_1 is the distance from the inner Lagrangian point to the center of mass, in units of the separation, a. As in Beer et al. (2007), if $\frac{M_{\rm NS}}{M_{\rm d}} \leq 10.0$ then L_1 is given by Warner (1976)

$$L_1 = 0.5 + 0.227\log\frac{M_{\rm NS}}{M_{\rm d}} \tag{7}$$

If $\frac{M_{\rm NS}}{M_{\rm d}} \geq 10.0$ then L_1 is given by Kopal (1959)

$$L_1 = \left|\frac{M_{\rm d}}{M_{\rm d}+M_{\rm NS}} - (1.0 - w_K + \frac{w_K^2}{3.0} + \frac{w_K^3}{9.0})\right| \tag{8}$$

$$w_K = \left(\frac{1.0}{3.0(1+(M_{\rm NS}/M_{\rm d}))}\right)^{1/3} \tag{9}$$

Thus, in our calculations, any mass that is released from

[1] Note that while Chen (2017) write that a magnetic braking index of 4 was used in their calculations, we can only replicate their published results with the default MESA value, which is 3. The correct magnetic braking index is not very well constrained (see Rappaport et al. 1983), so we simply adopt the MESA default value in this work.

the donor and not transferred to the accretor is ejected from the system with the specific angular momentum of the inner Lagrangian point. The results for the models we calculated including donor evaporation and mass ejection at the inner Lagrangian point are given in Section 3.4.

We also included irradiation of the donor star due to the X-ray accretion luminosity. We did not include irradiation due to heating caused by the pulsar luminosity, as this is typically orders of magnitude lower than the heating caused by accretion. We used the MESA accretion-powered irradiation prescription, which requires an accretor radius (11.2 km (Steiner et al. 2018)) and then calculates the X-ray luminosity as:

$$L_X = \frac{G M_{\rm NS} \dot{M}_{\rm NS}}{R_{\rm NS}} \tag{10}$$

where $\dot{M}_{\rm NS}$ is the accretion rate onto the neutron star.

The irradiation flux incident on the companion is then calculated as:

$$F_{\rm irr} = \epsilon_{\rm irr} \frac{L_X}{4\pi a^2} \tag{11}$$

where a is the binary separation.

We chose to deposit the extra heating due to irradiation at a column depth of $10\,{\rm g\,cm^{-2}}$, at the very surface of the companion star. Finally, we limited the maximum irradiation flux to $3\times10^9\,{\rm erg\,s^{-1}\,cm^{-2}}$, since there is an unknown irradiation efficiency of the accretion luminosity. It is likely the accretion disk could prevent some of the accretion flux being incident on the companion star, and most likely all of the accretion luminosity would not irradiate the companion. Tailo et al. (2018) assumed an irradiation efficiency in the range of 1%–2%. We arrive at a maximum irradiation flux of $3\times10^9\,{\rm erg\,s^{-1}\,cm^{-2}}$ by assuming $M_{\rm NS} = 1.4\,{\rm M_\odot}$, $R_{\rm NS} = 11.2\,{\rm km}$, the time-averaged long term accretion rate of the system, $\dot{M}_{\rm NS} = 2.55\times10^{12}$ msun/yr, $\epsilon_{\rm irr} = 0.015$, and an average orbital separation of $a = 1\times10^{11}\,{\rm cm}$. The companion star is consistently irradiated at $3\times10^9\,{\rm erg\,s^{-1}\,cm^{-2}}$ for the duration of accretion in our calculations.

The results for the models we calculated including donor evaporation, mass ejection at the inner Lagrangian point, and irradiation are given in Section 3.5.

We used the default MESA binary timestep controls for all evolutionary tracks calculated. As a test, we reduced all of the 'varcontrol' timestep parameters by a factor of 10 and observed no difference in the predicted evolutionary tracks for the smaller timesteps.

The observed orbital epheremeris and predicted system parameters for SAX J1808.4–3658, compiled from more than 20 years of observations of the source, are listed in Table 1. We calculated a grid of models with a range of initial companion star masses and initial orbital periods, fixing the neutron star mass to $1.4\,{\rm M_\odot}$, and the initial composition of the companion star to be $X = 0.7$, $Z = 0.02$. We determined the preferred initial companion star mass, and minimum and maximum possible orbital periods as outlined in Section 3, and varied the mass in increments of $0.05\,{\rm M_\odot}$, orbital period in increments of 0.05 d, and evaporation efficiency in increments of 0.01.

Table 1. Observed parameters for SAX J1808.4–3658

Parameter	Value	Units	Ref.
$P_{\rm orb}$	7249.1569±0.0001	s	1
$\dot{P}_{\rm orb}$	(1.6±0.7)×10^{-12}	s s^{-1}	2, 3, 4, 5
$M_{\rm NS}$	$1.5^{+0.6}_{-0.3}$	$M_\odot$	6
$M_{\rm c}$	$0.05^{+0.05}_{-0.03}$	$M_\odot$	7
$X_{\rm c}$	$0.57^{+0.13}_{-0.14}$		6

Ref.: 1. Papitto et al. (2005), 2. Hartman et al. (2008), 3. di Salvo et al. (2008), 4. Hartman et al. (2009), 5. Bult et al. (2019b), 6. Goodwin et al. (2019a), 7. Bildsten & Chakrabarty (2001)

3 RESULTS

3.1 Minimum initial mass of companion star

In order to set a strong lower bound on the minimum required mass of the companion star, we used MESA star to evolve a single star over the age of the Universe (which we assume is 14 billion years), to find the minimum mass star which can achieve a central hydrogen fraction of 0.57. We examined the central hydrogen fraction at the end of evolution for a range of initial masses, and found that a star with initial mass of $0.6\,{\rm M_\odot}$ is the minimum mass that has a central hydrogen fraction of 0.57 within 14 billion years of evolution.

3.2 Maximum and minimum initial orbital periods

The maximum initial period is set by the bifurcation period, which is the maximum period at which a system could evolve into a close low mass X-ray binary with an ultra-short period within the Hubble time (van der Sluys et al. 2005). For a SAX J1808.4–3658-like system the bifurcation period is approximately 3 d (van der Sluys et al. 2005).

We determined the minimum initial orbital period by calculating the Roche Lobe radius of the system for an adopted minimum mass ratio of $q = 0.5$ with $M_{\rm d} = 0.7\,{\rm M_\odot}$ and $M_{\rm NS} = 1.4\,{\rm M_\odot}$. We used the Roche Lobe formula from Eggleton (1983),

$$\mathrm{rL} = \frac{0.49 q^{2/3}}{0.6 q^{2/3} + \ln(1+q^{1/3})} \tag{12}$$

and then found the separation to be $\mathrm{R_{ZAMS}}/\mathrm{rL}$, where $\mathrm{R_{ZAMS}} = 6.234\times10^{10}\,{\rm cm}$ to infer the period. This minimum period is 0.4 d.

3.3 Evolution without donor evaporation

We first calculated models (labelled "A") assuming conservative mass transfer (setting $\beta_{\rm mt} = 0.5$) with no evaporative wind (i.e., $f_{\rm ev} = 0.0$) or donor irradiation. A full list of the best-fitting Model A initial conditions and results is given in Table 2.

We find that Model A is unable to reproduce the observed properties of SAX J1808.4–3658, in particular the orbital period derivative. In Figure 1, it is clear that, at the current observed orbital period of 2.01 hours, the predicted orbital period derivative of the system is approximately two orders of magnitude lower than the observed value for all

[p]

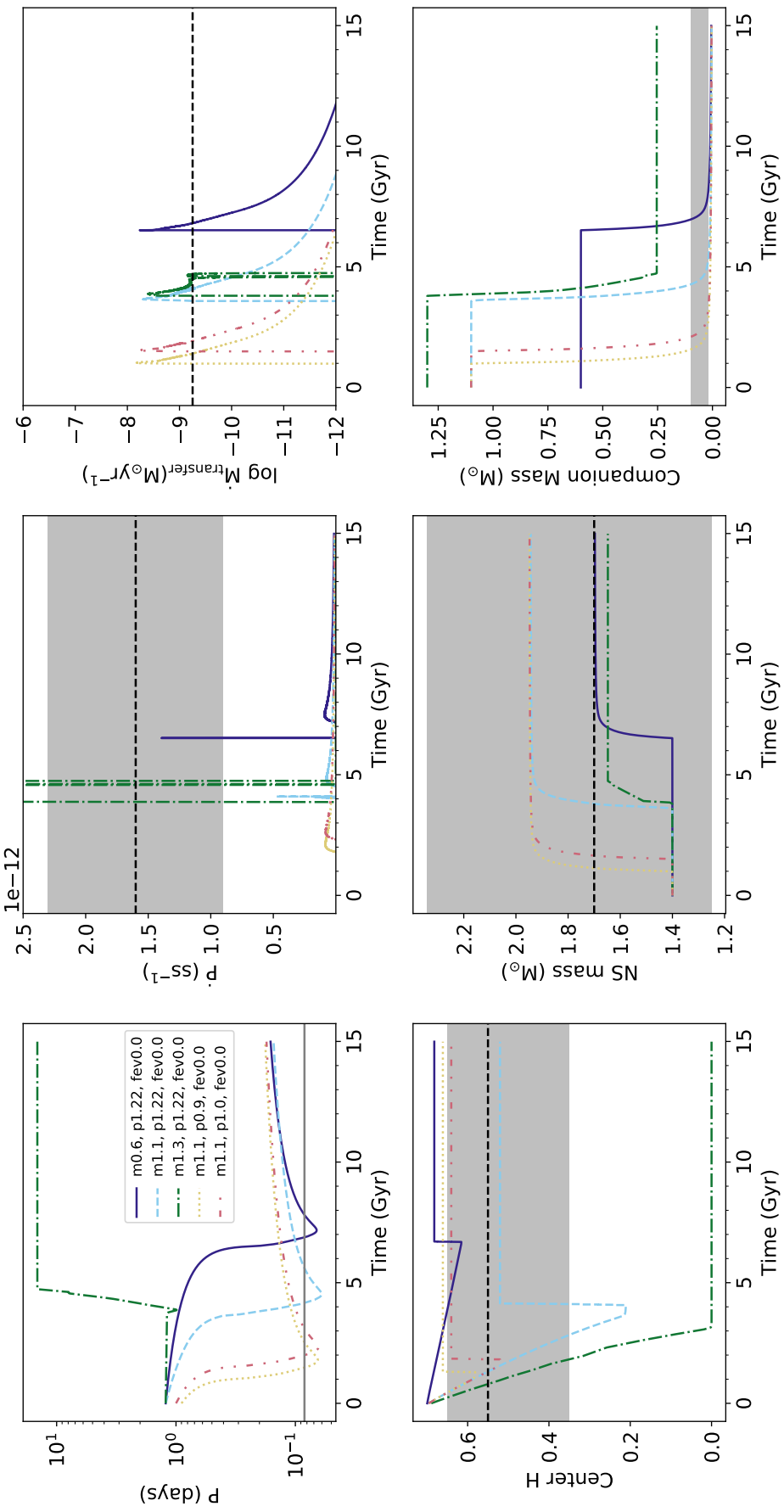

Figure 1. Model A results: evolution without donor evaporation or irradiation ($f_{\rm ev} = 0.0$) for a range of initial companion masses ($M_{\rm d,i}$) and orbital periods ($P_{\rm i}$). The different evolutionary tracks plotted are: $M_{\rm d,i} = 0.6\,{\rm M}_\odot$, $P_{\rm i} = 1.22$ d (purple solid line), $M_{\rm d,i} = 1.1\,{\rm M}_\odot$, $P_{\rm i} = 1.22$ d (blue dashed line), $M_{\rm d,i} = 1.3\,{\rm M}_\odot$, $P_{\rm i} = 1.22$ d (green dashed-dot line), $M_{\rm d,i} = 1.1\,{\rm M}_\odot$, $P_{\rm i} = 0.9$ d (orange dotted line), and $M_{\rm d,i} = 1.1\,{\rm M}_\odot$, $P_{\rm i} = 1.0$ d (red dashed-dot-dot line). All panels show the parameter evolution over time, with the individual panels showing: *Top panels, left to right:* Orbital period, orbital period derivative, mass transfer rate onto the NS. *Bottom panels, left to right:* Central hydrogen mass fraction of the donor star, NS mass, donor star mass. The dashed black line and grey regions indicate the current observed value of the parameter, and uncertainty, respectively.

Table 2. Model A results: evolution without donor evaporation

Parameter	Value	Units
$M_{\rm d,i}$	1.1	$M_\odot$
$M_{\rm d,f}$	0.02	$M_\odot$
$M_{\rm NS,i}$	1.4	$M_\odot$
$M_{\rm NS,f}$	1.94	$M_\odot$
$P_{\rm i}$	1.22	d
$P_{\rm f}$	0.0834	d
$\dot{P}_{\rm f}$	5.07e-14	$s\,s^{-1}$
$f_{\rm ev}$	0.0	
$X_{\rm c,i}$	0.7	
$X_{\rm c,f}$	0.52	

model combinations of initial companion masses and orbital periods that evolve to have a period as short as the current observed orbital period of the system. This finding is consistent with the earlier work of di Salvo et al. (2008) and Burderi et al. (2009), who showed that such a high orbital period derivative can not be accounted for by conservative mass transfer alone. As concluded by Hartman et al. (2008), Hartman et al. (2009), Patruno et al. (2017), Chen (2017), and Tailo et al. (2018), the rapid change in the orbit that is inducing such a high orbital period derivative could be caused by either a highly inefficient mass transfer scenario that this model does not account for, or the observed orbital period derivative could be a short term evolutionary phase caused by tidal dissipation and magnetic activity in the companion. This kind of short timescale orbital period evolution should have quasi-cyclic variability with timescales ~10 years. The latest outburst of SAX J1808.4–3658 (Bult et al. 2019a; Goodwin et al. 2019b) provided the 20th year of observations of the orbital period derivative, and has shown an interesting development. Bult et al. (2019b) measured a long-term orbital period derivative of $(1.6 \pm 0.7) \times 10^{-12}\,{\rm ss}^{-1}$, finding an interesting possible quasi-periodic variability in the orbit with a ≈ 7 s amplitude around an expanding orbit, or a ≈ 20 s amplitude modulation around a constant binary orbit. Additional monitoring of future outbursts would be necessary to differentiate between these scenarios. In the next section, we model the evolution assuming that the binary orbit is not constant, and is expanding at an accelerated rate.

3.4 Evolution with donor evaporation

We then evolved a grid of models with evaporation efficiencies ranging from 0.001–0.7, in which the evaporative wind is ejected at the inner Lagrangian point of the binary system with no irradiation of the donor star (labelled "Model B"), as described in Section 2. The parameters for the model with the closest match to the observed values, as well as selected models with different initial orbital periods, companion masses, and evaporation efficiencies, are listed in Table 3 and plotted in Figures 2 and 3.

The best fit model including only donor evaporation, with $M_{\rm d,i} = 1.1\,M_\odot$, $P_{\rm i} = 1.22$ d, and $f_{\rm ev} = 0.2$, matches all of the observed system parameters within their respective uncertainties. Due to the uncertainty of the measured orbital period derivative, a range of evaporation efficiencies (0.15–0.3) produce orbital period derivatives at the current observed orbital period of the system that match the observed change with time. Thus, we cannot constrain the evaporation efficiency with higher accuracy, but adopt $f_{\rm ev} \approx 0.2$ as the "best" value for Model B.

3.5 Evolution with donor evaporation and irradiation

3.5.1 Retracing the evolution of SAX J1808.4–3658

Finally, we evolved a grid of models with evaporation efficiencies ranging from 0.001–0.7, in which the evaporative wind is ejected at the inner Lagrangian point of the binary system and including the effects of irradiation of the donor star due to the accretion luminosity (labelled "Model C"), as described in Section 2. The parameters for the model with the closest match to the observed values, as well as selected models with different initial orbital periods, companion masses, and evaporation efficiencies, are listed in Table 4 and plotted in Figures 2 and 3.

When including the effect of irradiation of the donor star on the binary evolution, we require a much higher evaporation efficiency ($f_{\rm ev} = 0.5$) in order to match the observed orbital period derivative, for the model with $M_{\rm d,i} = 1.1\,M_\odot$, $P_{\rm i} = 1.22$ d. For Model C, including irradiation we find an equally good fit of the observed parameters for a shorter initial orbital period of $P_{\rm i} = 1.0$ d, but not for a smaller initial companion mass. Similarly to Model B, due to the uncertainty of the measured orbital period derivative, a range of evaporation efficiencies (0.4–0.6) produce orbital period derivatives at the current observed orbital period of the system that match the observed orbital period derivative. Thus, we cannot constrain the evaporation efficiency with higher accuracy, but adopt $f_{\rm ev} \approx 0.5$ as the "best" value for Model C.

3.5.2 The effect of evaporation and irradiation feedback on the donor star evolution

We explored the effect of evaporation and irradiation feedback on the evolution of the mass and radius of the donor star, and found that when the evaporative wind commences, the donor star immediately begins to expand while continuing to lose mass through Roche Lobe overflow. The evolution of the mass and radius of the donor star for Model B and Model C is plotted in Figure 4, where the black star indicates the commencement of the evaporative wind. This rapid expansion confirms that due to the effects of the pulsar irradiation on the donor star, the surface of the star heats up and the star expands to become a very fluffy, low mass "brown dwarf". Interestingly, for Model C, in which we include the effects of donor irradiation by the accretion luminosity, the donor star does not expand nearly as much as Model B, in which we only include evaporation feedback.

Figure 4 shows the evolution of the internal structure of the donor star as a Kippenhahn diagram (right panel). At t ≈ 3000 Myr, we see the convective envelope of the donor star reach all the way to the core of the star, and it becomes fully convective.

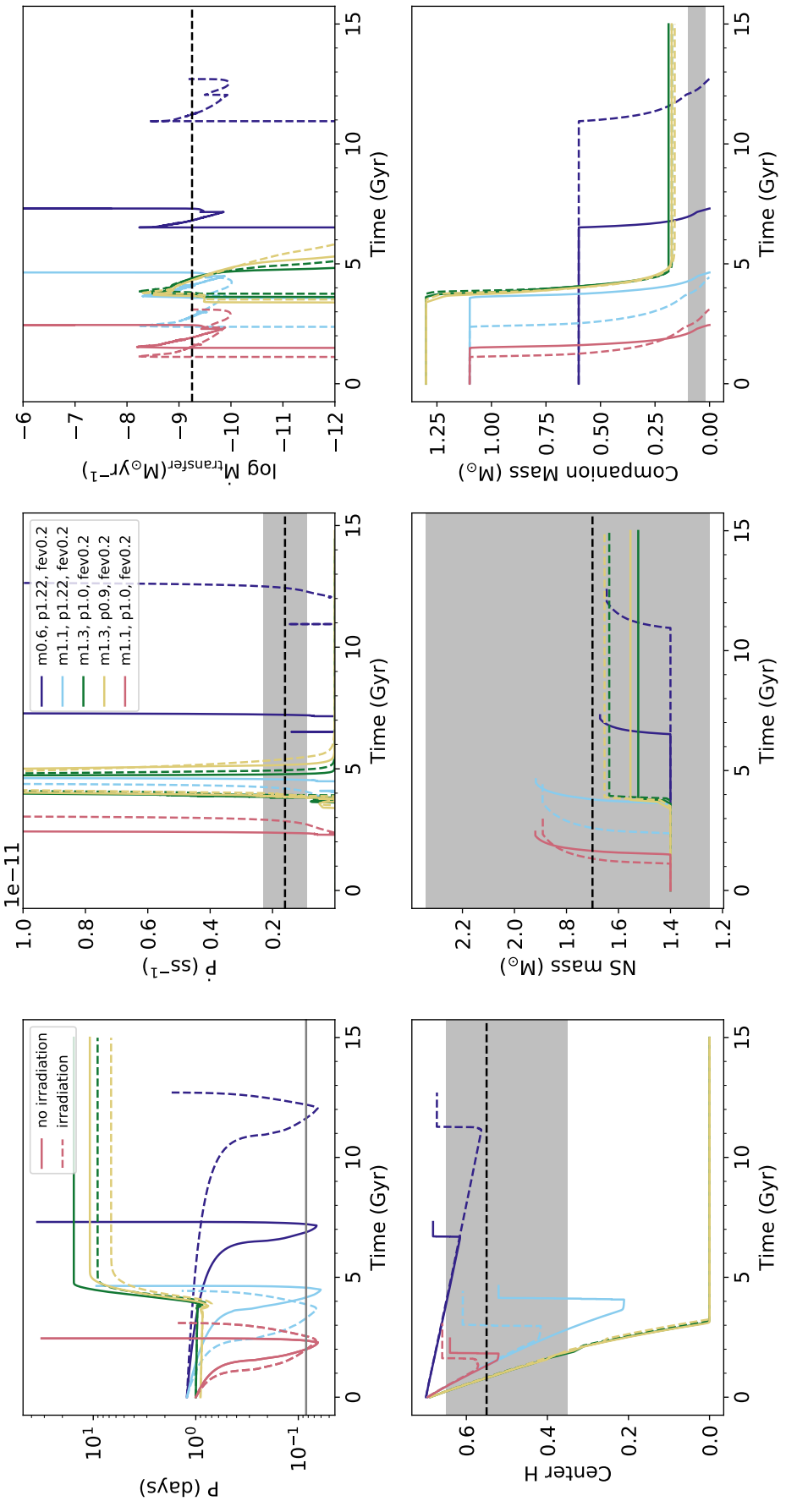

Figure 2. Model B (solid line) and Model C (dashed line) results: Evolution with donor evaporation and irradiation for a range of initial companion masses ($M_{\rm d,i}$) and orbital periods ($P_{\rm i}$), with fixed evaporation efficiency ($f_{\rm ev}$). The different evolutionary tracks plotted are: $M_{\rm d,i} = 0.6\,{\rm M}_\odot$, $P_{\rm i} = 1.22$ d, $f_{\rm ev} = 0.2$ (purple), $M_{\rm d,i} = 1.1\,{\rm M}_\odot$, $P_{\rm i} = 1.22$ d, $f_{\rm ev} = 0.2$ (blue), $M_{\rm d,i} = 1.3\,{\rm M}_\odot$, $P_{\rm i} = 1.0$ d, $f_{\rm ev} = 0.2$ (green), $M_{\rm d,i} = 1.3\,{\rm M}_\odot$, $P_{\rm i} = 0.9$ d, $f_{\rm ev} = 0.2$ (orange), and $M_{\rm d,i} = 1.1\,{\rm M}_\odot$, $P_{\rm i} = 1.0$ d, $f_{\rm ev} = 0.2$ (red). All panels show the parameter evolution over time, with the individual panels showing: *Top panels, left to right:* Orbital period, orbital period derivative, mass transfer rate onto the NS. *Bottom panels, left to right:* Central hydrogen mass fraction of the donor star, NS mass, donor star mass. The dashed black line and grey regions indicate the current observed value of the parameter, and uncertainty, respectively.

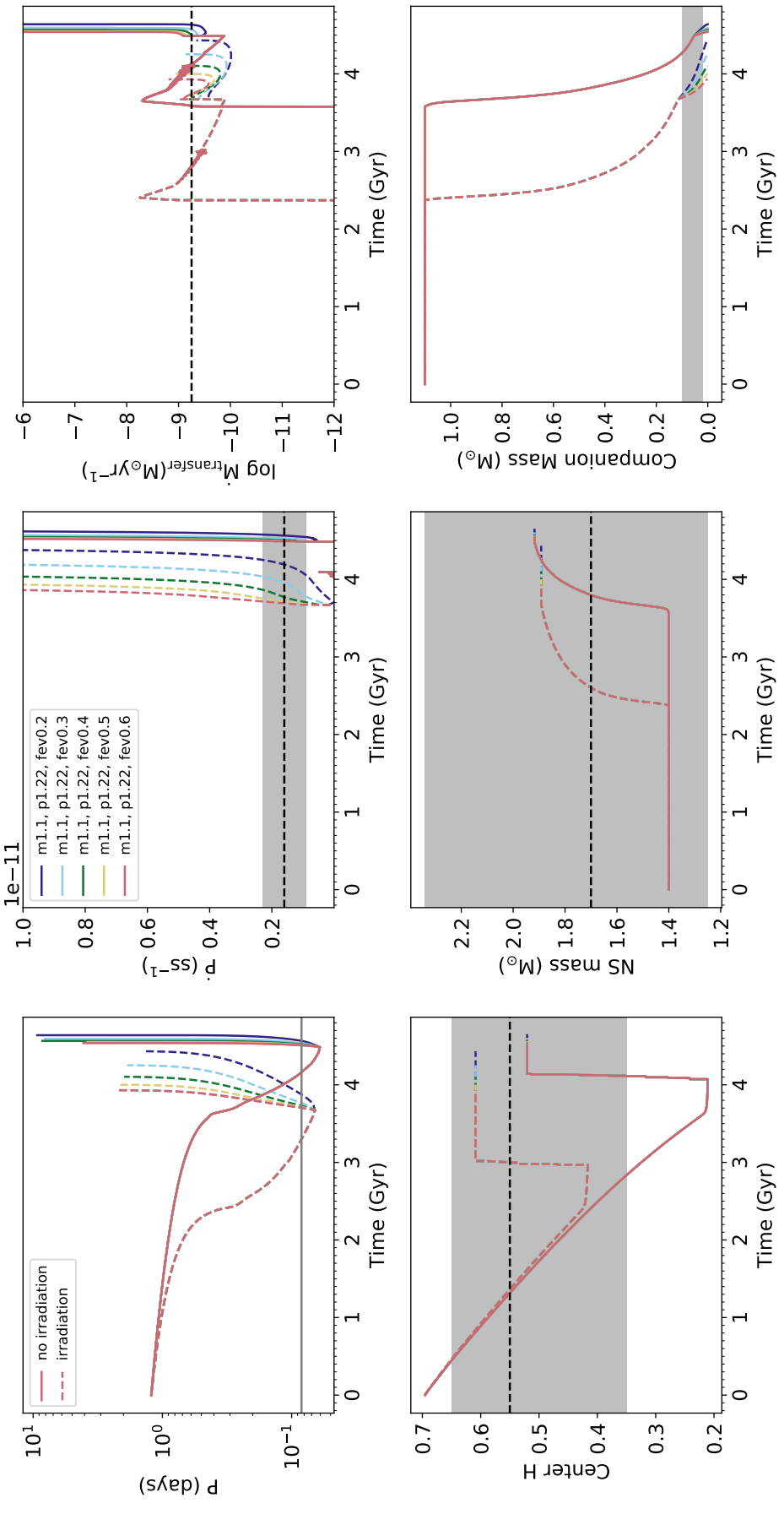

Figure 3. Model B (solid line) and Model C (dashed line) results: Evolution with donor evaporation and irradiation for a range of initial companion masses ($M_{d,i}$) and orbital periods (P_i), with fixed evaporation efficiency (f_{ev}). The different evolutionary tracks plotted are: $M_{d,i} = 1.1\,M_\odot$, $P_i = 1.22$ d, $f_{ev} = 0.2$ (purple), $M_{d,i} = 1.1\,M_\odot$, $P_i = 1.22$ d, $f_{ev} = 0.3$ (blue), $M_{d,i} = 1.1\,M_\odot$, $P_i = 1.22$ d, $f_{ev} = 0.4$ (green), $M_{d,i} = 1.1\,M_\odot$, $P_i = 1.22$ d, $f_{ev} = 0.5$ (orange), and $M_{d,i} = 1.1\,M_\odot$, $P_i = 1.22$ d, $f_{ev} = 0.6$ (red). All panels show the parameter evolution over time, with the individual panels showing: *Top panels, left to right:* Orbital period, orbital period derivative, mass transfer rate onto the NS. *Bottom panels, left to right:* Central hydrogen mass fraction of the donor star, NS mass, donor star mass. The dashed black line and grey regions indicate the current observed value of the parameter, and uncertainty, respectively.

Table 3. Model B results for different initial companion masses, orbital periods, and evaporation efficiencies.

Parameter	Best fit	Higher f_{ev}	Lower $M_{c,f}$	Lower P_i
$M_{d,i}$ ($M_\odot$)	1.1	1.1	0.6	1.1
$M_{d,f}$ ($M_\odot$)	0.031	0.035	0.038	0.036
$M_{NS,i}$ ($M_\odot$)	1.4	1.4	1.4	1.4
$M_{NS,f}$ ($M_\odot$)	1.92	1.92	1.67	1.92
P_i (d)	1.22	1.22	1.22	1.0
P_f (d)	0.0832	0.0832	0.0836	0.0832
$\dot{P}_f$ (10^{-12} s s^{-1})	1.65	3.27	1.41	1.29
f_{ev}	0.2	0.4	0.2	0.2
$X_{c,i}$	0.7	0.7	0.7	0.7
$X_{c,f}$	0.52	0.52	0.68	0.64

Table 4. Model C results for different initial companion masses, orbital periods, and evaporation efficiencies.

Parameter	Best fit	Lower f_{ev}	Lower $M_{c,f}$	Lower P_i
$M_{d,i}$ ($M_\odot$)	1.1	1.1	0.6	1.1
$M_{d,f}$ ($M_\odot$)	0.086	0.068	0.173	0.0920
$M_{NS,i}$ ($M_\odot$)	1.4	1.4	1.4	1.4
$M_{NS,f}$ ($M_\odot$)	1.89	1.89	1.61	1.89
P_i (d)	1.22	1.22	1.22	1.0
P_f (d)	0.0867	0.0830	0.0836	0.0831
$\dot{P}_f$ (10^{-12} s s^{-1})	1.73	0.492	-0.175	1.59
f_{ev}	0.5	0.2	0.5	0.5
$X_{c,i}$	0.7	0.7	0.7	0.7
$X_{c,f}$	0.42	0.42	0.57	0.57

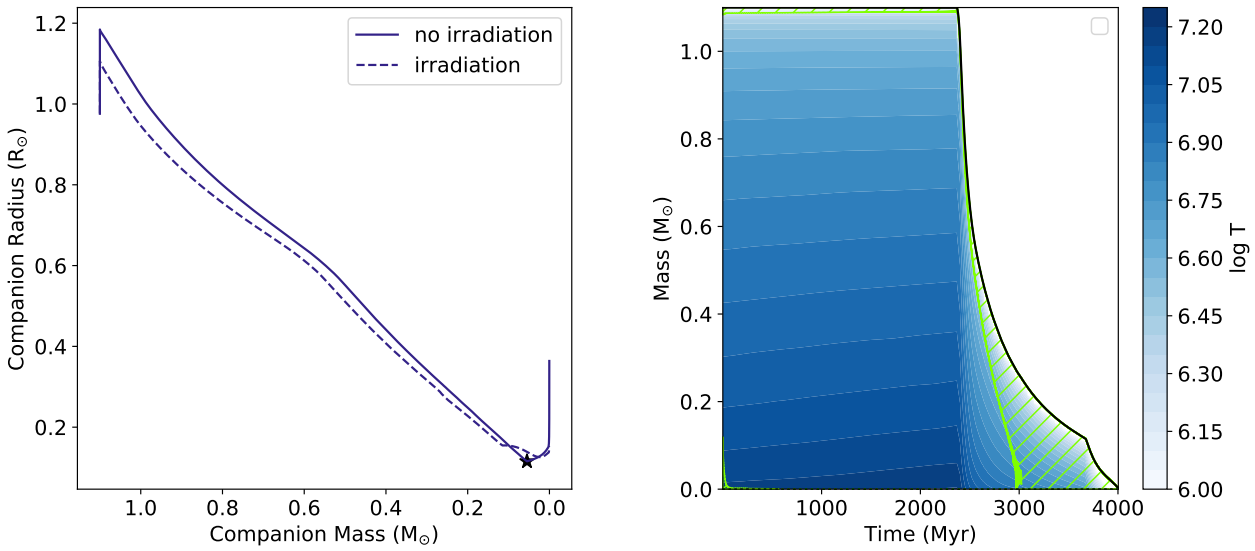

Figure 4. *Left:* The evolution of the mass and radius of the companion star for Model B (no irradiation, solid line) and Model C (including irradiation, dashed line) for a model with $M_{d,i} = 1.1\,M_\odot$, $P_i = 1.22$, $f_{ev} = 0.5$. The black star indicates when evaporation begins, and it is clear that this evaporative feedback causes the companion star to expand. *Right:* Kippenhahn diagram of the evolution of the internal structure of the donor star for a Model C calculation with $M_{d,i} = 1.1\,M_\odot$, $P_i = 1.22$, $f_{ev} = 0.5$. Green hatching indicates convective regions and blue shading is temperature (K).

4 DISCUSSION

We modelled the binary evolution of SAX J1808.4–3658, taking into account evidence that the donor star is significantly evolved, and the implications on the initial mass of the donor. We found the most likely progenitor of this system is a $1.1\,M_\odot$ companion star with an initial 1.0–1.22 day orbital period. In order to match the observed orbital period derivative, our model requires that a significant amount of mass is ejected from the inner Lagrangian point of the binary system, by an evaporative wind caused by radiation pressure from the pulsar evaporating the donor star during quiescence. We also explored the effects of donor irradiation due to the accretion luminosity and found this has a non-

negligible effect on the evolution of the system, particularly the donor star. These findings agree with previous calculations by Chen (2017) and Tailo et al. (2018).

In particular, our model requires a larger initial mass and orbital period than both Chen (2017) and Tailo et al. (2018) in order to match the observed composition constraints of the accreted fuel. This requirement has implications for the progenitor systems of low mass X-ray binaries, and requires that the donor star in SAX J1808.4–3658 has undergone significant mass loss during the evolution of the system, and more than previously suspected.

Interestingly, in order to match the current observed system parameters, our model requires that magnetic braking remains active throughout the entire evolution of the system, even after the companion star becomes fully convective. Tailo et al. (2018) found that, due to the effects of irradiation, the companion star did not become fully convective, thus justifying keeping magnetic braking active. However, we found that even including irradiation of the donor star did not prevent the companion star from becoming fully convective. There are two points to consider in this regard: Firstly, our MESA models may not be appropriately evaluating stability against convection for the conditions in the irradiated donor, and the donor should actually still be at least partially radiative at its present mass. Secondly, the donor star in SAX J1808.4–3658 could in fact still have a strong magnetic field despite being fully convective, and therefore magnetic braking continues unabated. There have been some observations of fully convective dwarf stars with evidence for strong, stable magnetic fields (e.g., Morin et al. 2008; Shulyak et al. 2017). On theoretical grounds, some have proposed that intense activity and strong magnetism in fully convective dwarfs could be due to non-solar dynamo processes, concluding that fully convective stars could have significant magnetic fields that are generated in lower convection zones, and differential rotation contributes very little to the magnetic field (e.g. Durney et al. 1993).

In our best fit model (Model C), it takes 3.73×10^9 years for the system to evolve from an orbital period of 1.22 d with a companion star of 1.1 $M_\odot$ to the current observed period of 2.01 hours with a 0.08 $M_\odot$ companion star. This model requires an evaporation efficiency of $f_{ev} = 0.5$. Since the initial primary must have been massive, and evolved very quickly through a common envelope (to bring it in to a short orbit) and a supernova, the timescale we find for the subsequent evolution of the donor is approximately the total present system lifetime, ~3.7 billion years.

As noted by numerous authors (e.g. Chakrabarty & Morgan 1998), the binary parameters of SAX J1808.4–3658 are reminiscent of a black widow millisecond radio pulsar, which are known to ablate their companions and have very low mass companion stars. This work confirms that SAX J1808.4–3658 could indeed be a hidden black widow pulsar, since we require that SAX J1808.4–3658 switches on as a radio pulsar during quiescence in order to evaporate the companion star and eject mass at the inner Lagrangian point of the system.

Optical observations of the 1998 and 2005 outbursts of SAX J1808.4–3658 revealed an optical i-band excess (Greenhill et al. 2006; Wang et al. 2001), which could be indicative of a circumbinary disk in this system. Future work could look into constraining theoretically the possibility of the existence of such a disk, and if the mass ejected at the inner Lagrangian point is sufficient to create it.

5 CONCLUSION

We have demonstrated the necessity of taking into account that SAX J1808.4–3658 has an evolved donor star when modelling the evolution of the binary system. Our model requires an initial companion mass of 1.1 $M_\odot$ and orbital period of 1.0–1.22 d in order to match the current observed system parameters (including for the first time the donor's measured hydrogen abundance) for an initial solar composition of the companion star and a 1.4 $M_\odot$ neutron star. As previous authors have found, conservative mass transfer models do not reproduce the observed orbital period derivative of the system. In this work, we find that including the effects of pulsar evaporation and irradiation on the donor star, ejecting the evaporative wind at the inner Lagrangian point of the binary system provides sufficient angular momentum losses to match the current observed rate of change of the orbital period. We emphasize that the effects of both irradiation of the donor star due to the accretion luminosity and evaporation of the donor star due to the pulsar luminosity are non-negligible, and both are a key component in describing the binary evolution of SAX J1808.4–3658.

ACKNOWLEDGEMENTS

We thank Prof Alexander Heger and A/Prof Duncan Galloway for helpful comments and discussions. AG acknowledges support by an Australian Research Training Program scholarship. TEW acknowledges support from the NRC-Canada Plaskett fellowship.

REFERENCES

Beer M. E., Dray L. M., King A. R., Wynn G. A., 2007, MNRAS, 375, 1000
Bhattacharya D., van den Heuvel E. P. J., 1991, Phys. Rep., 203, 1
Bildsten L., Chakrabarty D., 2001, ApJ, 557, 292
Bult P., et al., 2019a, arXiv e-prints, p. arXiv:1909.03595
Bult P., Chakrabarty D., Arzoumanian Z., Gendreau K. C., Guillot S., Malacaria C., Ray P. S., Strohmayer T. E., 2019b, arXiv e-prints, p. arXiv:1910.03062
Burderi L., D'Antona F., Di Salvo T., Burgay M., 2002, arXiv e-prints, pp astro–ph/0208021
Burderi L., di Salvo T., Riggio A., Papitto A., Menna M. T., 2009, in Revista Mexicana de Astronomia y Astrofisica Conference Series. pp CD291–CD296
Chakrabarty D., Morgan E. H., 1998, Nature, 394, 346
Chen W.-C., 2017, MNRAS, 464, 4673
Del Santo M., et al., 2015, The Astronomer's Telegram, 7380, 1
Durney B. R., De Young D. S., Roxburgh I. W., 1993, Sol. Phys., 145, 207
Eggleton P. P., 1983, ApJ, 268, 368
Galloway D. K., Cumming A., 2006, ApJ, 652, 559
Goodwin A. J., Galloway D. K., Heger A., Cumming A., Johnston Z., 2019a, MNRAS, 490, 2228
Goodwin A. J., Russell D. M., Galloway D. K., in't Zand J. J. M., Heinke C., Lewis F., Baglio M. C., 2019b, The Astronomer's Telegram, 12993, 1

Greenhill J. G., Giles A. B., Coutures C., 2006, MNRAS, 370, 1303
Hartman J. M., et al., 2008, ApJ, 675, 1468
Hartman J. M., Patruno A., Chakrabarty D., Markwardt C. B., Morgan E. H., van der Klis M., Wijnands R., 2009, ApJ, 702, 1673
Jia K., Li X.-D., 2015, ApJ, 814, 74
Johnston Z., Heger A., Galloway D. K., 2018, MNRAS, 477, 2112
Kopal Z., 1959, Close binary systems
Markwardt C. B., Swank J. H., 2008, The Astronomer's Telegram, 1728, 1
Markwardt C. B., Miller J. M., Wijnands R., 2002, The Astronomer's Telegram, 110, 1
Markwardt C. B., et al., 2011, The Astronomer's Telegram, 3733, 1
Morin J., et al., 2008, MNRAS, 384, 77
Nelson L. A., Rappaport S., 2003, ApJ, 598, 431
Papitto A., Menna M. T., Burderi L., Di Salvo T., D'Antona F., Robba N. R., 2005, ApJ, 621, L113
Papitto A., et al., 2013, Nature, 501, 517
Patruno A., Watts A. L., 2012, arXiv e-prints, p. arXiv:1206.2727
Patruno A., et al., 2017, ApJ, 841, 98
Paxton B., Bildsten L., Dotter A., Herwig F., Lesaffre P., Timmes F., 2011, ApJS, 192, 3
Paxton B., et al., 2013, ApJS, 208, 4
Paxton B., et al., 2015, ApJS, 220, 15
Paxton B., et al., 2019, ApJS, 243, 10
Peters P. C., 1964, Physical Review, 136, 1224
Podsiadlowski P., Rappaport S., Pfahl E. D., 2002, ApJ, 565, 1107
Rappaport S., Verbunt F., Joss P. C., 1983, ApJ, 275, 713
Ritter H., 1988, A&A, 202, 93
Shapiro S. L., Teukolsky S. A., 1983, Black holes, white dwarfs, and neutron stars : the physics of compact objects
Shulyak D., Reiners A., Engeln A., Malo L., Yadav R., Morin J., Kochukhov O., 2017, Nature Astronomy, 1, 0184
Steiner A. W., Heinke C. O., Bogdanov S., Li C. K., Ho W. C. G., Bahramian A., Han S., 2018, MNRAS, 476, 421
Stevens I. R., Rees M. J., Podsiadlowski P., 1992, MNRAS, 254, 19P
Tailo M., et al., 2018, MNRAS, 479, 817
Tauris T. M., van den Heuvel E. P. J., 2006, Formation and evolution of compact stellar X-ray sources. pp 623–665
Ventura P., D'Antona F., Mazzitelli I., 2008, Ap&SS, 316, 93
Wang Z., et al., 2001, ApJ, 563, L61
Warner B., 1976, in Eggleton P., Mitton S., Whelan J., eds, IAU Symposium Vol. 73, Structure and Evolution of Close Binary Systems. p. 85
Wijnands R., van der Klis M., 1998, Nature, 394, 344
di Salvo T., Burderi L., Riggio A., Papitto A., Menna M. T., 2008, MNRAS, 389, 1851
van den Heuvel E. P. J., van Paradijs J., 1988, Nature, 334, 227
van der Sluys M. V., Verbunt F., Pols O. R., 2005, A&A, 431, 647

This paper has been typeset from a TEX/LATEX file prepared by the author.

7

SUMMARY AND CONCLUSION

7.1 SUMMARY

7.1.1 *A simple relation to estimate X-ray burst energy*

In Chapter 3 we used `Kepler` to model thermonuclear X-ray bursts that can occur on the surface of accreting neutron stars and determined a simple relation for the total energy output of a burst based on the fuel composition of the material that is burned. We found that the total energy released can be well approximated by the relation $Q_{nuc} = 1.31 + 6.95\bar{X} - 1.92\bar{X}^2$ MeV nucleon^{-1}, where $\bar{X}$ is the average hydrogen mass fraction of the ignition column. This relation can be used in observational studies to determine the accreted fuel content, as in Chapter 4, or in simple modelling studies to estimate burst energy, as in Chapter 5. Using these burst models we were also able to constrain the total neutrino energy released during a burst, and found it ranged from $\approx$ 0–14% of the total burst energy, significantly less than the typically adopted value of 35% (e.g. Cumming and Bildsten, 2000). Finally, we measured how completely the energy available in the burned fuel was extracted in our models, and found that in some cases, $\approx$ 14% of the total energy available to be released in the burned fuel was leftover in the ashes of the burst.

7.1.2 *A 2D model of X-ray burst ignition location*

In Chapter 3 we presented a 2D model of heat conduction and transport in the accreted layers on the surface of accreting neutron stars, and found that a hotspot on the surface may induce off-equator ignition of bursts, if the hotspot is hotter than $\approx 1 \times 10^8$ K. This finding is contrary to the common assumption that bursts will always ignite at the equator due to the lower surface gravity at this location (e.g. Spitkovsky, Levin and Ushomirsky, 2002). This model is the first 2D study of the ignition location of bursts, and the first of its kind to consider an accretion hotspot on the surface. We found that the phase locking of accretion pulsations with burst oscillations in the two X-ray pulsars XTE J1814–338 and IGR 17480–2446 could be explained by burst ignition preferentially igniting under the hotspot due to heating induced in the deeper layers by the hotspot, but the continued phase-locking of the pulsations during the burst would also require "stalling" of the flame front. We independently confirmed in 2D models that ignition of bursts will preferentially occur at the equator if the neutron star surface is an approximately uniform temperature, due to the lower surface gravity.

7.1.3 *Detailed multiwavelength observations of the rise to outburst of an accreting neutron star*

In Chapter 4 we presented the first detailed multiwavelength observations of the rise to outburst of an accreting neutron star. The spectral temperature we inferred during the optical rise (and before any X-ray detection) corresponds to the temperature range at which hydrogen ionises, and thus our observations support the disk instability model theory that outbursts in the disks around accreting neutron stars are likely initiated by ionisation of the hydrogen in the disk. We measured a 12 d delay between the first optical activity in the system and the first X-ray detection, and inferred a 4 d optical to X-ray delay. This 4 d delay corresponds to the viscous time, or the time taken for the truncated disk to fill in to the surface of the neutron star, at which time UV and X-ray emission is detected. The 8 d of optical activity prior to the clear beginning of the outburst in optical that we observed is somewhat puzzling, and could be explained by either increased mass transfer from the companion star, geometric effects in the outer accretion disk, or fluctuations in the pulsar radiation pressure.

7.1.4 *A new ultracompact X-ray binary*

In Chapter 4 we also analysed X-ray bursts discovered in archival *RXTE* data from the accreting neutron star XMMU J181227.8–181234. These are the first bursts detected from this system. By analysing the burst energy and using the relation we developed in Chapter 3, we inferred that the accreted fuel in this system is most likely pure helium. We thus were able to classify the system as a candidate ultracompact X-ray binary. We also detected two short waiting time bursts, just 18 min apart, which could be the first short waiting time bursts observed with pure helium fuel composition.

7.1.5 `BEANS`*: Bayesian Estimation of Accreting Neutron Star parameters*

In Chapter 5 we presented a new method of obtaining accreting neutron star system parameters by matching observations of burst trains with the `Settle` model, called `BEANS`. The software documentation is publicly available on Github. We applied `BEANS` to observations of the 2002 outburst of SAX J1808.4–3658 and inferred the system has hydrogen depleted accreted fuel, that the system inclination is likely between 67–73 deg, and we were able to constrain the neutron star mass and radius to within 40% and 11% respectively. The method appears promising for studies of other accreting neutron stars, and enables an initial exploration of parameter space to determine reasonable ranges for parameters which could then be used in more detail models such as `Kepler` to model the systems in detail.

7.1.6 *The binary evolution of SAX J1808.4–3658*

Finally, in Chapter 6, we modelled the binary evolution of SAX J1808.4–3658 given our finding in Chapter 5 that the donor star is significantly evolved (with $X_c \approx$

0.57). SAX J1808.4–3658 shows peculiar binary evolution, with a larger than expected orbital period derivative that cannot be explained by conservative mass transfer models (e.g. Hartman et al., 2008). We modelled the binary evolution of this system using MESA, including evaporation of the companion due to pulsar radiation pressure with the evaporative wind being ejected at the inner Lagrangian point of the binary, and irradiation of the companion due to the accretion luminosity. We found that these phenomenon are a key requirement in describing the binary evolution of SAX J1808.4–3658, and many orbital evolutionary calculations do not account for irradiation or evaporation. Our models required an initial companion mass of 1.1 msun and an orbital period of 1.0-1.22 d for the system to accurately match the current observed system parameters. This result implies that the donor star has lost a significant amount of mass during the $\approx$ 3.7 Gyr evolution of the binary, with the neutron star stripping away $\approx$ 95 % of the donor stars mass. This study demonstrates that SAX J1808.4–3658 could indeed be a hidden black widow millisecond radio pulsar, as has been suggested by numerous authors (e.g., Chakrabarty and Morgan, 1998), since we require that the pulsar switches on as a radio pulsar during quiescence in order to evaporate the companion and eject mass at the inner Lagrangian point of the system.

7.2 CONCLUSION

In this thesis we have presented detailed modelling and observational studies of accreting neutron star systems. The primary results of this work include new observations and modelling techniques. In Chapter 3, we presented two modelling studies of X-ray bursts. The first study used a pre-existing state-of-the-art model to perform detailed simulations of the energy release and burning during X-ray bursts for different accretion rates and fuel compositions. The second study presented a 2D code we wrote to simulate heat conduction and transport in the accreted layers on the surface in the lead up to an X-ray burst, in order to model the ignition location of bursts. In Chapter 4 we presented two observational studies of accreting neutron star systems. We obtained the first, detailed, multiwavelength observations of the beginnings and rise to outburst of a transient accreting neutron star system, providing important observational constraints for the disk instability model. We also analysed X-ray bursts we discovered in archival data for the source XMMU J181227.8–181234, and were able to classify the source as a candidate rare ultracompact X-ray binary. In Chapter 5 through a case study of SAX J1808.4–3658, we demonstrated a new method of determining accreting neutron star parameters that are notoriously difficult to constrain, including neutron star mass, radius, fuel composition, and system inclination, by matching observations of X-ray burst trains with a simple X-ray burst model. In Chapter 6 we demonstrated the utility of using system constraints obtained from other modelling efforts to inform evolutionary studies of accreting neutron stars. We modelled the binary evolution of SAX J1808.4–3658 given our finding in Chapter 5 that the accreted fuel in this

system is likely hydrogen deficient, and also included a treatment of the effects of donor star irradiation and evaporation on the system evolution.

In summary, our main conclusions are:

1. Accretion outbursts in low mass X-ray binaries are likely caused by hydrogen ionisation in the accretion disk, and the heating front caused by an initial instability will propagate through the disk on the viscous timescale. We independently confirmed these postulations by obtaining detailed optical, UV, and X-ray observations of the rise to outburst of the accretion-powered millisecond pulsar SAX J1808.4–3658.

2. The total energy released during an X-ray burst is primarily dependent on the hydrogen content of the ignited material, and can be approximated by the relation $Q_{nuc} = 1.31 + 6.95\bar{X} - 1.92\bar{X}^2$ MeV nucleon^{-1}, where $\bar{X}$ is the average hydrogen fraction of the ignition column.

3. Hotspots on the surface of an accreting X-ray pulsar may induce heating deep into the accreted layers, causing burst ignition away from the equator at the location of the hotspot, if the hotspot is hotter than $\approx 1 \times 10^8$ K.

4. Observations of X-ray burst trains from accreting neutron stars combined with simple burst models can be used to infer system parameters that are difficult to observationally constrain, such as neutron star mass, radius, accreted fuel composition, and system inclination. We developed publicly available software that can be used to infer parameters for any accreting neutron star system with observations of a burst train.

5. An accreting neutron star can strip away $\approx 95\%$ of a donor stars mass during their evolution as a binary, and some donor stars may have once been significantly more massive than they are observed today. The effects of X-ray irradiation and evaporation of the donor star in accreting pulsar binary systems are non-negligible and must be accounted for in evolutionary track calculations. Certain accretion-powered millisecond X-ray pulsars could be the progenitors for radio black widow millisecond pulsar systems.

7.3 FUTURE WORK

Understanding the physics of accreting neutron star systems is crucial in obtaining a comprehensive picture of the extremes of physics: from strong gravitational fields, to nuclear reactions in extreme environments, to the densest matter we know. This thesis provides significant advancements in our understanding of accretion outbursts onto neutron stars, however, there is still much to explore and understand in our endeavour to understand the accreting neutron stars.

7.3.1 *Models of thermonuclear X-ray bursts*

Whilst the addition of complex nuclear reaction networks to 1D calculations of X-ray bursts has provided much insight into detailed studies of burst energetics

(e.g. `Kepler`, `MESA`), the 1D nature of these models significantly impedes their ability to accurately model burst flame spreading, ignition location, and other related physics. In this thesis, we developed a 2D ignition code to explore the ignition location of bursts, however, this code is static: there is no time-dependence or treatment of hydrodynamics. In future, this code could be upgraded to comprehensively model an X-ray burst by including a detailed nuclear reaction network, time-dependence of the integration, and hydrodynamics. This code, combined with multi-dimensional models of convection and in Type I X-ray bursts (e.g. Zingale et al., 2015), would then be extremely useful in understand the phenomenon of burst oscillations, and the phase locking of burst oscillations with accretion-powered pulsations in a couple of systems, as well as other poorly understood observational phenomenon such as the short waiting time bursts.

7.3.2 *Observations*

With new X-ray telescopes coming online (such as the already operational such as NICER) there are new possibilities for obtaining detailed observations of accreting neutron stars. In this thesis we presented observations of the rise to outburst of SAX J1808.4–3658 that we were able to obtain due to optical monitoring campaigns and our understanding of the recurrence time of outburst for the system. Catching accreting neutron stars in the act of switching on is crucial in providing observational constraints for the disk instability model theory, and our understanding of what causes accretion outbursts onto neutron stars. We observed some unexpected extended optical activity just prior to the commencement of outburst for SAX J1808.4–3658, and future observations of the lead up to outburst in this system as well as other similar systems is necessary in understanding the physics occurring during this time.

Furthermore, obtaining high duty cycle observations of accreting neutron stars in outburst maximises the likelihood of catching X-ray bursts and constraining the recurrence time. In the case of short waiting time bursts, more observations of this phenomenon would aid in understanding the mechanism behind it as well as the systems in which they occur.

The code we developed that matches observations of burst trains to the `Settle` model, `BEANS` can be applied to any system in which a train of bursts is observed (the more precisely the recurrence time is constrained through observations the better), and thus in future should be applied to as many systems as possible. Constraints obtained using this software will be useful in population studies of the accreting neutron stars as well as providing starting parameters for more detailed, time-intensive, models.

7.3.3 *Evolutionary Studies*

In this thesis we showed that SAX J1808.4–3658 could be the progenitor of a black widow millisecond pulsar system. There are few systems with parameters that are as observationally well constrained as SAX J1808.4–3658, however, with the addition of new observations and constraints from models, detailed evolutionary cal-

culations of each accretion-powered millisecond pulsar could be performed. These kinds of observationally constrained case studies that could be carried out in future are crucial in understanding the possible evolutionary pathways of the accreting X-ray pulsars, and binary populations.

APPENDIX - AUXILIARY DATA

Here we present the auxiliary data files for all chapters in this work. The data files are located at https://bridges.monash.edu/articles/software/Thesis_Auxiliary_Files/13049837. The repository is structured to contain a folder for each published work, and the folder contents are outlined below.

A.1 XTE J1812–182 OBSERVATIONAL DATA

This folder contains the observational data and spectral fits that were used for the analysis of XTE J1812–182 in Chapter 4. The observational data are archival *RXTE* data, and the spectral fits were performed using `HEASoft`.

A.2 SAX J1808.4–3658 2019 OUTBURST OBSERVATIONAL DATA

This folder contains the observational data that were used for the analysis of the 2019 outburst of SAX J1808.4–3658 in Chapter 4. There are folders for each telescope: LCO, *Swift* (UVOT and XRT), NICER, and SALT.

A.3 KEPLER GENERATOR FILES

This folder contains the `Kepler` generator files `hg` and `rpabg` that were used to perform the X-ray burst calculations in Chapter 3. It also contains an example `Kepler` dump file, lightcurve file, and convection file from one of the runs in the grid. The dump file contains information such as the `Kepler` version that was used. Additionally, there is a folder containing a summary of properties for the 84 `Kepler` runs in the grid, including the input parameters (X, Z, $\dot{m}$), and the results (number of bursts, total burst energy, neutrino energy, etc.)

A.4 MESA INLISTS

This folder contains the `MESA` inlists and extras routines that were used to perform the evolutionary track calculations in Chapter 6. There are two folders, one containing inlists for a run with no irradiation of the donor star due to the pulsar irradiation, and one containing inlists for a run including this irradiation.

A.5 IGNITION LOCATION CODE

The finite volume code written for the simulations in Chapter 3 is publicly available on Github via https://github.com/adellej/ignition-calculations. In the

ignition calculations folder there is a folder for the code, run scripts, opacity tables, and the `Kepler` dump files used by the code.

A.6 MCMC CHAINS AND BEANS

This folder contains the raw MCMC chains and `BEANS` input files that were used for the analysis in Chapter 5. Additionally, the software `BEANS` (Bayesian Estimation of Accreting Neutron Star parameters) is publicly available on Github (`https://github.com/adellej/beans`) and you can read the documentation on usage here (`https://beans-7.readthedocs.io/en/latest/`). Please note that `BEANS` has been updated since Goodwin et al. (2019a) was published, so the input files provided in this folder may not work out of the box, but all of the input parameters are contained in these files.

BIBLIOGRAPHY

Alpar, M. A. et al. (Dec. 1982). 'A new class of radio pulsars'. *NATURE* 300, pp. 728–730. DOI: 10.1038/300728a0.

Altamirano, D. et al. (Feb. 2008). 'Intermittent Millisecond X-Ray Pulsations from the Neutron Star X-Ray Transient SAX J1748.9-2021 in the Globular Cluster NGC 6440'. *ApJ* 674.1, p. L45. DOI: 10.1086/528983. arXiv: 0708.1316 [astro-ph].

Armitage, P. J. (Sept. 2015). 'Physical processes in protoplanetary disks'. *arXiv e-prints*, arXiv:1509.06382, arXiv:1509.06382. arXiv: 1509.06382 [astro-ph.SR].

Ayasli, S. and P. C. Joss (May 1982). 'Thermonuclear processes on accreting neutron stars - A systematic study'. *ApJ* 256, pp. 637–665. DOI: 10.1086/159940.

Baade, W. and F. Zwicky (July 1934). 'Remarks on Super-Novae and Cosmic Rays'. *Physical Review* 46.1, pp. 76–77. DOI: 10.1103/PhysRev.46.76.2.

Backer, D. C. et al. (Dec. 1982). 'A millisecond pulsar'. *NATURE* 300, pp. 615–618. DOI: 10.1038/300615a0.

Baglio, M. C. et al. (Apr. 2017). 'The puzzling case of the accreting millisecond X-ray pulsar IGR J00291+5934: flaring optical emission during quiescence'. *A&A* 600, A109, A109. DOI: 10.1051/0004-6361/201629524. arXiv: 1701.02321 [astro-ph.HE].

Baglio, M. C. et al. (Oct. 2020). 'Probing jet launching in neutron star X-ray binaries: the variable and polarized jet of SAX J1808.4–3658'. *ApJ* submitted.

Basinska, E. et al. (1984). 'X-ray observations of the burst source MXB 1728-34'. *ApJ* 281, pp. 337–353.

Berger, J. O. (1985). *Statistical decision theory and Bayesian analysis*.

Bhattacharya, D. and E. P. J. van den Heuvel (Jan. 1991). 'Formation and evolution of binary and millisecond radio pulsars'. *Phys. Rep.* 203.1-2, pp. 1–124. DOI: 10.1016/0370-1573(91)90064-S.

Bildsten, L. (Jan. 1998). 'Thermonuclear Burning on Rapidly Accreting Neutron Stars'. In *NATO Advanced Science Institutes (ASI) Series C*. Ed. by R. Buccheri, J. van Paradijs and A. Alpar. Vol. 515. NATO Advanced Science Institutes (ASI) Series C, p. 419. arXiv: astro-ph/9709094 [astro-ph].

Bildsten, L. (June 2000). 'Theory and observations of Type I X-Ray bursts from neutron stars'. In *American Institute of Physics Conference Series*. Ed. by S. S. Holt and W. W. Zhang. Vol. 522. American Institute of Physics Conference Series, pp. 359–369. DOI: 10.1063/1.1291736. eprint: astro-ph/0001135.

Bowyer, S. et al. (Mar. 1964). 'X-ray Sources in the Galaxy'. *NATURE* 201.4926, pp. 1307–1308. DOI: 10.1038/2011307a0.

Bult, P. (Mar. 2017). 'The X-Ray Variability of the Accreting Millisecond Pulsar MAXI J0911-655'. *ApJ* 837.1, 61, p. 61. DOI: 10.3847/1538-4357/aa607f. arXiv: 1702.04182 [astro-ph.HE].

Bult, P., A. Patruno and M. van der Klis (Dec. 2015). 'Coherent Timing of the Accreting Millisecond Pulsar NGC 6440 X-2'. *ApJ* 814.2, 138, p. 138. DOI: 10.1088/0004-637X/814/2/138. arXiv: 1510.06167 [astro-ph.HE].

Bult, P., M. van Doesburgh and M. van der Klis (Aug. 2017). 'Quasi-periodic Pulse Amplitude Modulation in the Accreting Millisecond Pulsar IGR J00291-5934'. *ApJ* 845.2, 124, p. 124. DOI: 10.3847/1538-4357/aa8172. arXiv: 1707.06445 [astro-ph.HE].

Camenzind, M. (2007). *Compact objects in astrophysics : white dwarfs, neutron stars, and black holes*. DOI: 10.1007/978-3-540-49912-1.

Cannizzo, J. K., J. C. Wheeler and P. Ghosh (1985). 'Accretion Instability Models for Dwarf Novae and X-Ray Transients'. In. *Cataclysmic Variables and Low-Mass X-ray Binaries*. Ed. by D. Q. Lamb and J. Patterson, p. 307. DOI: 10.1007/978-94-009-5319-2_36.

Casella, P. et al. (Feb. 2008). 'Discovery of Coherent Millisecond X-Ray Pulsations in Aquila X-1'. *ApJ* 674.1, p. L41. DOI: 10.1086/528982. arXiv: 0708.1110 [astro-ph].

Cavecchi, Y. et al. (July 2020). 'The efficiency of nuclear burning during thermonuclear (Type I) bursts as a function of accretion rate'. *arXiv e-prints*, arXiv:2007.08081, arXiv:2007.08081. arXiv: 2007.08081 [astro-ph.HE].

Cavecchi, Y. and A. Spitkovsky (Sept. 2019). 'Three-dimensional Instability of Flame Fronts in Type I X-Ray Bursts'. *ApJ* 882.2, 142, p. 142. DOI: 10.3847/1538-4357/ab3650. arXiv: 1905.13735 [astro-ph.HE].

Chadwick, J. (1932). 'Possible existence of a neutron'. *Nature* 129.3252, pp. 312–312.

Chakrabarty, D. (2005). 'Millisecond Pulsars in X-Ray Binaries'. In *Binary radio pulsars: proceedings of a meeting held in Aspen, Colorado, USA, 11-17 January 2004*. Vol. 328. Astronomical Society of the Pacific, p. 279.

Chakrabarty, D. and E. H. Morgan (July 1998). 'The two-hour orbit of a binary millisecond X-ray pulsar'. *NATURE* 394.6691, pp. 346–348. DOI: 10.1038/28561. arXiv: astro-ph/9804248 [astro-ph].

Chakrabarty, D. et al. (July 2003). 'Nuclear-powered millisecond pulsars and the maximum spin frequency of neutron stars'. *NATURE* 424.6944, pp. 42–44. DOI: 10.1038/nature01732. arXiv: astro-ph/0307029 [astro-ph].

Chen, W.-C. (Feb. 2017). 'An evolutionary channel towards the accreting millisecond pulsar SAX J1808.4-3658'. *MNRAS* 464.4, pp. 4673–4679. DOI: 10.1093/mnras/stw2747. arXiv: 1610.06767 [astro-ph.HE].

Chou, Y. et al. (May 2008). 'Precise Orbital Parameters and Anomalous Phase Variations of the Accretion-powered Millisecond Pulsar XTE J1807-294'. *ApJ* 678.2, pp. 1316–1323. DOI: 10.1086/529126. arXiv: 0801.0909 [astro-ph].

Cooper, R. L. and R. Narayan (May 2007). 'Hydrogen-triggered Type I X-Ray Bursts in a Two-Zone Model'. *ApJ* 661, pp. 468–476. DOI: 10.1086/513461. eprint: astro-ph/0702042.

Cromartie, H. T. et al. (Jan. 2020). 'Relativistic Shapiro delay measurements of an extremely massive millisecond pulsar'. *Nature Astronomy* 4, pp. 72–76. DOI: 10.1038/s41550-019-0880-2. arXiv: 1904.06759 [astro-ph.HE].

Cumming, A. (Oct. 2003). 'Models of Type I X-Ray Bursts from 4U 1820-30'. *ApJ* 595, pp. 1077–1085. DOI: 10.1086/377446. eprint: astro-ph/0306245.

Cumming, A. (2004). 'Thermonuclear X-ray bursts: theory vs. observations'. *Nuclear Physics B-Proceedings Supplements* 132, pp. 435–445.

Cumming, A. and L. Bildsten (2000). 'Rotational evolution during type I X-ray bursts'. *The Astrophysical Journal* 544.1, p. 453.

Cyburt, R. H. et al. (July 2010). 'The JINA REACLIB Database: Its Recent Updates and Impact on Type-I X-ray Bursts'. *ApJS* 189.1, pp. 240–252. DOI: 10.1088/0067-0049/189/1/240.

De Falco, V. et al. (Mar. 2017a). 'The 2015 outburst of the accretion-powered pulsar IGR J00291+5934: INTEGRAL and Swift observations'. *A&A* 599, A88, A88. DOI: 10.1051/0004-6361/201629575. arXiv: 1611.08218 [astro-ph.HE].

De Falco, V. et al. (July 2017b). 'The transitional millisecond pulsar IGR J18245-2452 during its 2013 outburst at X-rays and soft gamma-rays'. *A&A* 603, A16, A16. DOI: 10.1051/0004-6361/201730600. arXiv: 1704.04181 [astro-ph.HE].

Degenaar, N. et al. (Apr. 2013). 'X-Ray Emission and Absorption Features during an Energetic Thermonuclear X-Ray Burst from IGR J17062-6143'. *ApJ* 767.2, L37, p. L37. DOI: 10.1088/2041-8205/767/2/L37. arXiv: 1212.4869 [astro-ph.HE].

di Salvo, T. et al. (Oct. 2008). 'Orbital evolution of an accreting millisecond pulsar: witnessing the banquet of a hidden black widow?' *MNRAS* 389.4, pp. 1851–1857. DOI: 10.1111/j.1365-2966.2008.13709.x. arXiv: 0708.0498 [astro-ph].

Dubus, G., J. M. Hameury and J. P. Lasota (July 2001). 'The disc instability model for X-ray transients: Evidence for truncation and irradiation'. *A&A* 373, pp. 251–271. DOI: 10.1051/0004-6361:20010632. arXiv: astro-ph/0102237 [astro-ph].

Eggleton, P. P. (May 1983). 'Aproximations to the radii of Roche lobes.' *ApJ* 268, pp. 368–369. DOI: 10.1086/160960.

Falanga, M. et al. (May 2011). 'Spectral and timing properties of the accreting X-ray millisecond pulsar IGR J17511-3057'. *A&A* 529, A68, A68. DOI: 10.1051/0004-6361/201016240. arXiv: 1012.0229 [astro-ph.HE].

Falanga, M. et al. (Sept. 2012). 'Spectral and timing properties of the accreting X-ray millisecond pulsar IGR J17498-2921'. *A&A* 545, A26, A26. DOI: 10.1051/0004-6361/201219582. arXiv: 1208.1384 [astro-ph.HE].

Ferrigno, C. et al. (Jan. 2011). 'INTEGRAL, Swift, and RXTE observations of the 518 Hz accreting transient pulsar Swift J1749.4-2807'. *A&A* 525, A48, A48. DOI: 10.1051/0004-6361/201015033. arXiv: 1005.4554 [astro-ph.HE].

Ferrigno, C. et al. (July 2014). 'Hiccup accretion in the swinging pulsar IGR J18245-2452'. *A&A* 567, A77, A77. DOI: 10.1051/0004-6361/201322904. arXiv: 1310.7784 [astro-ph.HE].

Ferrigno, C. et al. (Apr. 2017). 'Discovery of a soft X-ray 8 mHz QPO from the accreting millisecond pulsar IGR J00291+5934'. *MNRAS* 466.3, pp. 3450–3459. DOI: 10.1093/mnras/stw3344. arXiv: 1611.07075 [astro-ph.HE].

Finzi, A. (Oct. 1965). 'Vibrational Energy of Neutron Stars and the Exponential Light Curves of Type-I Supernovae'. *Phys. Rev. Lett.* 15.15, pp. 599–601. DOI: 10.1103/PhysRevLett.15.599.

Fisker, J. L., H. Schatz and F.-K. Thielemann (2008). 'Explosive hydrogen burning during type I X-ray bursts'. *The Astrophysical Journal Supplement Series* 174.1, p. 261.

Fisker, J. et al. (2001). 'Shell model based reaction rates for rp-process nuclei in the mass range a= 44–63'. *Atomic Data and Nuclear Data Tables* 79.2, pp. 241–292.

Foreman-Mackey, D. et al. (Mar. 2013). 'emcee: The MCMC Hammer'. *PASP* 125.925, p. 306. DOI: 10.1086/670067. arXiv: 1202.3665 [astro-ph.IM].

Fragos, T. et al. (Oct. 2019). 'The Complete Evolution of a Neutron-star Binary through a Common Envelope Phase Using 1D Hydrodynamic Simulations'. *ApJ* 883.2, L45, p. L45. DOI: 10.3847/2041-8213/ab40d1. arXiv: 1907.12573 [astro-ph.HE].

Frank, J., A. King and D. J. Raine (2002). *Accretion Power in Astrophysics: Third Edition*.

Fujimoto, M. Y., T. Hanawa and S. Miyaji (July 1981). 'Shell flashes on accreting neutron stars and X-ray bursts'. *ApJ* 247, pp. 267–278. DOI: 10.1086/159034.

Fujimoto, M. Y. (Jan. 1988). 'Angular Distribution of Radiation from Low-Mass X-Ray Binaries'. *ApJ* 324, p. 995. DOI: 10.1086/165955.

Fushiki, I. and D. Q. Lamb (Dec. 1987a). 'New Insights from a Global View of X-Ray Bursts'. *ApJ* 323, p. L55. DOI: 10.1086/185056.

Fushiki, I. and D. Q. Lamb (June 1987b). 'S-Matrix Calculation of the Triple-Alpha Reaction'. *ApJ* 317, p. 368. DOI: 10.1086/165284.

Galloway, D. K. and A. Cumming (Nov. 2006). 'Helium-rich Thermonuclear Bursts and the Distance to the Accretion-powered Millisecond Pulsar SAX J1808.4-3658'. *ApJ* 652, pp. 559–568. DOI: 10.1086/507598. eprint: astro-ph/0607213.

Galloway, D. K. et al. (Jan. 2004a). 'Periodic Thermonuclear X-Ray Bursts from GS 1826-24 and the Fuel Composition as a Function of Accretion Rate'. *ApJ* 601, pp. 466–473. DOI: 10.1086/380445. eprint: astro-ph/0308122.

Galloway, D. K. et al. (Aug. 2019). 'High-Energy Transients: Thermonuclear (Type-I) X-Ray Bursts'. In *Southern Horizons in Time-Domain Astronomy*. Ed. by R. E. Griffin. Vol. 339. IAU Symposium, pp. 121–126. DOI: 10.1017/S1743921318002363. arXiv: 1803.00223 [astro-ph.HE].

Galloway, D. K. et al. (Mar. 2020). 'The Multi-INstrument Burst ARchive (MINBAR)'. *arXiv e-prints*, arXiv:2003.00685, arXiv:2003.00685. arXiv: 2003.00685 [astro-ph.HE].

Galloway, D. K., A. J. Goodwin and L. Keek (Apr. 2017). 'Thermonuclear Burst Observations for Model Comparisons: A Reference Sample'. *PASA* 34, e019, e019. DOI: 10.1017/pasa.2017.12. arXiv: 1703.07485 [astro-ph.HE].

Galloway, D. K. and L. Keek (Dec. 2017). 'Thermonuclear X-ray bursts'. *arXiv e-prints*, arXiv:1712.06227, arXiv:1712.06227. arXiv: 1712.06227 [astro-ph.HE].

Galloway, D. K. et al. (Sept. 2002). 'Discovery of a High-Latitude Accreting Millisecond Pulsar in an Ultracompact Binary'. *ApJ* 576.2, pp. L137–L140. DOI: 10.1086/343841. arXiv: astro-ph/0206493 [astro-ph].

Galloway, D. K. et al. (Jan. 2004b). 'Periodic Thermonuclear X-Ray Bursts from GS 1826-24 and the Fuel Composition as a Function of Accretion Rate'. *ApJ* 601.1, pp. 466–473. DOI: 10.1086/380445. arXiv: astro-ph/0308122 [astro-ph].

Galloway, D. K. et al. (2006). 'Intermittent pulsations in an accretion-powered millisecond pulsar'. *ApJ* 654.1, p. L73.

Galloway, D. K. et al. (Dec. 2008). 'Thermonuclear (Type I) X-Ray Bursts Observed by the Rossi X-Ray Timing Explorer'. *ApJS* 179.2, pp. 360–422. DOI: 10.1086/592044. arXiv: astro-ph/0608259 [astro-ph].

Giacconi, R. et al. (Dec. 1962). 'Evidence for x Rays From Sources Outside the Solar System'. *Phys. Rev. Lett.* 9.11, pp. 439–443. DOI: 10.1103/PhysRevLett.9.439.

Goldreich, P. and W. H. Julian (Aug. 1969). 'Pulsar Electrodynamics'. *ApJ* 157, p. 869. DOI: 10.1086/150119.

Goodman, J. and J. Weare (Jan. 2010). 'Ensemble samplers with affine invariance'. *Communications in Applied Mathematics and Computational Science* 5.1, pp. 65–80. DOI: 10.2140/camcos.2010.5.65.

Goodwin, A. J., A. Heger and D. K. Galloway (Jan. 2019). 'Neutrino Losses in Type I Thermonuclear X-Ray Bursts: An Improved Nuclear Energy Generation Approximation'. *ApJ* 870.2, 64, p. 64. DOI: 10.3847/1538-4357/aaeed2. arXiv: 1808.02225 [astro-ph.HE].

Goodwin, A. J. and T. E. Woods (May 2020). 'The binary evolution of SAX J1808.4-3658: implications of an evolved donor star'. *MNRAS* 495.1, pp. 796–805. DOI: 10.1093/mnras/staa1234. arXiv: 2003.02970 [astro-ph.HE].

Goodwin, A. J. et al. (Dec. 2019a). 'A Bayesian approach to matching thermonuclear X-ray burst observations with models'. *MNRAS* 490.2, pp. 2228–2240. DOI: 10.1093/mnras/stz2638. arXiv: 1907.00996 [astro-ph.HE].

Goodwin, A. J. et al. (July 2019b). 'XMMU J181227.8-181234: a new ultracompact X-ray binary candidate'. *MNRAS* 486.3, pp. 4149–4157. DOI: 10.1093/mnras/stz1094. arXiv: 1904.10970 [astro-ph.HE].

Goodwin, A. J. et al. (June 2020a). 'A 12 day delay between optical and X-ray activity during outburst rise in a low-mass X-ray binary'. *arXiv e-prints*, arXiv:2006.02872, arXiv:2006.02872. arXiv: 2006.02872 [astro-ph.HE].

Goodwin, A. J. et al. (Oct. 2020b). 'X-ray burst ignition location on the surface of accreting X-ray pulsars: Can bursts preferentially ignite at the hotspot?' *MNRAS* submitted.

Grindlay, J. et al. (May 1976). 'Discovery of intense X-ray bursts from the globular cluster NGC 6624.' *ApJ* 205, pp. L127–L130. DOI: 10.1086/182105.

Hameury, J. M. (Sept. 2020). 'A review of the disc instability model for dwarf novae, soft X-ray transients and related objects'. *Advances in Space Research* 66.5, pp. 1004–1024. DOI: 10.1016/j.asr.2019.10.022. arXiv: 1910.01852 [astro-ph.SR].

Hameury, J.-M. et al. (Aug. 1998). 'Accretion disc outbursts: a new version of an old model'. *MNRAS* 298.4, pp. 1048–1060. DOI: 10.1046/j.1365-8711.1998.01773.x. arXiv: astro-ph/9803242 [astro-ph].

Hansen, C. J. and H. M. van Horn (Feb. 1975). 'Steady-state nuclear fusion in accreting neutron-star envelopes.' *ApJ* 195, pp. 735–741. DOI: 10.1086/153375.

Hartman, J. M. et al. (Mar. 2008). 'The Long-Term Evolution of the Spin, Pulse Shape, and Orbit of the Accretion-powered Millisecond Pulsar SAX J1808.4-3658'. *ApJ* 675.2, pp. 1468–1486. DOI: 10.1086/527461. arXiv: 0708.0211 [astro-ph].

Hayakawa, S. and M. Matsuoka (Jan. 1964). 'Part V. Origin of Cosmic X-Rays'. *Progress of Theoretical Physics Supplement* 30, pp. 204–228. DOI: 10.1143/PTPS.30.204.

He, C. C. and L. Keek (Mar. 2016). 'Anisotropy of X-Ray Bursts from Neutron Stars with Concave Accretion Disks'. *ApJ* 819.1, 47, p. 47. DOI: 10.3847/0004-637X/819/1/47. arXiv: 1512.02889 [astro-ph.HE].

Heger, A., A. Cumming and S. E. Woosley (2007). 'Millihertz quasi-periodic oscillations from marginally stable nuclear burning on an accreting neutron star'. *The Astrophysical Journal* 665.2, p. 1311.

Henyey, L., M. S. Vardya and P. Bodenheimer (Oct. 1965). 'Studies in Stellar Evolution. III. The Calculation of Model Envelopes.' *ApJ* 142, p. 841. DOI: 10.1086/148357.

Hewish, A. et al. (Feb. 1968). 'Observation of a Rapidly Pulsating Radio Source'. *NATURE* 217.5130, pp. 709–713. DOI: 10.1038/217709a0.

Hōshi, R. (May 1979). 'Accretion Model for Outbursts of Dwarf Nova'. *Progress of Theoretical Physics* 61.5, pp. 1307–1319. DOI: 10.1143/PTP.61.1307.

in 't Zand, J. J. M. et al. (Mar. 1998). 'Discovery of the X-ray transient SAX J1808.4-3658, a likely low-mass X-ray binary'. *A&A* 331, pp. L25–L28. eprint: astro-ph/9802098.

in 't Zand, J. J. M. et al. (May 1999). 'A new X-ray outburst in the globular cluster NGC 6440: SAX J1748.9-2021'. *A&A* 345, pp. 100–108. arXiv: astro-ph/9902319 [astro-ph].

Ingham, J. and K. Arnaud. *The Xselect User's Guide*.

Jia, K. and X.-D. Li (Oct. 2016). 'Evolution of Low-mass X-Ray Binaries: The Effect of Donor Evaporation'. *ApJ* 830.2, 153, p. 153. DOI: 10.3847/0004-637X/830/2/153. arXiv: 1608.01076 [astro-ph.HE].

Johnston, Z., A. Heger and D. K. Galloway (June 2018). 'Simulating X-ray bursts during a transient accretion event'. *MNRAS* 477.2, pp. 2112–2118. DOI: 10.1093/mnras/sty757. arXiv: 1711.03970 [astro-ph.HE].

Joss, P. C. (Nov. 1978). 'Helium-burning flashes on an accreting neutron star - A model for X-ray burst sources'. *ApJ* 225, pp. L123–L127. DOI: 10.1086/182808.

Joyce, J. (2003). 'Bayes' theorem'.

Kaaret, P. et al. (Feb. 2006). 'Discovery of the Millisecond X-Ray Pulsar HETE J1900.1-2455'. *ApJ* 638.2, pp. 963–967. DOI: 10.1086/498886. arXiv: astro-ph/0510483 [astro-ph].

Keek, L. and A. Heger (Feb. 2016). 'Carbon production on accreting neutron stars in a new regime of stable nuclear burning'. *MNRAS* 456.1, pp. L11–L15. DOI: 10.1093/mnrasl/slv167. arXiv: 1508.06630 [astro-ph.HE].

Keek, L. et al. (Feb. 2017). 'X-Ray Reflection and an Exceptionally Long Thermonuclear Helium Burst from IGR J17062-6143'. *ApJ* 836.1, 111, p. 111. DOI: 10.3847/1538-4357/836/1/111. arXiv: 1610.07608 [astro-ph.HE].

King, A. R. (2006). 'Accretion in compact binaries'. In. *Compact stellar X-ray sources*. Vol. 39, pp. 507–546.

Kirsch, M. G. F. et al. (Aug. 2004). 'Studies of orbital parameters and pulse profile of the accreting millisecond pulsar XTE J1807-294'. *A&A* 423, pp. L9–L12. DOI: 10.1051/0004-6361:200400022. arXiv: astro-ph/0407017 [astro-ph].

Klis, M Van der et al. (1996). 'Discovery of submillisecond quasi-periodic oscillations in the X-ray flux of Scorpius X-1'. *ApJ* 469.1, p. L1.

Krimm, H. A. et al. (Oct. 2007). 'Discovery of the Accretion-powered Millisecond Pulsar SWIFT J1756.9-2508 with a Low-Mass Companion'. *ApJ* 668.2, pp. L147–L150. DOI: 10.1086/522959.

Kuiper, G. P. (Jan. 1941). 'On the Interpretation of β Lyrae and Other Close Binaries.' *ApJ* 93, p. 133. DOI: 10.1086/144252.

Kuiper, L. et al. (Sept. 2020). 'High-energy characteristics of the accretion-powered millisecond pulsar IGR J17591-2342 during its 2018 outburst. XMM-Newton, NICER, NuSTAR, and INTEGRAL view of the 0.3-300 keV X-ray band'. *A&A* 641, A37, A37. DOI: 10.1051/0004-6361/202037812.

Kuulkers, E. et al. (2003). 'Photospheric radius expansion x-ray bursts as standard candles'. *Astronomy & Astrophysics* 399.2, pp. 663–680.

Lampe, N., A. Heger and D. K. Galloway (Mar. 2016). 'The Influence of Accretion Rate and Metallicity on Thermonuclear Bursts: Predictions from KEPLER Models'. *ApJ* 819.1, 46, p. 46. DOI: 10.3847/0004-637X/819/1/46. arXiv: 1512.05769 [astro-ph.HE].

Lapidus, I. I. and R. A. Sunyaev (Nov. 1985). 'Angular distribution and polarization of X-ray-burster radiation (during stationary and flash phases)'. *MNRAS* 217, pp. 291–303. DOI: 10.1093/mnras/217.2.291.

Lasota, J.-P. (June 2001). 'The disc instability model of dwarf novae and low-mass X-ray binary transients'. *New Astronomy Rev.* 45.7, pp. 449–508. DOI: 10.1016/S1387-6473(01)00112-9. arXiv: astro-ph/0102072 [astro-ph].

Lewin, W. H. G., J. van Paradijs and R. E. Taam (Sept. 1993). 'X-Ray Bursts'. *Space Sci. Rev.* 62.3-4, pp. 223–389. DOI: 10.1007/BF00196124.

Lewin, W. H., W. D. Vacca and E. Basinska (1984). 'Precursors to X-ray bursts-The result of expansion and subsequent contraction of the neutron star's photosphere'. *ApJ* 277, pp. L57–L60.

Lewis, F. et al. (July 2010). 'The double-peaked 2008 outburst of the accreting millisecond X-ray pulsar, IGR J00291+5934'. *A&A* 517, A72, A72. DOI: 10.1051/0004-6361/201014382. arXiv: 1005.1178 [astro-ph.HE].

Lin, D. N. C., J. Papaloizou and J. Faulkner (Jan. 1985). 'On the evolution of accretion disc flow in cataclysmic variables - III. Outburst properties of constant and uniform -alpha model discs.' *MNRAS* 212, pp. 105–149. DOI: 10.1093/mnras/212.1.105.

MacKay, D. J. (2003). *Information theory, inference and learning algorithms*. Cambridge university press.

Manchester, R. N. (Sept. 2017a). 'Millisecond Pulsars, their Evolution and Applications'. *Journal of Astrophysics and Astronomy* 38.3, 42, p. 42. DOI: 10.1007/s12036-017-9469-2. arXiv: 1709.09434 [astro-ph.HE].

Manchester, R. N. (2017b). 'Pulsars and gravity'. In. *One Hundred Years of General Relativity: From Genesis and Empirical Foundations to Gravitational Waves*. Vol. 1, pp. 407–458. DOI: 10.1142/9789814635134_0009.

Manchester, R. N. et al. (Apr. 2005). 'The Australia Telescope National Facility Pulsar Catalogue'. *AJ* 129.4, pp. 1993–2006. DOI: 10.1086/428488. arXiv: astro-ph/0412641 [astro-ph].

Manchester, R. N. and J. H. Taylor (1977). *Pulsars*.

Markwardt, C. B., E. Smith and J. H. Swank (Feb. 2003). 'XTE J1807-294'. *IAU Circ.* 8080, p. 2.

Markwardt, C. B. et al. (Aug. 2002). 'Discovery of a Second Millisecond Accreting Pulsar: XTE J1751-305'. *ApJ* 575.1, pp. L21–L24. DOI: 10.1086/342612. arXiv: astro-ph/0206491 [astro-ph].

Meisel, Z. (June 2018). 'Consistent Modeling of GS 1826-24 X-Ray Bursts for Multiple Accretion Rates Demonstrates the Possibility of Constraining rp-process Reaction Rates'. *ApJ* 860.2, 147, p. 147. DOI: 10.3847/1538-4357/aac3d3. arXiv: 1805.05552 [astro-ph.HE].

Menou, K., J.-M. Hameury and R. Stehle (May 1999). 'Structure and properties of transition fronts in accretion discs'. *MNRAS* 305.1, pp. 79–89. DOI: 10.1046/j.1365-8711.1999.02396.x. arXiv: astro-ph/9811188 [astro-ph].

Menou, K. et al. (May 2000). 'Disc instability models for X-ray transients: evidence for evaporation and low α-viscosity?' *MNRAS* 314.3, pp. 498–510. DOI: 10.1046/j.1365-8711.2000.03357.x. arXiv: astro-ph/0001203 [astro-ph].

Metropolis, N. et al. (1953). 'Equation of state calculations by fast computing machines'. *The journal of chemical physics* 21.6, pp. 1087–1092.

Meyer, F. and E. Meyer-Hofmeister (Jan. 1981). 'On the elusive cause of cataclysmic variable outbursts.' *A&A* 104, pp. L10–L12.

Minkowski, R. (Jan. 1939). 'No. 602. The spectra of the supernovae in IC 4182 and in NGC 1003.' *Contributions from the Mount Wilson Observatory / Carnegie Institution of Washington* 602, pp. 1–62.

Nagase, F. (Jan. 1989). 'Accretion-powered X-ray pulsars.' *PASJ* 41, p. 1.

Narayan, R. and J. S. Heyl (2003). 'Thermonuclear stability of material accreting onto a neutron star'. *The Astrophysical Journal* 599.1, p. 419.

Nelemans, G., P. G. Jonker and D. Steeghs (July 2006). 'Optical spectroscopy of (candidate) ultracompact X-ray binaries: constraints on the composition of the donor stars'. *MNRAS* 370.1, pp. 255–262. DOI: 10.1111/j.1365-2966.2006.10496.x. arXiv: astro-ph/0604597 [astro-ph].

Ng, M. et al. (Oct. 2020). 'NICER detection of 376 Hz X-ray pulsations from IGR J17494-3030'. *The Astronomer's Telegram* 14124, p. 1.

Papitto, A. et al. (Mar. 2007). 'Timing of the accreting millisecond pulsar XTE J1814-338'. *MNRAS* 375.3, pp. 971–976. DOI: 10.1111/j.1365-2966.2006.11359.x. arXiv: astro-ph/0611942 [astro-ph].

Papitto, A. et al. (Jan. 2008). 'Measuring the spin up of the accreting millisecond pulsar XTEJ1751-305'. *MNRAS* 383.1, pp. 411–416. DOI: 10.1111/j.1365-2966.2007.12551.x. arXiv: 0710.1215 [astro-ph].

Papitto, A. et al. (Oct. 2010). 'The X-ray spectrum of the newly discovered accreting millisecond pulsar IGR J17511-3057'. *MNRAS* 407.4, pp. 2575–2588. DOI: 10.1111/j.1365-2966.2010.17090.x. arXiv: 1005.4827 [astro-ph.HE].

Patruno, A. and A. Watts (2012). 'Accreting millisecond X-ray pulsars'. *arXiv preprint arXiv:1206.2727*.

Patruno, A. et al. (Feb. 2012). 'Accelerated Orbital Expansion and Secular Spin-down of the Accreting Millisecond Pulsar SAX J1808.4-3658'. *ApJ* 746.2, L27, p. L27. DOI: 10.1088/2041-8205/746/2/L27. arXiv: 1111.6967 [astro-ph.HE].

Paxton, B. et al. (Jan. 2011). 'Modules for Experiments in Stellar Astrophysics (MESA)'. *ApJS* 192.1, 3, p. 3. DOI: 10.1088/0067-0049/192/1/3. arXiv: 1009.1622 [astro-ph.SR].

Paxton, B. et al. (Sept. 2013). 'Modules for Experiments in Stellar Astrophysics (MESA): Planets, Oscillations, Rotation, and Massive Stars'. *ApJS* 208.1, 4, p. 4. DOI: 10.1088/0067-0049/208/1/4. arXiv: 1301.0319 [astro-ph.SR].

Paxton, B. et al. (Sept. 2015). 'Modules for Experiments in Stellar Astrophysics (MESA): Binaries, Pulsations, and Explosions'. *ApJS* 220.1, 15, p. 15. DOI: 10.1088/0067-0049/220/1/15. arXiv: 1506.03146 [astro-ph.SR].

Paxton, B. et al. (Feb. 2018). 'Modules for Experiments in Stellar Astrophysics (MESA): Convective Boundaries, Element Diffusion, and Massive Star Explosions'. *ApJS* 234.2, 34, p. 34. DOI: 10.3847/1538-4365/aaa5a8. arXiv: 1710.08424 [astro-ph.SR].

Paxton, B. et al. (July 2019). 'Modules for Experiments in Stellar Astrophysics (MESA): Pulsating Variable Stars, Rotation, Convective Boundaries, and Energy Conservation'. *ApJS* 243.1, 10, p. 10. DOI: 10.3847/1538-4365/ab2241. arXiv: 1903.01426 [astro-ph.SR].

Peng, F., E. F. Brown and J. W. Truran (2007). 'Sedimentation and type I X-ray bursts at low accretion rates'. *The Astrophysical Journal* 654.2, p. 1022.

Peters, P. C. (1964). 'Gravitational radiation and the motion of two point masses'. *Physical Review* 136.4B, B1224.

Podsiadlowski, P., S. Rappaport and E. Pfahl (2002). 'Evolutionary sequences for low- and intermediate-mass X-ray binaries'. *The Astrophysical Journal* 565.2, p. 1107.

Pogson, N. (May 1857). 'On the Variable Star U Geminorum'. *MNRAS* 17, pp. 200–202. DOI: 10.1093/mnras/17.7.200.

Pringle, J. E. (Jan. 1981). 'Accretion discs in astrophysics'. *ARA&A* 19, pp. 137–162. DOI: 10.1146/annurev.aa.19.090181.001033.

Pringle, J. E. and M. J. Rees (Oct. 1972). 'Accretion Disc Models for Compact X-Ray Sources'. *A&A* 21, p. 1.

Rai, B. and B. C. Paul (Nov. 2019). 'NUSTAR and Swift observations of AMXP Swift J1756.9-2508 during its 2018 outburst'. *MNRAS* 489.4, pp. 5858–5865. DOI: 10.1093/mnras/stz2510.

Rappaport, S., F. Verbunt and P. C. Joss (Dec. 1983). 'A new technique for calculations of binary stellar evolution application to magnetic braking.' *ApJ* 275, pp. 713–731. DOI: 10.1086/161569.

Rauscher, T. and F.-K. Thielemann (May 2000). 'Astrophysical Reaction Rates From Statistical Model Calculations'. *Atomic Data and Nuclear Data Tables* 75.1-2, pp. 1–351. DOI: 10.1006/adnd.2000.0834. arXiv: astro-ph/0004059 [astro-ph].

Remillard, R. A., J. Swank and T. Strohmayer (May 2002). 'XTE J0929-314'. *IAU Circ.* 7893, p. 1.

Riggio, A. et al. (May 2008). 'Spin-up and Phase Fluctuations in the Timing of the Accreting Millisecond Pulsar XTE J1807-294'. *ApJ* 678.2, pp. 1273–1278. DOI: 10.1086/533578. arXiv: 0710.3450 [astro-ph].

Ritter, H. (Aug. 1988). 'Turning on and off mass transfer in cataclysmic binaries.' *A&A* 202, pp. 93–100.

Rosenbluth, M. N. et al. (Sept. 1973). 'Nuclear Fusion in Accreting Neutron Stars'. *ApJ* 184, pp. 907–910. DOI: 10.1086/152380.

Rosenthal, J. S. et al. (2011). 'Optimal proposal distributions and adaptive MCMC'. *Handbook of Markov Chain Monte Carlo* 4.10.1201.

Ruderman, M. A. and P. G. Sutherland (Feb. 1975). 'Theory of pulsars: polar gaps, sparks, and coherent microwave radiation.' *ApJ* 196, pp. 51–72. DOI: 10.1086/153393.

Sandage, A. et al. (Oct. 1966). 'On the optical identification of SCO X-1.' *ApJ* 146, p. 316. DOI: 10.1086/148892.

Sanna, A. et al. (Apr. 2017). 'Spectral and timing properties of IGR J00291+5934 during its 2015 outburst'. *MNRAS* 466.3, pp. 2910–2917. DOI: 10.1093/mnras/stw3332. arXiv: 1612.03865 [astro-ph.HE].

Sanna, A. et al. (Feb. 2018a). 'Discovery of 105 Hz coherent pulsations in the ultracompact binary IGR J16597-3704'. *A&A* 610, L2, p. L2. DOI: 10.1051/0004-6361/201732262. arXiv: 1711.03092 [astro-ph.HE].

Sanna, A. et al. (Oct. 2018b). 'NuSTAR and NICER reveal IGR J17591-2342 as a new accreting millisecond X-ray pulsar'. *A&A* 617, L8, p. L8. DOI: 10.1051/0004-6361/201834160. arXiv: 1808.10195 [astro-ph.HE].

Sanna, A. et al. (Aug. 2018c). 'XMM-Newton detection of the 2.1 ms coherent pulsations from IGR J17379-3747'. *A&A* 616, L17, p. L17. DOI: 10.1051/0004-6361/201833205. arXiv: 1807.08574 [astro-ph.HE].

Sanna, A. et al. (May 2020). 'Timing of the accreting millisecond pulsar IGR J17591-2342: evidence of spin-down during accretion'. *MNRAS* 495.2, pp. 1641–1649. DOI: 10.1093/mnras/staa1253. arXiv: 2003.05069 [astro-ph.HE].

Schatz, H et al. (2001). 'End point of the rp process on accreting neutron stars'. *Physical Review Letters* 86.16, p. 3471.

Schatz, H. et al. (May 2003). 'Nuclear physics in normal X-ray bursts and superblasts'. *Nucl. Phys. A* 718, pp. 247–254. DOI: 10.1016/S0375-9474(03)00722-X.

Shakura, N. I. and R. A. Sunyaev (June 1973). 'Reprint of 1973A&A....24..337S. Black holes in binary systems. Observational appearance.' *A&A* 500, pp. 33–51.

Shapiro, S. L. and S. A. Teukolsky (1983). *Black holes, white dwarfs, and neutron stars : the physics of compact objects*.

Shklovsky, I. S. (Apr. 1967). 'On the Nature of the Source of X-Ray Emission of Sco XR-1.' *ApJ* 148, p. L1. DOI: 10.1086/180001.

Smak, J. (Jan. 1984). 'Accretion in cataclysmic binaries. IV. Accretion disks in dwarf novae.' *Acta Astronaut.* 34, pp. 161–189.

Smarr, L. L. and R. Blandford (July 1976). 'The binary pulsar: physical processes, possible companions, and evolutionary histories.' *ApJ* 207, pp. 574–588. DOI: 10.1086/154524.

Spitkovsky, A., Y. Levin and G. Ushomirsky (Feb. 2002). 'Propagation of Thermonuclear Flames on Rapidly Rotating Neutron Stars: Extreme Weather during Type I X-Ray Bursts'. *ApJ* 566.2, pp. 1018–1038. DOI: 10.1086/338040. arXiv: astro-ph/0108074 [astro-ph].

Strohmayer, T. and L. Bildsten (Jan. 2003). 'New Views of Thermonuclear Bursts'. *ArXiv Astrophysics e-prints*. eprint: astro-ph/0301544.

Strohmayer, T. and L. Keek (Feb. 2017). 'IGR J17062-6143 Is an Accreting Millisecond X-Ray Pulsar'. *ApJ* 836.2, L23, p. L23. DOI: 10.3847/2041-8213/aa5e51. arXiv: 1702.05449 [astro-ph.HE].

Strohmayer, T. E. et al. (Sept. 1996). 'Millisecond X-Ray Variability from an Accreting Neutron Star System'. *ApJ* 469, p. L9. DOI: 10.1086/310261.

Strohmayer, T. E. et al. (Oct. 2003). 'X-Ray Bursts from the Accreting Millisecond Pulsar XTE J1814-338'. *ApJ* 596.1, pp. L67–L70. DOI: 10.1086/379158. arXiv: astro-ph/0308353 [astro-ph].

Suleimanov, V. F. et al. (Dec. 2017). 'Basic parameters of the helium-accreting X-ray bursting neutron star in 4U 1820-30'. *MNRAS* 472.4, pp. 3905–3913. DOI: 10.1093/mnras/stx2234. arXiv: 1708.09168 [astro-ph.HE].

Taam, R. E. (Oct. 1980). 'X-ray bursts from thermonuclear runaways on accreting neutron stars'. *ApJ* 241, pp. 358–366. DOI: 10.1086/158348.

Taam, R. E. (1984). 'The thermonuclear flash model for X-ray bursts'. In *High Energy Transients in Astrophysics*. Vol. 115. 1. AIP Publishing, pp. 263–272.

Taam, R. E., S. E. Woosley and D. Q. Lamb (Mar. 1996). 'The Effect of Deep Hydrogen Burning in the Accreted Envelope of a Neutron Star on the Properties of X-Ray Bursts'. *ApJ* 459, p. 271. DOI: 10.1086/176890.

Tasheva, R. P. and I. Z. Stefanov (Feb. 2019). 'The microquasar XTE J1807-294 - Mass evaluation by means of the relativistic precession model'. In *American Institute of Physics Conference Series*. Vol. 2075. American Institute of Physics Conference Series, p. 090007. DOI: 10.1063/1.5091221.

Tauris, T. M. and E. P. J. van den Heuvel (2006). 'Formation and evolution of compact stellar X-ray sources'. In. *Compact stellar X-ray sources*. Vol. 39, pp. 623–665.

Tetarenko, A. J. et al. (Feb. 2018a). 'A Radio Frequency Study of the Accreting Millisecond X-ray Pulsar, IGR J16597-3704, in the Globular Cluster NGC 6256'. *ApJ* 854.2, 125, p. 125. DOI: 10.3847/1538-4357/aaa95a. arXiv: 1801.05778 [astro-ph.HE].

Tetarenko, B. E. et al. (Feb. 2018b). 'Strong disk winds traced throughout outbursts in black-hole X-ray binaries'. *NATURE* 554.7690, pp. 69–72. DOI: 10.1038/nature25159. arXiv: 1801.07203 [astro-ph.HE].

Tse, K., Y. Chou and H.-E. Hsieh (Aug. 2020). 'Updated Spin and Orbital Parameters and Energy Dependent Pulse Behaviors of the Accreting Millisecond X-Ray Pulsar IGR J17591-2342'. *ApJ* 899.2, 120, p. 120. DOI: 10.3847/1538-4357/aba18f.

van den Heuvel, E. P. J. (Jan. 1994). 'Interacting binaries: topics in close binary evolution.' In *Saas-Fee Advanced Course 22: Interacting Binaries*, pp. 263–474.

van Paradijs, J. (June 1996). 'On the Accretion Instability in Soft X-Ray Transients'. *ApJ* 464, p. L139. DOI: 10.1086/310100.

van Paradijs, J., W. Penninx and W. H. G. Lewin (July 1988). 'On the relation between X-ray burst properties and the persistent X-ray luminosity'. *MNRAS* 233, pp. 437–450. DOI: 10.1093/mnras/233.2.437.

Vetterling, W. T. et al. (2002). *Numerical Recipes (C++): The Art of Scientific Computing*. Cambridge University Press.

Wallace, R. K. and S. E. Woosley (Feb. 1981). 'Explosive hydrogen burning'. *ApJS* 45, pp. 389–420. DOI: 10.1086/190717.

Watts, A. L. (Sept. 2012). 'Thermonuclear Burst Oscillations'. *ARA&A* 50, pp. 609–640. DOI: 10.1146/annurev-astro-040312-132617. arXiv: 1203.2065 [astro-ph.HE].

Weaver, T. A., G. B. Zimmerman and S. E. Woosley (Nov. 1978). 'Presupernova evolution of massive stars.' *ApJ* 225, pp. 1021–1029. DOI: 10.1086/156569.

Wijnands, R. (June 2004). 'An observational review of accretion-driven millisecond X-ray pulsars'. *Nuclear Physics B Proceedings Supplements* 132, pp. 496–505. DOI: 10.1016/j.nuclphysbps.2004.04.084. eprint: astro-ph/0309347.

Wijnands, R. and M. Van der Klis (1998). 'A millisecond pulsar in an X-ray binary system'. *NATURE* 394.6691, pp. 344–346.

Woosley, S. E. and R. E. Taam (Sept. 1976). 'γ-ray bursts from thermonuclear explosions on neutron stars'. *NATURE* 263.5573, pp. 101–103. DOI: 10.1038/263101a0.

Woosley, S. E. et al. (Mar. 2004). 'Models for Type I X-Ray Bursts with Improved Nuclear Physics'. *ApJS* 151.1, pp. 75–102. DOI: 10.1086/381533. arXiv: astro-ph/0307425 [astro-ph].

Zhang, W. et al. (Mar. 1998). 'Millisecond Oscillations in the Persistent and Bursting Flux of Aquila X-1 during an Outburst'. *ApJ* 495.1, pp. L9–L12. DOI: 10.1086/311210. arXiv: astro-ph/9712300 [astro-ph].

Zingale, M. et al. (July 2015). 'Comparisons of Two- and Three-Dimensional Convection in Type I X-Ray Bursts'. *ApJ* 807.1, 60, p. 60. DOI: 10.1088/0004-637X/807/1/60. arXiv: 1410.5796 [astro-ph.HE].

Zwicky, F. (Nov. 1938). 'On Collapsed Neutron Stars.' *ApJ* 88, pp. 522–525. DOI: 10.1086/144003.